

Deposition and characterisation of bismuth layer-structured ferroelectric films

Xiaobing Hu
Downing College
University of Cambridge



A dissertation submitted for the degree of Doctor of Philosophy at the
University of Cambridge

February 2006

To my parents

致 父 母

Table of contents

Declaration	i
Summary	ii
Acknowledgements	iii
Publications	v
Glossary of Acronyms	vi
Chapter 1 Introduction	1
1.1 Background.....	1
1.2 Purpose of the research.....	5
1.3 Contents of the research	6
1.4 Outline	7
1.5 References	8
Chapter 2 Ferroelectric thin films	10
2.1 Ferroelectricity.....	10
2.2 Ferroelectric Random Access Memory (FeRAM).....	13
2.2.1 <i>Ferroelectric memories</i>	13
2.2.2 <i>Principle of basic operation</i>	15
2.3 Ferroelectric film materials for memories	17
2.4 Pulsed laser deposition (PLD)	21
2.5 Chemical solution deposition (CSD).....	23
2.5.1 <i>Selection and preparation of precursors</i>	24
2.5.2 <i>Film deposition -- Spin coating and baking</i>	26
2.6 Epitaxial thin films	28
2.7 Piezoelectricity	30
2.7.1 <i>Piezoelectric effect</i>	30
2.7.2 <i>Piezoresponse force microscopy (PFM)</i>	31
2.8 References	34
Chapter 3 Experimental techniques	36
3.1 Film fabrication	36
3.1.1 <i>PLD</i>	36
3.1.1.1 Preparation	36
3.1.1.2 Deposition	38
3.1.2 <i>CSD</i>	41
3.1.2.1 Selection of precursors.....	41
3.1.2.2 Preparation of precursor solutions	41
3.1.2.3 Film deposition	43
3.2 Film characterisations.....	43
3.2.1 <i>Structural characterisations</i>	43

3.2.1.1 X-ray diffraction (XRD) studies	43
3.2.1.2 Atomic force microscopy (AFM) studies.....	45
3.2.1.3 Piezoresponse force microscopy (PFM) studies	47
3.2.1.4 Thickness measurement of thin films	52
3.2.1.5 Raman and infrared spectroscopy	53
3.2.1.6 Scanning electron microscopy (SEM) and energy dispersive X-ray spectrometry (EDX).....	54
3.2.2 <i>Electrical characterisations</i>	56
3.2.2.1 Dielectric properties	56
3.2.2.2 Ferroelectric properties and leakage current measurement.....	56
3.2.2.3 Low temperature electrical measurement	68
3.3 References	69
Chapter 4 PLD-grown W-substituted strontium bismuth tantalate (SBT) thin films	70
4.1 Background and motivation.....	70
4.2 Experimental details	71
4.2.1 <i>Target fabrication</i>	71
4.2.2 <i>Film deposition and growth process</i>	71
4.3 Results and discussion	73
4.3.1 <i>Effect of processing on film properties</i>	73
4.3.1.1 <i>Structural properties</i>	73
4.3.1.2 <i>Electrical properties</i>	77
4.3.2 <i>Effect of doping level on film properties</i>	81
4.3.2.1 <i>Structural properties</i>	81
4.3.2.2 <i>Electrical properties</i>	83
4.4 Conclusions	85
4.5 References	86
Chapter 5 Epitaxial Nd-doped bismuth titanate thin films on single crystal substrates	87
5.1 Background and motivation.....	87
5.2 Experimental details	88
5.3 Results and discussion	89
5.3.1 <i>Structural properties of the targets</i>	89
5.3.2 <i>Structural properties of the films</i>	92
5.3.2.1 Crystallographic orientations and epitaxial relationships	92
5.3.2.2 Surface morphological studies	97
5.3.3 <i>Electrical properties</i>	98
5.3.3.1 Ferroelectric properties	98
5.3.3.2 Leakage current properties	103
5.3.3.3 Electrical fatigue properties	105
5.4 Conclusions	106
5.5 References	108
Chapter 6 PLD-grown Sm-doped bismuth titanate polycrystalline ferroelectric thin films	110
6.1 Background.....	110
6.2 Effect of processing temperatures on film properties.....	111
6.2.1 <i>Experimental details</i>	111

6.2.1.1 Target fabrication	111
6.2.1.2 Film deposition and characterisations	112
6.2.2 Results and discussion	112
6.2.2.1 Structural properties	112
6.2.2.2 Electrical properties	120
6.3 Effect of Pt layer orientations	122
6.3.1 Motivation	122
6.3.2 Experimental details	122
6.3.3 Results and discussion	123
6.3.3.1 Structural properties	123
6.3.3.2 Electrical properties	127
6.4 Effect of different doping level.....	129
6.4.1 Motivation	129
6.4.2 Structural properties	130
6.4.2.1 XRD studies	130
6.4.2.2 AFM studies	131
6.4.2.3 Raman spectroscopy.....	131
6.4.3 Electrical properties.....	135
6.4.3.1 Ferroelectric properties	135
6.4.3.2 Dielectric properties	137
6.4.3.3 Leakage current properties.....	137
6.4.3.4 Electrical fatigue properties	137
6.4.4 Discussion and conclusions	138
6.5 Effect of LaNiO ₃ (LNO) buffer layer	141
6.5.1 Motivation	141
6.5.2 Experimental details	142
6.5.3 Results and discussion	142
6.5.3.1 AFM studies	142
6.5.3.2 Ferroelectric properties	143
6.5.3.3 Leakage current properties.....	145
6.6 References	147

Chapter 7 CSD-derived Sm- and Nd-doped bismuth titanate polycrystalline ferroelectric thin films150

7.1 Background.....	150
7.2 CSD-derived BSmT films.....	151
7.2.1 Experimental results.....	151
7.2.1.1 Characterisation of precursors: <i>in-situ</i> FT-IR study.....	151
7.2.1.2 Structural properties	154
7.2.1.3 Electrical properties	160
7.2.2 Discussion and conclusions	166
7.3 Low temperature properties of BSmT films.....	167
7.3.1 Motivation	167
7.3.2 Results and discussion	168
7.3.3 Conclusions.....	174
7.4 CSD-derived BNdT films	174
7.4.1 Results and discussion	174
7.4.1.1 Structural properties	174
7.4.1.2 Electrical properties	179
7.4.2 Conclusions.....	183

7.5 Effect of annealing atmospheres on CSD-derived BNdT films	184
7.5.1 Motivation	184
7.5.2 Experimental procedure	184
7.5.3 Results and discussion	185
7.5.3.1 Structural properties	185
7.5.3.2 Electrical properties	188
7.5.4 Conclusions	192
7.6 Discussion and conclusions	192
7.7 References	195
Chapter 8 Piezoelectric properties of Sm-doped bismuth titanate ferroelectric thin films	200
8.1 Motivation	200
8.2 Results and discussion	202
8.2.1 Domain imaging.....	202
8.2.2 Domain manipulation (writing and switching).....	205
8.2.3 Local ferroelectric measurement - d_{33} hysteresis measurement.....	207
8.2.4 Local piezoelectric measurement – Q_{eff}	210
8.2.5 Piezoelectric properties of PLD- and CSD-derived BSmT films	220
8.3 Conclusions	224
8.4 References	225
Chapter 9 Conclusions and future work.....	227
9.1 Conclusions	227
9.1.1 PLD-grown W-substituted SBT thin films	227
9.1.2 PLD-grown epitaxial BNdT films.....	227
9.1.3 PLD-grown polycrystalline BSmT films.....	228
9.1.4 CSD-derived polycrystalline BSmT and BNdT films.....	230
9.1.5 Piezoelectric properties of BSmT films	233
9.2 Future work.....	233

Declaration

This dissertation is submitted for the degree of Doctor of Philosophy at the University of Cambridge. It contains the work carried out between October 2002 and February 2006 in the Department of Materials Science and Metallurgy, University of Cambridge, under the supervision of Dr. Zoe H. Barber.

I certify that, except where indicated, the work described is, to the best of my knowledge, original and my own work. No part of this dissertation has previously been submitted for any qualifications at this or any other university or other establishment. This dissertation does not exceed 60,000 words.

Xiaobing Hu

Downing College, Cambridge
February 2006

Summary

Bismuth layer-structured ferroelectrics have been recognised as promising film materials for ferroelectric random access memory application due to their excellent fatigue resistance and other electrical properties. This work deals with the deposition and characterisation of epitaxial and polycrystalline W-doped $\text{SrBi}_2\text{Ta}_2\text{O}_9$ (SBT) and lanthanide-doped bismuth titanate (BiT) films.

SBT and W-doped SBT films were fabricated by pulsed laser deposition (PLD) on platinised silicon substrates. The effects of fabrication temperature and W-doping level on film properties were studied. The crystallinity of SBTW films improved with increasing fabrication temperatures, resulting in enhanced ferroelectric properties and dielectric properties above the fabrication temperature of 750 °C.

Dense ceramic samples of Nd- and Sm-doped BiT (BNdT and BSmT) were successfully fabricated for PLD targets by solid state processing. Highly epitaxially (001)-, (118)-, and (104)-oriented Nd-doped bismuth titanate (BNdT) films were grown by PLD on (001)-, (011)-, and (111)-oriented SrTiO_3 (STO) single crystal substrates, respectively. A three-dimensional orientation relationship between films and substrates was derived as: BNdT(001)//STO(001), BNdT[$\bar{1}10$]/STO[100]. Films showed strong dependence of structural and ferroelectric properties on the crystal orientation.

PLD-grown BSmT films on platinised silicon substrates were studied as a function of fabrication temperature, effects of Pt bottom layer orientation, Sm doping level, and LaNiO_3 buffer layer.

An alkoxide-salt chemical solution deposition (CSD) method was adopted to prepare the precursors for BSmT (BNdT) film fabrication. Precursors of Bi-Sm(Nd)-Ti which were stable for at least eight months in air ambient were successfully developed. *In-situ* FT-IR studies suggest that acetic acid serves as chelating agent to improve the homogeneity of the precursor solution by generating a dense and homogeneous Ti-O-Ti polymeric network. The electrical properties of the films fabricated in this study (dielectric and ferroelectric properties, leakage current characteristics and electrical fatigue properties), are comparable or superior to these previously reported for similar films developed by other techniques or with other doping elements. Low temperature electrical properties of BSmT films suggest that the films are very promising for extremely low temperature nonvolatile memory applications.

The results of BNdT films annealed at different oxygen partial pressure (O_2 , air, N_2) showed that oxygen ambience affected structural properties of the films by enhancing the growth of perovskite phase (phase formation), increasing grain size (grain growth), and assisting the growth of (117)-oriented grains (crystallographic orientations).

Piezoresponse force microscopy (PFM) was adopted to characterise BSmT films. Domain structures were clearly observed in a PLD-grown BSmT film, which were closely related to the grain structures. Domain manipulation was carried out in a CSD-derived BSmT film, showing that the film can be nearly uniformly polarised, which can be used in nanoscale device fabrication. Clear hysteresis loops were measured by PFM, which was an important proof of ferroelectricity. Large spatial variations of piezoelectric hysteresis loops of a CSD-derived BSmT film were observed across the film surface. Effective electrostriction coefficient (Q_{eff}) of a PLD-grown BSmT film was measured, showing that BSmT films had better piezoelectric properties (higher Q_{eff} , higher d_{zz}) than SBT films, un-doped BiT ceramics and films. It suggests that BSmT films are promising piezoelectric materials for MEMS use.

Acknowledgements

There are a lot of people whom I would like to thank, but first and foremost, I would like to thank Dr. Zoe H. Barber for her supervision, guidance, patience, and support throughout the years.

I am extremely grateful to Dr. Ashish Garg for his advice and help, as well as teaching me experimental skills. I would like to thank Professor John Wang (from National University of Singapore) for offering me a lot of useful guidance during my first year.

Thanks are also due to Prof. James F. Scott and his group members: Dr. Finlay Morrison, Mr. (now Dr.) DJ Jung, and Mr. (and Dr.-ing) Xiaojie Lou, at Department of Earth Sciences, for their great help with the measurement of electrical properties: Mr. Xiaojie Lou and Dr. Ming Zhang offered great help on some of the measurement of Raman and FT-IR measurements; Dr. Finlay Morrison gave useful help on some of the film annealing and measurements; Mr. DJ Jung helped me with some of the electrical measurements.

Daily laboratory work is enjoyable and yet challenging, and I would like to thank many of my fellow colleagues for their assistance that facilitated the work. I would also like to express my appreciation towards many of my colleagues in their kind assistance throughout the project, in no particular order: Karen Yates (for her help with Raman spectroscopy), Edward Tarte (for his useful discussion and suggestions on my work). Mary Vickers (for her help with X-ray diffraction measurements), James Chapman (for his help with the PLD deposition system); Nadia Stelmashenko (for her help with lots of general issues); Rumen Tomov (for his help with some of the PLD deposition), Alex Michtchenko (for his useful discussion and invitations to formal hall and guest nights...). Help from other members of Device Materials group are also greatly appreciated.

I would like to express my deepest thanks and love to my parents for their endless support, encouragement, and attention towards my study. Thirteen years ago, I left my hometown for study and research, -- it has never stopped since. They have not seen much of me since then. During these years, I missed seeing them at almost all of the most important festivals and holidays with them: Chinese New Year (spring festival), mid-autumn festivals, *etc.*

I would also like to thank Ms. Karen Lubarr of Downing College Library for offering me great help with my work and life in Cambridge, and the encouragement during my job hunting.

My years in Downing College will be unforgettable, especially the days with my housemates:

Alicia, Ming and Wei. I will remember the days we sat in the kitchen talking, and had fun together in Cambridge.

I should also thank all my other friends in Cambridge, especially the Chinese Gates scholars, Cambridge Tsinghua Alumni, Cambridge EAP (English for Academic Purposes) 2002 class, my tennis and squash partners. Without you, my life in Cambridge would not be so colourful and enjoyable.

I would also like to acknowledge the financial support from Gates Cambridge Trust and the ORS committee.

Xiaobing Hu
胡晓冰

Downing College, Cambridge
February 2006

Publications

Parts of this thesis have been published (or to be submitted) as detailed below.

1. **Xiaobing Hu**, Ashish Garg, Zoe H. Barber, *Structural and electrical properties of samarium-substituted bismuth titanate ferroelectric thin films on Pt/TiO_x/SiO₂/Si substrates*. Thin solid films. 484 (2005) 188~195.
2. **Xiaobing Hu**, Ashish Garg, Zoe H. Barber, *Growth and characterization of pulsed-laser-deposited polycrystalline Bi_{3.33}Sm_{0.67}Ti₃O₁₂ ferroelectric thin films*. Materials Letters. 59 (2005) 2583~2587.
3. **Xiaobing Hu**, Ashish Garg, John Wang, Zoe H. Barber, *Ferroelectric Bi_{4-x}Sm_xTi₃O₁₂ thin films fabricated by pulsed laser deposition for Nv-RAM applications*. Integrated Ferroelectrics. 61 (2004) 123.
4. **Xiaobing Hu**, Ashish Garg, Zoe H. Barber, *Deposition and characterisation of pulsed-laser-deposited and chemical-solution-derived Sm-substituted bismuth titanate films*. Integrated Ferroelectrics. (In press).
5. **Xiaobing Hu**, Ashish Garg, Zoe H. Barber. (To be submitted). *Effect of annealing atmospheres on properties of Nd-substituted bismuth titanate ferroelectric thin films*.
6. **Xiaobing Hu**, Ashish Garg, Zoe H. Barber. (To be submitted). *Low-temperature electrical properties of Sm-substituted bismuth titanate ferroelectric thin films for nonvolatile memory applications*.
7. **Xiaobing Hu**, Zoe H. Barber (To be submitted). *Investigations into local piezoelectric properties and determination of the effective electrostriction coefficients of ferroelectric thin films*
8. **Xiaobing Hu**, Zoe H. Barber (Under preparation). *Piezoelectric properties of Sm-doped bismuth titanate ferroelectric thin films*.
9. Xiaojie Lou, **Xiaobing Hu**, Ming Zhang, S. A. T. Redfern, E. A. Kafadaryan, and James F. Scott. *Nano-shorts*. Review on Advanced Materials Science. 10. (2005) 197.
10. Xiaojie Lou, **Xiaobing Hu**, Finlay D. Morrison, James F. Scott. *Phase separation in lead zirconate-titanate (PZT) and bismuth titanate during electrical shorting and fatigue*. Journal of Applied Physics. (2006, in press).
11. Ashish Garg, **Xiaobing Hu**, and Zoe H. Barber, *Structure and Properties of Lanthanide Doped Bi₄Ti₃O₁₂ Films*, Ferroelectrics. 328 (2005) 93~97.
12. Ashish Garg, A. Snedden, P. Lightfoot, James F. Scott, **Xiaobing Hu**, and Zoe H. Barber. *Investigation of structural and ferroelectric properties of pulsed-laser-ablated epitaxial Nd-doped bismuth titanate films*. Journal of Applied Physics. 96 (2004) 3408.
13. Ashish Garg, A. Snedden, P. Lightfoot, **Xiaobing Hu**, James F. Scott, and Zoe H. Barber, *Pulsed Laser Deposition and Characterization of Nd-doped Bi₄Ti₃O₁₂ Thin Films*, Ferroelectrics (2006, in press).

Glossary of Acronyms

<i>Acronyms</i>	<i>Full name</i>
AFM	Atomic Force Microscopy / Microscope
BiT	$\text{Bi}_4\text{Ti}_3\text{O}_{12}$; Bismuth Titanate
BLaT	La-doped Bismuth Titanate
BLnT	Lanthanide-doped Bismuth Titanate
BLSF	Bismuth Layer-structured Ferroelectric
BNdT	Nd-doped Bismuth Titanate
BSEI	Backscattered Electron Image
BSmT	Sm-doped Bismuth Titanate
BST	$\text{Ba}_x\text{Sr}_{1-x}\text{TiO}_3$
CSD	Chemical Solution Deposition
DRO	Destructive Readout
E_c	Coercive Electric Field
EDX	Energy dispersive X-ray spectrometry
EEPROM	Electrically Erasable Programmable Read Only Memory
EFM	Electrostatic Force Microscopy
EPROM	Erasable Programmable Read Only Memory
FeFET	Ferroelectric Field Effect Transistor
FeRAM	Ferroelectric Random Access Memory
FE-SEM	Field-Emission Scanning Electron Microscopy / Microscope
FFM	Friction Force Microscopy
FT-IR	Fourier Transform Infrared Spectroscopy
FWHM	Full Width at Half Maximum
KDP	KH_2PO_4
JCPDS	Joint Committee on Powder Diffraction Standards
LNO	LaNiO_3

MEMS	Microelectromechanical System
MOCVD	Metalorganic Chemical Vapor Deposition
MOD	Metalorganic Deposition
MOSD	Metalorganic Sol Decomposition
Nv-RAM	Nonvolatile Random Access Memory
NDRO	Non-destructive Readout
PFM	Piezoresponse Force Microscopy / Microscope
PLD	Pulsed Laser Deposition
P_r	Remanent Polarisation
PST	$\text{PbSr}_{1/2}\text{Ta}_{1/2}\text{O}_3$
PUND	Positive-Up-Negative-Down
PZT	$\text{Pb}(\text{Zr}_x\text{Ti}_{1-x})\text{O}_3$; Lead Zirconate Titanate
RAM	Random Access Memory
RMS	Root Mean Square
SBT	$\text{SrBi}_2\text{Ta}_2\text{O}_9$; Strontium Bismuth Tantalate
SBTW	W-substituted SBT; W-substituted Strontium Bismuth Tantalate
SCLC	Space Charge Limited Current
SCM	Scanning Capacitance Microscopy
SEI	Secondary Electron Imaging
SEM	Scanning Electron Microscope / Microscopy
SPM	Scanning Probe Microscope / Microscopy
SRAM	Static Random Access Memory
SRO	SrRuO_3
STO	SrTiO_3
ULSI	Ultra Large Scale Integration
XRD	X-ray Diffraction

Chapter 1 Introduction

1.1 Background

Much emphasis in integrated circuit technology is being focused on miniaturisation, with the result that significant advantages in the application of small dimension ferroelectric thin films offer great potential for ready integrability. Earlier attempts at deposition of ferroelectric thin films were limited mostly to development of thin-film capacitors that use large permittivity materials such as barium titanate. In addition, the complexities of the process involved in depositing multi-component material systems created another limitation. Current activity in ferroelectric thin-film research, motivated by the latest advances in thin-film growth processes, offers the opportunity to exploit several phenomena in ferroelectric materials including polarisation hysteresis,¹ pyroelectricity,^{2,3,4} piezoelectricity,^{5,6} and electro-optic activity.^{7,8}

There has been considerable effort dedicated in recent years to ferroelectric materials for *nonvolatile random access memory* (Nv-RAM; or *ferroelectric random access memory*, FeRAM) applications.⁹ With ferroelectric memories rather than conventional memories, high-speed writing, low dissipation, power and high endurance can be achieved for the first time. The term nonvolatile means that the information is retained in the memory device even if the power is lost. These memories promise fast read-and-write cycles, low switching voltages (3~5 V and lower) nonvolatility in the unpowered mode, and long endurance (10^{12} cycles).

Several attempts were made to make ferroelectric nonvolatile memories between the 1950s and 1970s. Unfortunately, these efforts were not successful because of serious

problems, including fatigue (decrease in remanent polarisation with bipolar cycling), imprint (development of a bias field), and retention (decrease in remanent polarisation with time) as a result of the nature of the materials used or the integration process. Due to these material issues, the first commercial FeRAM was not available until about twenty years ago.

A good understanding of fatigue in ferroelectric materials was necessary before the industry could manufacture memories in sufficient quantity and with good endurance. Fatigue in nonvolatile memories is a phenomenon that occurs when data are not correctly rewritten after experiencing switching cycles. For some ferroelectric materials, fatigue occurs when the direction of the polarisation is reversed (by an applied electric field) and the spontaneous polarisation decreases, *i.e.* the ferroelectric hysteresis loop, or polarisation versus electric field curve, gradually disappears.

The existence of the bismuth layer-structured ferroelectrics (BLSFs) was first reported by Aurivillius in 1949.¹⁰ BLSFs have been recognised as promising film materials for FeRAM applications due to their excellent fatigue-free nature and other electrical properties.

The representative materials of BLSFs are SBT ($\text{SrBi}_2\text{Ta}_2\text{O}_9$)¹¹ and La-doped $\text{Bi}_4\text{Ti}_3\text{O}_{12}$ (BLaT)¹². However these materials require optimisation. That is, SBT has a low remanent polarisation ($2P_r < 10 \mu\text{C}/\text{cm}^2$) and BLaT has a large coercive field ($E_c > 100 \text{ kV}/\text{cm}$). For most memory applications, a larger polarisation density and lower operating voltage is preferable. Therefore, the challenge is to improve the polarisation density and minimise the operating voltage of ferroelectric thin films^{13,14,15}, and many groups are involved in doing just that^{16,17}.

Another problem concerning practical applications of ferroelectrics is that most pure

BLSFs have a relatively low electrical resistivity. Several researchers have reported that V- and W-substitution will improve the electrical properties of BLSF compounds.^{15,18,19}

BLSFs have a crystal structure and a general formula of $(\text{Bi}_2\text{O}_2)^{2+}(\text{A}_{m-1}\text{B}_m\text{O}_{3m+1})^{2-}$ in which bismuth oxide layers $[(\text{Bi}_2\text{O}_2)^{2+}$ layers] are interleaved with pseudo-perovskite blocks along the c axis.²⁰ Recent studies revealed that Bi^{3+} ions in the $\text{Bi}_4\text{Ti}_3\text{O}_{12}$ (BiT) structure could be substituted by trivalent rare earth ions, such as La^{3+} , Nd^{3+} , and Sm^{3+} , to improve its properties as was the case of A-site substitution in BLSFs. It was reported that A-site or B-site substitution can lead to large remanent polarisations (P_r).^{17,21} It was also found that the coercive field (E_c) became larger in the A-site-substituted BiTs (including BLaT) and smaller in the B-site-substituted BiTs.

Besides the effect of dopant type on ferroelectric properties, film orientation has a significant effect on the film properties. Due to the anisotropic nature of ferroelectric properties, orientation of the crystallites in BiT films is relevant for attaining high P_r and low E_c values. In the Aurivillius phases one would expect the largest P_r along the a -axis of the film and almost negligible P_r along the b - and c -axis (for pure BiT, $2P_r$ ($//a$ -axis) = $36 \mu\text{C}/\text{cm}^2$ and $2P_r$ ($//c$ -axis) = $4 \mu\text{C}/\text{cm}^2$).^{22,23,24}

Most of the films mentioned above were randomly oriented polycrystalline films. Recent efforts have concentrated on the growth of epitaxial films with non- c -axis orientations,^{25,26,27} including (118) and (104) for BLaT and (116) and (103) for SBT. These orientations have the spontaneous polarisation vector inclined to the normal direction of the film plane.

High temperature synthesis is required to: eliminate pyrochlore phase formation,

transform fluorite micrograins to Bi-layered structures, improve the microstructure and attain a critical grain size. To enable the integration of BLSF films into silicon-based microelectronics, the films should be grown on electroded silicon substrates.

Along with high switching polarisation and excellent fatigue resistance, the high values of piezoelectric coefficients of lanthanide-doped BiT (BLnT) films offer promise for microelectromechanical systems (MEMS).^{28,29} Recently, Maiwa *et al.*²⁹ have demonstrated that Nd-doped BiT (BNdT) thin films are very promising candidates for lead-free thin-film piezoelectrics.

BLSF thin films have been fabricated using several techniques, which include metalorganic chemical vapour deposition (MOCVD),¹⁷ sputtering,³⁰ pulsed laser deposition (PLD),³¹ and chemical solution deposition (CSD).³² A major thrust of these deposition techniques developed to deposit BiT films has been to overcome the twin issues of minimising the processing temperature and time and improving the ferroelectric properties like remanent polarisation, coercive field and dielectric constant. The requirement is for formation of a proper Bi-layered crystalline phase with minimum defects, without inclusion of any secondary phases, and with optimum orientation of the crystallites. As these are highly dependent on processing methods and parameters, several process variables of PLD and CSD have been attempted in the past to form BiT films meeting the structural criteria.^{31,32}

PLD consists of the laser ablation process and the kinetics of nucleation controlled growth. Here, the substrate temperature, laser conditions, ambient pressure, *etc.*, all have direct impacts on the crystalline phase, microstructure, and composition of the deposited films.

CSD has been extensively employed in the past few years, including sol-gel process and metalorganic deposition (MOD). It has several advantages including accurate composition control which is very important for multicomponent systems, ease of process integration with standard semiconductor manufacturing technology and relatively low costs.

1.2 Purpose of the research

The current research is an effort to realise and solve the problems which could be encountered while fabricating a ferroelectric capacitor for a high density FeRAM cell. In a high density memory structure, the ferroelectric capacitor is fabricated on the top of a poly-silicon plug, which in turn is connected to the drain of the transistor. Such a configuration would result in constraints for processing and choice of the ferroelectric material:

- (1) In a high-density memory configuration, the transistor is fabricated prior to the fabrication of the capacitor. In order to preserve the integrity of the transistor, the processing temperature of the ferroelectric capacitor should be as low as possible (e.g. $< 500\text{ }^{\circ}\text{C}$).
- (2) Even using low processing temperatures, a ferroelectric capacitor should exhibit well defined ferroelectric properties.
- (3) The ferroelectric capacitor should possess high $2P_r$ so that the memory stored in these capacitors could be read in an unambiguous manner.
- (4) E_c required to switch the memory from one state to the other state should be as low as possible.

(5) The ferroelectric capacitor should possess reproducible properties.

(6) The ferroelectric capacitor should possess minimal fatigue while maintaining low leakage current density.

1.3 Contents of the research

In view of fundamental ferroelectric properties, namely remanent polarisation P_r and coercive field (E_c), there are two potential ferroelectric materials for FeRAM applications. These materials are SBT and BLnT.

1. SBT. As discussed earlier, B-site doping can improve the electrical properties of BLSF compounds. This research includes the study of the effect of W-substitution on the structural and electrical properties of SBT.

2. BLnT. As stated in the earlier section, integration of BLnT thin films into high density memory structures requires lowering processing temperatures while improving the $2P_r$ of BLnT based capacitors. In order to achieve lower processing temperatures for BLnT thin films, firstly the structure-property relationships of BLnT thin films were studied. Structure-property studies performed consisted of three different categories: the effects of (1) grain orientation, (2) composition and (3) grain size (or surface topography) on ferroelectric film properties. Consequently, processing parameters were manipulated to obtain desirable grain orientation and grain size at low processing temperatures. The research includes PLD-grown epitaxial BLnT films on single crystal substrates and PLD- and CSD-derived polycrystalline BLnT films on platinised silicon substrates.

3. Piezoelectric properties of BLnT films were also studied, as high values of

piezoelectric coefficients of such films offer promise for microelectromechanical systems (MEMS)²⁸.

1.4 Outline

Chapter 2 discusses aspects of ferroelectric films, including ferroelectricity, some points about FeRAM and the criteria of ferroelectric thin films for FeRAM. Background knowledge of the PLD and CSD techniques are also described.

Chapter 3 describes the experimental techniques, which include details of film fabrication (PLD and CSD) and film characterisations.

Chapter 4 presents the results and discussion of PLD-grown W-doped SBT thin films.

Chapter 5 shows the results of epitaxial BNdT films on single crystal substrates.

Chapter 6 presents the results of PLD-grown polycrystalline BSMT films on platinised silicon substrates, including the effect of processing parameters, Pt layer orientations, doping levels, and bottom electrodes.

Chapter 7 presents the study of CSD-derived BSMT and BNdT thin films on platinised silicon substrates. Low-temperature properties of the CSD-derived BSMT films are studied.

Chapter 8 presents the results of piezoelectric properties of ferroelectric thin films using PFM, which includes domain imaging and manipulation and local ferroelectric and piezoelectric measurements.

Chapter 9 concludes these studies and provides directions for future work.

1.5 References

- 1 J. F. Scott and C. A. Paz de Araujo, *Science* **246**, 1400 (1989).
- 2 R. W. Whatmore, *Ferroelectrics* **118**, 241 (1991).
- 3 C.M. Wang, M.C. Kao, and Y.C. Chen, *Journal of Applied Physics* **42**, 170 (2003).
- 4 R. Waton and M.A. Todd, *Ferroelectrics* **118**, 279 (1991).
- 5 Y. Kaga, H. Kikuchi, and J. Watanabe, *Journal of the Ceramic Society of Japan* **111**, 73 (2003).
- 6 A.L. Kholkin, V.V. Shvartsman, and A.Y. Emelyanov, *Applied Physics Letters* **82**, 2127 (2003).
- 7 T. Nagata, A. Ashida, and N. Fujimura, *Journal of Applied Physics* **41**, 6916 (2003).
- 8 D.Y. Kim, S.E. Moon, and E.K. Kim, *Applied Physics Letters* **82**, 1455 (2003).
- 9 S. Y. Lee, D. J. Jung, Y. J. Song, B. J. Koo, and S. O. Park, presented at the 1999 Symposium on VLSI Technology, 1999 (unpublished).
- 10 B. Aurivillius, *Arkiv for Kemi* **1**, 499 (1949).
- 11 C. A. Paz de Araujo, J. D. Cuchiaro, L. D. McMillan, M. C. Scott, and J. F. Scott, *Nature (London)* **324**, 627 (1995).
- 12 P. H. Park, B. S. Kang, S. D. Bu, T. W. Noh, J. Lee, and W. Jo, *Nature (London)* **401**, 682 (1999).
- 13 Y. Noguchi, A. Kitamura, L. C. Woo, M. Miyayama, K. Oikawa, and T. Kamiyama, *Journal of Applied Physics* **94**, 6749 (2003).
- 14 Y. Noguchi, M. Miyayama, K. Oikawa, T. Kamiyama, M. Osada, and M. Kakihana, *Japanese Journal of Applied Physics Part 1-Regular Papers Short Notes & Review Papers* **41**, 7062 (2002).
- 15 Y. Noguchi and M. Miyayama, *Applied Physics Letters* **78**, 1903 (2001).
- 16 H. N. Lee and D. Hesse, *Applied Physics Letters* **80**, 1040 (2002).
- 17 T. Kojima, T. Sakai, T. Watanabe, H. Funakubo, K. Saito, and M. Osada, *Applied Physics Letters* **80**, 2746 (2002).
- 18 T. Sakai, T. Watanabe, M. Osada, M. Kakihana, Y. Noguchi, M. Miyayama, and H. Funakubo, *Japanese Journal of Applied Physics Part 1-Regular Papers Short Notes & Review Papers* **42**, 2850 (2003).

- ¹⁹ J. S. Kim, S. S. Kim, J. K. Kim, and T. K. Song, Japanese Journal of Applied Physics Part 1-Regular Papers Short Notes & Review Papers **41**, 6451 (2002).
- ²⁰ H. Irie, M. Miyagawa, and T. Kudo, Journal of Applied Physics **90**, 4089 (2001).
- ²¹ Y. Noguchi, I. Miwa, Y. Goshima, and M. Miyayama, J. Appl. Phys. **39**, L1259 (2000); Yuji Noguchi, Appl. Phys. Lett. **78**, 1903 (2001).
- ²² S. E. Cummins and L. E. Cross, Journal of Applied Physics **39**, 2268 (1968).
- ²³ T. Watanabe, T. Kojima, H. Uchida, I. Okada, and H. Funakubo, Japanese Journal of Applied Physics Part 2-Letters **43**, L309 (2004).
- ²⁴ H. Matsuda, S. Ito, and T. Iijima, Applied Physics Letters **83**, 5023 (2003).
- ²⁵ J. Lettieri, M. A. Zurbuchen, Y. Jia, and D. G. Schlom, Applied Physics Letters **76**, 2937 (2000).
- ²⁶ K. Ishikawa and H. Funakubo, Applied Physics Letters **75**, 1970 (1999).
- ²⁷ H. N. Lee, N. Zakharov, S. Senz, A. Pignolet, and D. Hesse, Applied Physics Letters **79**, 2961 (2001).
- ²⁸ W. H. Ma and D. Hesse, Applied Physics Letters **85**, 3214 (2004).
- ²⁹ H. Maiwa, N. Iizawa, D. Togawa, T. Hayashi, W. Sakamoto, M. Yamada, and S. Hirano, Applied Physics Letters **82**, 1760 (2003).
- ³⁰ M. Tanaka, T. Higuchi, K. Kudoh, and T. Tsukamoto, Japanese Journal of Applied Physics Part 1-Regular Papers Short Notes & Review Papers **41**, 1536 (2002).
- ³¹ A. Garg, Z. H. Barber, M. Dawber, J. F. Scott, A. Snedden, and P. Lightfoot, Applied Physics Letters **83**, 2414 (2003).
- ³² D. Wu, A. D. Li, and N. B. Ming, Journal of Applied Physics **95**, 4275 (2004).

Chapter 2 Ferroelectric thin films

2.1 Ferroelectricity

Ferroelectricity was discovered in the beginning of last century by J. Valasek in Rochelle salt (potassium sodium tartrate)¹. The phenomenon of ferroelectricity is analogous to that of ferromagnetism. Just as ferromagnetic materials may exhibit a spontaneous magnetic moment at zero magnetic field, ferroelectric materials exhibit a spontaneous electric dipole moment (per unit volume) or polarisation at zero electric field.¹

In order to describe the essential features of ferroelectricity,² we assume a hypothetical model of a two dimensional crystal AB (which is oversimplified), shown in Fig. 2.1. The A ions, which we assume carry a negative charge, are located at the lattice points and B ions, which carry a positive charge, are located on the horizontal lines joining A ions. At equilibrium, B ions always lie closer to one of the two adjacent A ions than to the other. This situation can be explained in terms of potential between two adjacent A ions. There are two equilibrium positions in which a B ion can stay, but to change from one state to another, energy must be provided to overcome an energy barrier ΔE . Let us assume that at a given temperature T , all the B ions are closer to the A ions on the left and consider each AB group as an electric dipole. In this situation the structure can be visualised as the top two layers of Fig. 2.1(a) and this assembly of dipoles can be expressed as the top two rows in Fig 2.1(b). In this state, the crystal is said to be spontaneously polarised: with a finite dipole moment per unit volume *i.e.* a spontaneous polarisation. Crystals exhibiting this property are called

pyroelectric and the direction of spontaneous polarisation is called the *polar axis*.²

Alignment of dipoles in one of the polar directions may extend only over a region of the crystal and there can be different regions in the crystal with aligned dipoles which are oriented in many different directions with respect to one another. Regions of uniform polarisation are called domains, and they are separated by a boundary from one another called a domain wall. Ferroelectric domain walls (of the order of 1~10 nm wide) are much narrower than the domain walls in ferromagnetic materials.

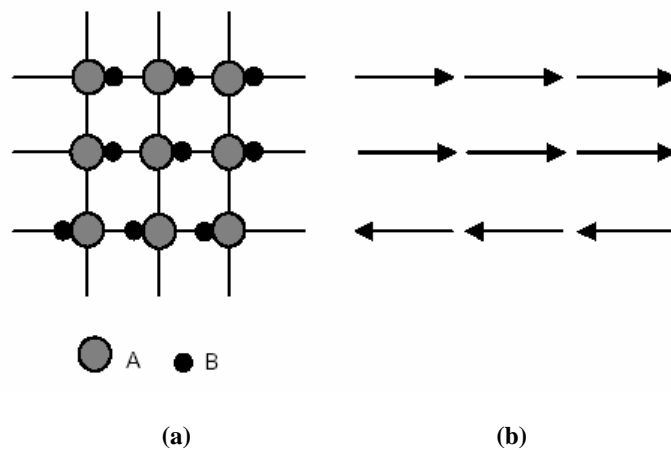


Fig. 2.1 Schematic representation of structure and dipoles in a hypothetical 2D crystal²

Upon application of a DC electric field in the horizontal direction of Fig. 2.1, the dipoles which were already aligned in the field direction will remain aligned but those which are antiparallel will have a tendency to reorient themselves in the direction of electric field. Upon application of sufficiently large electric field, such dipoles will be able to align themselves in the direction of the applied field. This phenomenon of polarisation reversal takes place by way of nucleation of favourably oriented domains and domain wall motion.

If we assume that our hypothetical crystal has an equal number of positive and negative domains then the net polarisation of the crystal will be zero. Upon

application of an electric field E , initial polarisation P increases linearly with the increasing electric field and the crystal behaves like a dielectric because the applied field is not large enough to switch any of the domains oriented opposite to its direction. A plot of P versus E is shown in Fig. 2.2 and this linear region is shown as AB. Upon further increasing the electric field, oppositely oriented domains start to reorient themselves and polarisation increases rapidly (BC) until all the domains are aligned in the direction of the electric field *i.e.* the crystal has reached a single domain state (CD) when polarisation saturates to a value called saturation polarisation (P_s).

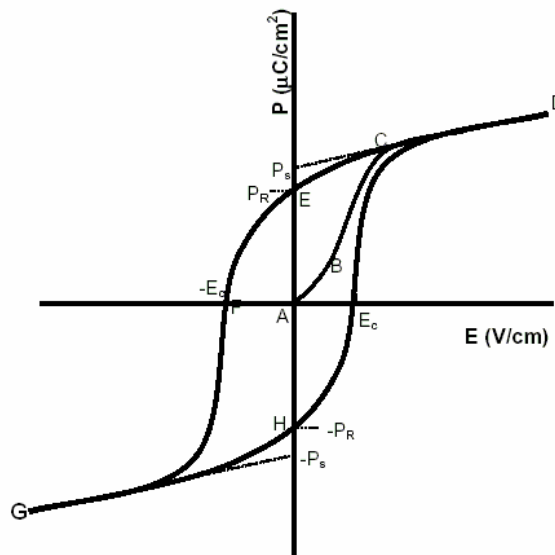


Fig. 2.2 Characteristic hysteresis loop of a ferroelectric material

Upon decreasing the electric field, the polarisation generally does not return to zero but follows path DE and at zero field some of the domains still remain aligned in the positive direction and the crystal exhibits a remanent polarisation (P_r). To bring the crystal back to zero polarisation state, a negative electric field is required (along the path EF) which is called the coercive field (E_c). Further increase of the electric field in the negative direction will cause complete reversal of all domains in the direction of the field (path FG) and the loop can be completed by following the path GHD. This

relationship between P and E is called a ferroelectric hysteresis loop, which is an important characteristic of a ferroelectric crystal. The principle feature of a ferroelectric crystal is not only the presence of spontaneous polarisation but also the fact that this polarisation can be reversed by application of an electric field. Ferroelectric hysteresis loops can be experimentally measured using a Sawyer-Tower circuit.³

2.2 Ferroelectric Random Access Memory (FeRAM)

Nonvolatile memories with ferroelectric capacitor materials are also known as ferroelectric random access memories (FeRAMs). Present research focuses on integration of ferroelectric materials into high-density Nv-RAM.

2.2.1 Ferroelectric memories

There are different kinds of digital memories in use today, which range from slow, inexpensive tapes or discs used for archival storage to fast but expensive static random access memories (SRAMs) and dynamic random access memories (DRAMs). Some of the more expensive memories include electrical erasable programmable read only memories (EEPROMs). While EEPROMs suffer from a drawback of a very limited lifetime, SRAMs need continuously to be supplied with battery power.

With current DRAM, the data is stored as a form of charge in a linear capacitor. In order to safely maintain the stored data, it is necessary to supply constant voltage to the capacitors, which are recharged hundreds of times per second by refresh circuitry. If the power is interrupted, DRAM loses all data stored in it, that is to say DRAM is volatile. In contrast, data in a ferroelectric capacitor is stored as a remanent polarisation state of the ferroelectric material itself. The ferroelectric capacitor has a

nonlinear dielectric property with permanent charge retention capabilities after the voltage application. Therefore, the stored data does not disappear, even though the power is turned off, that is, FeRAM is nonvolatile. The principal advantages of FeRAM over other nonvolatile memories are fast write/erase access times at the nanoseconds level, low operating voltage below 5 V, high endurance on read/write repeating cycle, and high radiation hardness which is especially useful for military and space applications. In terms of lifetime, FeRAMs have been shown to be potential candidates for Nv-RAMs, where the lifetime could extend at least to a value of 10^8 cycles.⁴

In principle, FeRAM could replace EPROM (erasable programmable read only memory), EEPROM (electronically erasable programmable ROM), SRAM, and DRAM. Furthermore, if high density FeRAM could be developed and the production cost could be reduced down to the level of the magnetic core, then FeRAM could also replace the hard disk as the primary mass storage device because of its faster access speed and the absence of mechanical wear problems. Some of the state-of-art FeRAM available commercially are 4 Mbit RAMs from Samsung,⁵ 1Mbit RAMs from NEC and 256 kbit RAMs from Matsushita.⁶ Low density FeRAM is already replacing EPROM and EEPROM in some areas such as video game consoles and smart cards. Use of FeRAMs is limited to applications which only require low density memories like video game devices, TV sets, fax machines, printers, mobile phones and fully embedded ferroelectric memories in silicon microprocessors and microcontrollers. Matsushita, the largest consumer-electronics firm in the world, expects the market for FeRAM to amount to \$690 million a year by 2005. Explosive demands in video games, cellular phones, portable computers and other portable electronic goods, indicate that annual sales of these speedy nonvolatile memories could amount to more

than \$20.7 billion by 2010.⁷

2.2.2 Principle of basic operation

Most of the ferroelectric materials which could be potential candidates for ferroelectric devices, including memories, are oxides such as barium titanate, lead titanate, lead zirconate titanate ($\text{PbZr}_x\text{Ti}_{1-x}\text{O}_3$, PZT) *etc.*, and these are based on the perovskite ABO_3 structure.⁸ The crystal structure of the characteristic tetragonal perovskite unit cell is shown in Fig. 2.3, where A^{+2} ions occupy the corner of the unit cell, B^{+4} ion lies at the centre of the unit cell and O^{-2} ions are at the face centres of the unit cell.⁸ Since the cubic phase is centrosymmetric, having no polar axis, there is no net spontaneous polarisation in the crystal. However, structural distortion below the Curie temperature causes the structure to change to a non-centrosymmetric tetragonal structure, which then gives rise to a net dipole moment (or spontaneous polarisation). Movement of the central atom B is the key to the ferroelectricity. It works as a switch and can be moved up or down relative to other ions by application of an electric field. This characteristic gives rise to the hysteresis behaviour in a ferroelectric material as shown previously in Fig. 2.2.

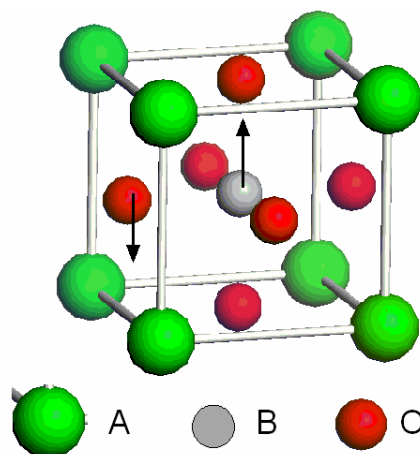


Fig. 2.3 A typical ABO_3 perovskite unit-cell (e.g. BaTiO_3). Remanent polarisation is zero when the structure is cubic (paraelectric phase) and it is non-zero in the (lower temperature) ferroelectric phase which has a tetragonal structure

At zero field we have two stable states of polarisation $+P_r$ and $-P_r$, arbitrarily defined as states '0' and '1'. Binary information in the form of '0' and '1' can be stored by moving the central atom up or down. When the power is interrupted, the atom stays in its current position thereby preserving the data in the memory device. This property of a ferroelectric can be utilised to make a memory device which is nonvolatile.

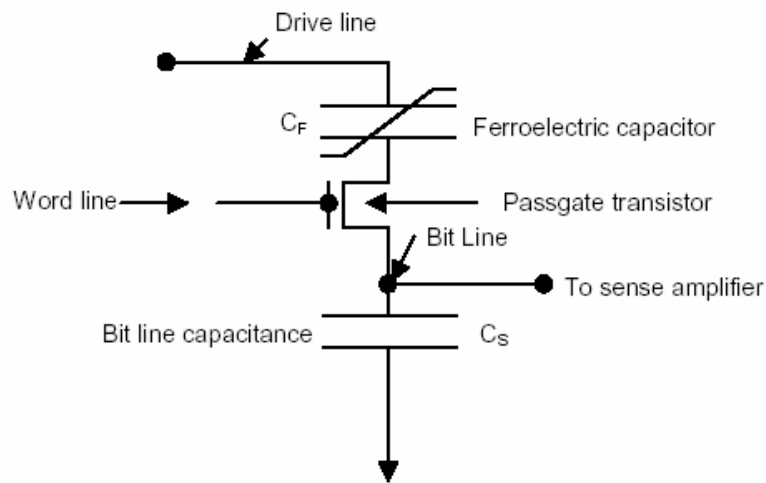


Fig. 2.4 Schematic diagram of a typical memory cell⁹

A typical memory cell is schematically shown in Fig. 2.4. In current devices, the memory cells are arranged in a square matrix. Therefore, a 1-megabit memory cell will have 1000 rows (drive line) and 1000 columns (word line). To overcome the crosstalk problem between two neighbouring cells, each memory cell capacitor is isolated from its neighbours by means of a passgate transistor. Each bit is written by applying one half a short voltage pulse along a row and the other half along a column. In this state, pulses add up to switch the polarisation state only at the specifically addressed cell. Two reading schemes for the FeRAMs are being explored,⁹ namely destructive readout (DRO) where the information must be rewritten after every read operation and non-destructive readout (NDRO) where information can be read over

and over again until the next write operation. DRO is the most commonly used scheme in the present generation FeRAMs because it closely resembles a DRAM. In DRO, the bit is read when a positive switching voltage is applied to the memory cell in the same way as the writing voltage is applied. If the data was already stored as state '0' or $+P_r$, then only a linear non-switching response is measured in the form of a voltage across a 10~50 ohm resistor. If the data was stored as state '1' or $-P_r$, a switching response greater than the linear response is measured because it contains the additional displacement current term dP/dt where P is the polarisation. A sense amplifier then compares this response with that of a reference cell which is always polarised in the $+P_r$ or state '0'. A sense amplifier and other associated circuitry is used in a FeRAM device to determine this transient current and thereby read the state of the device.

2.3 Ferroelectric film materials for memories

The fabrication of memory devices using ferroelectric materials was intensively studied between the 1950s and 1970s by many market-leading companies such as IBM and Bell Laboratories. Due to the incompatibility with the silicon process, the research was almost abandoned after 1975. However, since 1986, it has exploded as a result of the improvements in thin film technology, especially $\text{Pb}(\text{Zr}_x\text{Ti}_{1-x})\text{O}_3$ (PZT) sol-gel and sputtering deposition techniques¹⁰. Ferroelectric memories have been investigated by many semiconductor memory industries as well as by the defense industries, because of the nonvolatility, radiation hardness, high speed, low power and compatibility with silicon process.^{5,11}

In general, there are two major applications of ferroelectric materials for memory devices. Firstly, ferroelectric materials could be utilised for DRAMs. Secondly, they

are applicable for FeRAMs. Capacitance, by definition, could be improved by expanding the area, increasing the dielectric constant or decreasing the thickness of dielectric layer. In fact, the thickness of the dielectric layer has already been minimised to barely block tunnelling current, which is below 100 Å. The remaining choice, then, is to look for dielectric materials that have considerably higher dielectric constant. Because ferroelectric materials generally have high dielectric constants, ferroelectric thin films have been considered to be a capacitor material for high-density DRAM. As the integration density of DRAM reaches 4 Gbit, the device size can be tremendously decreased. As a result, current silicon-based dielectric materials, namely SiO₂ and Si₃N₄, have proved to be rather inadequate, due to their low dielectric constants. Considerable effort has been made to overcome the low dielectric constant problem by geometric methods such as developing a trench or stack structure to provide wider surface area and increase the capacitance values. Ferroelectric thin films, which are known to have dielectric constants about two orders higher than that of SiO₂, were selected as capacitor materials in 4 Gbit DRAM and beyond.

Along with the high dielectric constant, ferroelectric materials also exhibit characteristic polarisation responses to an applied electric field, which makes them potential candidate materials for nonvolatile memory devices. Several attempts to integrate such devices on a scale larger than 1 Mbit by using advanced silicon ultra large scale integration (ULSI) technologies, have been reported using PZT or SBT ferroelectric thin films. However, there are still several issues concerning the integration to be solved for the realisation of high-density FeRAM.

In a commercial memory technology, there are some issues for integration of

ferroelectric capacitors:

1. A suitable ferroelectric thin film material,
2. Development of an appropriate electrode technology,
3. A thin film deposition process which can be scaled up and which has capability to deposit thin films with good conformal coverage over nonplanar surfaces,
4. Suitable and compatible lithography and etching technology to produce submicron patterns with extreme precision and
5. A fitting device integration process.

For FeRAM device applications, an ideal material should have the properties as follows:¹²

1. Low electrical conductivity,
2. Good leakage and breakdown characteristics,
3. Large switching polarisation,
4. A low switching time (5~200 ns) for faster devices,
5. High Curie temperature, at least above 100 °C,
6. Good aging and retention (decrease in P_r with time⁶) characteristics,
7. Fatigue resistance up to a minimum of 10^{12} switching cycles,
8. Low power consumption *i.e.* low switching voltage (1~5 V) and
9. Low imprint (*imprint* is caused by development of an internal field in the ferroelectric capacitor which leads to a progressive shift of the hysteresis loop along the field axis).

Of the many hundreds or even thousands of known ferroelectric materials, only a few are suitable for switching applications and can be integrated into semiconductor technology. Research towards the development of memory materials has been going

on since the 1950s. First generation materials were KNO_3 , $\text{Bi}_4\text{Ti}_3\text{O}_{12}$ (in DRAMs and ferroelectric field effect transistors: FeFETs), BaMgF_4 (in FeFETs). Later, PZT emerged as a promising candidate for these applications. However, PZT films on metal electrodes suffer from fatigue upon switching for 10^{10} switching cycles. Also PZT films are not easy to fabricate with controlled stoichiometry due to the presence of lead, which has high volatility under PZT processing conditions. It also leads to severe processing complications including environmental hazard issues and contamination problems. BLSFs have been recognised as promising film materials for FeRAM applications due to their excellent fatigue-free nature and other electric properties and the representative materials are SBT^{11} and BLaT^{13} .

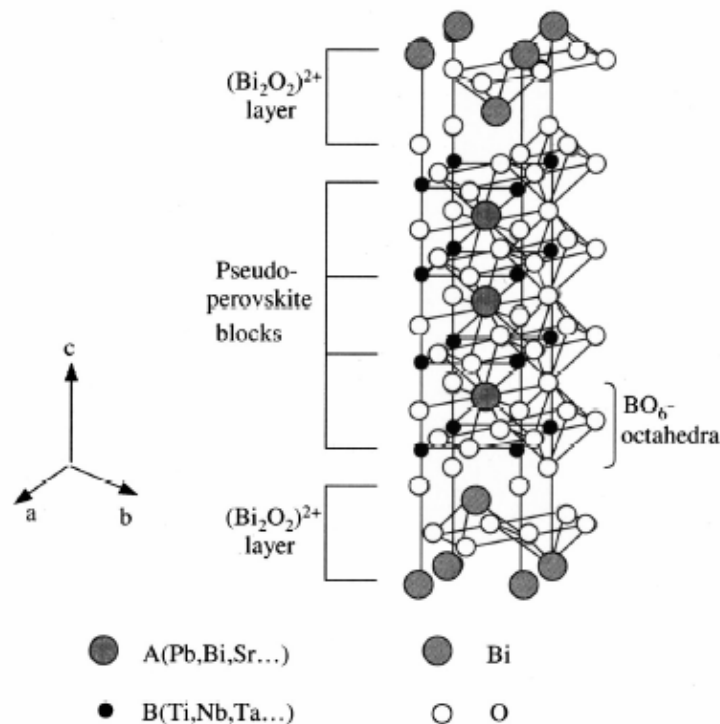


Fig. 2.5 Schematic drawing of the crystal structure of BLSF ($m=4$). One half of the pseudo-tetragonal unit cell¹⁴

BLSFs have a crystal structure and a general formula of $(\text{Bi}_2\text{O}_2)^{2+}(\text{A}_{m-1}\text{B}_m\text{O}_{3m+1})^{2-}$, as shown in Fig. 2.5. The pseudo-perovskite blocks have a formula of $(\text{A}_{m-1}\text{B}_m\text{O}_{3m+1})^{2-}$,

where A is a mono-, di-, or trivalent ion (e.g., K^+ , Na^+ , Ca^{2+} , Ba^{2+} , Sr^{2+} , Pb^{2+} , Bi^{3+}), B is a tetra-, penta-, or hexavalent ion (e.g. Fe^{4+} , Ti^{4+} , Ta^{5+} , Nb^{5+} , W^{6+} , Mo^{6+} , V^{5+}) and m represents the number of BO_6 octahedra between two neighbouring Bi_2O_2 layers ($m=1,2,3,4,5,\dots$). For example, $SrBi_2Ta_2O_9$ (SBT, $m=2$), $Bi_4Ti_3O_{12}$ (BiT, $m=3$), $SrBi_4Ti_4O_{15}$ (SBTi4, $m=4$) and $Sr_2Bi_4Ti_5O_{18}$ (SBTi5, $m=5$) have 2, 3, 4 and 5 octahedra, respectively.

2.4 Pulsed laser deposition (PLD)

Pulsed laser deposition (PLD) is known for its ability to produce films whose stoichiometry are very close to that of the targets because of the extremely high temperatures at the focus point on the targets. In PLD, one takes advantage of a short and intense laser pulse to ablate the surface of a desired target material. At low-pressure conditions, the laser-ablation process leads to the formation of an expanding plume that consists of neutral atoms and various ionised species of the target material. This plume expands in the direction perpendicular to the target surface and can be collected onto a substrate to form a thin film a short distance away from the target. In the case of oxide materials like SBT and BiT, the film growth can be carried out by an *in-situ* process which involves substrate heating and an oxygen gas atmosphere in the ablation chamber leading to direct crystallisation of the ablated species reaching the substrate surface. Alternatively, ablation can be carried out without substrate heating or with a lower substrate temperature (termed as *ex-situ* process). In this case, amorphous as-deposited films can be crystallised with a post-annealing treatment.

There are several important parameters to consider with PLD deposition.¹⁵

Laser

The most commonly used range of laser wavelength for thin film growth by PLD lies in the UV region (195 to 508 nm) between 200 to 400 nm. Most materials used for deposition exhibit strong absorption in this spectral region.

The absorption coefficients of materials tend to increase at the shorter wavelengths in this range, and thus the penetration depths into the target materials are reduced.

Laser Beam

A homogeneous, uniform beam is essential for good quality deposition. Poor beam quality can result in non-stoichiometric films as well as undesirable droplet formation.

Target

Successful depositions can be made from pressed powders, sintered pellets, cast material, single crystals and metal foils. Porous and inhomogeneous targets yield poor quality films. High density and smooth target surfaces are desirable features of a target material in order to avoid splashing due to defoliation of the surface. To achieve uniform target erosion and consumption, the target is usually rotated during deposition.

Plume

Evaporants from the ablated target form a plume, which consists of a mixture of energetic species including atoms, molecules, electrons, ions, clusters, micron-sized solid particulates, and molten globules. The plume is always perpendicular to the target regardless of the angle of the incident laser beam.

Due to collisions between the laser produced plume and the background gas, the plume expansion decreases as the background gas pressure increases. The substrate to be coated should be placed at a distance on the edge, but just within, the visible part of

the laser plume.

In-situ and ex-situ

In-situ deposition techniques usually also consist of two steps, *i.e.* the deposition at high temperature and a post-deposition oxygen treatment to ensure correct stoichiometry and phase formation.

Essentially the *ex-situ* route uses the same deposition steps as the *in-situ* method except that deposition takes place at much lower temperatures (e.g. 300 °C ~ 400 °C) in microcrystalline or amorphous form followed by film phase transformation via an *ex-situ* annealing step.¹⁶

2.5 Chemical solution deposition (CSD)

The chemical solution deposition (CSD) process is simple and compatible with conventional integrated circuit materials and processes. The process starts with preparing a precursor solution containing each of the metals in the desired thin film compound.¹⁷

There are three general methods for the preparation of precursor solution for the fabrication of oxide thin films: (1) alkoxide method, (2) alkoxide-salt method, and (3) other methods. An oxide network is formed in these techniques via hydrolysis and condensation of molecular precursors. This chemistry is controlled by parameters including the hydrolysis ratio, catalysis or molecular structure of precursors. The latter can be simply modified by oligomerisation, solvation or addition of chemical additives which lead to the tailoring of the coordination shell of the metal. The selection of precursor compounds and the solvents is the most important step in the precursor solution approach for the fabrication of thin films. The most important

points to be taken into consideration are: nature of initial species, whether there is a formation of mixed metal species, the stoichiometry of the various elements in the solution with respect to the formulation required, influence of the solvent, the temperature of the reaction as it effects the homogeneity at a molecular level, elimination of organics from the deposited film and temperature of crystallisation.

2.5.1 Selection and preparation of precursors

Normally, the all-alkoxide method will be considered in the first instance, since alkoxide precursors are mixed at the molecular level directly in the solution to enable a high degree of homogeneity.

However, for some metals it is inconvenient to use all alkoxides because of preparation problems or unavailability and alternative starting materials must be found. This is particularly the case with Group I and Group II elements whose alkoxides are solid, nonvolatile and in many cases of low solubility; consequently, it is sometimes difficult to obtain pure samples. Metal salts provide a viable alternative provided that they are readily converted to the oxide by thermal or oxidative decomposition and are preferentially soluble in organic solvents. They can usually be obtained at a high purity analytical grade.¹⁷

A major problem in forming homogeneous multicomponent solutions is the unequal hydrolysis and condensation rates of the metal alkoxides.¹⁷ This may result in phase separation, during hydrolysis or thermal treatment, leading to higher crystallisation temperatures or even undesired crystalline phases. It is therefore necessary to prepare solutions of high homogeneity in which cations of different types are uniformly distributed at an atomic scale through M-O-M (M: metal atoms) bridges. The initial

solution should therefore be treated such that bonds are first formed between the various alkoxide precursors prior to gelation. A difficulty of the all-alkoxide approach, especially for soluble alkoxides, is to understand the formation or not of the mixed-metal species and the stoichiometry between the metals. Solubilisation of one metal alkoxide in the presence of another is a criterion to be handled with care since it does not necessarily imply the formation of a mixed-metal species and thus homogeneity at a molecular level.

The choice of solvent is also important in the alkoxide-salt approach. The influence of the solvent can be multiple: it can generate and/or stabilise intermediates and thus allow, preclude or modify reactions. Most metal alkoxides are very reactive towards hydrolysis and condensation. They must be stabilised to avoid precipitation. These reactions are controlled by adding complexing agents that react with metal alkoxides at a molecular level, giving rise to new molecular precursors of different structure, reactivity, and functionality. The carboxylic acids, such as acetic acid and acetylacetone, which act as hydroxylated nucleophilic ligands, help in controlling the hydrolysis rates by decreasing the functionality of the precursor. The reaction between alkoxide and nitrates in the presence of water and carboxylic acids proceeds with the formation of the smallest possible aggregate, which allows the metals to achieve their most usual coordination number and thus hydrolysis becomes more difficult.

The precursors for individual metal should have a long shelf life. The selected precursors should have high solubility in the selected solvents and the various solvents should be compatible when mixed. The final precursor solution should have a relatively long shelf life so that it can be made in large volumes ahead of time and used as needed.

2.5.2 Film deposition -- Spin coating and baking

The films can be prepared from the precursor solution using spin, dip, or spray technique. Acidic solutions are generally capable of wetting all metal substrates, oxide substrates or metal-semiconductor substrates with a thin oxide layer on the surface. Almost any substrate that will support a thin film and is compatible with the materials and processes may be used. Spin coating technique is a well known form of deposition in which the precursor is placed on a wafer and the wafer is spun to evenly distribute the precursor over the wafer. The spinning speed and the viscosity of the solutions need to be optimised to control the thickness of the films.

Bornside *et al.*¹⁸ divide spin coating into four stages: deposition, spin up, spin off, and evaporation, although evaporation may accompany any of the other stages, as shown in Fig. 2.6.

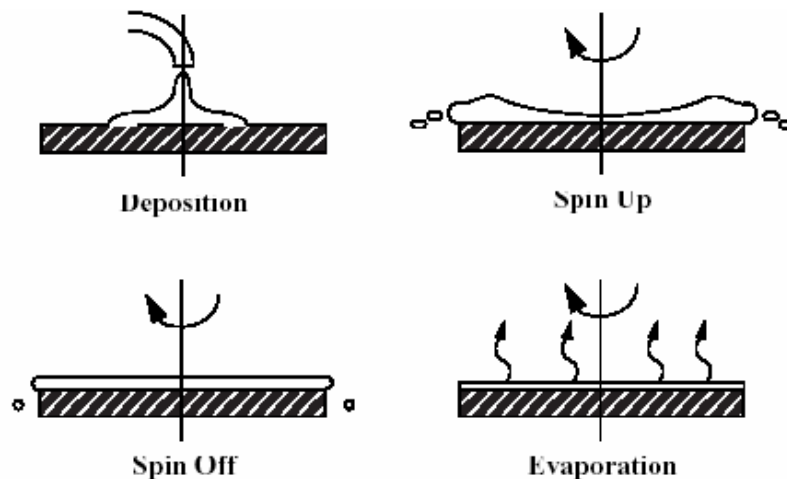


Fig. 2.6 Four stages of spin coating¹⁸

The deposition process involves dispensing of an excess amount of fluid onto a stationary or slowly spinning substrate. The fluid is deposited through a nozzle at the centre of the substrate or over some programmed path. An excess amount of fluid is used to prevent coating discontinuities caused by the fluid front drying prior to it

reaching the wafer edge.

In the spin up stage, the substrate is accelerated to the final spin speed. As rotational forces are transferred upward through the fluid, a wave front forms and flows to the substrate edge by centrifugal force, leaving a uniform layer of solution behind.

The spin off stage is the spin coating stage where the excess solvent is flung off the substrate surface as it rotates at speeds between 2000 and 8000 rpm. The fluid is being thinned primarily by centrifugal forces until enough solvent has been removed to increase viscosity to a level where flow ceases. The spin off stage takes place for approximately 10 seconds after spin up.

Though present throughout the spin coating process, evaporation becomes the primary method of film thinning once fluid flow ceases. Evaporation is the complex process by which a portion of the excess solvent is absorbed into the atmosphere. If significant evaporation occurs prematurely, a solid skin forms on the fluid surface which impedes the evaporation of solvent trapped under this skin and can cause coating defects when the sample is subjected to the centrifugal forces of the spinning substrate.

Spin coating has many advantages in coating operations with its biggest advantage being its lack of coupled process variables. The spin speed, and fluid viscosity are the only degrees of freedom, making the spin coating process very robust. Therefore, film thicknesses are easily changed by changing the spin speed, or switching to a different viscosity spinning solution. During film formation the condensation rate can be controlled by varying the pH of the coating bath.

After the coating process, the wafer is transferred to a hot plate on which it is baked. Alternatively, an oven may be used in baking if it is desirable to control ambient air

conditions.

If the desired thickness is not obtained in a single coating, then the spin, dry, and bake steps are repeated until the desired thickness is achieved. After the last layer is coated and baked, the film is annealed in a diffusion furnace or in a rapid thermal annealing system. The annealing is preferably optimised. Depending on the type of substrate and the processing procedure, crystalline films with different morphologies can be obtained.

2.6 Epitaxial thin films

Epitaxy, ideally, refers to formation of a single crystal film on the top of a single crystal substrate with a specific crystallographic orientation relationship between the film and the substrate as growth commences. The orientation relationship is governed by the crystal systems and lattice parameters of the two phases. There can be more than one orientation relationship in the case of deviation from the single crystalline structure of the film. The concept of matching of lattice parameters between the film and the substrate is an important aspect of epitaxy. The fundamental criterion for epitaxy is defined by the lattice mismatch, which can be written as

$$f=(a_f-a_s)/a_s, \quad (2.1)$$

where a_f and a_s are the lattice parameters of the film and the substrate.

Ideally, for high quality epitaxy of the film, the lattice mismatch should be as small as possible (generally less than 10%). One way to avoid large misfit strain, at least along the interface, is by tilting of the growth planes of the film relative to the substrate

plane, as illustrated in Fig. 2.7.

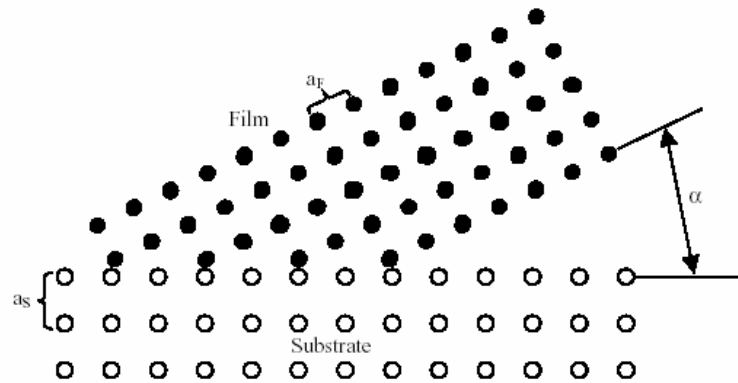


Fig. 2.7 Schematic representation of the epitaxy of the film and the substrate plane¹⁹

The most important factor affecting epitaxy is the nature of the substrate. Normally, the substrate for epitaxial film growth should be a single crystal substrate. The choice of substrate is limited by various factors such as crystal symmetry, orientation, minimum lattice parameter mismatch, surface energy considerations, chemical nature, coefficient of thermal expansion and most importantly, the application for which the film is being deposited. Substrate preparation is also an important step towards depositing epitaxial films. In many instances, surface contamination can lead to dramatic changes in the epitaxy. Substrate temperature during the deposition also plays an important role in determining the epitaxy. In general, for *in-situ* film growth, the higher the deposition temperature, the better the chances of achieving the epitaxy. This is due to the improved ad-atom mobility at the substrate surface. Moreover, increase in the substrate temperature may also lead to purification of the substrate by desorption of any contaminants. Epitaxial temperature (temperature at and above which epitaxial growth is favoured) is also affected by the deposition rate.

2.7 Piezoelectricity

2.7.1 Piezoelectric effect

Piezoelectric materials are a class of materials which can be polarised, in addition to an electric field, also by application of mechanical stress. The linear relationship between stress X_{ik} applied to a piezoelectric material and resulting charge density D_i is known as the direct piezoelectric effect and may be written as

$$D_i = d_{ijk}X_{jk} \quad (2.2)$$

where d_{ijk} ($C N^{-1}$) is a third-rank tensor of piezoelectric coefficients. The piezoelectric materials have another interesting property, in that they change their dimensions and contract or expand when an electric field E is applied. The converse piezoelectric effect describes the strain that is developed in a piezoelectric material due to the applied electric field.

$$x_{ij} = d_{kij}E_k = d_{ijk}^t E_k \quad (2.3)$$

where t denotes the transposed matrix. The units of the converse piezoelectric coefficient (d_{ijk}^t) are (m/V). The piezoelectric coefficients d for the direct and converse piezoelectric effects are thermodynamically identical *i.e.* $d_{\text{direct}} = d_{\text{converse}}$. Note that the sign of the piezoelectric charge D_i and strain x_{ij} depends on the direction of the mechanical force and electric fields, respectively. The piezoelectric coefficient d can be either positive or negative. It is common to call a piezoelectric coefficient

measured in the direction of applied field the longitudinal coefficient and that measured in the direction perpendicular to the field the transverse coefficient. Other piezoelectric coefficients are known as shear coefficients.

Because the strain and stress are symmetrical tensors, the piezoelectric coefficient tensor is symmetrical with respect to the same indices, $d_{ijk} = d_{ikj}$. The number of independent piezoelectric coefficients is thus reduced from 27 to 18. The number of independent elements of d_{ijk} may be further reduced by the symmetry of the material. Piezoelectric coefficients must be zero and the piezoelectric effect is absent in all 11 centrosymmetric point groups and in point group 432. Materials that belong to other symmetries may exhibit the piezoelectric effect.

Examples of piezoelectric materials are quartz (SiO_2), zinc oxide (ZnO), and PZT. The direct piezoelectric effect is the basis for force, pressure, vibration and acceleration sensors and the converse effect for actuator and displacement devices.

2.7.2 Piezoresponse force microscopy (PFM)

Progress in oxide electronic devices including microelectromechanical systems (MEMS), FeRAMs, and ferroelectric heterostructures necessitates an understanding of local ferroelectric properties at the nanometre level, which has motivated a number of studies of ferroelectric materials with various scanning probe microscopies (SPM).^{20,21}

Most SPM techniques allow local poling of ferroelectric materials with subsequent imaging of induced charges. From the materials scientists' point of view, the information on domain structure and orientation obtained from SPM images is extremely valuable and numerous observations of local domain dynamics as related to

the polarisation switching process, ferroelectric fatigue, phase transitions, and mechanical stresses, *etc.* have been made.

Table 2.1 SPM techniques for ferroelectric imaging²²

Technique	Measured signal	Relation to ferroelectric properties
EFM (Electrostatic Force Microscopy)	Electrostatic force gradient	Characterise electrostatic stray fields above the ferroelectric surface induced by surface polarisation charge. Sensitive only to out-of-plane polarisation component.
PFM (Piezoresponse Force Microscopy)	Vertical (v-PFM) and lateral (l-PFM) surface displacement induced by tip bias.	Characterises piezoelectric properties of the surface. Vertical and lateral components of the signal are related to in-plane and out-of-plane polarisation components.
SCM (Scanning Capacitance Microscopy)	Voltage derivative of tip-surface capacitance	Based on polarisation-induced hysteresis in tip-surface capacitance. Only out-of-plane polarisation component can be determined.
FFM (Friction Force Microscopy)	Friction forces	Characterises the effect of polarisation charge on surface friction.

Table 2.1 summarises some of the most common SPM imaging techniques used for the characterisation of ferroelectric materials and presents the information obtained.²² Among the techniques for ferroelectric surface imaging listed in Table 2.1, the most widely used currently is piezoresponse force microscopy (PFM), due to the ease of implementation, high resolution and relative insensitivity to topography and the state of the surface. PFM is rapidly becoming one of the primary imaging tools in ferroelectric thin film research that routinely allows high resolution (~ 10 nm) domain imaging. In contrast to X-ray techniques, which are limited to the averaged analysis of

domain structure, PFM yields spatially resolved information on domain size, correlations, domain behaviour near the inhomogeneities and grain boundaries. PFM can be used for imaging static domain structure in thin film, single crystals and polycrystalline materials, selective poling of specified regions on ferroelectric surface, studies of thermal evolution of domain structures, quantitative measurements of thermal phenomena and local hysteresis measurements.²²

2.8 References

- 1 J. Valasek, *Physical Review* **17**, 475 (1921).
- 2 F. Jona, *Ferroelectric Crystals*. (Dover Publications, New York, 1993).
- 3 F. Jona and G Shirane, *Ferroelectric Crystals*. (Pergamon, New York, 1962).
- 4 J. F. Scott and C. A. Paz de Araujo, *Science* **246**, 1400 (1989).
- 5 S. Y. Lee, D. J. Jung, Y. J. Song, B. J. Koo, and S. O. Park, presented at the 1999 Symposium on VLSI Technology, 1999 (unpublished).
- 6 J. F. Scott, *Ferroelectric Memories*. (Springer, Berlin, 2000).
- 7 in *The Economist*, Aug 22nd (1998), pp. 63.
- 8 H. D. Megaw, *Acta Crystallographica* **5**, 739 (1952).
- 9 S. Sinharoy, H. Buhay, D. R. Lampe, and M. H. Francombe, *Journal of Vacuum Science & Technology a-Vacuum Surfaces and Films* **10**, 1554 (1992).
- 10 K. D. Budd, S. K. Dey, and D. A. Payne, *British Ceramic Transactions* **36**, 107 (1985).
- 11 C. A. Paz de Araujo, J. D. Cuchiario, L. D. McMillan, M. C. Scott, and J. F. Scott, *Nature (London)* **324**, 627 (1995).
- 12 Ashish Garg, Ph.D thesis, University of Cambridge, 2001.
- 13 B. H. Park, B. S. Kang, S. D. Bu, T. W. Noh, J. Lee, and W. Jo, *Nature* **401**, 682 (1999).
- 14 H. Irie, M. Miyagawa, and T. Kudo, *Journal of Applied Physics* **90**, 4089 (2001).
- 15 B.S.H. Pang, Ph.D thesis, University of Cambridge, 2004.
- 16 R. Wordenweber, *Superconductivity Science and Technology* **12**, R86 (1999).
- 17 L. C. Klein, *Sol-Gel Technology for Thin Films, Fibers, Preforms, Electronics, and Specialty Shapes*. (Noyes Publications, Norwich, 1988).
- 18 D. E. Bornside, C. W. Maocosko, and L. E. Scriven, *Journal of Imaging Technology* **13**, 122 (1987).
- 19 D. Smith, *Thin films deposition: Principles and Practice*. (McGraw Hill, 1995).
- 20 A. Gruverman, O. Auciello, and H. Tokumoto, *Annual Reviews of Material Science* **28**, 101 (1998).

- ²¹ L. M. Eng, S. Grafstrom, C. Loppacher, F. Schlaphof, S. Trogisch, A. Roelofs, and R. Waser, *Advances in Solid State Physics* **41**, 287 (2001).
- ²² M. Alexe and A. Gruverman, *Nanoscale characterisation of ferroelectric materials: scanning probe microscopy approach*. (Berlin, 2004).

Chapter 3 Experimental techniques

3.1 Film fabrication

Films in this study were fabricated by two methods: pulsed laser deposition (PLD) and chemical solution deposition (CSD).

3.1.1 PLD

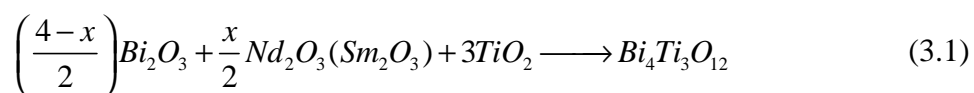
3.1.1.1 Preparation

1. Ablation targets– solid state processing

It is not economical to buy a series of targets in our present studies; therefore, targets were fabricated using solid state processing.

For PLD, attention must be paid to the target composition for the BiT system due to different species having different sticking coefficients on the substrate and evaporation rates that could vary significantly, especially at high growth temperature. Due to the fact that bismuth can form volatile oxides at high temperature during target fabrication and film growth, Bi rich targets were prepared.

Pure BiT and $\text{Bi}_{4-x}\text{R}_x\text{Ti}_3\text{O}_{12}$ (R=Nd, Sm; $x = 0.55, 0.70, 0.85, 1.00$) bulk ceramic samples were prepared by a conventional solid state reaction technique with starting materials Bi_2O_3 , TiO_2 and Nd_2O_3 (or Sm_2O_3) powders (Alfa, 99.9%) according to equation (3.1):



The required proportions of powders were mixed in acetone. An excess Bi_2O_3 of 10 mol% of the stoichiometric composition was added to the starting powders to compensate the bismuth loss during sintering and later deposition stages.

The mixtures were then ball milled with ZrO_2 ball milling media for 72 hours, followed by drying at room temperature for 12 hours to remove the acetone. The as-dried mixtures were then calcined at 850 °C for 8 hours. To obtain dense samples, disks of about 15 mm in diameter and 2~3 mm thick were pressed and sintered in air at temperatures of 1050~1150 °C for 2 hours. After holding at these temperatures, the samples were slowly cooled to 25 °C over about 8 hours. These sintering processes led to a high relative density of over 90% of the theoretical value.

There was some wastage because the target making procedure failed (irregular shapes) or they shattered during cooling to room temperature. SrRuO_3 targets were commercially available.

Surfaces of targets were polished before they were used for PLD. They were pre-ablated immediately before film growth, which was necessary because of possible surface contamination by impurities and also allowed stabilisation of the laser energy. This is important, since the initial film layers produced by the first several pulses are critical for epitaxial film growth.

2. Substrate treatment

Single-crystal SrTiO_3 substrates with (001), (011), and (111)-orientations, and silicon substrates were placed parallel to the target surface after a cleaning treatment. The structures of the silicon substrates were Pt(150 nm)/ TiO_x (40 nm)/ SiO_2 (400 nm)/Si(100) purchased from *PI-KEM*.

The substrates required cleaning before film deposition. The procedure of cleaning adopted was as follows. The substrates were soaked in a bath of chloroform and ultrasonically treated for about 10 minutes. These substrates were then washed once more by using acetone and finally by 2-propanol in a similar manner to the chloroform treatment. It was very important to give a final wash using propanol because acetone tends to leave some spots on the surface of the substrates after evaporation. After the final wash the samples were dried by dry nitrogen or compressed air.

3.1.1.2 Deposition

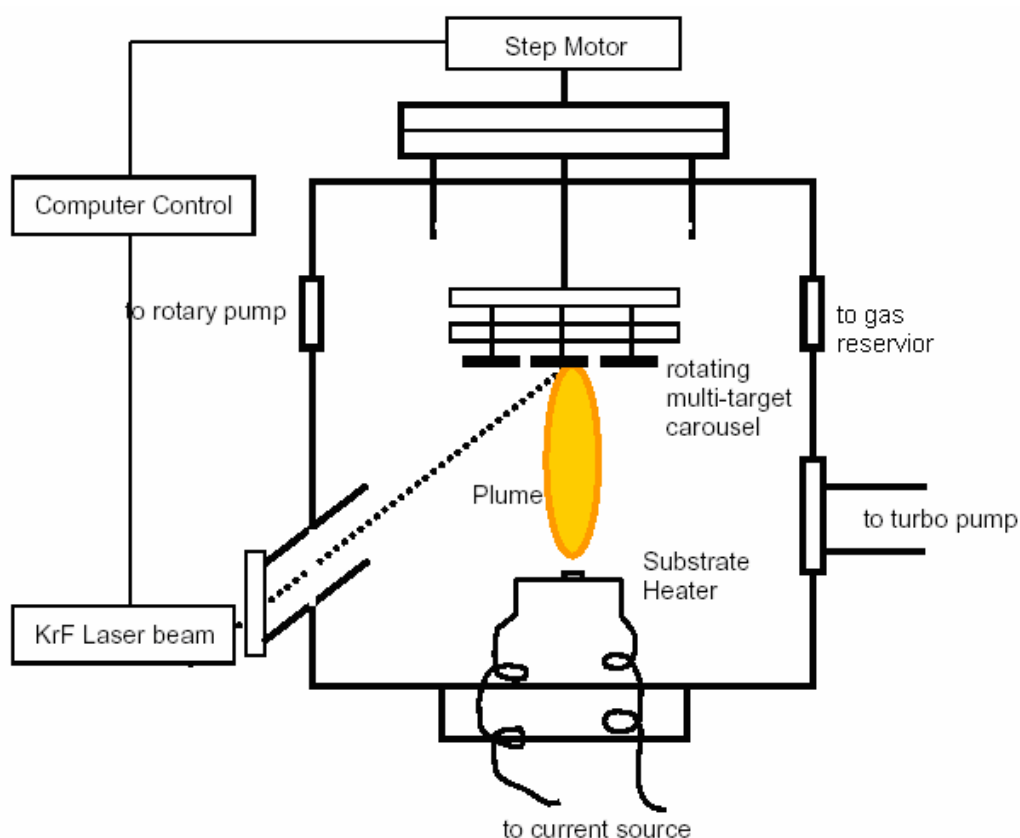


Fig. 3.1 Schematic drawing of the PLD system ¹

A PLD system consists of a target holder and a substrate stage / heater housed in a

vacuum chamber. A high powered laser (KrF) is used as an external energy source to vaporise materials (from the targets) which will be deposited as thin films.

1. System

During pulsed laser deposition, a pulsed laser beam is focussed onto the surface of a target at an oblique angle so that a substrate can be placed directly in front of the target surface (see Figure 3.1). This focussing action produces a laser spot of high enough energy which can ablate the target material which subsequently deposits onto the substrate. A mixture of Ar and O₂ or pure O₂ gas is used for the deposition of oxides with a pressure range of 20~50 Pa in most cases. The interaction of the laser beam with the target surface gives rise to a powerful plasma-like bright plume which emanates perpendicular to the target surface.

2. Procedure

In this study, a pulsed KrF-excimer laser with a wavelength of 248 nm and pulse duration of 20 ns was used for the pulsed laser ablation processes to deposit thin films. The laser pulse repetition rate was 1~10 Hz. The path of the laser beam was an enclosed pathway and adjusted through mirrors and lenses to the target. The beam enters the chamber through a window and is directed towards the target at an oblique angle. The distance between the target surface and the substrate was fixed at 6.5 mm and the angle between the target surface and incident laser beam was 45°. The spot size of the laser beam was about 8 mm². The energy of the laser pulse was measured with a Power/Energy meter by averaging the energies of 20 pulses. The energy of the beam incident on the target was about 90% of the energy of the beam before entering the chamber. The other 10% was absorbed in passing through the optical pathways and the MgF₂ window.

After loading the target and substrates inside the chamber, the chamber was evacuated to between 10^{-6} and 10^{-7} mbar, achieved after overnight baking. The substrate support heater was heated to the desired temperature and held at this temperature for about 30 minutes in order to preheat the substrates and also to evaporate any volatile matter from the substrate surface. During the preheating period, the laser energy was set to obtain the desired laser fluence (laser energy unit area, J/cm^2) on the target.

After preheating, O_2 was leaked into the system opening the leak valve with the gate valve throttled and the desired O_2 pressure was set by carefully controlling its flow through both valves. It was ensured that the backing pressure did not exceed 6×10^{-2} mbar during the whole deposition process.

The target was then pre-ablated for about 200 pulses with the substrates covered by a shield to remove any dirt and impurities from the target surface. Final ablation was carried out at a selected laser repetition rate for a desired number of pulses to get a particular thickness of the film. The substrate temperature was varied between 600 and 800 °C.

The post-annealing procedure was necessary since it ensured that the film composition was stoichiometric and there were no oxygen deficiencies. In order to achieve a well-crystallised thin film with an appropriate perovskite-type structure, the annealing temperatures of at least 650 ~ 800 °C had to be used.

The film growth reported was performed by *in-situ* growth. The as-deposited films were annealed for 30 ~ 60 minutes in approximately half an atmosphere of oxygen immediately after the film deposition, using the same substrate temperature as the film growth.

3.1.2 CSD

3.1.2.1 Selection of precursors

In this study, for compounds containing bismuth, the selection of the precursor is critical because of the lack of reactivity of some bismuth alkoxides. The bismuth alkoxide, $\text{Bi}(\text{OR})_3$ ($\text{R} = -\text{C}_2\text{H}_5$ or $-\text{C}_3\text{H}_7$), has been found to show lack of reactivity towards a variety of metal alkoxides including niobium, tantalum, titanium and lead. In addition to the technical problem, the costs for an all-alkoxide method is also an issue, since alkoxides may be extremely expensive, thus it would be preferable to find salt substitutions for them to reduce the production costs.

Therefore, we adopted the alkoxide-salt method, which means alkoxides and salts were used to introduce metal elements. The term salt basically refers to carboxylates but also includes the use of nitrates, sulfates, carbonates, chlorides, and hydroxides. In this study, we adopted nitrates for introducing Bi and Sm (Nd) elements since they are commercially available and cheap. To minimise the amount of organic materials that had to be vapourised, and thus minimise the size of the pores and other microscopic defects in the film, we selected Ti-isopropoxide to introduce Ti, and used Bi, Sm (Nd) nitrates to introduce Bi, Sm (Nd). To optimise the solubility and viscosity to obtain high quality coatings, in this study, we chose acetic acid as the main solvent.

3.1.2.2 Preparation of precursor solutions

Bismuth nitrate $[\text{Bi}(\text{NO}_3)_3 \cdot 5\text{H}_2\text{O}]$ and samarium nitrate $[\text{Sm}(\text{NO}_3)_3 \cdot 6\text{H}_2\text{O}]$ (or neodymium nitrate for Nd-doped) were dried at 70 °C in an oven for 24 hours. This procedure was used to remove the water in the compounds, so as to prevent the uncontrolled hydrolysis in the later stage. They were then separately dissolved in

acetic acid with a constant rate of stirring. The temperature for dissolving the nitrates was very critical, and was optimised to be ~ 90 °C after several trials. At a lower temperature, the nitrates would not dissolve completely; above this temperature, the solvent will evaporate quickly. These solutions were then mixed completely by stirring. Titanium isopropoxide $[\text{Ti}(\text{OC}_3\text{H}_7)_4]$ was mixed with 2-methoxyethanol $[\text{CH}_3\text{OC}_2\text{H}_4\text{OH}]$, stirred for 10 minutes and then added to the Bi-Sm acetic acid solution and a stable Bi-Sm (or Nd)-Ti sol was achieved with ~ 12 hours continuous stirring. The pH value was then adjusted with acetic acid and water and the concentration of the final stock solution was adjusted accordingly. The pH value was set to be ~ 1.0 .² The amount of each source material used in the preparation of Bi-Sm-Ti or Bi-Nd-Ti solution was according to the molar ratio of Bi:(Sm or Nd):Ti = $(4.0-x):x:3.0$ (x varies) with 10 mol% Bi excess precursor added to compensate for Bi loss during annealing. The BSmT/BNdT sol was stable against precipitation for at least eight months. Fig. 3.2 shows the flowchart for preparation of Bi-Sm (or Nd)-Ti precursors.

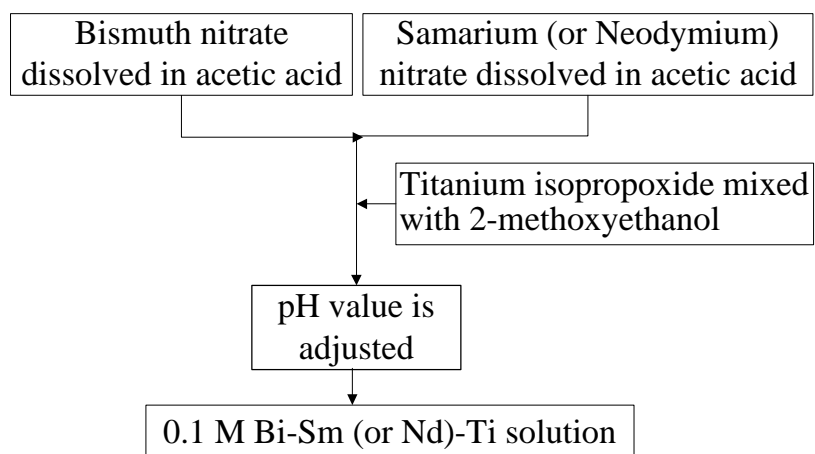


Fig. 3.2 Flowchart for the preparation of Bi-Sm (or Nd)-Ti complex solution

3.1.2.3 Film deposition

In our study, to make thin films, stock solutions were spun onto substrates which were mounted on the sample holder of a spin coater using a vacuum and rotated at 4500 rpm for 30 seconds and then pre-baked on a hotplate at 300 °C for 5 minutes. The procedure was repeated 3~5 times to produce the required thickness. During each coating procedure which lasted for 30 seconds, 15 drops of solution was applied to the rotating surface of the substrate. Films were then annealed in the range of 600 ~ 750 °C for 10 minutes in a flowing oxygen atmosphere (or other ambient, if necessary).

The rotating speed of the spin coater was adjusted from 1000 to 5000 rpm for several trial runs. According to the results of the surface coverage and morphology of the substrates, 4500 rpm was chosen to spin the films in our study. To expose bottom electrodes, during each deposition, a corner of the film was removed by acetone before the heat treatment.

Similarly, in this study, to generate a flat non-porous film surface, the pre-baking temperature was optimised at ~300 °C.

3.2 Film characterisations

3.2.1 Structural characterisations

3.2.1.1 X-ray diffraction (XRD) studies

The structures of targets and thin films were studied using X-ray diffraction (XRD) experiments with a Cu-K α ($\lambda = 1.54056 \text{ \AA}$) X-ray source and a Phillips X-ray diffractometer (Philips XPERT PW1710) operated at 40 kV and 40mA.

Samples were placed on a piece of glass slide and held flat by plasticine with the aid of a pair of supporting slides on both sides (Figure 3.3)³. These steps were important as they ensured that the whole assembly clamped to the pair of supporting slides, rotated about an axis lying on the surface of the film. Failure to do so would lead to errors in the measured peak positions given by

$$d(2q) = \frac{2x \cos q}{R} \quad (3.2)$$

x is the displacement of the sample surface from the rotation axis, and R is the distance from the beam source to the axis. A sample displacement of 0.1 mm, for instance, would lead to an error of about 0.07° for 2θ below 60° ($R = 173$ mm from the diffractometer geometry used in this project).

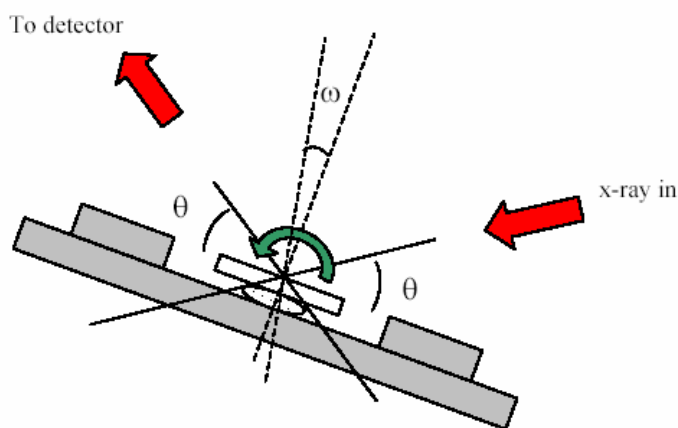


Fig. 3.3 X-ray sample set-up and measurement geometry³

A normal θ – 2θ scan of a sample over a wide angular range can give an idea about the degree of preferred orientation of the sample.

For ceramic targets, θ – 2θ scans consisted usually of recording the XRD intensities at 2θ angles from 5° to 55° with a constant speed of $1^\circ/\text{min}$.

For epitaxial films, two techniques were adopted to characterise samples, which are θ – 2θ scans and film texture characterisation by measuring the pole figures.

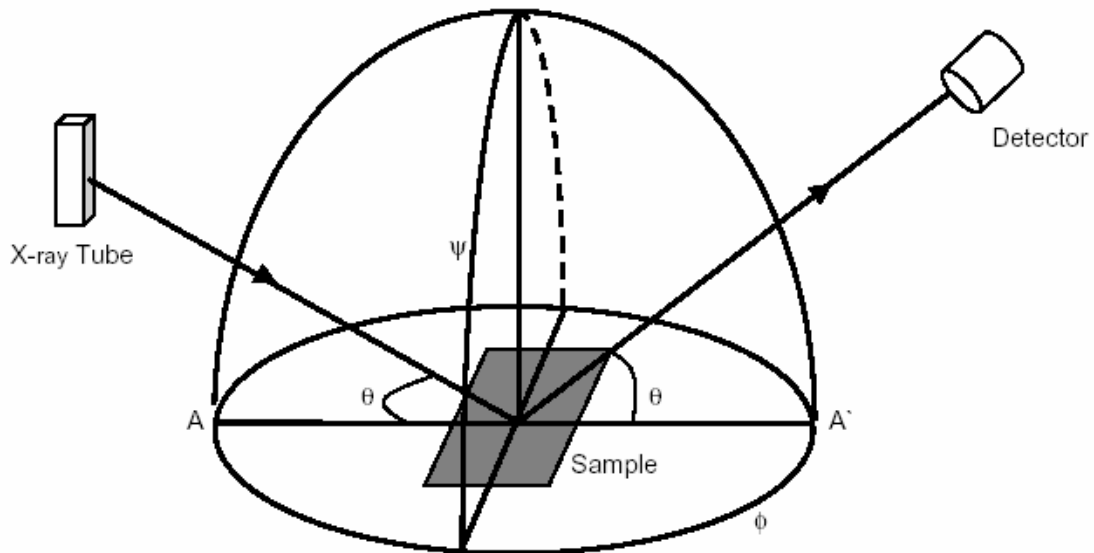


Fig. 3.4 Geometry of goniometer for pole figure analysis ¹

In an extreme case of good epitaxy, peaks from only one or a few particular type of planes are observed in a θ – 2θ scan. These intense peaks are from the planes which are preferentially oriented with the substrate plane. Another method of determining the degree of texture in epitaxial films by XRD is pole-figure analysis. As Fig. 3.4 shows, the texture cradle mounted on the sample stage enables the sample to be rotated in the plane normal to both its surface and the plane containing the incident X-ray beam (ψ scan, rotation about AA' axis) and also in its own plane (ϕ scan). To produce a 2-D representation of the 3-D distribution the poles which lie on the surface of a sphere may be projected onto the equatorial plane, producing a pole figure.

3.2.1.2 Atomic force microscopy (AFM) studies

In order to study the surface morphology, an AFM (Digital Instruments Nanoscope III)

was used. Commercially purchased microfabricated cantilevers with Si_3N_4 tips were used to image the film surfaces in the tapping mode configuration. The determination of surface roughness as well as the size of the surface features was carried out using the analysis program included in the software of the Nanoscope III.

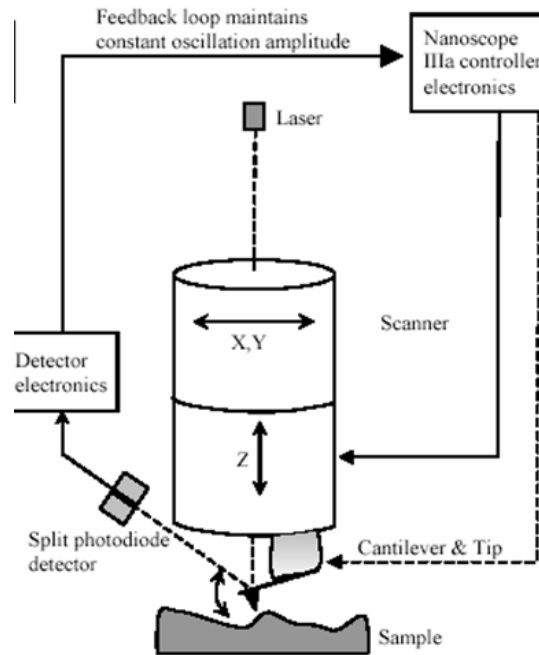


Fig. 3.5 Schematic diagram showing the AFM tapping mode ⁴

The AFM was operated in tapping mode in order to avoid any damage to the film surface. In the tapping mode the cantilever is oscillating as it is dragged across the surface of the sample as shown in Fig. 3.5. As the tip comes across surface features with varying heights the tip interacts with the surface, inducing a change in the amplitude of oscillation. Such oscillations are detected by a laser spot reflecting at the back of the cantilever, which is probed by a photodiode and converted into surface profile information. Resolution at atomic height scales can be achieved. The changes in voltage in order to maintain a constant distance between the sample surface and the tip are translated into the topographical variation of the sample surface when the tip scans it. AFM measurements were performed in air with Si_3N_4 probes having a ~ 260

kHz resonant frequency.

3.2.1.3 Piezoresponse force microscopy (PFM) studies

1. System setup and basic operations

The piezoresponse force microscopy (PFM) was developed for detection of polarised regions in ferroelectric copolymer films of vinylidene fluoride and trifluoroethylene^{5,6,7} and later was applied for visualisation of domain structure in PZT thin films.⁸

It is based on the detection of the local electromechanical vibration of the ferroelectric sample caused by an external AC voltage. The voltage is applied through the probing tip, which is used as a movable top electrode. The modulated deflection signal from the cantilever, which oscillates together with the sample, is detected using the lock-in technique, as in the case of non-contact imaging. However, in the piezoresponse mode the frequency of the imaging voltage should be far lower than the cantilever resonant frequency to avoid mechanical resonance of the cantilever. An external voltage with a frequency ω causes a sample vibration with the same frequency due to the converse piezoelectric effect. Vibration of the sample under the AC voltage also has a second harmonic component at 2ω due to the electrostrictive effect and dielectric constant.⁸ Analysis of the second harmonic signal showed that for PZT films the contribution of the latter effect dominates the influence of electrostriction⁹.

The domain structure can be visualised by monitoring the first harmonic signal (piezoresponse signal). The phase of the piezoresponse signal depends on the sign of the piezoelectric coefficient (and therefore on the polarisation direction) and reverses when the coefficient is opposite. This means that regions with opposite orientation of

polarisation, vibrating in counter phase with respect to each other under the applied AC field, should appear as regions of different contrast in the piezoresponse image.

Macroscopic ferroelectric characterisation techniques are of limited use in domain-level investigations of the properties of ferroelectric thin films and a more sensitive, highly localised measurement technique is required. The advent of PFM in 1992 provided such capabilities, allowing high-resolution, non-destructive investigations of ferroelectric thin films and devices at the nanoscale. First used by GÜthner and Dransfeld to image copolymer films⁵, PFM has been steadily developed to offer domain imaging, local ferroelectric measurements and domain manipulation.

The piezoresponse experimental configuration used in this study is shown in Fig. 3.6. It consists of an AFM, a Signal Recovery 7265 lock-in amplifier, and a custom-built voltage generator (to provide AC and DC voltages and a range of digitally-synthesised waveforms). The AFM used was a Digital Instruments MultiMode II with a NanoScope II Controller and Basic Extender Module. For piezoresponse imaging the AFM was used in contact mode with two modifications. Firstly, a Signal Access Module was added to allow the input of signals to the AFM and the monitoring of output signals from the AFM. And secondly, the tapping-mode cantilever holder (to which the cantilever tips are mounted) was replaced with one designed for Electrostatic Force Microscopy (EFM), in order to provide an electrical connection to the cantilever.

During piezoresponse imaging, the AFM cantilever is required to mechanically oscillate in a controlled manner at frequencies up to 20 kHz.¹⁰ A PtIr₅-coated silicon cantilever (NanoWorld) with a nominal resonant frequency of 75 kHz and a typical tip radius less than 30 nm was therefore used in this study. The PtIr₅ coating can provide a

conducting pathway to the sharpened tip at the end of the cantilever. The amplitude-frequency plot showed that 20 kHz lies well below the resonance peak of one of these cantilevers, which has a FWHM (full width at half maximum) of 321 Hz.

In this study thin film samples were mounted on a magnetic stainless steel puck using silver paint, which was also used to make electrical contact to an exposed area of the bottom electrode. The puck was then mounted on the electrically grounded piezoelectric scanner head.

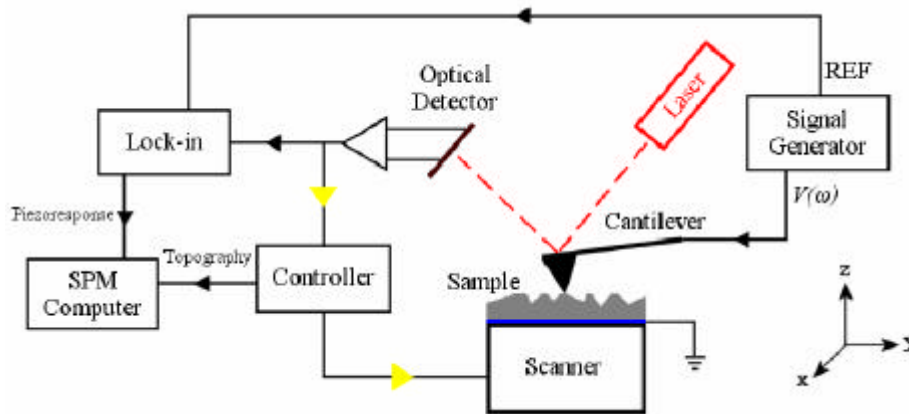


Fig. 3.6 Experimental configuration of the piezoresponse force microscopy system. $V(\omega)$ is the imaging voltage applied to the tip and REF the reference signal (also of frequency ω) of the lock-in amplifier ¹¹

The PFM was set to operate in contact mode on bare ferroelectric film surfaces (Fig. 3.6). Both piezoresponse domain images and hysteresis loops were recorded. For piezoresponse imaging, a small AC voltage (~ 18.0 kHz, 2.0 V) was applied between the oscillating tip and bottom electrode of the film, connected to the magnetic stainless steel puck sample holder using silver paint. Local piezoelectric coefficient hysteresis loops were measured by positioning the AFM tip at various sites on the film surface and measuring the AFM signal as a function of a triangular waveform bias DC voltage. The conversion factor between the photodiode signal of the AFM and the

mechanical displacement of the tip was obtained by careful calibration using a standard SrTiO₃ substrate¹¹.

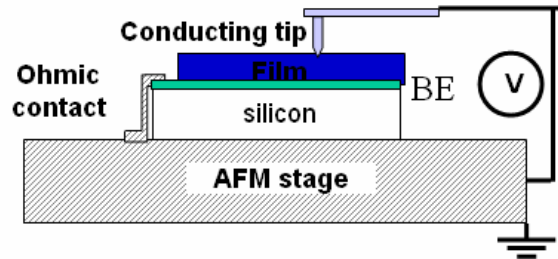


Fig. 3.7 Configuration of the PFM measurement

2. Measurement procedure--Domain imaging

The detailed measurement procedure of domain imaging is as follows:

- 1) Determine a size of area of the sample surface to be observed (such as $1\ \mu\text{m} \times 1\ \mu\text{m}$, or $10\ \mu\text{m} \times 10\ \mu\text{m}$).
- 2) Scan the surface with a DC bias voltage applied to the PFM tip, sufficient to induce an electric field greater than the local out-of-plane coercive field. This will locally pole the ferroelectric film and thus domains with a polarisation opposing the field will have their polarisation switched. The bias voltage required for switching will vary between differently oriented domains due to the fixed out-of-plane orientation of the electric field, *i.e.* a greater voltage is required to switch domains with a largely in-plane polarisation vector.
- 3) Subsequently scan the surface again without the DC bias. The effects of applying such a bias voltage (either to individual points on the film or to an area by scanning the tip) can then be observed by piezoresponse imaging. The surface topographic and

piezoresponse images of the films will then be acquired simultaneously by the PFM software.

4) Depending on the experimental requirement, another poling with an opposite direction of DC bias voltage may be required to reverse the domain polarisation and a subsequent scanning without a DC bias can give information of domain switching after the reverse poling.

3. Local ferroelectric measurement – d_{33} hysteresis measurement

The vibration amplitude measured with a lock-in amplifier provides information about the value of the piezoelectric coefficient. Amplitude of less than 0.1 nm can be detected in PFM, which provides a vertical sensitivity of about 5×10^{-12} m/V for an applied voltage of 10 V. Such a high vertical sensitivity makes this method nondestructive because in thin films with high piezoelectric constants, the imaging voltage can be reduced to a value lower than the coercive voltage, and as a result, the imaging process will have no effect on the existing domain configuration. However, it might be problematic to apply this technique to materials with low piezoelectric constants. Because only a change in the sample surface height is detected in the piezoresponse mode, it also allows one to avoid the effect of surface roughness on domain contrast and makes possible imaging of a domain structure even underneath a rough surface dielectric layer, although at the expense of the lateral resolution¹².

The most important characterisation and also proof of ferroelectricity is the presence of piezoelectric hysteresis. The hysteresis loops are obtained by sweeping the bias voltage and recording the piezoresponse signal.

The probing AC voltage is superimposed on the DC bias which is varied in steps from

zero to V_{\max} , then decreased down to V_{\min} (generally $-V_{\max}$) and increased again up to zero, in order to measure the piezoelectric coefficient as a function of the DC field. Each step of the bias has a duration t_{bias} . The loop obtained in this manner is referred to as the in-field loop and represents a typical d - E curve, as it is often used for the characterisation of the macroscopic piezoelectric properties of thin films.

3.2.1.4 Thickness measurement of thin films

For film thickness measurement of PLD samples (not for CSD films due to the nature of the deposition technique), a platinum (Pt) strip was placed across the centre of a substrate prior to the deposition. After deposition, the Pt strip was removed, leaving a step in the film, as shown in Fig. 3.8. The step height gave a measure of the film thickness, determined using a profilometer. The profilometer consists of a diamond tip that travels across the sample along its length, and vertical downward movement of the tip at the step gives a measure of the step height which represents the film thickness. The sensitivity of the profilometer is about 10 nm.

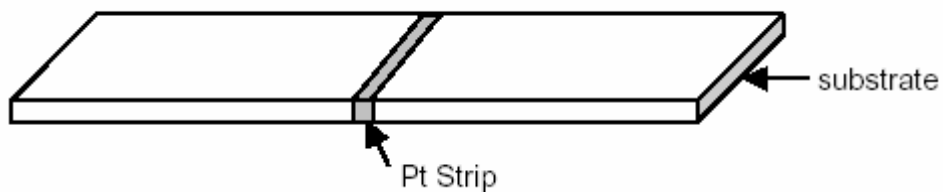


Fig. 3.8 Schematic representation of the thickness monitor ¹

More precise measurement of film thickness, applicable for both PLD- and CSD-derived films, was measured by thin film cross-sectional analysis using field-emission scanning electron microscopy (FE-SEM) (JEOL 6340F) operated at 10 kV. The samples for measurement were broken and mounted on a sample holder for measuring their cross section, which enabled direct visualisation of different layers of

the films.

3.2.1.5 Raman and infrared spectroscopy

1. Theory

Raman scattering and infrared spectroscopy measure optical vibrations of long wavelength, *i.e.* the optical modes at the Brillouin zone centre, via either a monochromatic light scattering experiment (Raman scattering) or via direct polychromatic light absorption (infrared spectroscopy). The set of vibrations for any molecules or crystals are unique (providing fingerprints) to that particular material, which makes vibrational spectroscopy a valuable tool for molecule and phase identification. Besides, they are more sensitive to local molecular structure compared with XRD technique. They are non-destructive methods and allow the investigations of samples in any physical state and of surfaces at any temperature or pressure.

Raman spectroscopy is an analytical method commonly applied to molecules or atom assemblies in any physical state. It identifies materials through the characteristic vibrations of their functional groups or their collective oscillations (phonons) in the solid state. Otherwise, when these molecules or atom assemblies interact with other chemical agents, the frequency, intensity and band-shape of their vibrations can change and therefore yield information on the nature, the localisation and the force of the interaction.¹³

Infrared spectroscopy is the study of the interaction of infrared electromagnetic radiation with matter, specifically optical vibrations of molecules or crystals. Classically, the electric component of electromagnetic radiation can couple with a normal vibration (normal mode) of dipoles in a crystal or a molecule fluctuating at the

same frequency. Vibrational energies lie approximately in the energy order of 0~5000 cm^{-1} (or 0~60 kJ/mol) and so they fall in the infrared region of the spectrum.

2. Procedure

In this study, Raman back scattering experiments were performed at room temperature by a Renishaw Ramascope-1000 micro-Raman spectrometer, using 514.5 nm photons from an Ar^+ laser (20 mJ) with the light focused onto the sample through a 50 \times optical microscope objective.

Some of the Raman spectra were recorded using a 632.8 nm He-Ne laser for excitation (LamRam 300, Jobin Yvon, located at the Department of Earth Sciences, University of Cambridge). The laser power is approximately 20 mJ within a spot of 1~2 micrometers in diameter using a 100 \times objective lens.

Infrared spectra were recorded using Bruker 113v and Bruker 66v spectrometers located at the Department of Earth Sciences, University of Cambridge. The Bruker 66v spectrometer attached to a microscope was used for *in situ* decomposition study of the precursors, heated by a home made heating stage from room temperature up to 300 °C. A Globar source, a liquid-nitrogen-cooled mercury cadmium telluride (MCT) detector and a KBr beamsplitter were chosen for measurement between 650 cm^{-1} and 6000 cm^{-1} . The resolution was set at 4 cm^{-1} . Every spectrum was Fourier transformed after 200 interference scans.

3.2.1.6 Scanning electron microscopy (SEM) and energy dispersive X-ray spectrometry (EDX)

This technique is useful for monitoring the surfaces with grain size above ~10 nm and for carrying out composition analysis using electron dispersive X-ray spectrometry

(EDX) over a selected area.

The EDX operates exclusively as a photon-to-charge detector and it directly measures the energy of the photon through photoelectric capture in a silicon diode.¹³ The nature of the EDX detection process permits the measurement of an extremely broad range of X-ray energies, effectively covering the complete range of interest.

The microscope used was JEOL JSM-5800LV, which was generally operated at 20 kV. Samples were coated with gold (for grain size analysis) or carbon (for composition analysis) to avoid any charging effects which could be present due to the non-metallic nature of the samples. They were processed using VOYAGER (Therone Ael Ltd., Crawley, U.K.) program, using standard reference spectra. Each datum presented in this study is an average of 5 to 10 readings when using EDX based in SEM. Spectra collected over $2\ \mu\text{m} \times 2\ \mu\text{m}$ area were taken on different areas of the film surface.

For thin films, cross sectional images are important to obtain the detailed information about grain shape, grain size, film thickness, and film density. In our study, field emission scanning electron microscope (FE-SEM; JEOL 6340F, Japan Electron Optics, Ltd., Tokyo) was used. It was operated in two modes: secondary electron imaging (SEI) mode and back scattered electron image (BSEI) mode. The SEI mode monitors secondary electrons, which are low energy electrons emitted from very near the sample surface. This signal provides an image of the sample topography, and hence, external morphology. The BSEI mode uses backscattered electrons, which have higher energies than secondaries and are produce when electrons from the primary beam are 'bounced' back out of the sample by elastic collisions with atoms. The number of electrons a given atom will backscatter is proportional to its atomic number. Materials composed of larger, heavier atoms will backscatter more electrons,

producing brighter gray tones in the images than lower mass materials (differences in average atomic mass of 0.1 amu can be resolved). Backscattered electrons thus produce an image that is related to material composition, providing both spatial and chemical information.¹⁴

3.2.2 Electrical characterisations

For electrical characterisations, top Pt electrodes of $4 \times 10^{-4} \text{ cm}^{-2}$ ($200 \mu\text{m} \times 200 \mu\text{m}$) were deposited by DC sputtering on top of the films through copper masks. After the deposition, samples were annealed on a hotplate at 250 °C for 5 minutes, to improve contacts between the electrodes and the film surface.

3.2.2.1 Dielectric properties

In this study, the dielectric behaviours of the films studied were characterised using an HP 4192A Impedance Analyser (located at the Earth Science Department, University of Cambridge) by measuring the frequency dispersion characteristics of the capacitance and dissipation factor in a frequency range from 10^3 Hz to 10^6 Hz with an oscillating voltage of 50 mV, which was considerably less than the coercive field of the material so that the AC field does not affect the polarisation state.

3.2.2.2 Ferroelectric properties and leakage current measurement

1. Theory and details of the measurement -- ferroelectric hysteresis loops

For ferroelectric hysteresis loop measurement, a voltage waveform is applied to the sample in a series of voltage steps. At each voltage step, the current induced in the sample by the voltage step is integrated and the integral value is captured and

converted into polarisation ($\mu\text{C}/\text{cm}^2$) by ¹⁵

$$\frac{\mu\text{C}}{\text{cm}^2} = \frac{Q}{\text{Area}} = \frac{CV}{\text{Area}} = \frac{\text{IntegratorVolts} \times \text{SenseCapacitor}}{\text{SampleArea}} \quad (3.3)$$

Equation (3.3) is scaled by appropriate factors to properly adjust computed values to the standard polarisation units of $\mu\text{C}/\text{cm}^2$.

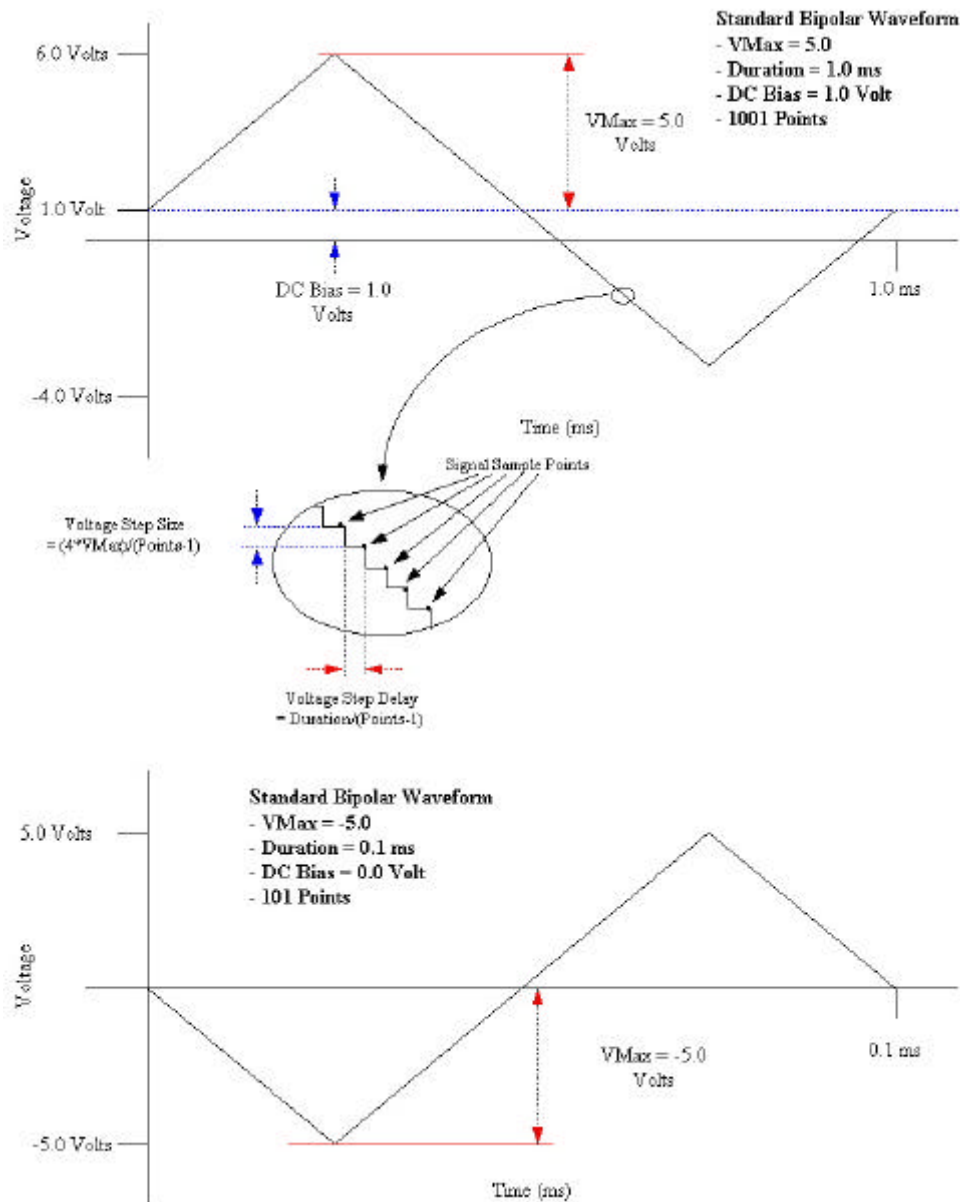


Fig. 3.9 Details of the standard bipolar hysteresis drive profile ¹⁵

The voltage waveform is normally a standard bipolar triangular waveform that can be

simply defined by providing the maximum voltage and the duration of the waveform in milliseconds. The sign of the voltage indicates the direction of the first leg of the waveform. The number of sampling points is controlled primarily by the duration of the waveform, though it may also be adjusted by the voltage. The waveform begins at 0.0 volts and steps to a maximum value of the assigned voltage. It then proceeds to step to the negative of the assigned maximum. Finally it steps back to zero volts. The entire standard bipolar waveform structure is shown in the Fig. 3.9.

The standard bipolar waveform produces five derived parameters of interest. These are shown in Table 3.1.¹⁵

Table 3.1 Derived parameters of a ferroelectric hysteresis loop¹⁵

P_{\max}	The polarisation at the maximum applied voltage. Note that this will be the polarisation at +5.0 Volts in both the examples.
$+P_r$	The polarisation at zero volts when voltage is moving from positive to negative. If V_{\max} is negative, this will be the polarisation at the final sample point.
$-P_r$	The polarisation at zero volts when voltage is moving from negative to positive. If V_{\max} is positive, this will be the polarisation at the final sample points.
$+V_c$	The voltage at which polarisation is zero when switching from negative to positive.
$-V_c$	The voltage at which polarisation is zero when switching from positive to negative.

Hysteresis loops are normally used as primary characteristics for ferroelectric

materials, which shows the nonlinear polarisation response of the ferroelectric material to a bipolar triangular voltage stimulus waveform, where polarisation is the nonvolatile memory property of a ferroelectric sample.

The standard hysteresis measurement is a particularly effective tool as it shows the total sample response to the stimulus voltage. This response can be modelled as the superposition of a number of parasitic linear elements along with the non-linear ferroelectric mechanism. The linear components of the ferroelectric model include linear capacitance, resistance and diode effects. In a quality sample, these response components will be very small with respect to the non-linear signal, which is of most interest to researchers. But the non-linear polarisation response of the sample can also be modelled as two or more non-linear components.

The two components of primary concern are the remanent polarisation and the non-remanent polarisation. Remanent polarisation is the polarisation of the most interest. It is that bi-state ferroelectric parameter that maintains its state once switched and serves as the memory characteristic of the sample. Non-remanent polarisation also switches with the remanent. However, once the sample has returned to a quiescent voltage, the non-remanent polarisation does not maintain its switched state, but returns to the random situation; therefore, this polarisation does not contribute to the memory properties of the sample.¹⁵

Normal hysteresis measurement normally captures the superpositive response of all of the linear and non-linear components. Normally the linear components may be ignored. As a result,

Hysteresis response = resistance + linear capacitance + diode effects + remanent

polarisation + non-remanent polarisation

$$\approx \text{remanent polarisation} + \text{non-remanent polarisation} \quad (3.4)$$

Equation (3.4) applies to the measurement of the sample response to the second leg of the standard bipolar triangular stimulus voltage in all hysteresis measurements. It applies to the first leg only if the sample is pre-switched into a state that ensures that the first leg will switch the sample into the opposite state. If the sample is pre-switched into a polarisation state that ensures that the first leg reinforces (does not switch) the preset state, then only non-remanent polarisation will be switched and measured, as the remanent polarisation is already switched into the particular state. This leaves a tool for directly measuring both the combined remanent and non-remanent polarisation values and the non-remanent only. Subtracting the non-remanent measurement from the remanent plus non-remanent (non-switching from switching) allows the remanent-only hysteresis loop to be derived. Repeating the experiment at the opposite polarisation state allows both halves of the bipolar non-remanent sample response to be independently derived. Recombining the two halves results in a full non-remanent hysteresis loop being constructed.

In the present study, the films are principally considered used for nonvolatile memory use, so that it would be preferable to know the ‘real’ remanent hysteresis response of the achieved films.

A typical remanent hysteresis loop was measured at 1 kHz and different parts of polarisations were shown as a function of time, as shown in Fig. 3.10, which is an alternative method of displaying the unprocessed data. In this case, three plots are generated with a common x -axis, and x is given as time (ms). Both the drive voltage

and the polarisation response are plotted as independent functions of time, rather than as functions of each other. The polarisation response is plotted for both the derived remanent hysteresis measurement and the original Logic 1 measurement.

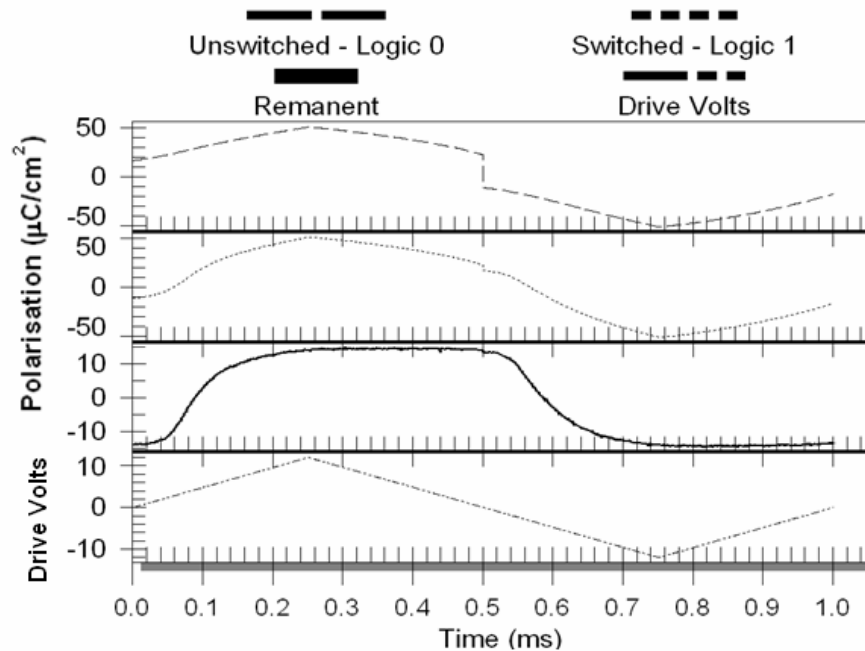


Fig. 3.10 Polarisations as a function of time

We can see that the unswitched polarisation was basically linear to the driving voltage, while the switched polarisation was non-linear to the driving voltage, as we described in the previous section. The remanent polarisation was calculated based on Equation (3.4) and is shown in Fig. 3.10.

For clarification, three hysteresis loops were drawn as a function of applied bias voltage, as shown in Fig. 3.11. The unswitched part of hysteresis loop was subtracted from the switched hysteresis loop, which is the total combination of the unswitched and remanent loops. Therefore, the remanent loop shown in this figure is its true capability to maintain ferroelectric bi-states and thus reflect its ‘real’ memory characteristics.

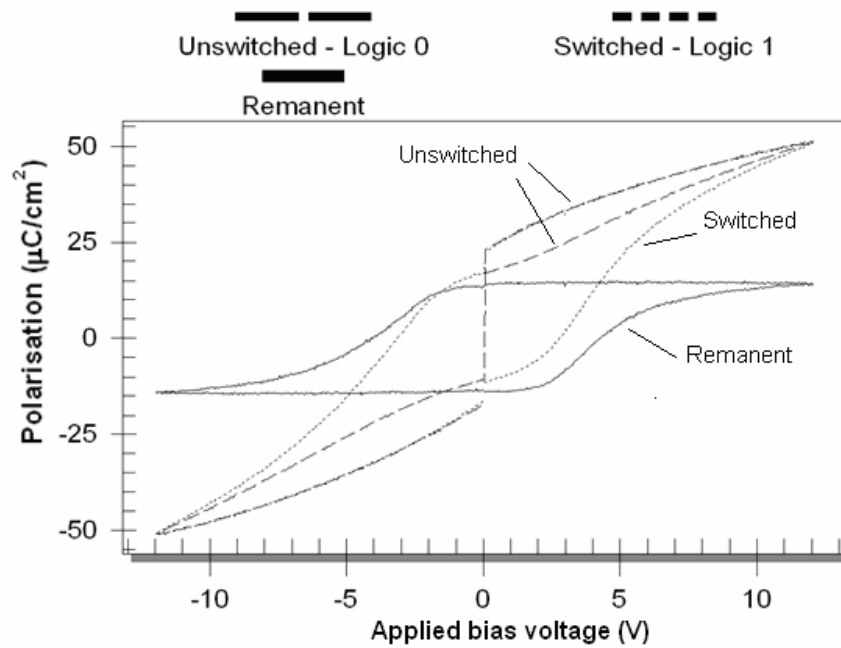


Fig. 3.11 Hysteresis loops of a ferroelectric film

2. Leakage current measurement.

The leakage current of ferroelectric oxide materials is a limiting factor for memory applications as the stored charge can leak through a capacitor due to excessive leakage of the current making the binary state unrecognisable.

In the measurement of leakage current, the steady state current through the test element connected to the tester is sampled by placing a constant DC bias voltage across the sample. A programmable delay or 'soak' period passes before the measurement begins. This is intended to allow any polarisation switching current or other currents induced by the application of the voltage to settle so that the sample is in steady state. After the delay period, a measurement period begins in which the current through the device under test is regularly sampled and recorded. The profile is shown in the Fig. 3.12.

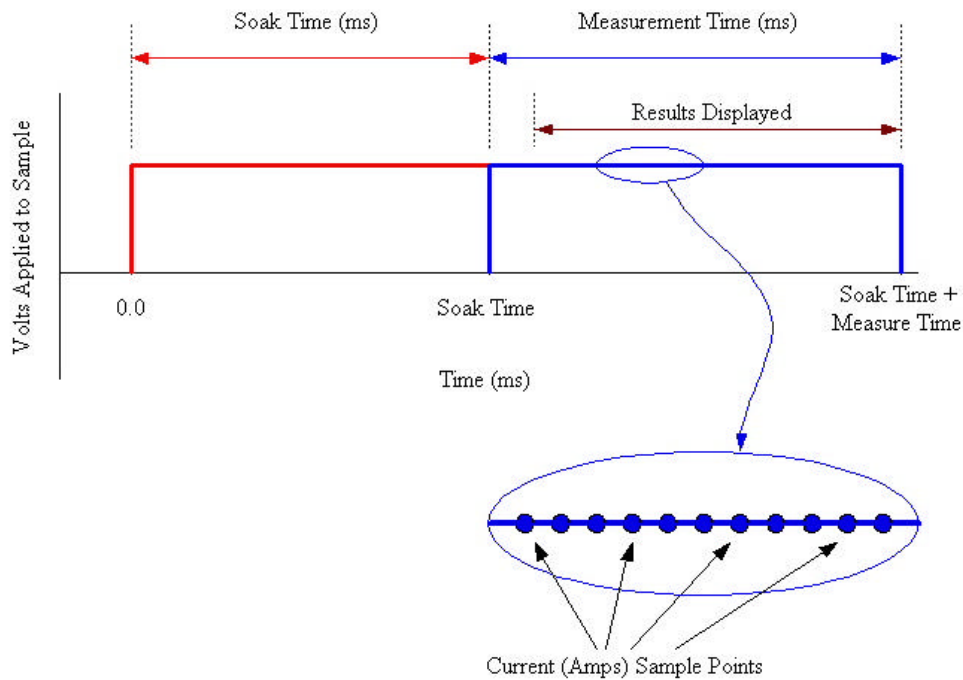


Fig. 3.12 Leakage test stimulus and measurement profile ¹⁵

The I - V measurement (or J - V , for leakage current density-voltage) was principally used, which performs a series of leakage measurements as voltage is stepped from point to point along a voltage profile. At each step, current, resistance and resistivity are recorded as a function of the voltage at the step.

I - V test profile consists of a series of voltage steps of a user-defined number. At each step, a leakage measurement is made. A single step consists of the following elements:

- Delay for the step delay time.
- Step to the DC voltage for the measurement.
- Delay for the soak time.
- Measure the leakage over the measure time.
- Compute current (Amps), resistance (Ohms) and resistivity (Ohms cm).
- Return to zero volts.

- Repeat at the next voltage.

A schematic of a single step in an I - V measurement is shown in Fig. 3.13.

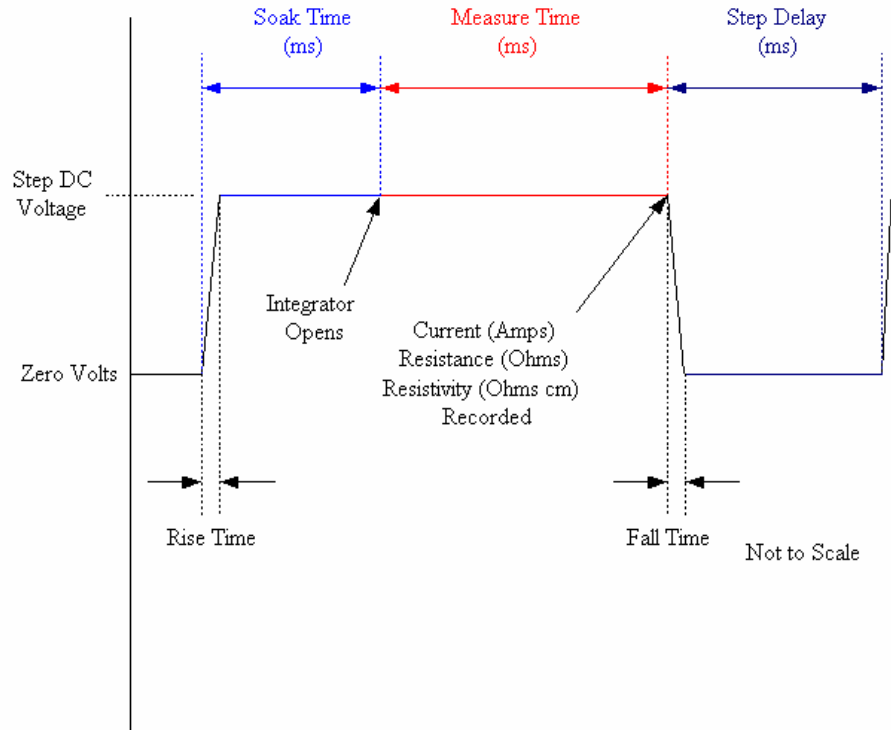


Fig. 3.13 A schematic of a single step in an I - V measurement ¹⁵

The appropriate starting status for the sample is a key point, which can determine whether or not the sample is switched during the measurement. The I - V measurement is normally a very lengthy process, which takes up to several hours to complete.

3. Electrical fatigue measurement

To measure a sample's fatigue, a PUND (Positive-Up-Negative-Down) measurement method is used to extract the remanent polarisation during switching. The PUND measurement is a standard pulse measurement consisting of five pulses of identical pulse width and magnitude.¹⁵ The first pulse presets the sample to a given polarisation state. The second pulse switches the sample to the opposite state and measures the

switched polarisation. A second measurement is made after the pulse returns to zero volts and a programmable delay occurs. The delay is intended to allow non-remanent polarisation components to dampen before the measurement is made.

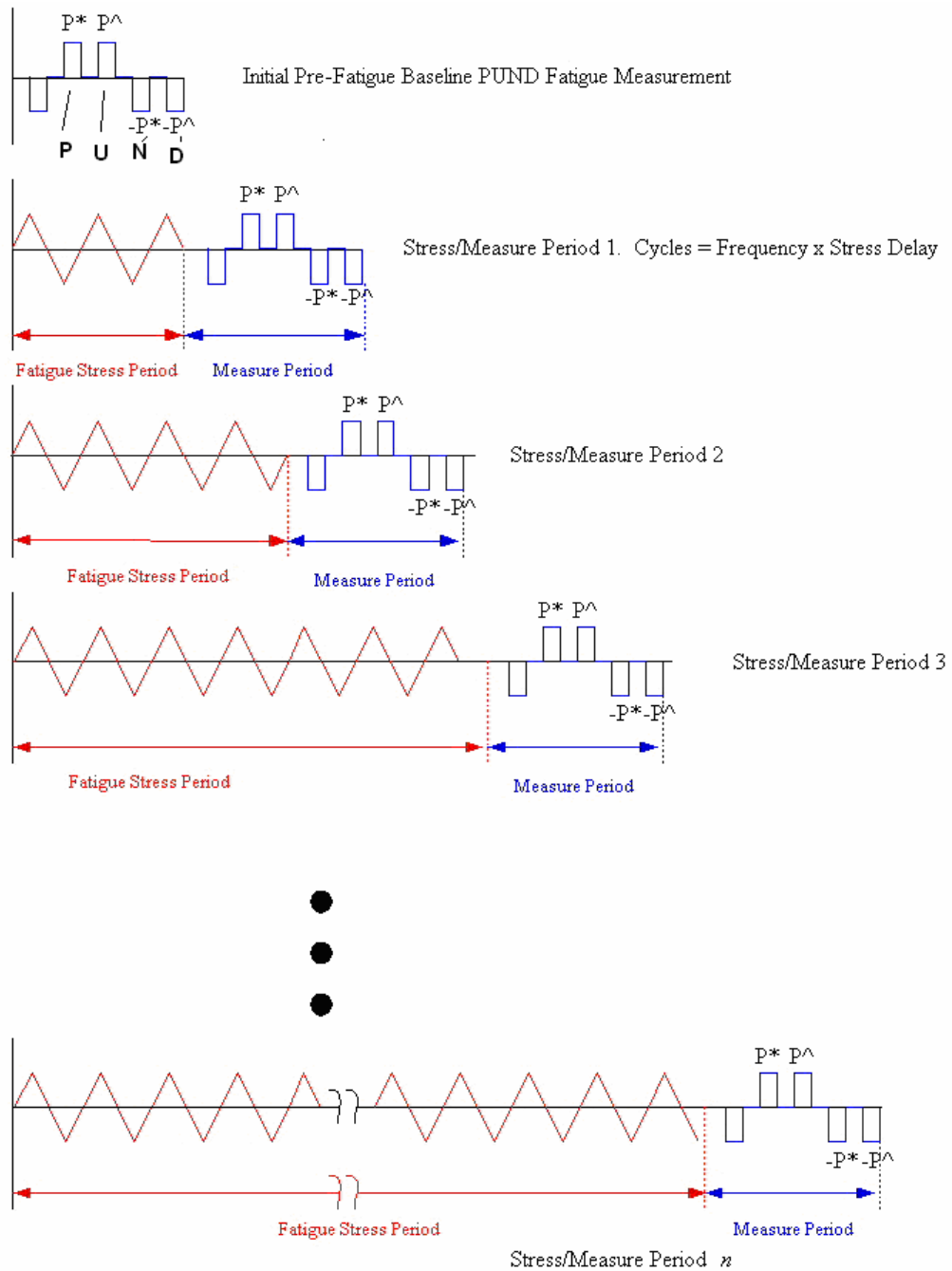


Fig. 3.14 The signal profile of the fatigue measurement ¹⁵

To determine that fatigue has occurred, it is necessary to perform an additional PUND

measurement before the application of the stressing waveform to provide a pre-fatigue baseline against which to compare the measurement on the stressed sample. This algorithm provides a discrete and absolute measure of the fatigue damage mechanism after some number of switching cycles. (The number of cycles is given by the stress waveform frequency \times the duration.) It does not characterise the progress of the fatigue as the number of cycles grows. A refinement would shorten the stress period and repeat the stress/measure event several times producing several fatigue sample points and characterising the growth of the damage mechanism. Here, then, a stress/measure event, or stress/measure cycle, consists of a period of the application of the fatigue stress waveform to the sample, followed by a PUND measurement. (Note that the term 'cycle' has taken on two meanings. It signifies a single complete switch of the sample from one polarisation state to the other and back during the application of the stress waveform. It also signifies a single stress/measure event.)

Fatigue is best characterised when its growth is displayed as a function of the log of the total number of stress waveform cycles that have been applied to the sample at the time of the measurement. This suggests a final refinement in which the duration of the stress period (and therefore the number of waveform cycles applied) can be adjusted. Under normal circumstances, each subsequent stress/measure cycle would be of longer duration than the previous, thereby applying a greater number of stress waveform cycles. The entire algorithm is simplistically represented in Fig. 3.14.

The waveform depicted in Fig. 3.14 is a triangle wave, which is simply defined by specifying only the frequency and voltage. Other waveform options include sine, square, pulse, arbitrary custom waveform, *etc.*

There are several critical parameters for switching pulses in fatigue measurement:

pulse voltage, pulse width, frequency. The polarisation switching process can be characterised by the following parameters: amplitude of cycling voltage (V), remanent polarisation (P_r), switchable polarisation (P^*), P^\wedge , and dP ($dP=P^*-P^\wedge$, also as P_{nv} , nonvolatile polarisation) (see Fig. 3.14). The occurrence of fatigue is usually described by plotting P_r , P^* , P^\wedge , or dP , as a function of the number of switching cycles N in log scale.

4. Procedure

The ferroelectric properties and leakage currents of the films were investigated using a RT 6000 ferroelectric test system (Radiant Technologies) in virtual ground mode. The frequency of the waveform used for hysteresis loop measurements is normally 1 kHz.

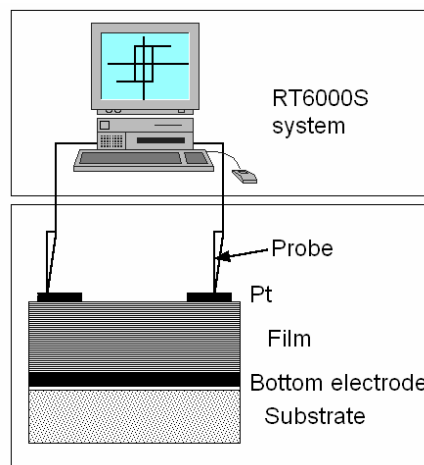


Fig. 3.15 Drawing of the measurement system

The leakage current characteristics of the films were measured by applying a staircase-shaped DC-bias voltage (with a 0.1 V step and 1 second span at each step, up to ~ 300 kV/cm) to the top electrode while the bottom electrode was grounded. The films were probed as shown in Fig. 3.15. It should be noted that for electrical leakage

current measurement, a pair of top and bottom electrodes were probed to avoid additional information from surface charge or other possible path for electrons which may complicate the issue.

3.2.2.3 Low temperature electrical measurement

Low temperature measurements were conducted with a cryostat system (CTI-Crogenics He-refrigerator) in the temperature regime of 35 to 300 K. The system consists of a source of high pressure helium gas, a refrigerator, a vacuum pump, and a cold stage which is in a vacuum chamber evacuated by the pump to decrease the heat transfer.

Eight electrical feed-throughs provide access to the interior of the vacuum chamber. This provides eight lines for wire-bonding. The shielding provided by the vacuum chamber provides a low noise environment. To minimise heat flow into the temperature stage, the following sample preparation technique was used. The sample was mounted in a 10-pin brass dual inline circuit chip. The pins were removed from the chip carrier and the bottom was sanded with diamond sand paper until smooth, to ensure good thermal transfer. The chip carrier was mounted using a screw to the cold stage. The samples were attached to the carrier by silver epoxy, with the entire bottom of the sample coated, again to ensure good thermal transfer. Contacts were made to the electrodes on the sample by wire-bonding.

The temperature cycle was 300 K \rightarrow 35 K \rightarrow 300 K when measuring electrical properties. At each temperature point, the dwell time was 2 minutes before the sample was measured. The temperature descending and ascending rate was \sim 4 K/ min.

3.3 References

- 1 Ashish Garg, Ph.D thesis, University of Cambridge, 2001.
- 2 J. Wang (Private communication).
- 3 C.W. Leung, Ph.D thesis, University of Cambridge, 2002.
- 4 D. Morecroft, Ph.D thesis, University of Cambridge, 2003.
- 5 H. Guthner and K. Dransfeld, *Applied Physics Letters* **61**, 1137 (1992).
- 6 D. Sarid and V. Elings, *Journal of Vacuum Science & Technology B* **9**, 431 (1991).
- 7 H. Birk, J. Glatz-Reichenbach, J. Li, E. Schreck, and K. dransfeld, *Journal of Vacuum Science & Technology B* **9**, 1162 (1991).
- 8 K. Franke, J. Besold, W. Haessler, and C. Seegebarth, *Surface Science* **302**, L283 (1994).
- 9 K. Franke and M. Weihnacht, *Ferroelectrics Letters* **19**, 25 (1995).
- 10 M. Alexe, C. Harnagea, W. Erfurth, D. Hesse, and U. Gosele, *Applied Physics A-Materials Science & Processing* **70**, 247 (2000).
- 11 P.S. Roberts, M. Phil. thesis, University of Cambridge, 2004.
- 12 A. Gruverman, O. Auciello, J. Hatano, and H. Tokumoto, *Ferroelectrics* **184**, 11 (1996).
- 13 M. Grasserbauer and H. W. Werner, *Analysis of microelectronic materials and devices*. (John Wiley and Sons, Chichester, 1991).
- 14 <http://research.ou.edu/microprobe/imaging.html>, (2005).
- 15 Radiant Technologies Inc., RT6000 Standardised ferroelectric test system operation manual.

Chapter 4 PLD-grown W-substituted strontium bismuth tantalate (SBT) thin films

4.1 Background and motivation

SBT is perhaps the most studied compound among the BLSF and is one of the most promising materials for application to Nv-RAMs due to its excellent ferroelectric properties, characterised by limited polarisation fatigue and low coercive field.¹

The electrical conductivity in BLSF is highly anisotropic, with maximum value in the same plane as the polarisation.^{2,3} The main problem concerning its practical application as a ferroelectric is that pure BLSF has a relatively high electrical conductivity.

Villegas *et al.*⁴ reported that W-doped BiT ceramics showed an electrical conductivity value 2-3 orders of magnitude lower than undoped ceramics. V-substitution increased the $2P_r$ value and also lead to a reduction in electrical conductivity in SBT thin films.⁵ Noguchi *et al.*⁶ reported a remarkable improvement in ferroelectric properties in the BiT ceramic by doping V to B sites, which was explained by a decrease in the defects affecting the domain pinning. Sakai *et al.*⁷ and Kim *et al.*⁸ have reported the effects of W-substitutions on BiT thin films fabricated by MOCVD and sol-gel processing, respectively. The substitution of W improved not only ferroelectric properties ($2P_r$ and E_c),^{7,8} but also the electrical properties such as leakage current and fatigue properties⁷. Since it has a similar crystal structure to BiT, we can expect that W-substitution will also have the same effect on the SBT thin film system,.

The annealing temperature is another issue. For the pure SBT thin film, the optimised

annealing temperature was higher than what we used ($\sim 850\text{ }^\circ\text{C}$)^{9,10}, which would be impractical for the silicon substrates used. W-doping can reduce the sintering temperature (from $1150\text{ }^\circ\text{C}$ to $900\text{ }^\circ\text{C}$) in bulk ceramic form as reported by Villegas *et al.*⁴, therefore, we can expect that W-doping in thin film form can have a similar effect.

In the present work we studied the effect of W substitution on the structural and electrical properties of SBT thin films on Pt-coated silicon substrates fabricated by PLD.

4.2 Experimental details

4.2.1 Target fabrication

W-doped SBT (SBTW) targets were supplied from *National University of Singapore* (fabricated by a conventional solid-state technique).¹¹ The formula of the ceramic targets was $\text{SrBi}_{2+y}(\text{W}_x\text{Ta}_{1.0-x})_2\text{O}_9$, ($x = 0, 0.10$ and 0.20 , denoted as SBT, SBTW1 and SBTW2 respectively in the following text; $y = 0.10$, which means a 5 atom% bismuth excess). The XRD pattern of the targets did not show any detectable impurity phase other than pure bismuth layered structure.¹¹

4.2.2 Film deposition and growth process

In this study, the laser wavelength was automatically limited by the deposition system. The pulse frequency and laser fluence both affect the interaction of the laser with the target. However, previous studies carried out in our group by Garg¹² demonstrated that the pulse frequency does not severely influence the film quality as compared to other parameters such as temperature and laser fluence.¹² In Garg's study, the

morphology (RMS roughness) of the SBT films deposited at frequencies of 1 and 4 Hz was approximately 1.0~1.5 nm, whilst it was about 2.0 nm for the films deposited at 7 Hz and rose to 3.0~4.0 nm at 10 Hz.¹² In our study, due to the time limitations, to balance of deposition rate and surface morphology of the films, the pulse frequency was set to 5 Hz.

Several studies have been carried out in various research groups on the ambient gas pressure (partial oxygen pressure) dependence of the film quality.^{13,14,9,15} Most of the results suggested the optimised value of 13.3~26.6 Pa (100 ~ 200 mTorr).^{13,14,15} One of the typical studies by Pak *et al.*¹⁵ showed that films prepared at 50 mTorr (6.7 Pa) are oxygen deficient while those prepared at 500 mTorr (67 Pa) have excessive oxygen resulting in a co-existing ferroelectric and pyrochlore phase. As for the film prepared at 200 mTorr (27 Pa), the dense surface with an average grain size of 50 nm revealed good ferroelectric properties.¹⁵

Combining the previous similar studies in our research group,^{12,10} the ambient gas pressure in the present study was set to 27 Pa.

Table 4.1 Deposition parameters used for the SBTW film growth

Deposition parameters	SBTW
Laser pulse frequency (Hz)	5
Total number of pulses	7200
Pulse energy per spot (mJ)	175
Substrate temperature (°C)	700~800
Oxygen pressure (Pa)	27
Anneal pressure (kPa) (O ₂)	~65
Thickness (nm)	~ 350 nm

The deposition parameters used for film growth are shown in Table 4.1. SBTW thin films were deposited on Pt (150 nm)/TiO_x (40 nm)/SiO₂ (400 nm)/Si(100) substrates.

After deposition, the film was annealed in a pure oxygen atmosphere for 30 mins and then cooled down to room temperature in ~90 minutes.

4.3 Results and discussion

Here we discuss the effect of processing procedure and W doping on properties of the films.

4.3.1 Effect of processing on film properties

SBTW1 films were deposited under the same conditions, grown and annealed at 700 °C, 750 °C, and 800 °C, respectively.

4.3.1.1 Structural properties

Fig. 4.1 shows the XRD patterns of SBTW1 thin films annealed at various temperatures. The film orientations (*hkl*) were indexed by assuming the films are orthorhombic. The perovskite phase was fully formed with a mixture of (115) and (00*l*) peaks. This indicates that the films are polycrystalline. The (115) peak was enhanced after growth and annealing at 750 °C. Since the spontaneous polarisation of SBT exists parallel to the (Bi₂O₂)²⁻ layers, the (115) orientation is effective for a memory device application in which a large remanent polarisation needs to be aligned normal to the film plane.

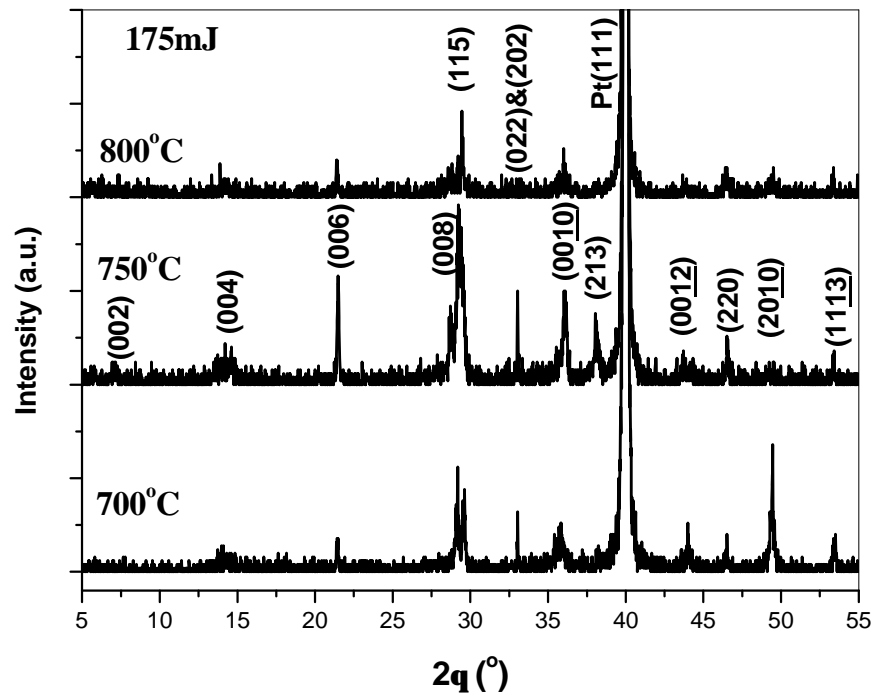
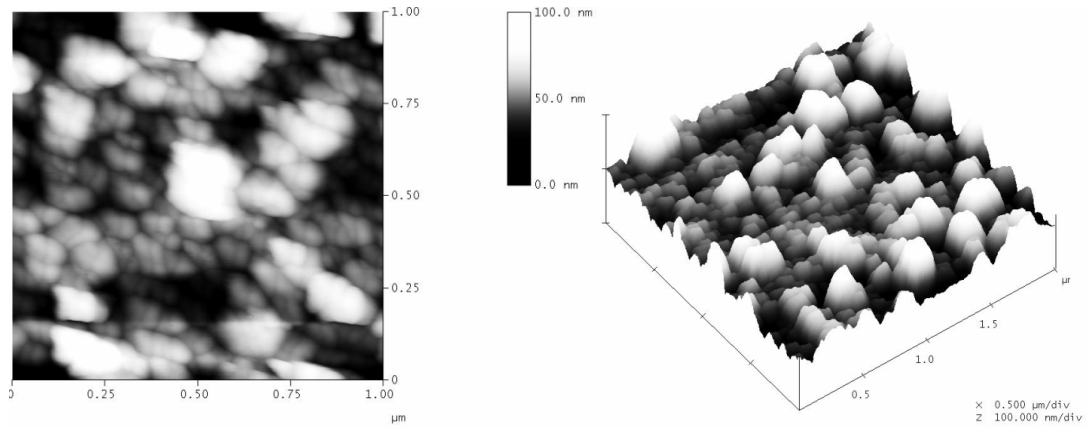
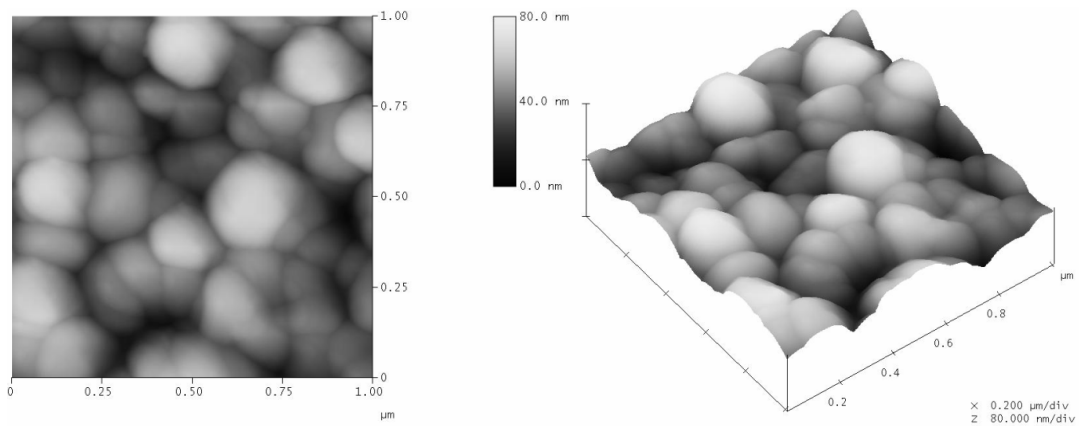
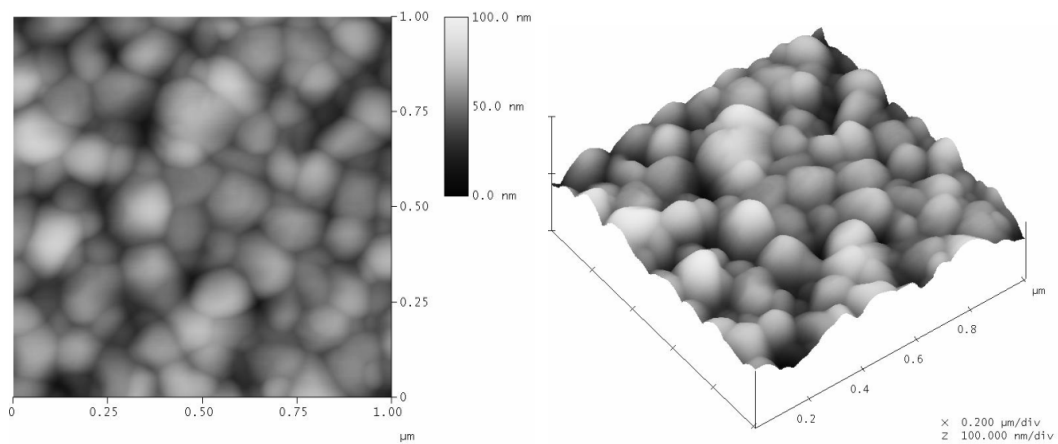


Fig. 4.1 XRD patterns of SBTW1 films following various fabricated temperatures

Fig. 4.2 show $1 \mu\text{m} \times 1 \mu\text{m}$ AFM images illustrating the changes to the surface morphology of SBTW1 films following growth and annealing at various temperatures. These films showed similar morphology, all basically having spherical surface features (These represent the tops of ‘columns’, but for convenience, the term ‘grains’ will be used in the following text). The surface of the 700 °C-fabricated film consisted of small spherical grains ~ 8 nm in size. These form aligned structures by coalescing into bigger grains. These aligned columns fused and formed larger columns at 750 °C and the lateral size of the columns reached a peak. With an annealing temperature of 800 °C, the grain size decreased but grains became more uniform.

**a) 700 °C****b) 750 °C****c) 800 °C****Fig. 4.2 AFM images of SBTW1 films following various growth and annealing temperatures**

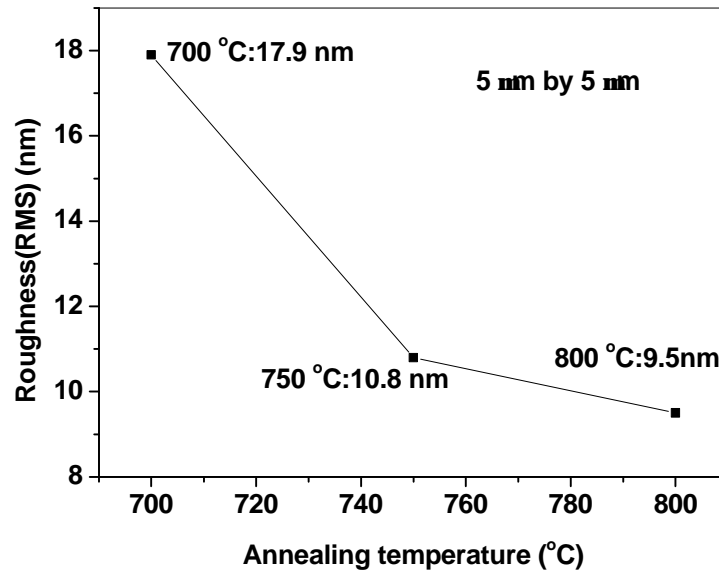


Fig. 4.3 Root-mean-square (RMS) roughness of films fabricated at various temperatures

Fig. 4.3 shows the influence of the growth and annealing temperature on the average surface roughness of SBTW1 films. As we can see, the surface roughness decreases with an increase in temperature. The roughness of the film annealed at 700 °C was 17.9 nm over a size of 5 μm by 5 μm . The roughness sharply decreased at 750 °C, which may be correlated to the disappearance of impurity phases. From 750 °C to 800 °C, with a decrease in grain size, the roughness also decreased.

Fig. 4.4 shows the fabrication temperature dependence of Raman scattering spectra of SBTW1 thin films from 200 to 1000 cm^{-1} . This is similar to previous reports about Aurivillius structure.^{16,17,18} The internal and external modes were found, which might be attributed to SrO (240 cm^{-1}) and Ta₂O₅ (600 cm^{-1} , 814 cm^{-1} , and 918 cm^{-1}). Small variations of internal mode of TaO₆ slightly above 600 cm^{-1} , and the band near 240 cm^{-1} which was assigned to the transverse-optical mode of SrO, imply that the Ta site in the perovskite slab and SrO structures did not change much above the fabrication temperature of 700 °C. With increasing temperature, the number of bands reduces gradually. More bands were observed in the low temperature annealed films,

which might come from impurities and other phases.

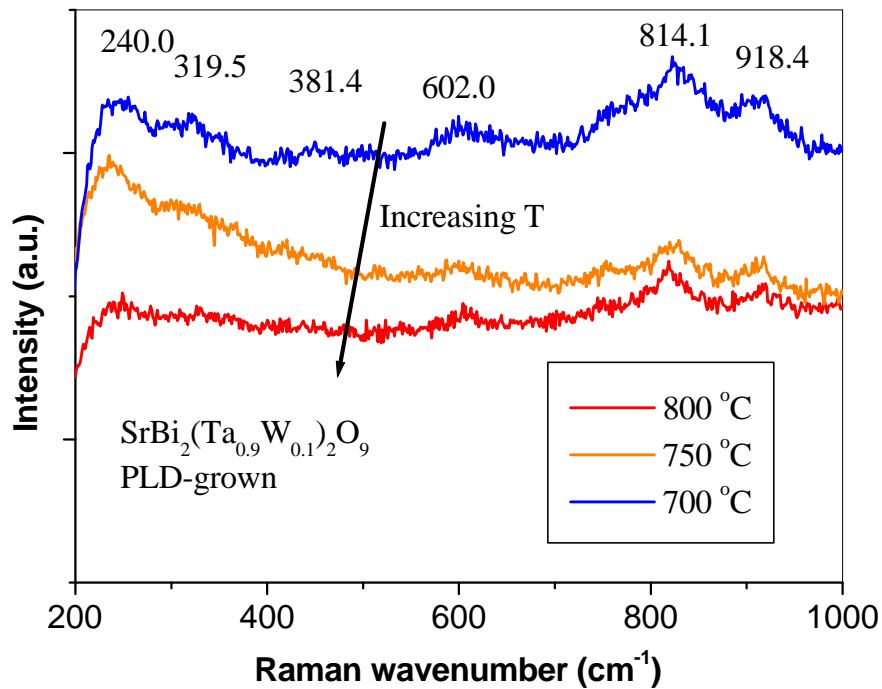


Fig. 4.4 Raman spectra of SBTW films fabricated at various temperatures

4.3.1.2 Electrical properties

Ferroelectric hysteresis measurements were conducted on the films in metal/ferroelectric/metal configuration at an applied voltage of 15 V using standard RT 6000 ferroelectric test system. The P - V hysteresis loops of films fabricated at various temperatures are shown in Fig. 4.5. It was observed that just saturated hysteresis loops can be developed by 800 °C.

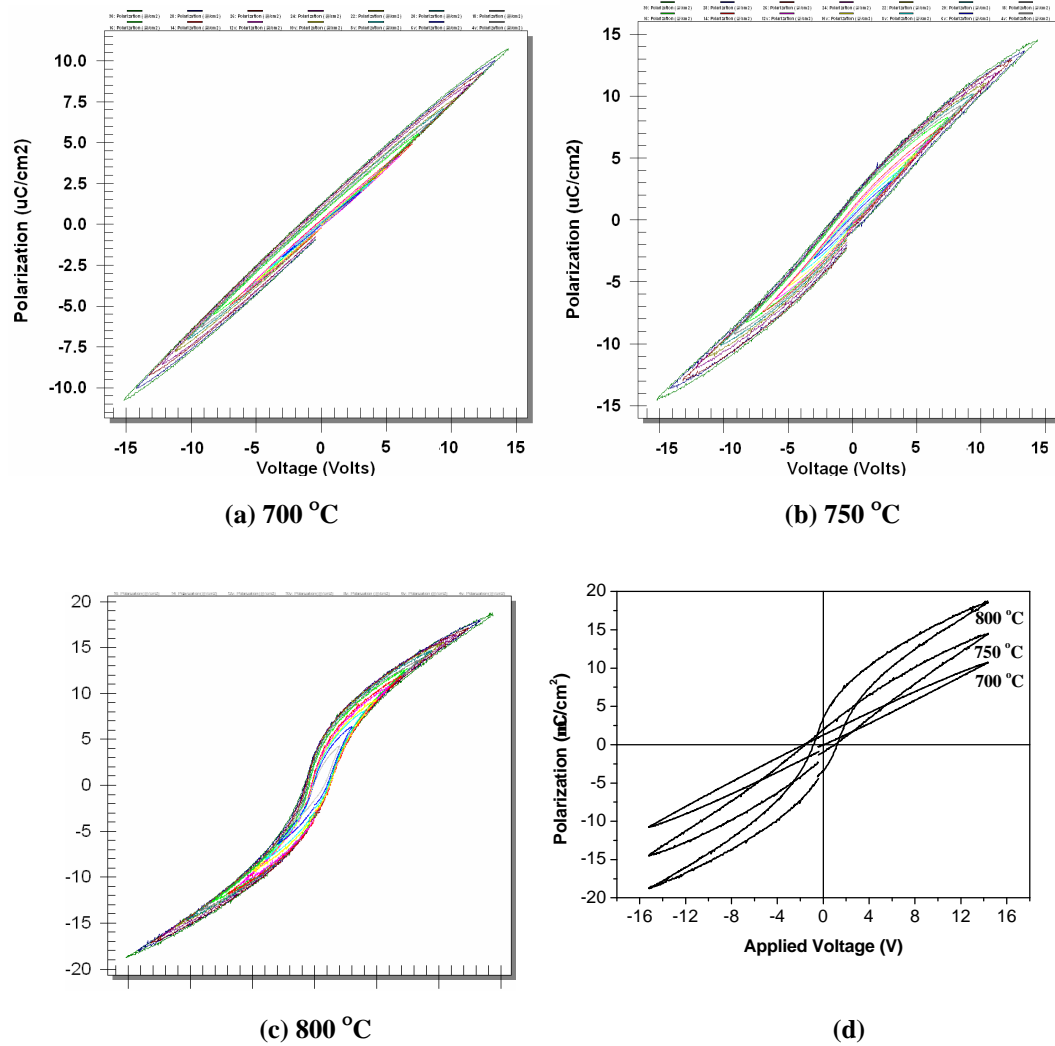


Fig. 4.5 P - V loops of SBTW1 films fabricated at various temperatures

Fig. 4.6 shows variations of $2P_r$ values of the films as a function of the applied maximum voltages. The films are saturated over ~ 8 V for films fabricated at 800 °C. The $2P_r$ values increase from $\sim 2 \mu\text{C}/\text{cm}^2$ for 700 °C-fabricated film to $\sim 4 \mu\text{C}/\text{cm}^2$ for 750 °C-fabricated, to $\sim 8 \mu\text{C}/\text{cm}^2$ for 800 °C-fabricated film.

The AFM images and Raman results suggest that there are still fluorite or pyrochlore phases remaining in 700 °C-fabricated film, which results in a lower $2P_r$. More uniform grain size and lower roughness were observed in the 800 °C-fabricated film than that of 750 °C-fabricated one (shown in AFM images), which might account for the further increase of $2P_r$ for the 800 °C-fabricated film.¹⁹

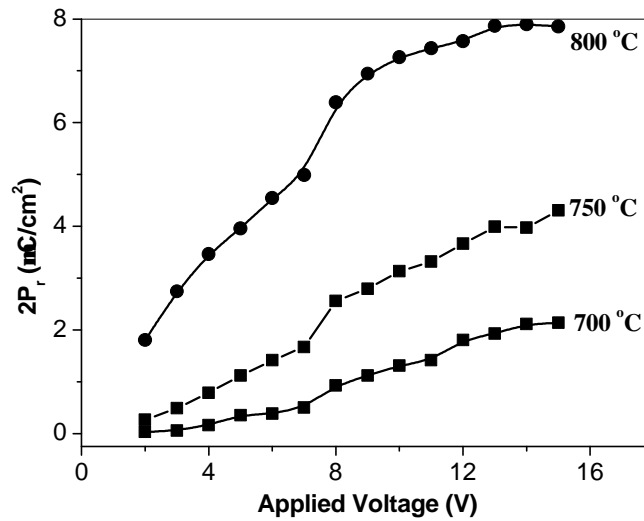


Fig. 4.6 Variations of $2P_r$ values of the films fabricated at different temperatures as a function of the applied maximum electric voltage

Fig. 4.7 shows J - V curves of the films fabricated at different temperatures. The 700 °C-fabricated film shows the highest leakage current density (1×10^{-2} A/cm² at ~200 kV/cm), while the films fabricated at 750 °C and 800 °C demonstrate much lower electrical conductance ($2\sim 5 \times 10^{-6}$ A/cm² at ~200 kV/cm).

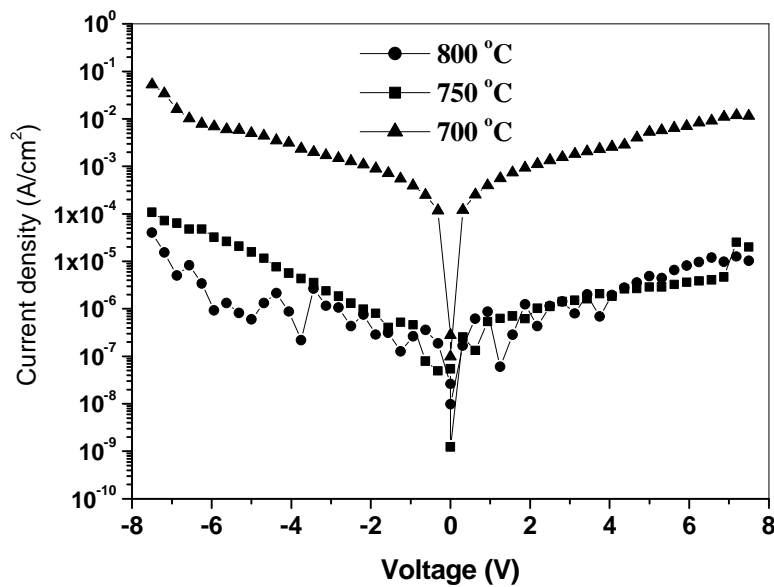


Fig. 4.7 Leakage current characteristics of the films

The room temperature dielectric constant (ϵ_r) was measured as a function of frequency from 1 kHz to 4 MHz. The capacitance values measured using different top electrodes varied within less than 4%, indicating a high degree of uniformity in the films. Fig. 4.8 shows the dielectric spectrum of the film fabricated at 800 °C. From the figure, we can see that ϵ_r was relatively unchanged from 10 kHz to 1 MHz (maximum variation: 7%). The other two films show a very similar result.

Table 4.2 is a summary of the electrical properties of these films. Both dielectric constant and $2P_r$ increase with increasing fabricating temperatures. V_c increased from 700 °C to 750 °C, and then decreased beyond 750 °C.

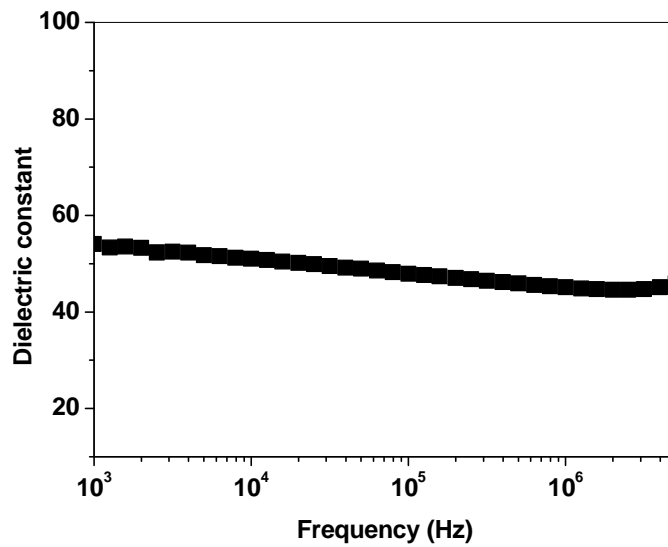


Fig. 4.8 Dielectric spectrum of the 800 °C-fabricated film

Table 4.2 Summary of the properties

Fabrication temperature	Dielectric constant (ϵ_r , at 100 kHz)	Dissipation factor ($\tan \delta$, at 100 kHz)	$2P_r$ (at 15V)	$2V_c$ (at 15 V)	J (A/cm^2) at 6V
800 °C	269.0	0.045	7.8	4.1	5×10^{-6}
750 °C	179.7	0.033	4.2	2.6	2×10^{-6}
700 °C	153.4	0.041	2.0	3.5	1×10^{-2}

4.3.2 Effect of doping level on film properties

Films of different W-doping level $\text{SrBi}_{2.1}(\text{W}_x\text{Ta}_{1.0-x})_2\text{O}_9$ ($x = 0, 0.10$ and 0.20 , denoted as SBT, SBTW1 and SBTW2) were deposited under the conditions shown in Table 4.1 and fabricated at 750°C .

4.3.2.1 Structural properties

Fig. 4.9 shows the XRD patterns of the films of different doping levels. For films of SBTW1 and SBTW2, the perovskite phase was formed with a mixture of (115) peak and (00 l) peaks. This indicates that the films are polycrystalline. Since W-doping has been shown to decrease annealing temperature,⁴ which can explain the better crystallinity of SBTW2 film since it starts crystallising at a lower temperature.⁴

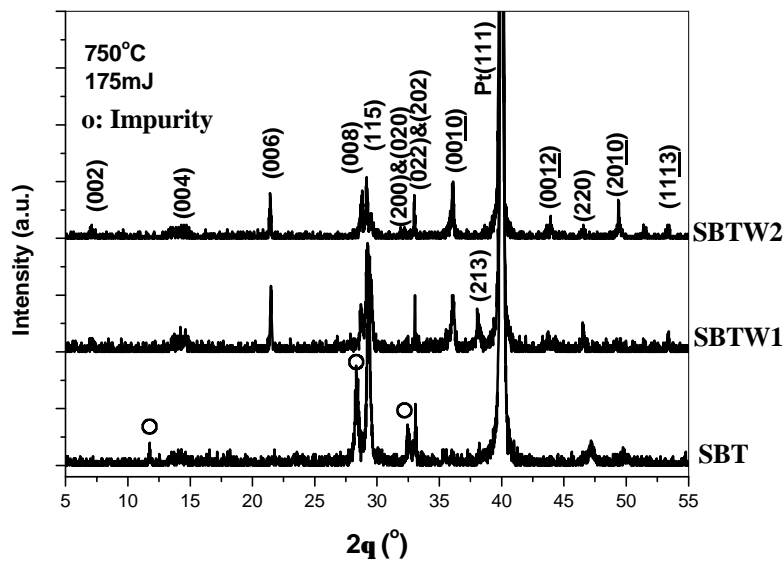
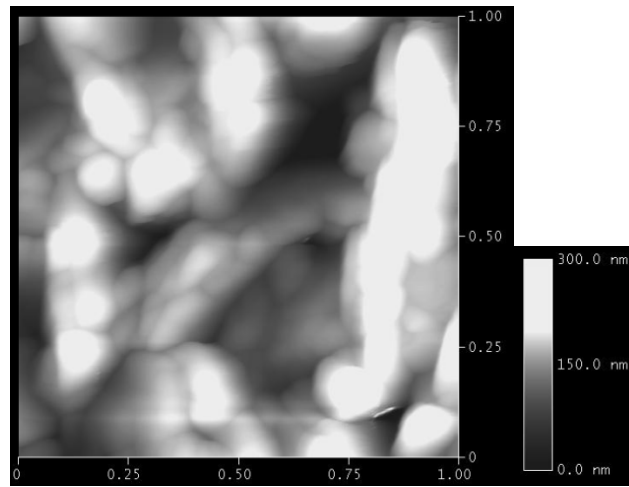


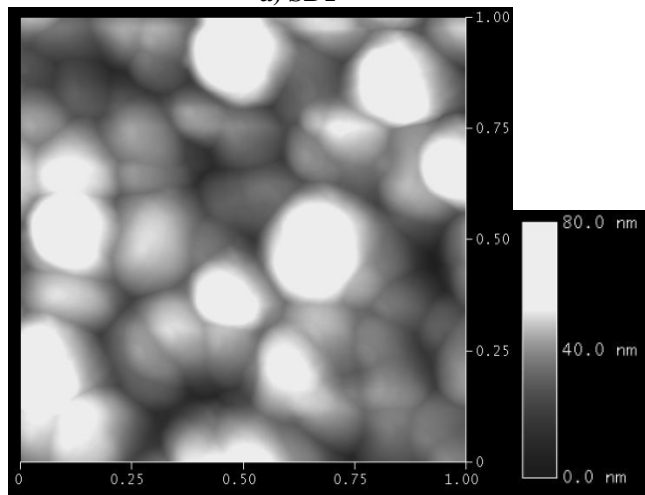
Fig. 4.9 XRD patterns of SBTW films of different doping levels

Figs. 4.10 (a)-(c) show $1\ \mu\text{m} \times 1\ \mu\text{m}$ AFM images of the films. These films showed the similar morphology, all basically having spherical grains. Both SBTW1 and SBTW2 films show more uniform spherical grains, with SBTW2 having slightly

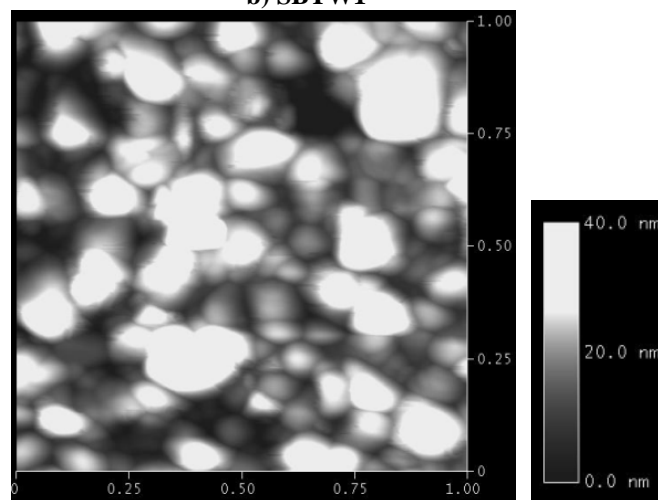
smaller grains and a flatter surface than SBTW1.



a) SBT



b) SBTW1



c) SBTW2

Fig. 4.10 AFM images of SBTW films of different doping levels

4.3.2.2 Electrical properties

The P - V hysteresis loops of films of different doping levels measured at various voltages are shown in Figs. 4.11 (a)-(c). The hysteresis loops of the films measured at 15 V are shown in Fig. 4.11(d).

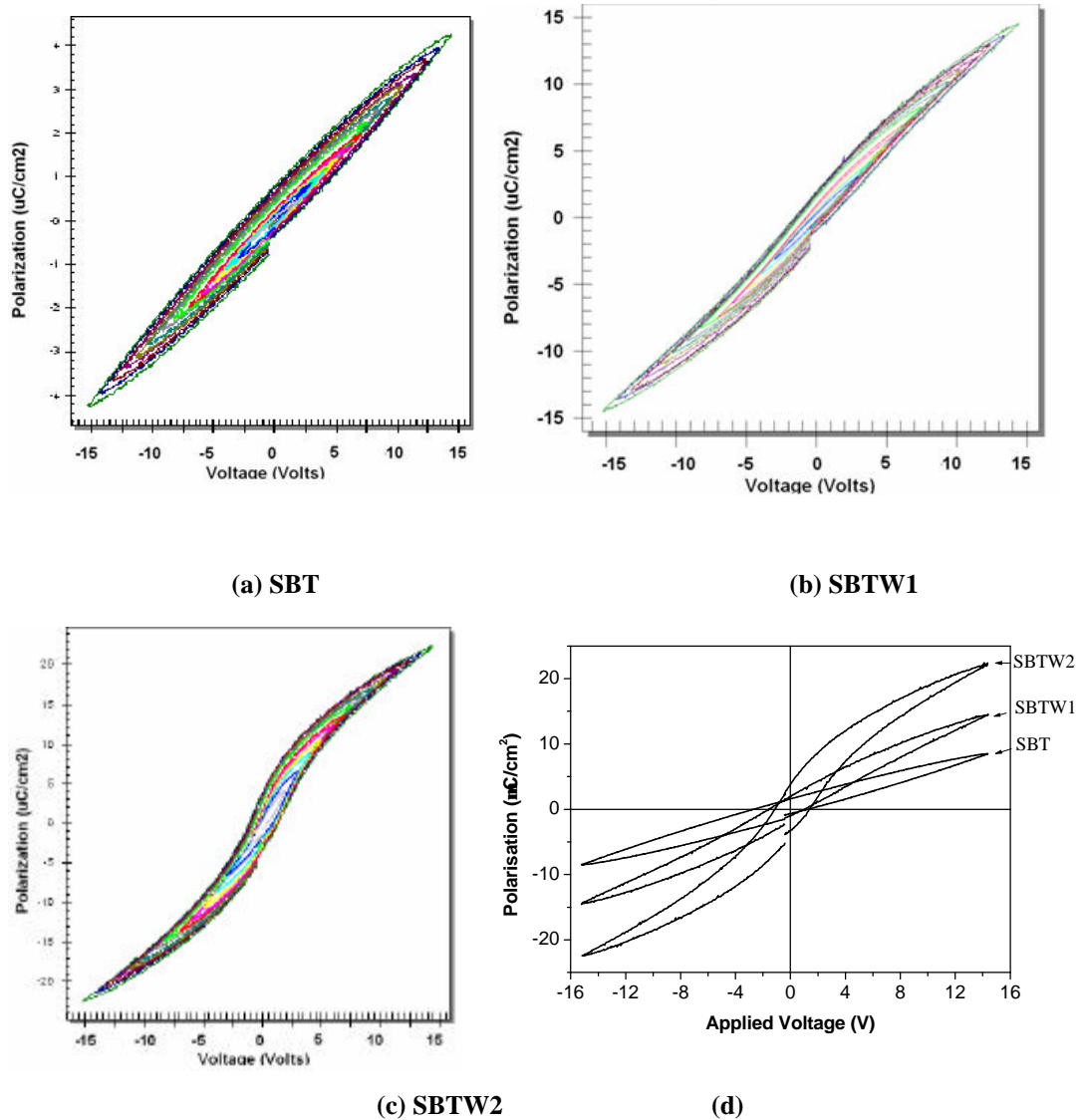


Fig. 4.11 (a)-(c): P - V loops of SBTW of different doping levels fabricated at 750 °C, (d): Hysteresis loops of the films measured at 15 V

Fig. 4.12 shows variations of $2P_r$ values of the films of different doping levels as a function of the applied maximum voltage. The SBTW1 and SBTW2 films are saturated over ~ 8 V. With increasing doping level, the $2P_r$ values increase from ~ 1

$\mu\text{C}/\text{cm}^2$ for SBT film to $\sim 4 \mu\text{C}/\text{cm}^2$ for SBTW1, to $\sim 9 \mu\text{C}/\text{cm}^2$ for SBTW2. The enhancement of ferroelectric properties may stem from the crystallinity and uniformity suggested by XRD and AFM results. As shown in Fig. 4.9, there are still impurity phases remaining in pure SBT film when annealed at 750°C , which results in a much lower $2P_r$.

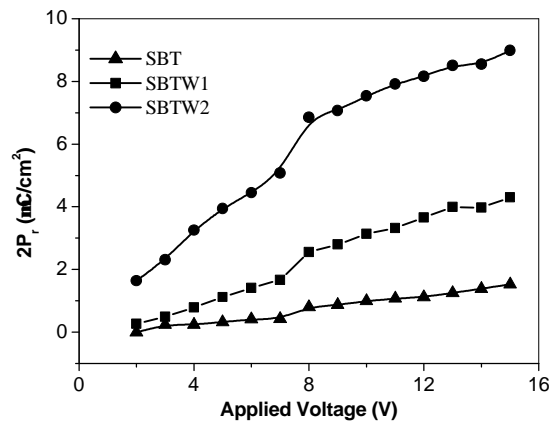


Fig. 4.12 Variations of $2P_r$ of the SBTW thin films of different doping levels fabricated at 750°C as a function of the applied maximum voltage

Fig. 4.13 shows J - V curves of the films of different doping levels. Pure SBT film shows the highest leakage current density ($2 \times 10^{-2} \text{ A}/\text{cm}^2$ at $\sim 200 \text{ kV}/\text{cm}$). SBTW1 film has the lowest leakage current density ($5 \times 10^{-6} \text{ A}/\text{cm}^2$ at $\sim 200 \text{ kV}/\text{cm}$), while that of SBTW2 films was 2~3 orders of magnitude higher than SBTW1 film.

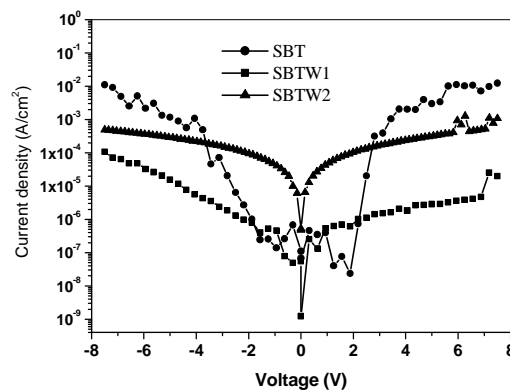


Fig. 4.13 J - V curves of the films of different doping levels

Table 4.3 is a summary of the electrical properties of the films of different doping levels. Both dielectric constant and $2P_r$ increase with the increasing doping level. V_c decreases with increasing doping levels. Leakage current density decreases after doping 10 mol % W, but increases with 20 mol% doping. This suggests that excess doping as much as 20 % may deteriorate the film electrical resistivity.

Table 4.3 Summary of the properties

Sample	Dielectric constant (ϵ_r)	Dissipation factor ($\tan \delta$, at 100 kHz)	$2P_r$ (at 15V)	$2V_c$ (at 15 V)	J (A/cm^2) (at 6V)
SBT	50.0	0.044	1.4	4.0	1×10^{-2}
SBTW1	179.7	0.033	4.2	2.6	2×10^{-6}
SBTW2	280.5	0.049	8.9	2.5	3×10^{-4}

4.4 Conclusions

- (1) We successfully fabricated SBT and W-doped SBT films by PLD.
- (2) The crystallinity of SBTW films improved with increasing growth and annealing temperatures, resulting in enhanced ferroelectric properties and dielectric properties beyond the fabrication temperature of 750 °C.
- (3) W-doping lowered the required annealing temperature of SBT films, which can explain the improvement of crystallinity, dielectric and ferroelectric properties. The lowered growth temperature will increase the chances of applications of SBT films in silicon integrated technology. However, excess W-doping (20 %) lead to an increase in leakage current. Thus, further work is required to optimise the W-doping level in SBT thin films.

4.5 References

- 1 C. A. Paz de Araujo, J. D. Cuchiaro, L. D. McMillan, M. C. Scott, and J. F. Scott, *Nature (London)* **324**, 627 (1995).
- 2 A. Fouskova and L. E. Cross, *Journal of Applied Physics* **41**, 2834 (1970).
- 3 H.S. Shulman and K. Sakata, *Journal of Applied Physics* **55**, 1092 (1984).
- 4 M. Villegas, A.C. Caballero, C. Moure, P. Duran, and J.F. Fernandez, *Journal of European Ceramic Society* **19**, 1183 (1999).
- 5 S. Y. Chen, B. C. Lan, and C. S. Taso, *Journal of Applied Physics* **91**, 10032 (2002).
- 6 Y. Noguchi and M. Miyayama, *Applied Physics Letters* **78**, 1903 (2001).
- 7 T. Sakai, T. Watanabe, M. Osada, M. Kakihana, Y. Noguchi, M. Miyayama, and H. Funakubo, *Japanese Journal of Applied Physics Part 1* **42**, 2850 (2003).
- 8 J. S. Kim, S. S. Kim, J. K. Kim, and T. K. Song, *Japanese Journal of Applied Physics Part 1-Regular Papers Short Notes & Review Papers* **41**, 6451 (2002).
- 9 R. R. Das, P. Bhattacharya, W. Perez, R. S. Katiyar, and S. B. Desu, *Applied Physics Letters* **80**, 637 (2002).
- 10 A. Garg, S. Dunn, and Z. H. Barber, *Integrated Ferroelectrics* **31**, 13 (2000).
- 11 J. Wang (Private communication).
- 12 Ashish Garg, Ph.D thesis, University of Cambridge, 2001.
- 13 N. Maffel and S. B. Krupanidhi, *Journal of Applied Physics* **74**, 7551 (1993).
- 14 W. Jo, G. C. Yi, T. W. Noh, D. K. Ko, Y. S. Cho, and S. I. Kwun, *Applied Physics Letters* **61**, 1516 (1992).
- 15 J. Pak, K. Nam, J. Lee, and G. Park, *Journal of Physics: Condensed Matter* **16**, 4983 (2004).
- 16 V. Srikanth, H. Idink, W. B. White, E. C. Subbarao, H. Rajagopal, and A. Sequeira, *Acta Crystallographica Section B: Structural Science* **51**, 432 (1996).
- 17 S. Kojima, *Journal of Physics: Condensed Matter* **10**, L327 (1998).
- 18 J. K. Lee, B. Park, and K. S. Hong, *Journal of Applied Physics* **88**, 2825 (2000).
- 19 R. R. Das, P. Bhattacharya, and R. S. Katiyar, *Applied Physics Letters* **81**, 1672 (2002).

Chapter 5 Epitaxial Nd-doped bismuth titanate thin films on single crystal substrates

5.1 Background and motivation

In 1999 Park *et al.*¹ showed that fatigue-free BLaT films on Pt electrodes exhibited higher remanent polarisation ($2P_r \approx 24 \mu\text{C}/\text{cm}^2$) and required lower deposition temperature ($\leq 750 \text{ }^\circ\text{C}$) in comparison to other Bi-layered ferroelectrics (e.g. SBT). The crystal structure of BLaT can be described as a stack of alternating layers of bismuth oxide and perovskite ($\text{Bi}_2\text{Ti}_3\text{O}_{10}$)²⁺ units containing Ti-O octahedra with La substituting for Bi in the perovskite units.² Undoped bismuth titanate (BiT) films show low remanent polarisation and suffer from bi-polar fatigue.³

It is also possible to dope BiT with other lanthanide elements such as Nd,⁴ Sm,⁵ Pr,⁶ *etc.* These elements are of interest because the extent of enhancement of remanent polarisation in BiT and Bi-layered oxides is dependent upon structural distortion within the perovskite block (rotation of TiO_6 octahedra in the a - b plane accompanied by a tilt of the octahedra away from the c -axis), governed by the size difference between Bi and the dopant ion: the higher the distortion, the higher the P_r will most likely be.^{7,8} Ionic radii for eight-fold coordination of these element are: Bi^{3+} 0.117 nm, La^{3+} 0.116 nm, Nd^{3+} 0.111 nm, Sm^{3+} 0.108 nm;⁹ it can be deduced from these data that Nd- and Sm-doping will lead to larger distortion than La-doping and should, in principle, result in a larger P_r . This has been proved experimentally by studies comparing the effects of doping of BiT with various lanthanide elements.^{10,11}

In the Aurivillius phases one would expect the largest P_r along the a -/ b -axis of the

film and almost negligible P_r along the c -axis (for pure $\text{Bi}_4\text{Ti}_3\text{O}_{12}$, $2P_r$ ($//a$ -axis) = 36 $\mu\text{C}/\text{cm}^2$ and $2P_r$ ($//c$ -axis) = 4 $\mu\text{C}/\text{cm}^2$)¹². However, in a recent report by Chon *et al.*,¹³ it was shown that sol-gel derived c -axis-oriented BNdT films exhibited $2P_r$ as high as $\sim 100 \mu\text{C}/\text{cm}^2$. This unexpected behaviour was attributed to the tilting of the P_r vector towards the c -axis of the film.

Most of these studies were conducted on films prepared by chemical processes such as sol-gel processing and chemical vapor deposition. This chapter reports on the detailed investigation of the structural and electrical properties of BNdT films of various crystallographic orientations (c -axis and non- c -axis oriented) grown by PLD from a single target of composition $\text{Bi}_{3.15}\text{Nd}_{0.85}\text{Ti}_3\text{O}_{12}$ on single crystal (100)-, (110)- and (111)-oriented SrTiO_3 (STO) substrates.

5.2 Experimental details

Table 5.1 Deposition parameters for the growth of SRO and BNdT

Deposition parameters	SRO	BNdT
Laser pulse frequency (Hz)	4	5
Total number of pulses	2000	7200
Pulse energy per spot (mJ)	160	175
Substrate temperature ($^{\circ}\text{C}$)	675	750
Oxygen pressure (Pa)	15	27
Annealing pressure (O_2) (kPa)	65	65
Thickness (nm)	~ 40 -60	~ 250 -300

BNdT thin films were deposited on SrRuO_3 (SRO)-covered STO substrates of (001), (011) and (111) orientations. The deposition parameters used for the growth of SRO and BNdT are shown in Table 5.1. All the layers were deposited in a pure oxygen atmosphere. To form the desired phase of SRO, after the deposition of SRO, the film

was annealed in a pure oxygen atmosphere of about 65 kPa and naturally cooled down to room temperature, then the chamber was pumped again for two and a half hours to reach the desired vacuum, the BNdT film was then deposited and annealed with a similar procedure. Most of the parameters for film growth were optimised based on previous work in our group.¹⁴

5.3 Results and discussion

5.3.1 Structural properties of the targets

Fig. 5.1 shows XRD patterns from the polished surface of the dense samples of $\text{Bi}_4\text{Ti}_3\text{O}_{12}$, $(\text{Bi}_{4-x}\text{Nd}_x)\text{Ti}_3\text{O}_{12}$ (nominal $x = 0.55, 0.70, 0.85, 1.00$) and $(\text{Bi}_{4-x}\text{Sm}_x)\text{Ti}_3\text{O}_{12}$ (nominal $x = 0.55, 0.70, 0.85, 1.00$) ceramic targets (Sm-doped BiT ceramics were fabricated for comparison and also used for the BSmT film deposition in the later chapters). The diffraction peaks were identified and indexed using the XRD data of the perovskite $\text{Bi}_4\text{Ti}_3\text{O}_{12}$ phase compiled in the JCPDS (Joint Committee on Powder Diffraction Standards) card (35-0795). There was one-to-one correspondence between these two patterns despite some peak shifts and changes in relative intensity. These results show no evidence of the formation of neodymium or samarium oxide or associated compounds that contain bismuth or titanium, *i.e.* that the neodymium or samarium ions in the BNdT or BSmT do not form minority phases or segregate, but are incorporated into the perovskite lattice.

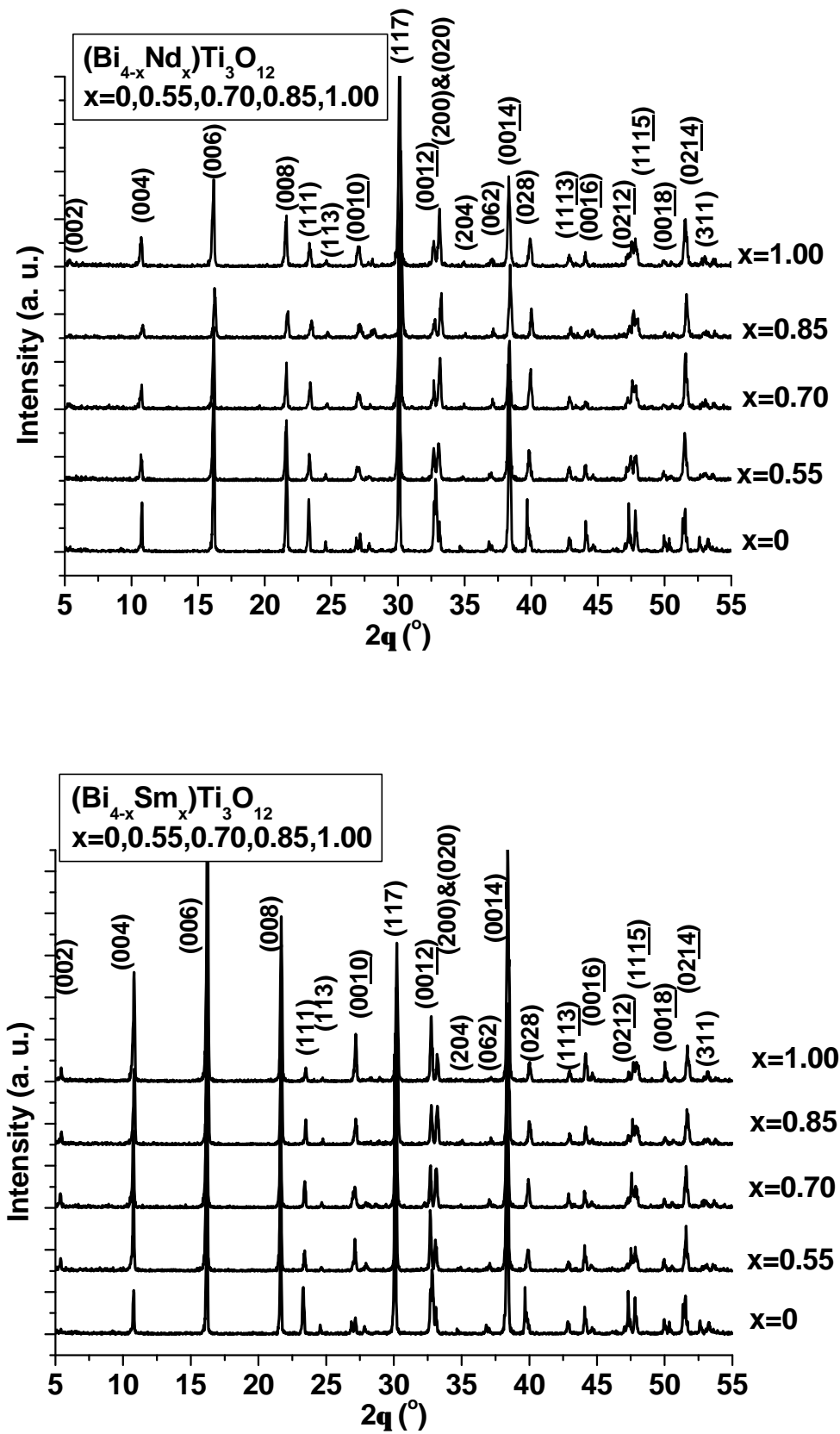


Fig. 5.1 XRD patterns of $\text{Bi}_{4-x}\text{Nd}_x\text{Ti}_3\text{O}_{12}$ and $\text{Bi}_{4-x}\text{Sm}_x\text{Ti}_3\text{O}_{12}$ ceramic samples

The patterns obtained were analysed by the Rietveld method (X-CELL mode in MATERIALS STUDIO program) on the basis of the $B2cb$ orthorhombic symmetry. (Strictly speaking, BiT has a slight monoclinic distortion, however, this distortion is very small and the symmetry of BiT can be regarded as orthorhombic.) All of the measured XRD patterns could be fitted well by the profiles calculated under the BiT structure. The refined lattice constants based on an orthorhombic unit cell are shown in Table 5.2.

Table 5.2 Refined lattice constants of the BiT, BNdT and BSmT systems

	a (nm)	b (nm)	c (nm)	Cell volume (nm^3)	Reference
BiT	0.5449	0.5409	3.284		[18] ¹⁸
BiT	0.545	0.541	3.283	0.96798	[16] ¹⁶
BiT	0.5454	0.5415	3.285	0.97017	[17] ¹⁷
BiT	0.5455	0.5412	3.284	0.96955	This work
BNdT (x=0.40)	0.5426	0.5393	3.2783		[15] ¹⁵
BNdT (x=0.55)	0.5413	0.5396	3.2755	0.95683	This work
BNdT (x=0.70)	0.5410	0.5393	3.2867	0.95677	This work
BNdT (x=0.80)	0.5414	0.5407	3.2820		[15] ¹⁵
BNdT (x=0.85)	0.5414	0.5400	3.2846	0.96032	This work
BNdT (x=1.00)	0.5414	0.5406	3.2786	0.96063	This work
BNdT (x=1.20)	0.5413	0.5395	3.2823		[15] ¹⁵
BNdT (x=1.60)	0.5398	0.5393	3.2840		[15] ¹⁵
BSmT (x=0.55)	0.5415	0.5400	3.2846	0.96049	This work
BSmT (x=0.70)	0.5414	0.5403	3.2829	0.96041	This work
BSmT (x=0.85)	0.5413	0.5347	3.2725	0.95716	This work
BSmT (x=1.00)	0.5400	0.5389	3.2809	0.95431	This work
BSmT (x=2.00)	0.5435	0.5408	3.2822	0.9647	[18] ¹⁸

Diffraction patterns were compared particularly with results reported in some

previous references^{15,16,17,18}. The refined lattice constants of the BiT were practically the same as the theoretical value previously identified,^{16,17} within 0.1% reported range. The lattice constants of the BNdT system and BSmT were comparable with the values previously identified,^{15,18} respectively. All diffraction data processed confirmed the existence of an orthorhombic cell. It is known that the size of the trivalent bismuth ion is comparable with that of samarium or neodymium⁹: Bi³⁺ 0.117 nm, Nd³⁺ 0.111 nm, Sm³⁺ 0.108 nm, so we can expect that the Sm and Nd ions enter the crystal cell and substitute for Bi ions.

5.3.2 Structural properties of the films

5.3.2.1 Crystallographic orientations and epitaxial relationships

1. θ - 2θ scans

Fig. 5.2 shows XRD θ - 2θ scans of BNdT/SRO heterostructures deposited on (001)-, (011)-, and (111)-oriented STO substrates at 750 °C. Since the lattice misfit between SrRuO₃ ($a_{\text{cubic}}=0.3928$ nm) and SrTiO₃ ($a_{\text{cubic}}=0.3905$ nm) is only 0.6%, the orientations of SRO are basically identical with those of STO, as can be seen in Fig. 5.2. We assume that the lattices are identical and refer to STO instead of SRO, unless specified.

Fig. 5.2 suggests that highly epitaxially (001)-, (118)-, and (104)-oriented BNdT films have been grown on (001)-, (011)-, and (111)-orientated STO substrates, respectively: Fig. 5.2(a) shows a series of (00 l) peaks of the BNdT films; Fig. 5.2(b) shows a film peak of only (2216); Fig. 5.2(c) shows film peaks of only (104) and (4016).

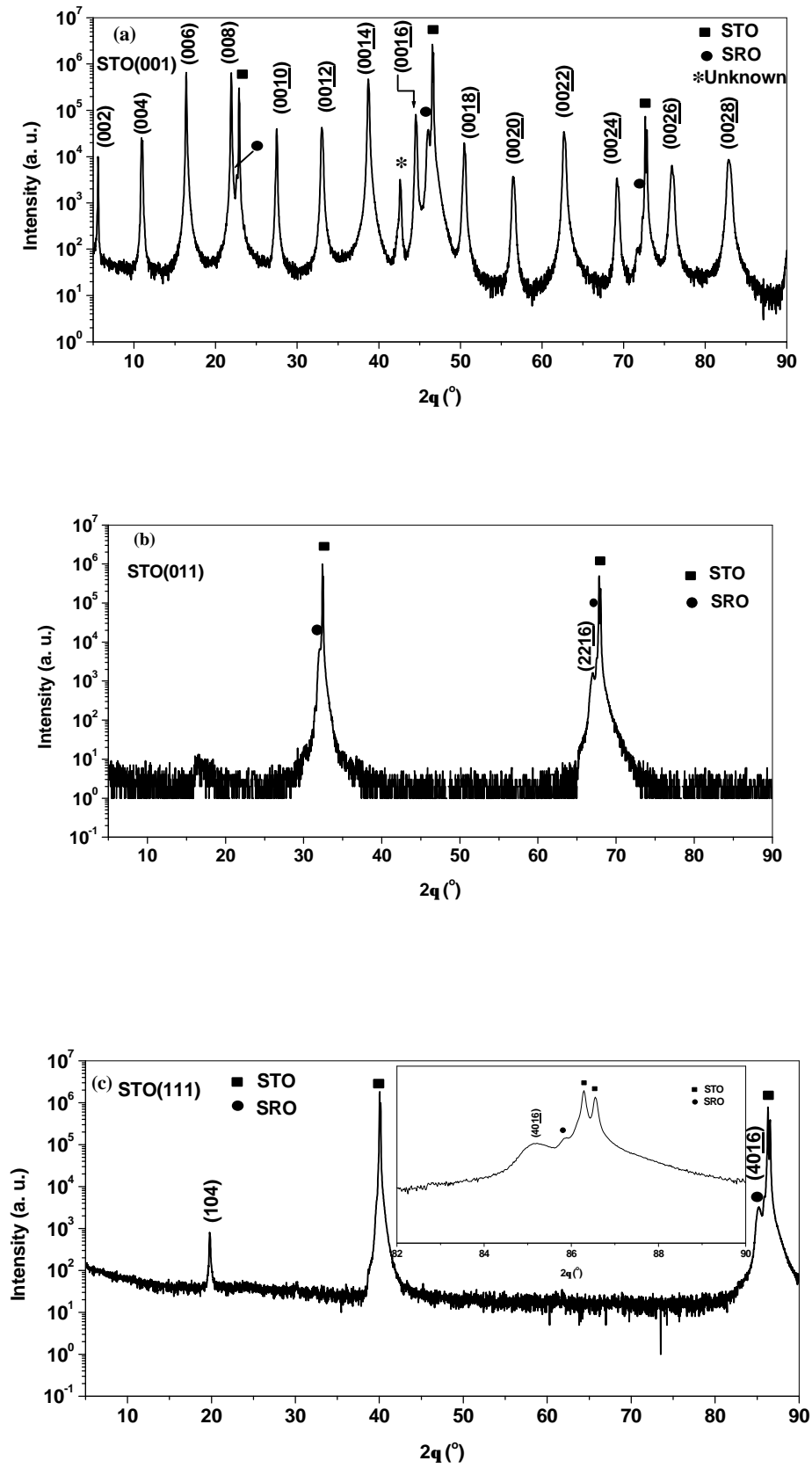


Fig. 5.2 XRD 2θ scans of BNdT thin films on SRO-covered (a) (001)-, (b) (011)-, and (c) (111)-oriented STO substrates (inset of (c) shows a detailed range of the spectrum)

2. Pole figure scans

Pole figure analyses were conducted to determine whether the BNdT/SRO/STO heterostructures were epitaxial and to confirm the BNdT crystallographic orientations.

Fig. 5.3 shows pole figures of the BNdT thin films on STO substrates of different orientations. The fixed 2θ angle used to record the pole figures was 30.1° , corresponding to the BNdT $\{117\}$ planes. The pole figures were plotted with the pole distance angle $\phi=0^\circ$ (centre) to $\phi=90^\circ$ (rim). $\phi=90^\circ$ corresponds to the substrate surface being parallel to the plane defined by the incident and reflected x-ray beams.

In the case of (001)-oriented BNdT, as shown in Fig. 5.3(a), four diffraction peaks with a fourfold symmetry are observed at $\phi=50^\circ$, illustrating a very good in-plane orientation; BNdT $\{117\}$ planes have a tilt angle of 50.66° with respect to the BNdT $\{001\}$ plane, which is parallel to the substrate surface (that is, $\angle\{117\}, \{001\}=50.66^\circ$).

In Fig. 5.3(b), the innermost two $\{117\}$ peaks are located at $\phi=5^\circ$. This pole figure confirms that BNdT (118) plane is parallel to the substrate surface, because the angle between the (118) and (117) planes of BNdT is 3.78° ($\angle\{117\}, \{118\} = \angle\{118\}, \{001\} - \angle\{117\}, \{001\} = 50.66^\circ - 46.88^\circ = 3.78^\circ$). Moreover, the diffraction peaks from the $(11\bar{7})$ plane and the $(1\bar{1}7)/(\bar{1}17)$ planes are also present at $\phi=65^\circ$ and $\phi=85^\circ$, respectively, indicating a double-domain situation (two-fold symmetry).

In the case of (104)-oriented BNdT as shown in Fig. 5.3(c), six peaks situated at $\phi=36^\circ$ and $\phi=85^\circ$ were observed. This corresponds to a triple-domain situation: the inner six peaks correspond to (117) and $(1\bar{1}7)$ planes as marked in the figure, and the outer six peaks are related to $(11\bar{7})$ and $(1\bar{1}\bar{7})$ planes.

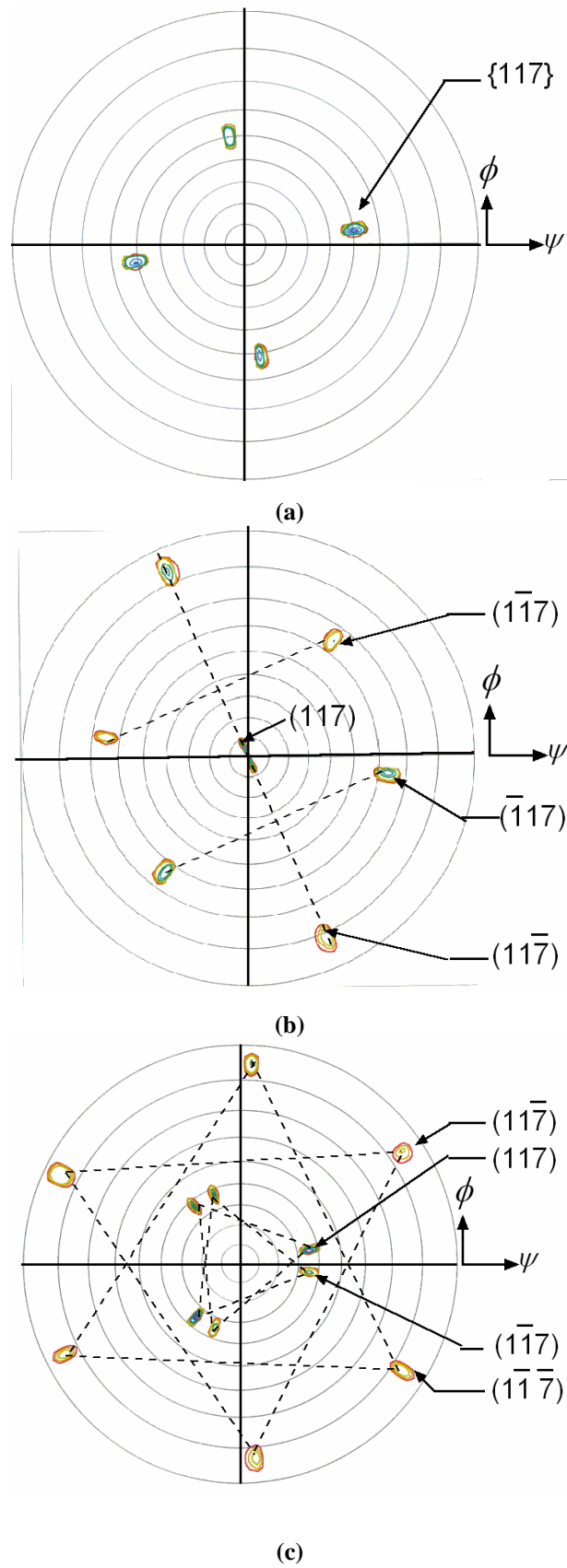


Fig. 5.3 X-ray pole figures of BNdT thin films on SRO-covered (a) (001)-, (b) (011)-, and (c) (111)-oriented STO substrates

Summarising the results of Figs. 5.2 and 5.3, the two-dimensional epitaxial relationships between the BNdT films and their corresponding STO substrates can be derived as follows:

$$\text{BNdT}(001)//\text{STO}(001); \text{BNdT}[\bar{1}10]//\text{STO}[100] \quad (5.1)$$

$$\text{BNdT}(118)//\text{STO}(011); \text{BNdT}[\bar{1}10]//\text{STO}[100] \quad (5.2)$$

$$\text{BNdT}(104)//\text{STO}(111); \text{BNdT}[\bar{1}10]//\text{STO}[100] \quad (5.3)$$

However, these relationships are not unique, because grains can grow in variants allowed by the crystallographic symmetry. The crystallographically allowed rotations are 90° for STO (001), 180° for STO (011) (leading to the double-domain situation), and 120° for STO (111) (leading to the triple-domain situation).

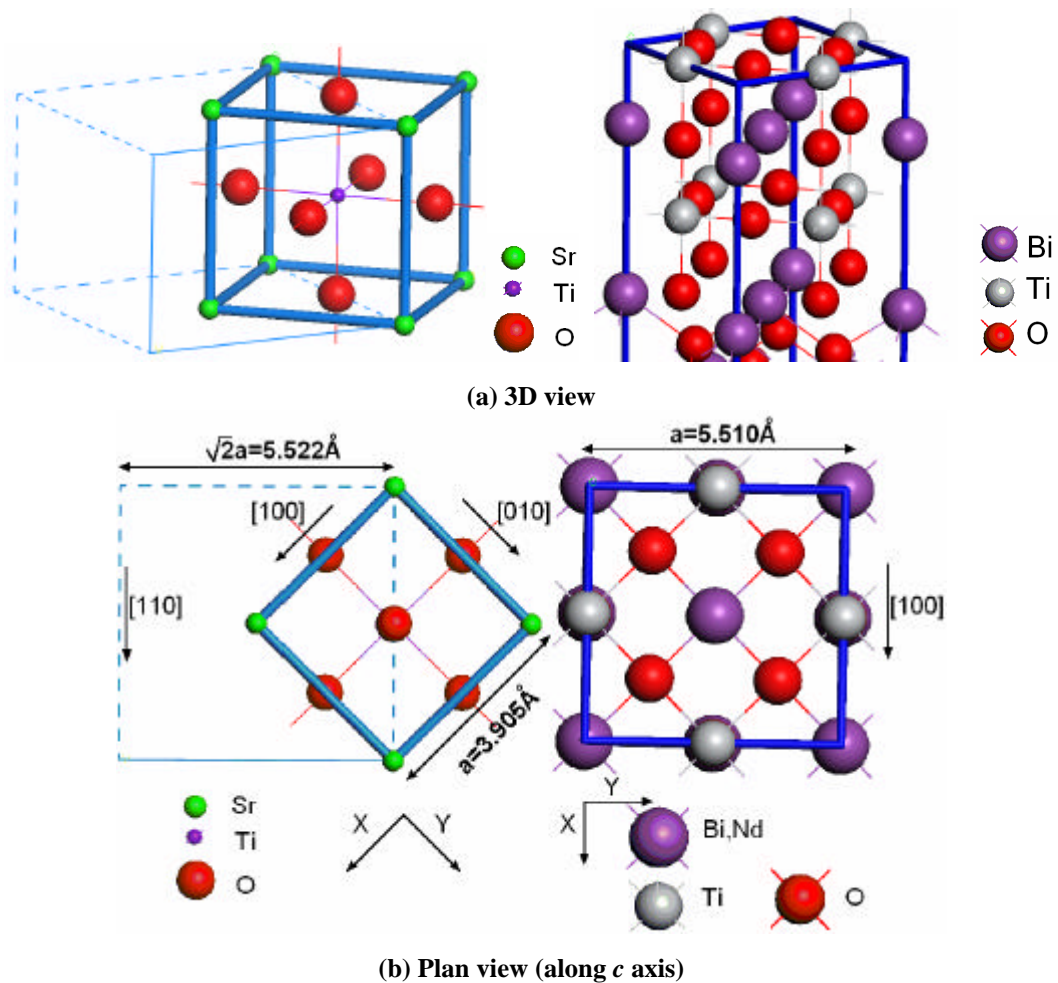


Fig. 5.4 Schematic of proposed epitaxial relationship between BNdT films and STO (001)

A three-dimensional representation of the proposed epitaxy between BNdT films and STO (001) is shown in Fig. 5.4. The misfit values between the film and electrode (SRO), and electrode and substrate are approximately -0.8% and 0.6% (for SRO: $a = 0.3928$ nm), respectively.

Fig. 5.5 shows that all the three relationships, observed on the three substrate orientations, correspond to the same three-dimensional orientation relationship. This three-dimensional orientation relationship may be written as

$$\text{BNdT}(001)//\text{STO}(001), \text{BNdT}[\bar{1}10]//\text{STO}[100] \quad (5.4)$$

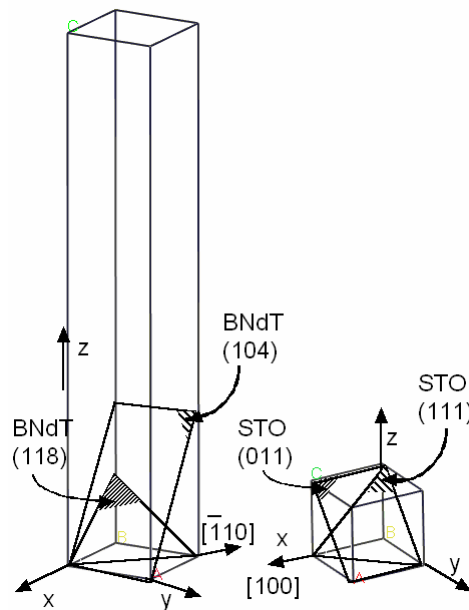


Fig. 5.5 Three-dimensional schematic drawing of the BNdT and STO unit cells illustrating the three-dimensional epitaxial orientation relationship

5.3.2.2 Surface morphological studies

AFM images of the BNdT film surfaces are shown in Fig. 5.6. In the case of (001)-oriented BNdT, submicron-sized columns are clearly visible in Fig. 5.6(a). The

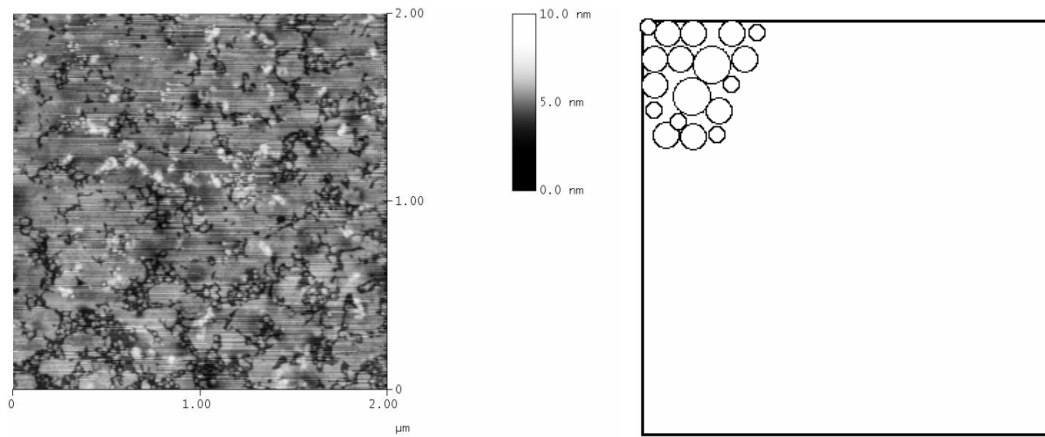
root-mean-square (RMS) surface roughness of BNdT(001) over areas of $2 \times 2 \mu\text{m}^2$ was about 0.7 nm. In Fig. 5.6(b), the (118)-oriented BNdT film shows rectangular-shaped columns arranged principally along one direction. The column length was 50~80 nm and the length ratio of the column shape was about 6~8. This film revealed a much higher RMS roughness of about 10 nm than that of the *c*-axis-oriented film. This morphology is comparable with the morphology observed in SBT films deposited on similar substrates.¹⁹ A three-fold symmetry of the column distribution was found on the (104)-oriented BNdT surface as shown in Fig. 5.6(c). Columns are oriented along three directions at 120° to each other, showing a triple-domain structure. The surface roughness is ~14 nm.

This observed surface roughness increase as the film orientation moves further towards the *a* axis, *i.e.*, $R(001) < R(118) < R(104)$, may be due to the more complex nature of the growth with increasing domain orientations from STO (001) to STO (110) to STO (111).

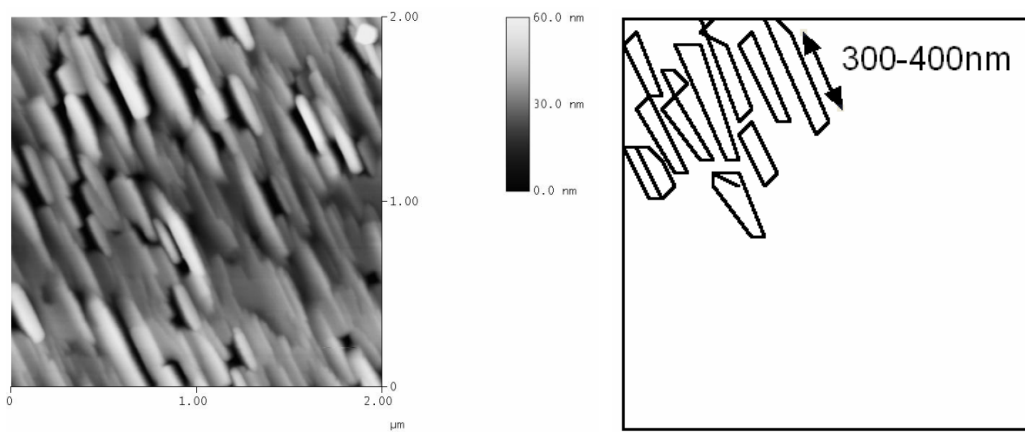
5.3.3 Electrical properties

5.3.3.1 Ferroelectric properties

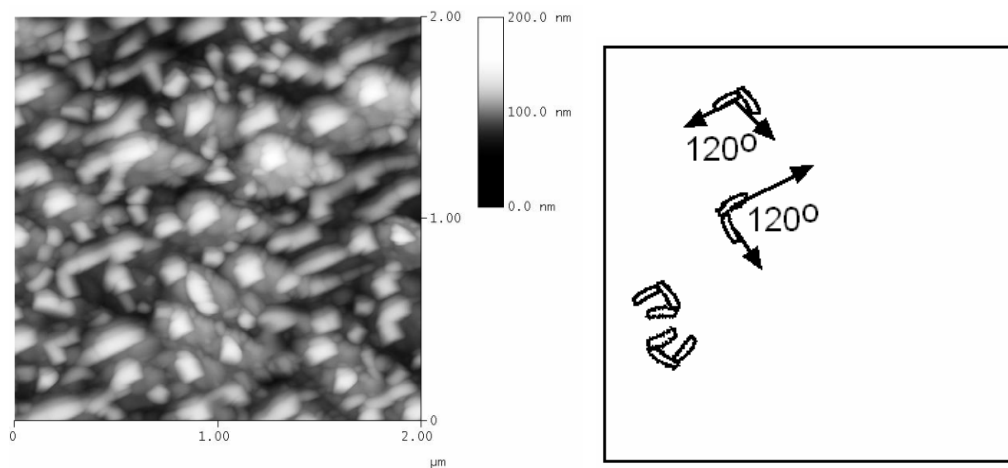
Ferroelectric hysteresis loops were recorded in order to evaluate the dependence of ferroelectricity on different crystallographic orientations in BNdT films. Fig. 5.7 shows ferroelectric loops recorded at 6~12 V from (001)-, (118)-, (104)-oriented BNdT films deposited on (001)-, (011)-, and (111)-oriented SRO electrodes, respectively.



(a) BNdT films on (001)-oriented STO (RMS roughness = 0.657 nm)



(b) BNdT films on (011)-oriented STO (RMS roughness = 10.8 nm)



(c) BNdT films on (111)-oriented STO (RMS roughness = 14.2 nm)

Fig. 5.6 AFM images of BNdT films on SRO-covered (001)-, (011)- and (111)-STO

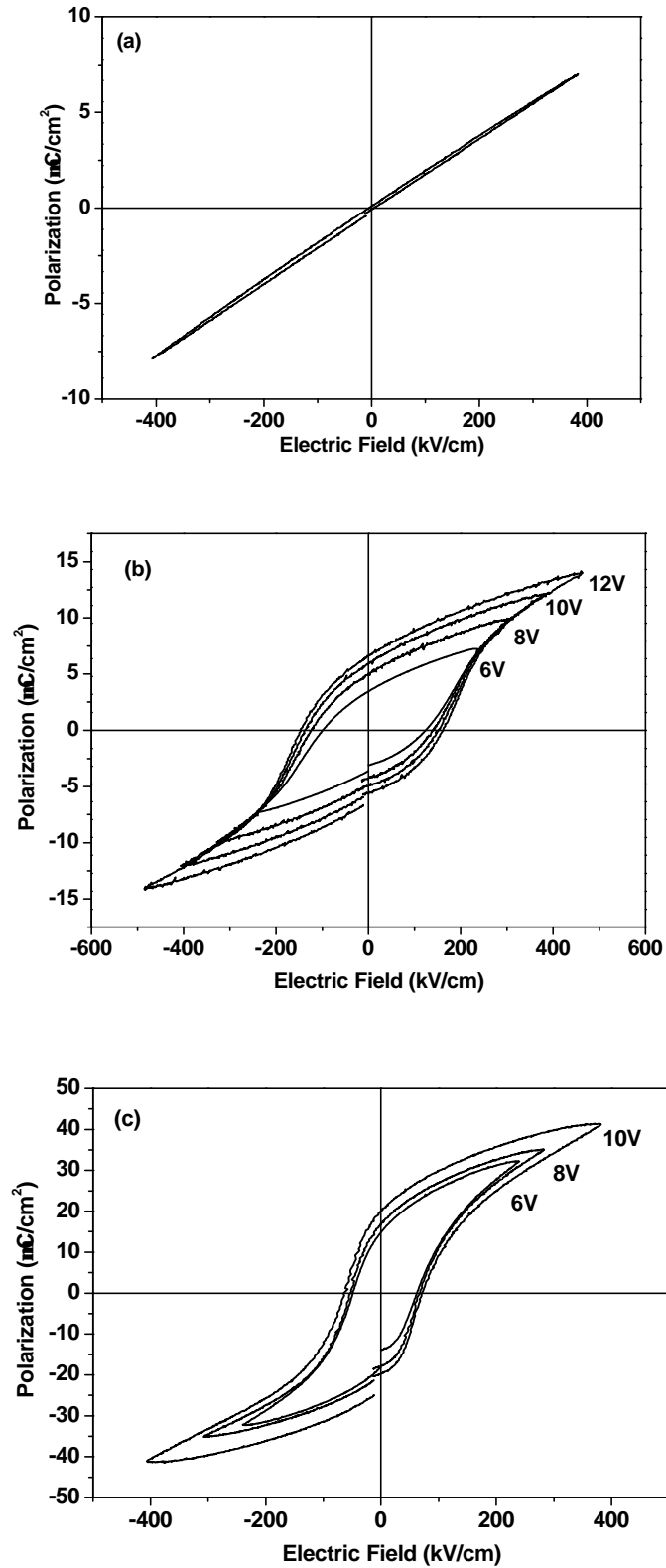


Fig. 5.7 *P-E* hysteresis loops of (a) (001)-, (b) (118)-, (c) (104)-oriented BNdT films at various applied voltages

The ferroelectric anisotropy of BNdT is clearly demonstrated: the measured $2P_r$ and $2E_c$ of the (104)-orientated BNdT films were $45.0 \mu\text{C}/\text{cm}^2$ and $134.1 \text{ kV}/\text{cm}$, respectively, for a maximum applied electric field of $400 \text{ kV}/\text{cm}$ (film thickness $\sim 250 \text{ nm}$); the $2P_r$ and $2E_c$ of the (118)-orientated BNdT films were $13.0 \mu\text{C}/\text{cm}^2$ and $300 \text{ kV}/\text{cm}$, respectively. The (104)-orientated films have clearly saturated P - E loops with larger P_r and lower E_c (also shown in Fig. 5.8). On the other hand, only a small polarisation component ($2P_r = 0.5 \mu\text{C}/\text{cm}^2$ and $2E_c = 10.0 \text{ kV}/\text{cm}$, Fig. 5.7(a)) along the normal to the film plane was found in the (001)-oriented films. This result confirms that the P_r of BiT along the c axis is much smaller than that along a (b) axis.¹⁷ This result also confirms the results of Miyayama *et al.*,²⁰ which experimentally confirmed that there is no spontaneous polarisation in the c -axis direction in compounds with an even numbered m , and very weak polarisation in an odd numbered m , in $(\text{Bi}_2\text{O}_2)^{2+}(\text{M}_{m-1}\text{R}_m\text{O}_{3m+1})^{2-}$ bismuth-layered structures (for $\text{Bi}_4\text{Ti}_3\text{O}_{12}$, $m = 3$).

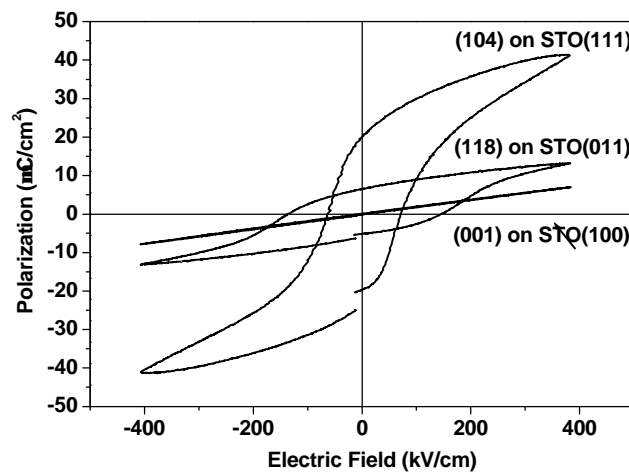


Fig. 5.8 P - E hysteresis loops of BNdT films of different orientations

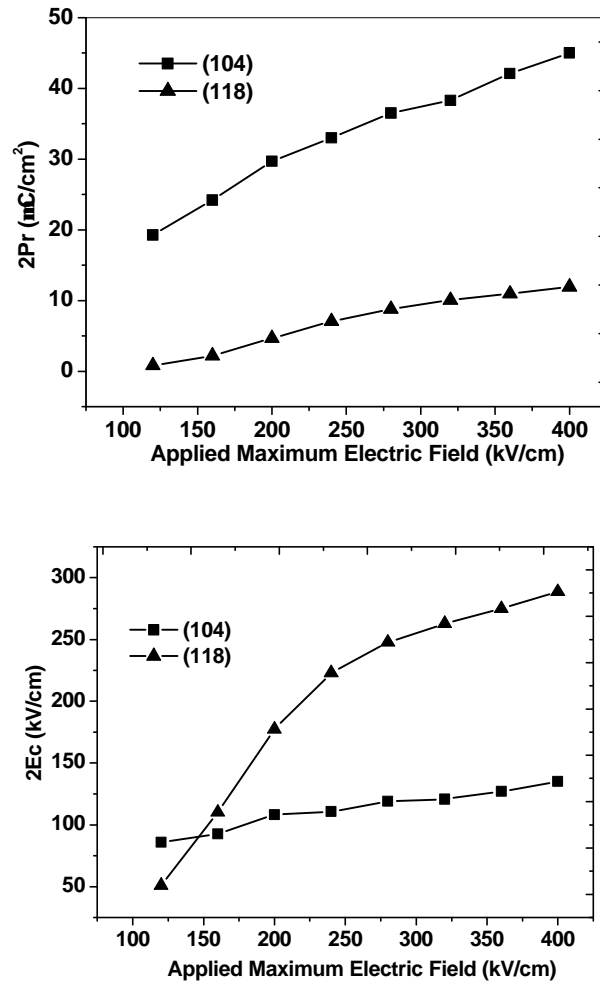
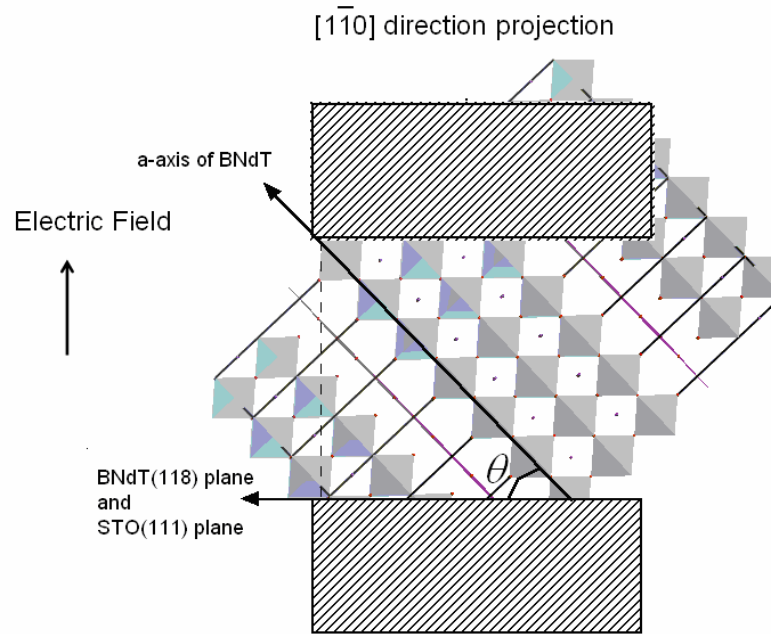


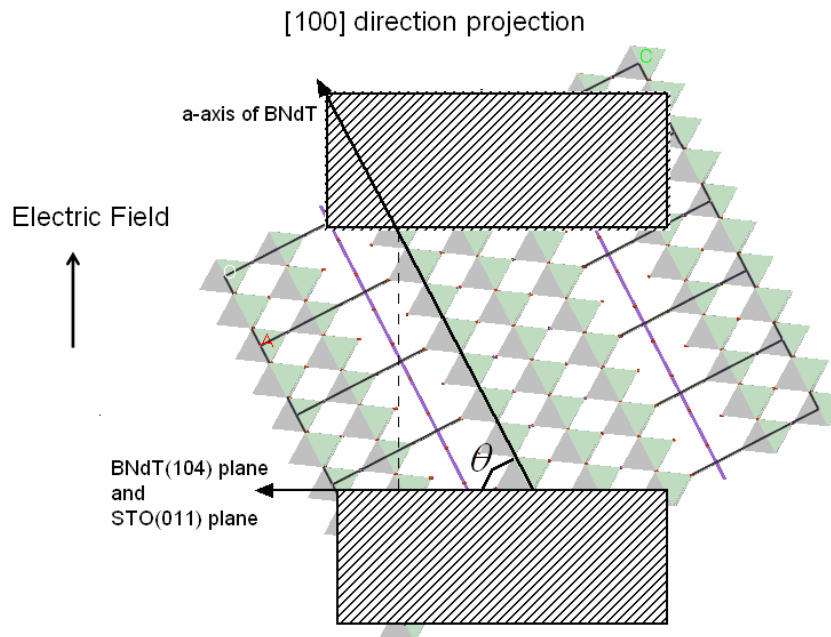
Fig. 5.9 $2P_r$ and $2E_c$ of (118)- and (104)-oriented films as functions of applied field

The field dependence of $2P_r$ and $2E_c$ is displayed in Fig. 5.9. Both $2P_r$ and $2E_c$ tend to saturate above 300 kV/cm. From these values, information about the spontaneous polarisation of BNdT can be obtained. The angles of the (118) and (104) planes with respect to the a - b plane of BNdT are 56.5° and 47.0° , respectively. Hence, it is expected that the (104)-oriented BNdT film has a larger P_r value since its a -axis is close to the applied electric field, as shown in Fig. 5.10. That also explains the very weak ferroelectricity of the (001)-oriented (*i.e.*, c -axis-oriented) film since the polar axis (a/b -axis) of the film lies in the film surface, therefore, very few octahedra blocks can be poled under the applied field, which is along the normal to the film surface

plane.



(a) [110] direction projection of (118)-oriented BNdT thin film



(b) [100] direction projection of (104)-oriented BNdT thin film

Fig. 5.10 Schematic drawing of the relationships between a -axis and applied electric field

5.3.3.2 Leakage current properties

Fig. 5.11 shows the leakage behaviour (plot of current density J vs electric field E) of

(118)- and (104)-oriented films. At a glance, it can be seen from this figure that a (104)-oriented film shows better leakage characteristics than a (118)-oriented film. The current density was between 10^{-6} and 10^{-5} A/cm² for a (104)-oriented film and almost an order of magnitude higher for (118)-oriented films. This difference can possibly be explained by the resistivity anisotropy (and hence leakage current anisotropy) which is well known in layered-structure perovskites, with Payne²¹ reporting resistivity of 3.6×10^{14} ohm-cm along the *c*-axis in SBT, almost 25-times that along the *a*-axis. This explains why a (104)-oriented film, whose *a/b*-axis lies closer to the normal direction of the film surface plane, will have lower leakage current. Leakage characteristics of (104)-oriented films are also in agreement with the results of Kojima *et al.*¹⁰

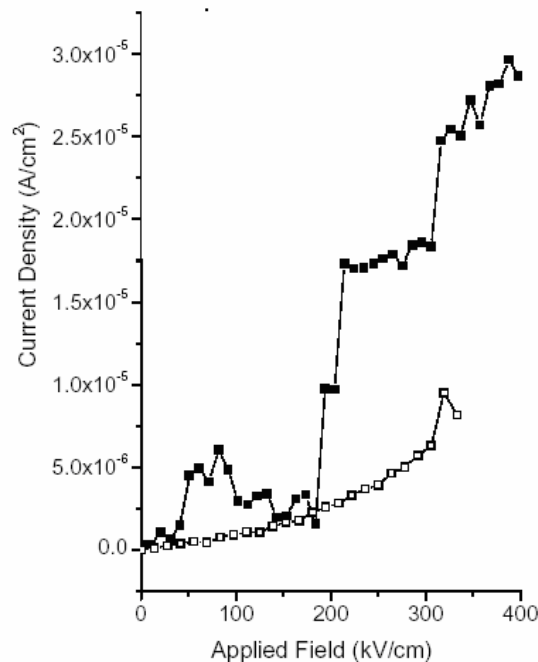


Fig. 5.11 Comparison of the leakage characteristics of (104)-oriented (□) and (118)-oriented (■) BNT films

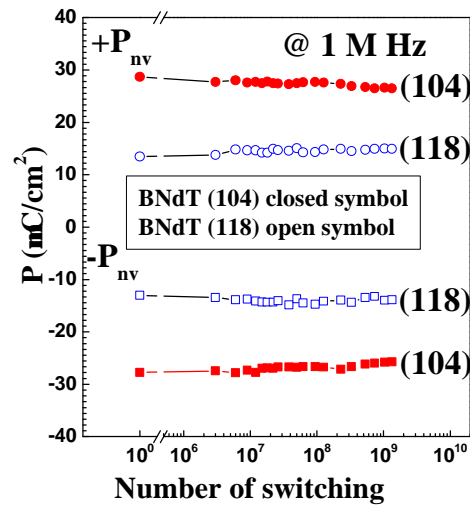
The difference in the leakage characteristics of (118)- and (104)-oriented films may also arise due to grain size and surface roughness effects. Previous studies on

ferroelectric perovskite oxides indicate that conduction mechanisms are affected by the grain size^{22,23}. However, our specimens have different grain geometry for each orientation so we cannot assess such effects in the present work. What is anticipated is a sharp change in the relative contribution of grain boundary conduction as a function of grain size. All electrical analysis in this study is at the macroscopic and not atomic level, therefore the electrical properties were an average of results over the electrode area (200 μm by 200 μm). For our (118)- and (104)-oriented films, the difference in the roughness is not appreciably large to observe any appreciable effect on the leakage characteristics, unlike the results of T. Watanabe *et al.* on MOCVD-derived epitaxial BiT films.²⁴ These authors also found that leakage increases appreciably with the roughness, not in agreement with our results. Their films had very different thicknesses for different orientations, and microstructural aspects may have an effect on the leakage properties. In another study, Kojima *et al.*¹⁰ did not find any effect of surface roughness on the leakage in their lanthanide-doped epitaxial BiT films, implying that lanthanide doping may have some effect on altering the leakage characteristics of BiT films.

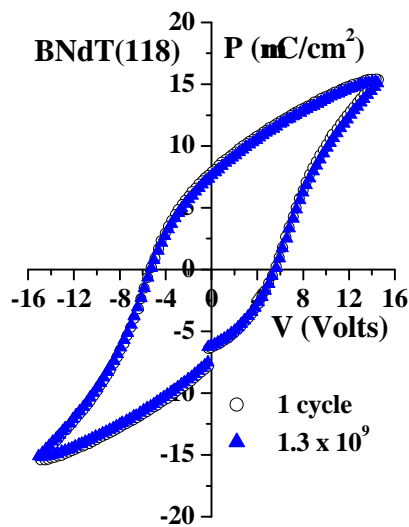
5.3.3.3 Electrical fatigue properties

Fatigue measurements were performed up to 10^9 cycles on (104)- and (118)-oriented BNdT films using 1 MHz bipolar pulses at an applied voltage of 10 V and the results are shown in Fig. 5.13(a). Films showed little change in the nonvolatile polarisation (P_{nv}) up to 10^9 switching cycles. It was observed that the hysteresis loops remained almost identical after 10^9 cycles for both films, demonstrating good fatigue resistance (Figs. 5.12(b) and 5.12(c)). It should be noted that, despite the differences in the conduction behaviour of the two film orientations, their fatigue characteristics are

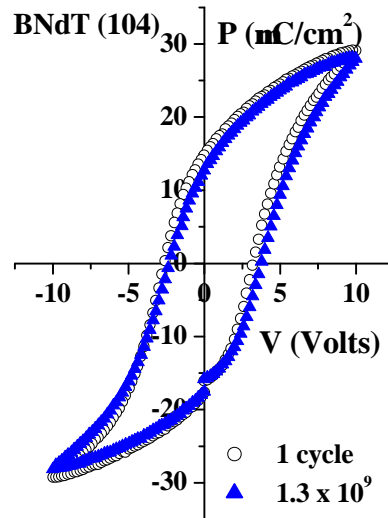
similar.



(a)



(b)



(c)

Fig. 5.12 Electrical fatigue characteristics of (a) (118)- and (104)-oriented BNdT films; (b)(c) hysteresis loops measured before and after 10^9 switching test

5.4 Conclusions

Epitaxial BNdT films of *c*-axis and non-*c*-axis-orientations were deposited on STO substrates of different orientations. Films showed strong dependence of ferroelectric properties on the crystal orientation. The highest remanent polarisation was exhibited

by a (104)-oriented film, whilst a *c*-axis-oriented film showed very weak ferroelectric activity. In addition, the (104)-oriented film showed better leakage characteristics than a (118)-oriented film. No significant fatigue was observed in the films of (118)- and (104)-oriented after 10^9 switching cycles.

5.5 References

- 1 P. H. Park, B. S. Kang, S. D. Bu, T. W. Noh, J. Lee, and W. Jo, *Nature (London)* **401**, 682 (1999).
- 2 E. C. Subbarao, *Journal of Physics and Chemistry of Solids* **23**, 665 (1962).
- 3 P. C. Joshi and S. B. Krupanidhi, *Applied Physics Letters* **62**, 1928 (1993).
- 4 R. E. Melgarejo, M. S. Tomar, S. Bhaskar, P. S. Dobal, and R. S. Katiyar, *Applied Physics Letters* **81**, 2611 (2002).
- 5 U. Chon, K. B. Kim, H. M. Jang, and G. C. Yi, *Applied Physics Letters* **79**, 3137 (2001).
- 6 H. Matsuda, S. Ito, and T. Iijima, *Applied Physics Letters* **83**, 5023 (2003).
- 7 A. D. Rae, J. G. Thompson, and R. L. Withers, *Acta Crystallographica, Section B: Structural Science* **48**, 418 (1992).
- 8 Y. Shimakawa, Y. Kubo, Y. Tauchi, H. Asano, T. Kamiyama, F. Izumi, and Z. Hiroi, *Applied Physics Letters* **79**, 2991 (2001).
- 9 R. D. Shannon, *Acta Materialia* **A32**, 751 (1976).
- 10 T. Kojima, T. Sakai, T. Watanabe, H. Funakubo, K. Saito, and M. Osada, *Applied Physics Letters* **80**, 2746 (2002).
- 11 H. Maiwa, N. Iizawa, D. Togawa, T. Hayashi, W. Sakamoto, M. Yamada, and S. Hirano, *Applied Physics Letters* **82**, 1760 (2003).
- 12 S. E. Cummins and L. E. Cross, *Journal of Applied Physics* **39**, 2268 (1968).
- 13 U. Chon, H. M. Jang, M. G. Kim, and C. H. Chang, *Physical Review Letters* **89**, art. no. 087601 (2002).
- 14 A. Garg (Personal communication).
- 15 Jose L. Pineda-Flores, E. Chavira, J. Reyes-Gasga, A.M. Gonzalez, and A. Huanosta-Tera, *Journal of the European Ceramic Society* **23**, 839 (2003).
- 16 H. N. Lee, D. Hesse, N. Zakharov, and U. Gosele, *Science* **296**, 2006 (2002).
- 17 H. Irie, M. Miyagawa, and T. Kudo, *Journal of Applied Physics* **90**, 4089 (2001).
- 18 O. AlvarezFregoso, *Journal of Applied Physics* **81**, 1387 (1997).
- 19 A. Garg, S. Dunn, and Z. H. Barber, *Integrated Ferroelectrics* **31**, 13 (2000).
- 20 M. Miyagawa and I. S. Yi, *Ceramics International* **26**, 529 (2000).

- ²¹ D. A. Payne, presented at the European Electroceramics Conference, Portoroz, Solvenia, 2000 (unpublished).
- ²² H. Chen, K. R. Udaykumar, and L. E. Cross, MRS Proceeding **433**, 325 (1996).
- ²³ M. M. Gallego and A. R. West, Journal of Applied Physics **90**, 394 (2001).
- ²⁴ T. Watanabe, H. Funakubo, and K. Saito, Journal of Materials Research **16**, 303 (2001).

Chapter 6 PLD-grown Sm-doped bismuth titanate polycrystalline ferroelectric thin films

6.1 Background

Chapter 5 described BNdT films grown by PLD on single crystal substrates, showing that Nd-doping of BiT leads to an increase in the polarisation in comparison to La-doped films and a strong dependence of ferroelectric properties on the film orientation, which confirmed that the polar axis remains in the a - b plane. Sm-doping may result in a higher $2P_r$ than Nd-doping, since the radius of Sm^{3+} (0.108 nm) is smaller than Nd^{3+} (0.111 nm) and La^{3+} (0.116 nm), all of which are smaller than Bi^{3+} (0.117 nm). Therefore, Sm-doped BiT films were also studied.

Silicon substrates are widely used in microelectronic integrated circuit technology, since they are cheap and widely available. Standard microelectronic processing, such as oxidation, patterning, implantation, diffusion, etching and metallisation, have all been widely researched and standardised on silicon.¹ Therefore, for practical use, electroded silicon substrates have great advantage over single crystal substrates.

Due to the anisotropic nature of ferroelectric properties, the orientation of the crystallites in BiT films is critical for attaining high $2P_r$ and low E_c values.

Therefore, the essential approach of the deposition techniques is crystallisation of the required Bi-layered phase with minimum defects without inclusion of any secondary phases and orientation of the crystallites with a preferred (a - b) plane perpendicular to the film surface. As these requirements are highly dependent on processing methods

and parameters, several process variables have been attempted in the past to form BiT films meeting the structural criterion.

Combining the above analysis (doping element, substrates and deposition techniques) in order to achieve improved ferroelectric film properties, we have adopted PLD to fabricate BSmT thin films on platinised silicon. In this chapter, we present some detailed results on the structural and ferroelectric investigation of the BSmT films. First, we will study the effect of processing temperature on film properties; then we will investigate the effect of Pt layer orientation, Sm-doping level, and buffer layer, on film properties.

6.2 Effect of processing temperatures on film properties

We principally varied the substrate temperature during deposition and annealing, since for different materials, the crystallisation temperature is quite sensitive and critical to the film fabrication.

6.2.1 Experimental details

6.2.1.1 Target fabrication

A series of $\text{Bi}_{4-x}\text{Sm}_x\text{Ti}_3\text{O}_{12}$ ($x = 0, 0.55, 0.70, 1.00$) bulk ceramic targets with 10 mol% bismuth excess were prepared by a conventional solid-state reaction route as described in Chapter 3. In this section, the $\text{Bi}_{3.63}\text{Sm}_{0.70}\text{Ti}_3\text{O}_{12}$ bulk ceramic targets were used to optimise the film fabrication. The XRD profile of the targets was shown in the previous chapter (see Fig. 5.1). We used undoped $\text{Bi}_4\text{Ti}_3\text{O}_{12}$ and $\text{Bi}_{4.4}\text{Ti}_3\text{O}_{12}$ (10 mol% bismuth excess) targets to study the effect of bismuth excess on film properties.

6.2.1.2 Film deposition and characterisations

Commercially available Pt(150 nm)/TiO_x(40 nm)/SiO₂(400 nm)/Si substrates with (111)-preferred-orientation Pt layer were used for film deposition. The deposition parameters used for the growth of films are shown in Table 6.1. Substrate temperatures of higher than 750 °C were not used because silicon substrates are greatly damaged and the interdiffusion between films and substrates increases at this temperature.^{2,3,4,5}

Table 6.1 Deposition parameters used for the growth of BiT and BSmT thin films

Deposition parameters	Values
Laser pulse frequency (Hz)	5
Total number of pulses	6000
Pulse energy per spot (mJ)	150 (for BiT), 225 for (BSmT)
Substrate temperature (°C)	650, 700, and 750
Oxygen Pressure (Pa)	27
Anneal pressure (kPa) (O ₂)	~65
Annealing duration (minutes)	~60
Thickness (nm)	450~520

6.2.2 Results and discussion

6.2.2.1 Structural properties

1. X-ray diffraction results

First, the effect of excess bismuth in PLD targets on structural properties of the films was studied. Fig. 6.1 shows XRD profiles of the films deposited using pure BiT and BiT (10 mol% Bi excess) deposited and annealed at 650 °C (Figs. 6.1(a) and 6.1(b)) and that of the same film subsequently annealed at 750 °C (Figs. 6.1(c) and 6.1(d)).

From the comparison of the profiles, we can clearly see that the peak located at 15° (2 θ position), which is a fluorite phase due to incomplete crystallisation, exists for both films annealed at 650 °C, but is significantly lower in the film deposited using the Bi-excess target. Further annealing at 750 °C converts the film from the Bi excess target completely to a perovskite phase (Fig. 6.1(d)), but not the film from the pure BiT target (which has even more pyrochlore phase, Fig. 6.1(c)). Increased annealing temperature results in further Bi loss (the bismuth content (weight percentage) of Bi₂Ti₂O₇ is lower than that of Bi₄Ti₃O₁₂). From this we can see that using bismuth excess target can facilitate the crystallisation of the perovskite phase.

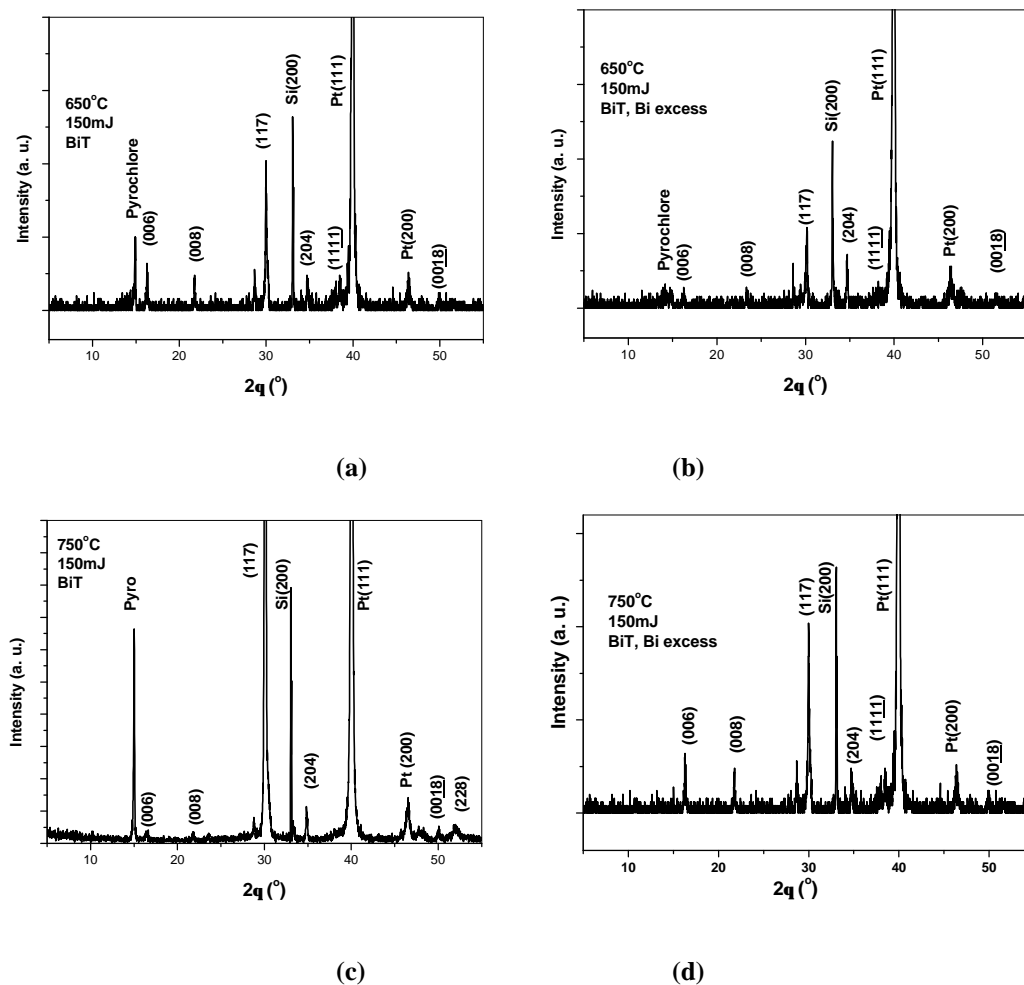


Fig. 6.1 XRD profiles of films from (a) pure BiT and (b) BiT with bismuth excess targets annealed at 650 °C; (c) pure BiT and (d) BiT with bismuth excess targets annealed at 750 °C

Fig. 6.2 shows the XRD 2θ scans of BSmT films deposited and annealed at different temperatures. We can see that the film was crystallised at 650 °C with no evidence of amorphicity, but with a fluorite phase (around 15° 2θ position), which was indexed as the $\text{Bi}_2\text{Ti}_2\text{O}_7$ cubic phase (JCPDS card, 32-0118). With an increase in the deposition and annealing temperature, the intensity of the fluorite peak decreased and the (00 l) peaks of perovskite phase were enhanced, indicating loss of the fluorite structure and the enhancement of the perovskite phase. No other phase other than the perovskite phase was observed at 750 °C with a predominant (117) peak and secondary (006), (008), (0018), (1111) and (204) peaks, which indicates that the films are polycrystalline.

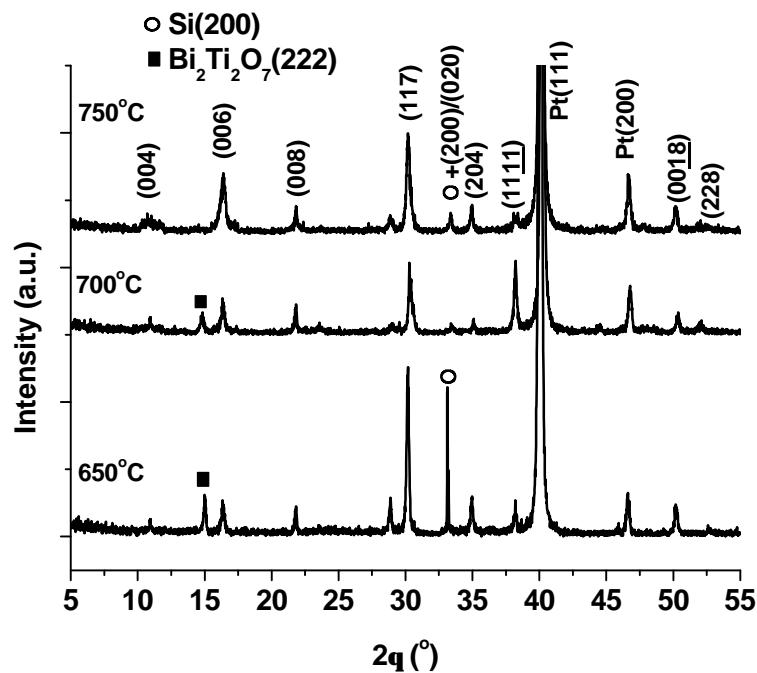


Fig. 6.2 XRD profiles of BSmT films deposited at different temperatures

It has been reported that $\text{Bi}_2\text{Ti}_2\text{O}_7$ is an intermediate and unstable phase that occurs in the formation of $\text{Bi}_4\text{Ti}_3\text{O}_{12}$.^{6,7} According to the phase diagram of the Bi_2O_3 - TiO_2 system, the phase $\text{Bi}_2\text{Ti}_2\text{O}_7$ can be converted into $\text{Bi}_4\text{Ti}_3\text{O}_{12}$ at 700 °C.⁸ Kojima⁹

found that BiT powder annealed at 770 °C was crystalline $\text{Bi}_2\text{Ti}_2\text{O}_7$ with the fluorite structure, whereas the powder annealed at 1000 °C was crystalline $\text{Bi}_4\text{Ti}_3\text{O}_{12}$ with the layered perovskite structure.

The degree of the (00 l)-type preferential growth was estimated using Lotgering's orientation factor¹⁰

$$(00l)\% = \frac{I_{(00l)}}{I_{(00l)} + I_{(117)}} \times 100\% \quad (6.1)$$

(00 l)% is 17%, 31%, 36%, for the BSmT films annealed at 650 °C, 700 °C, 750 °C, respectively, as shown in Fig. 6.3, which suggests that the increasing temperature favours the growth of c -axis-oriented grains.

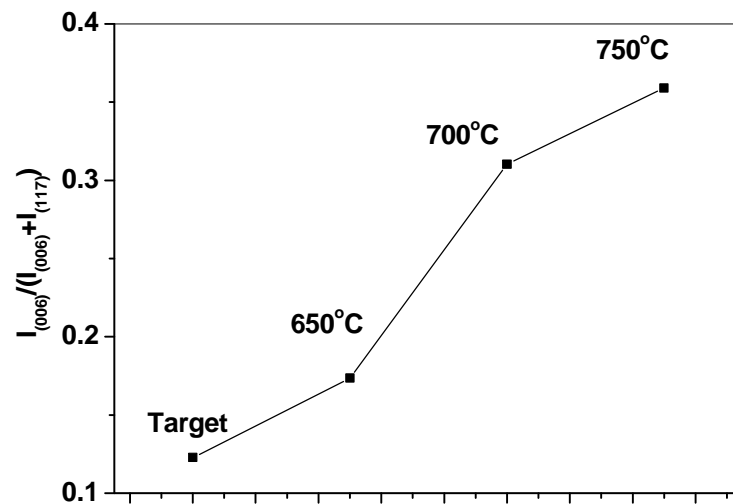


Fig. 6.3 Degrees of (00 l)-type preferential growth

2. Morphological studies (AFM and SEM)

Fig. 6.4 shows 1 $\mu\text{m} \times 1 \mu\text{m}$ AFM images of the surface morphology of the BSmT ($x = 0.70$) films grown at 750 °C. The film RMS roughness was 23.2 nm, over an area of 2 $\mu\text{m} \times 2 \mu\text{m}$. The average lateral size of columns for the film was 150~200 nm.

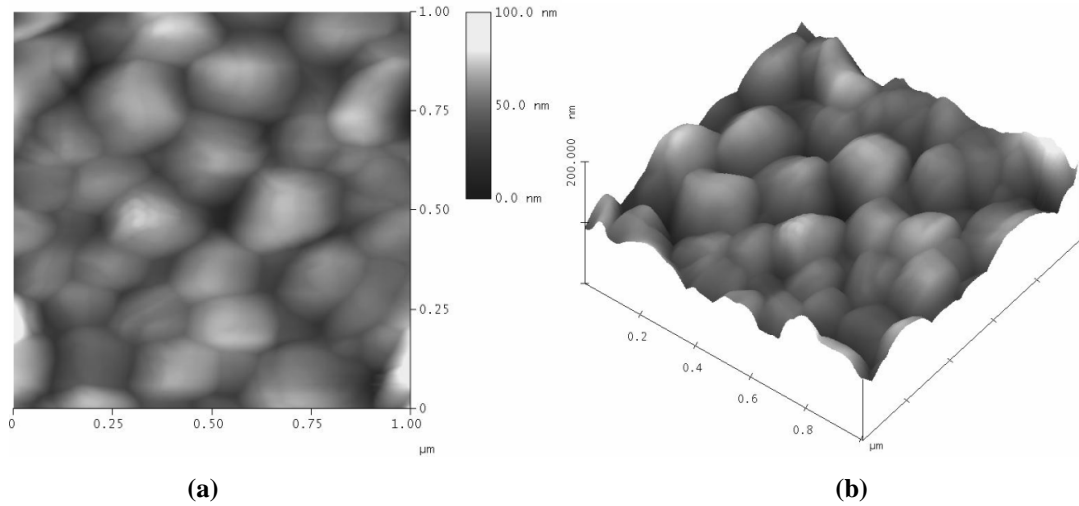


Fig. 6.4 AFM images of BSmT films deposited at a substrate temperature of 750 °C

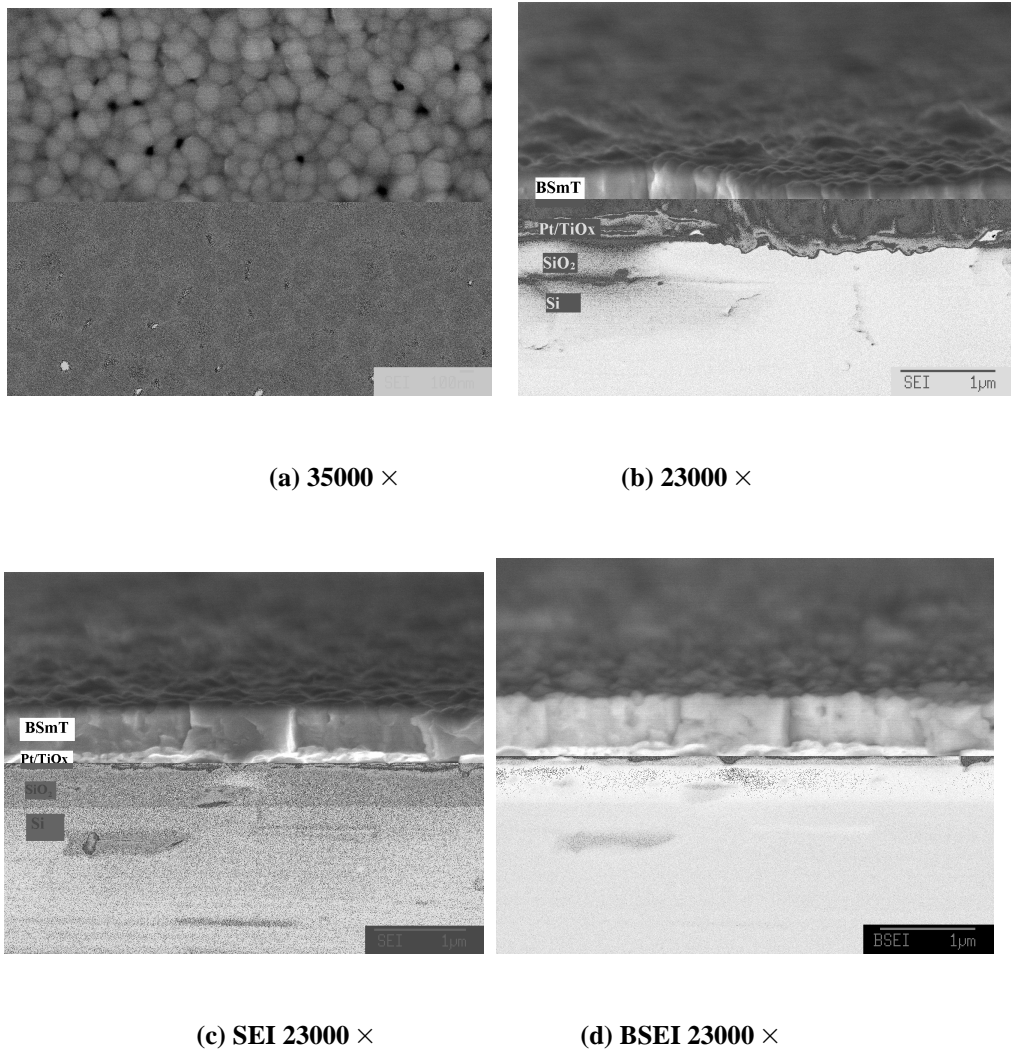


Fig. 6.5 SEM image of BSmT (a) plan view; (b)-(d) cross sectional view

Fig. 6.5 shows FE-SEM images of the film. Figs. 6.5(a) and 6.5(b) shows the plan

view and cross-sectional view of the film, showing a uniform surface with circular grains and relatively closely packed grains, as the AFM images indicated. The cross-sectional image (Fig. 6.5(b)) shows that the film has a dense columnar structure.

Figs. 6.5(c) and 6.5(d) show the cross-sectional view of the same film obtained from the SEI mode and the BSEI mode, respectively. From the images, we can see that the film is continuous and chemically homogenous, with very clear boundaries between the film and bottom electrode layer (Pt/TiO_x).

EDX spectra were also collected at 11 keV at various points on samples. To ensure that the voltage used (11 kV) is not too high for the probe electrons to penetrate the whole film thickness and collect the background information from the bottom electrode, a simulation was carried out using Monte Carlo Simulation software (Developed by Kimio Kanda, 1996), shown in Fig. 6.6. The result shows that the electrons can go as far as about 400 nm, for an average composition of $\text{Bi}_{3.3}\text{Sm}_{0.7}\text{Ti}_3\text{O}_{12}$ (film thickness: 450 nm ~ 520 nm). Thus we can be sure that the information obtained from the EDX was solely from the films and not the substrate.

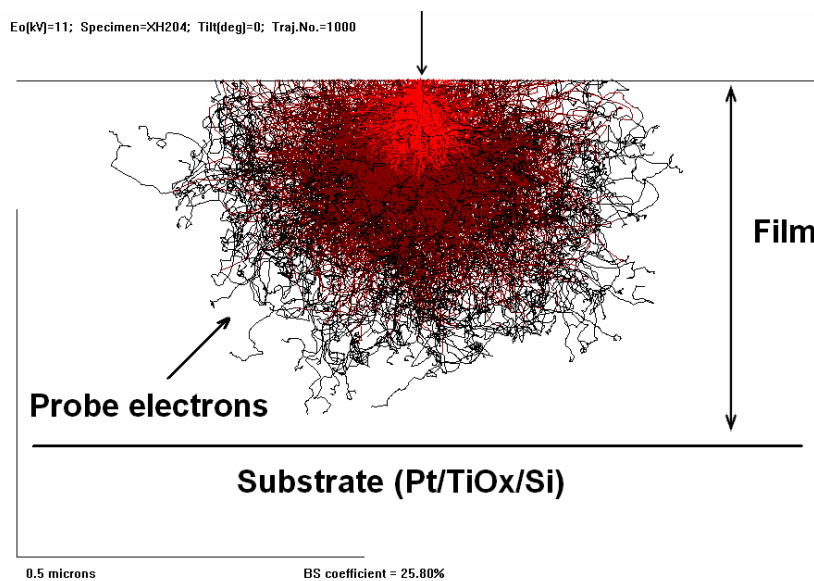
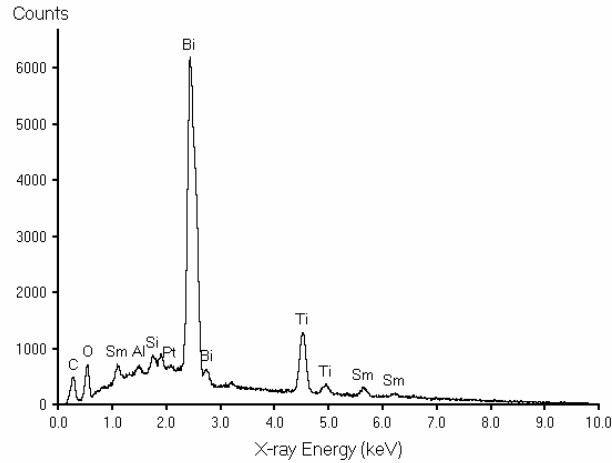
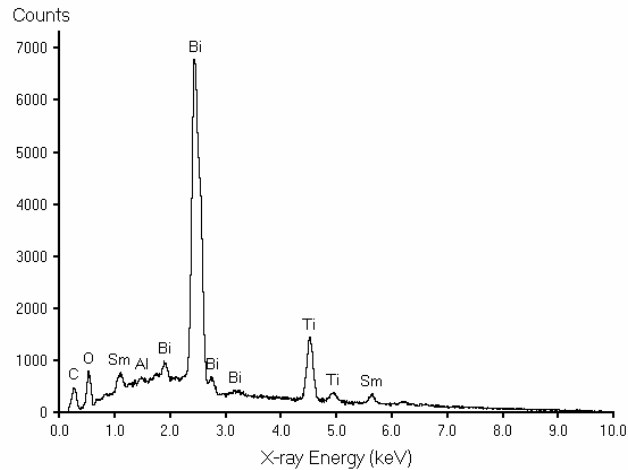


Fig. 6.6 Simulation of interaction of electrons and the film



(a)



(b)

Fig. 6.7 EDX spectra collected over 60.0 live seconds for (a) edge area; (b) centre area

Typical EDX spectra collected over 60.0 live seconds at different points from films grown at 750 °C are shown in Figs. 6.7(a) and 6.7(b), respectively, and clearly show Bi, Sm, Ti, and O peaks, with other possible Si and Al small peaks (Al peaks may come from the sample holder). The spectrum lines that were used are Ti-L, Si-K, Bi-L, O-K, Pt-M, and Sm-L.

In order to avoid complications arising from the large uncertainty of quantitative EDX measurements with oxygen, the Bi:Sm and (Bi+Sm):Ti ratios were acquired and the results are shown in Table 6.2. Values of the Bi:Sm and (Bi+Sm):Ti ratios for

$\text{Bi}_{3.30}\text{Sm}_{0.70}\text{Ti}_3\text{O}_{12}$ are 4.71 and 1.33, respectively.

Table 6.2 EDX analyses from different selected area of the film surface

Element	1 (edge)	2 (edge)	3 (centre)	4 (centre)	Calculated (Mean) (C)	Intended (I)	Deviation (C-I)/I × 100%
Bi (at. %)	19.25	18.53	19.67	18.27			
Sm (at. %)	4.00	4.34	3.94	4.03			
Ti (at. %)	16.42	15.57	16.66	16.49			
O (at. %)	60.32	61.56	59.74	61.01			
Bi:Sm	4.813	4.270	4.992	4.533	4.65 ± 0.34	4.71	-1.3%
(Bi + Sm):Ti	1.416	1.469	1.417	1.352	1.41 ± 0.06	1.33	6.0%

The results suggest a successful substitution of Sm for Bi in the film by comparison with the intended value (4.71; a deviation of -1.3%).

The second conclusion that may be drawn from the range of the Bi:Sm ratios (4.270~4.992; 4.65 ± 0.34 ; deviation of ± 0.7 at. %) is that there may be some small spatial variation in stoichiometry, although it is close to the ultimate accuracy of the equipment.

From the mean values of Bi:Sm and (Bi + Sm):Ti, the composition of the film was calculated to be $\text{Bi}_{3.48 \pm 0.15}\text{Sm}_{0.75 \pm 0.04}\text{Ti}_4\text{O}_{12}$. The maximum deviation of the calculated value of the film from the intended value is ~6.0% (the intended film composition was $\text{Bi}_{3.30}\text{Sm}_{0.70}\text{Ti}_4\text{O}_{12}$), suggesting a successful control of the transfer of the composition

from the target to the film (after taking the Bi loss into account).

6.2.2.2 Electrical properties

The P - E hysteresis loops of $\text{Bi}_{4-x}\text{Sm}_x\text{Ti}_3\text{O}_{12}$ ($x = 0.70$) films deposited at 750°C using laser energy of 225 mJ are shown in Fig. 6.8. Well-saturated loops were measured.

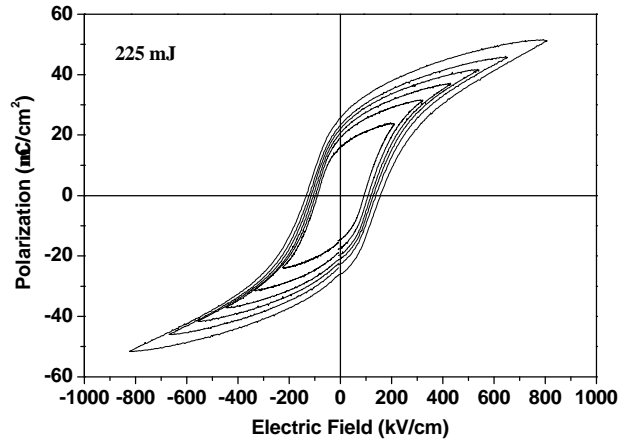


Fig. 6.8 P - E loops of films deposited at 750°C

Fig. 6.9 summarises the variations of $2P_r$ and $2E_c$ of BSmT with the applied maximum electric field. The $2P_r$ values increase rather steeply at a low applied maximum electric field but do not change much beyond 350 kV/cm. $2P_r$ value of the film is $42 \mu\text{C}/\text{cm}^2$ at an applied maximum electric field of 450 kV/cm. This value is comparable to the $2P_r$ of $49 \mu\text{C}/\text{cm}^2$ for Chon's BSmT films deposited using metalorganic sol decomposition (MOSD).¹¹ $2E_c$ value of the film is about 220 kV/cm at an applied maximum electric field of 450 kV/cm, slightly smaller than that of Chon (230 kV/cm)¹¹.

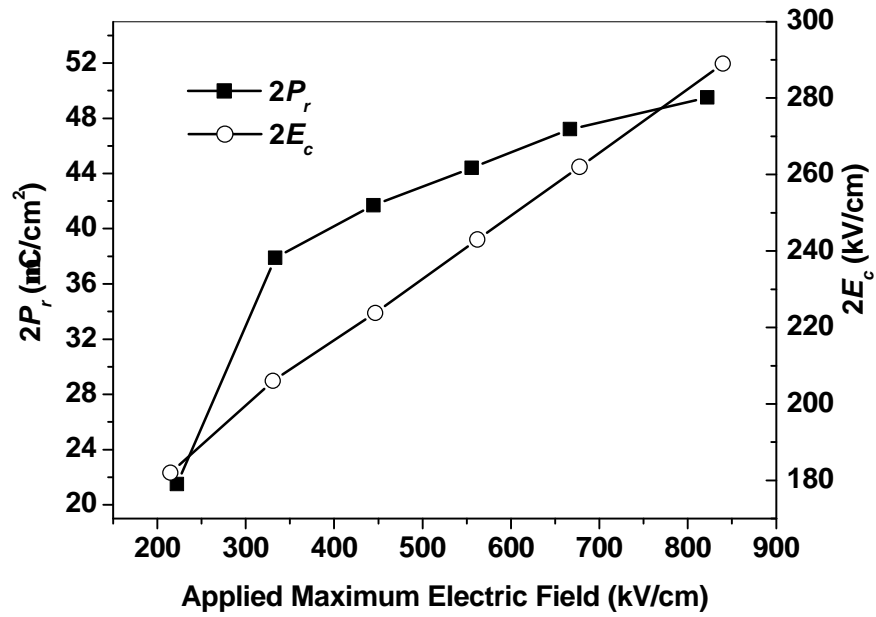


Fig. 6.9 Variations of $2P_r$ and $2E_c$ values of the BSmT thin film as a function of the applied maximum electric field

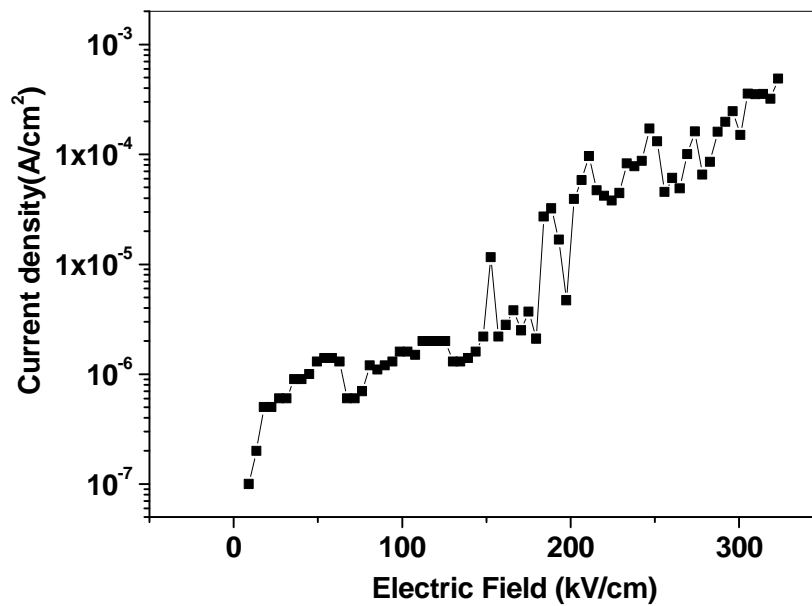


Fig. 6.10 J - E characteristics of the BSmT film

Typical leakage current density - electric field (J - E) characteristics of the film is shown in Fig. 6.10. The leakage current density was found to be $\sim 10^{-6}$ A/cm²,

respectively, when the applied electric field was smaller than 200 kV/cm. At 200 kV/cm, the value of current density was 5×10^{-6} A/cm².

Therefore, the BSmT film deposited at 750 °C and 225mJ/spot has both superior ferroelectric and insulating properties. The film also showed excellent fatigue resistance, as will be discussed in Section 6.4.3.4.

6.3 Effect of Pt layer orientations

6.3.1 Motivation

As suggested in the previous section, the orientation of the lower Pt electrode might influence the film orientation as grown by PLD, thus affecting the film ferroelectric and electrical properties. With preferred orientation of polycrystalline ferroelectric films, key properties such as polarisation, coercivity and dielectric constant can approach those of single crystals, and even lower coercive fields are achievable with near epitaxial films. To confirm this, we carried out a further study on the different substrates using different orientations in Pt bottom layers.

6.3.2 Experimental details

The parameters for film deposition by PLD were kept the same as the previous section using different substrates. In this section, the target of $\text{Bi}_{3.63}\text{Sm}_{0.70}\text{Ti}_3\text{O}_{12}$ was used, which was prepared by a conventional solid-state reaction route mentioned in Chapter 3. Commercially available Pt(150 nm)/TiO_x(40 nm)/SiO₂(400 nm)/Si substrates with preferred (111)- and (200)-oriented-Pt layers (abbreviated as Pt(111)/Si and Pt(200)/Si, respectively) were used for film deposition. The films were deposited at a substrate temperature 750 °C.

6.3.3 Results and discussion

6.3.3.1 Structural properties

Fig. 6.11 shows XRD profiles of the two different substrates (only showing the range which contains peaks of the Pt layers).

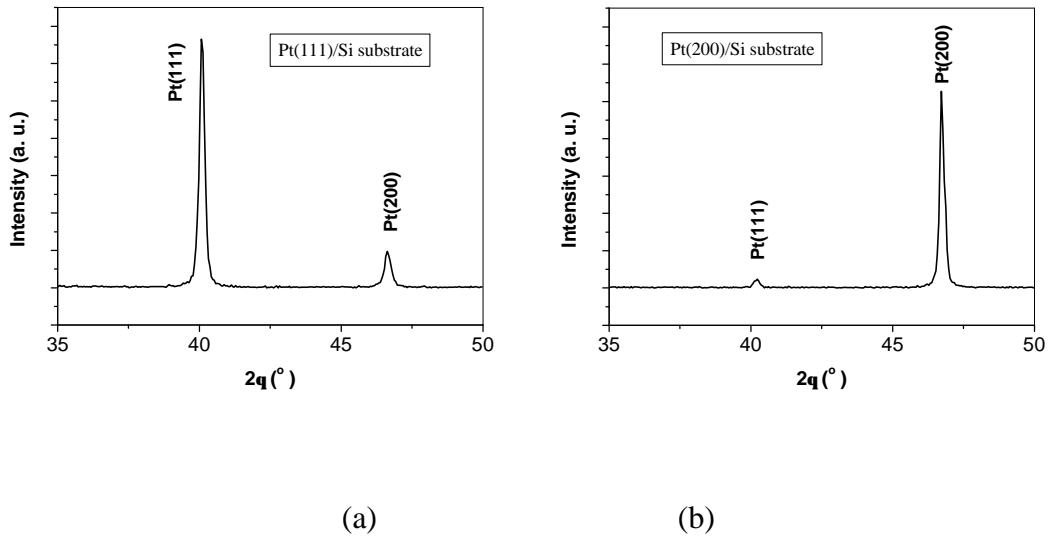


Fig. 6.11 XRD profiles of two different substrates of (a) Pt(111)/Si; (b) Pt(200)/Si

The proportion of the (111) oriented grains for Pt(111) is calculated using Lotgering's equation¹⁰

$$Pt(111)\% = \frac{I_{(111)}}{I_{(111)} + I_{(200)}} \times 100\% = 87.3\% \quad (6.2)$$

Similarly, the proportion of the (200)-oriented grains for Pt(200) is:

$$Pt(200)\% = \frac{I_{(200)}}{I_{(111)} + I_{(200)}} \times 100\% = 96.5\% \quad (6.3)$$

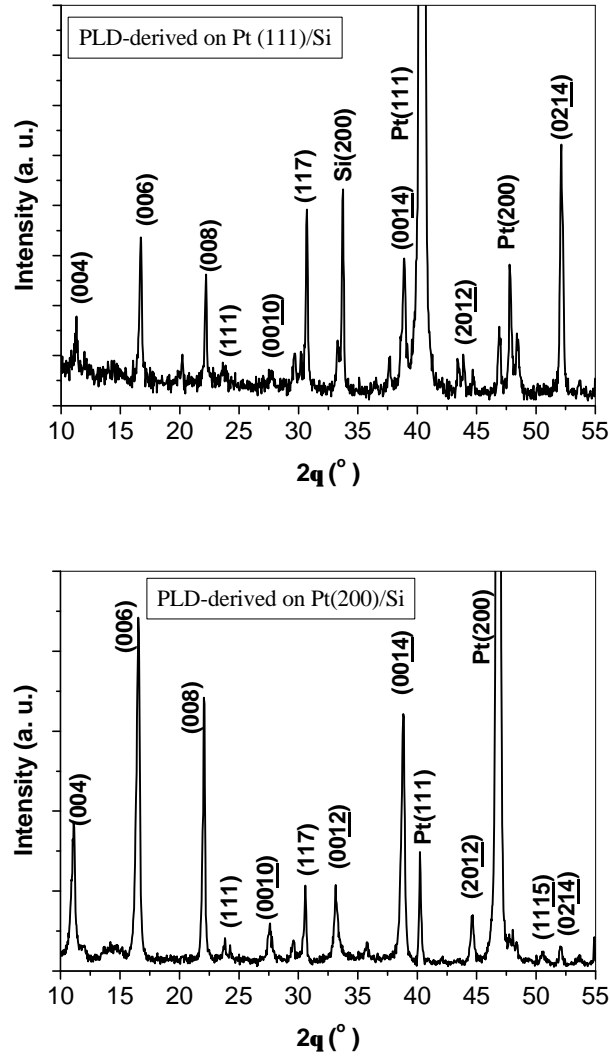


Fig. 6.12 XRD profiles of BSmT films deposited on two different substrates

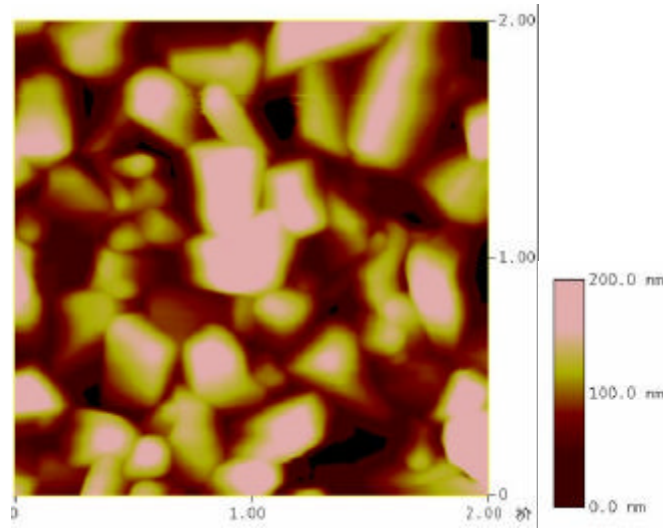
The XRD profiles of BSmT films deposited on the two different substrates are shown in Fig. 6.12. We can see that both films are fully crystallised and have a single phase of bismuth layered structure showing mixed $(00l)$ and (117) orientations.

The proportion of (117) -oriented grains is calculated for the two films by the equation

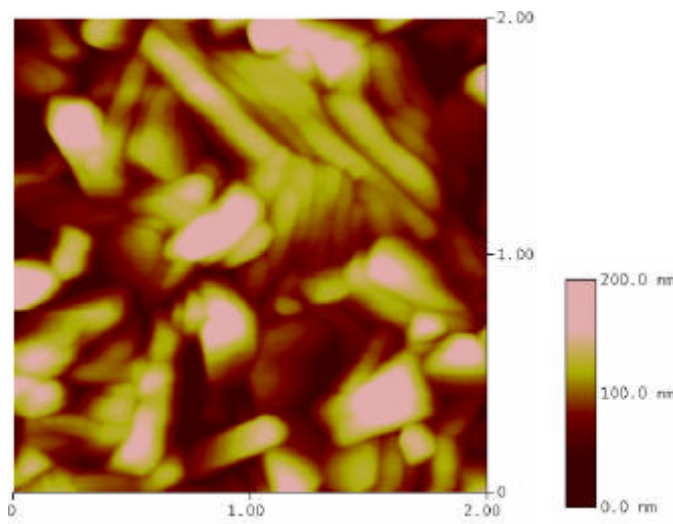
$$(117)\% = \frac{I_{(117)}}{I_{(006)} + I_{(117)}} \times 100\% \quad (6.4)$$

The proportions of $(117)\%$ in the two films are 54.0% and 19.5%, respectively, for the

films deposited on Pt(111)/Si and Pt(200)/Si substrates.



(a)



(b)

Fig. 6.13 AFM images ($2\ \mu\text{m} \times 2\ \mu\text{m}$) of BSmT films deposited on two different substrates: (a) Pt (111)/Si (rms = 20.9 nm); (b) Pt(200)/Si (rms = 18.9 nm)

Fig. 6.13 shows the AFM images of the two films. Both films show similar surface topography and the values of surface roughness are 20.9 nm and 18.9 nm, respectively, for the films deposited on Pt (111)/Si and Pt (200)/Si substrates.

In order to investigate the origin of the preferred growth orientations, we closely

examined the atomic configurations at the BSmT/Pt interfaces.

The atomic arrangements in the Pt (200) and BSmT (00*l*) planes are shown in Fig. 6.14. From this, we can see that there is a good match between these two planes if the following orientation relationship is satisfied:

$$\text{BSmT } (00l) // \text{Pt } (200) \quad (6.5)$$

$$\text{BSmT } [001] // \text{Pt } [110] \quad (6.6)$$

The mismatch along the Pt[110] and BSmT[001] directions is quite small (-0.71%). Therefore, we would expect that BSmT films tend to grow with (00*l*)-preferred orientation, in Pt (200) plane.

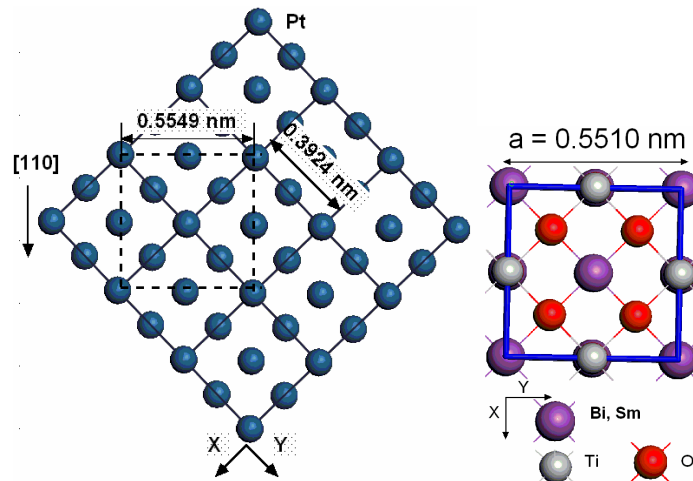
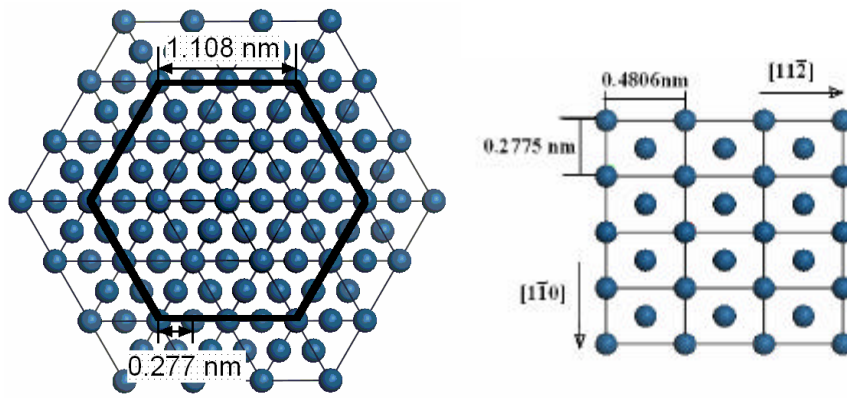


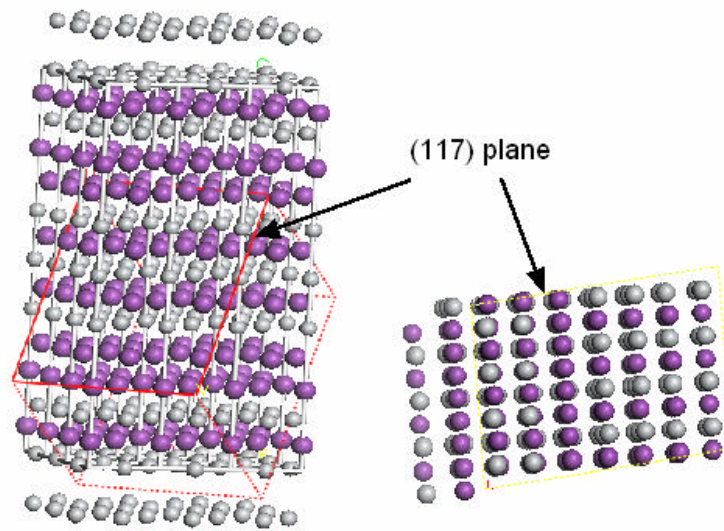
Fig. 6.14 Schematic representations of atomic configurations in the Pt (200) plane and those in the BSmT (001) plane

Schematic representations of atomic configurations of Pt(111) and BSmT(117) are shown in Fig. 6.15. There are some similarities between the two structures, although there are no strict one-to-one corresponding atoms for the two planes. This may partly

explain the increase in (117)-oriented grains in BSmT films grown on the Pt (111) plane.



(a)



(b)

Fig. 6.15 Schematic representations of atomic configurations of (a) Pt (111) plane; (b) BSmT (117) plane

6.3.3.2 Electrical properties

Fig. 6.16 shows ferroelectric loops recorded at various applied voltages and the field dependence of $2P_r$ and V_c of both films. The fluctuation in the V_c voltage dependence curve of the films on Pt (111) appeared in several measurements, which may be related to a domain de-pinning procedure around the range of 12-16 V.

The measured $2P_r$ and V_c of the films on Pt(200) were $\sim 11.0 \mu\text{C}/\text{cm}^2$ and 4.5 V, respectively, for a maximum applied electric voltage of 30 V; the $2P_r$ and V_c values of the films on Pt (111) were $\sim 30.0 \mu\text{C}/\text{cm}^2$ and 6.0 V, respectively, for a maximum applied electric voltage of 23 V. The BSmT films deposited on Pt(111)/Si have more clearly saturated P - V loops with larger $2P_r$, than those of the film on Pt(200)/Si.

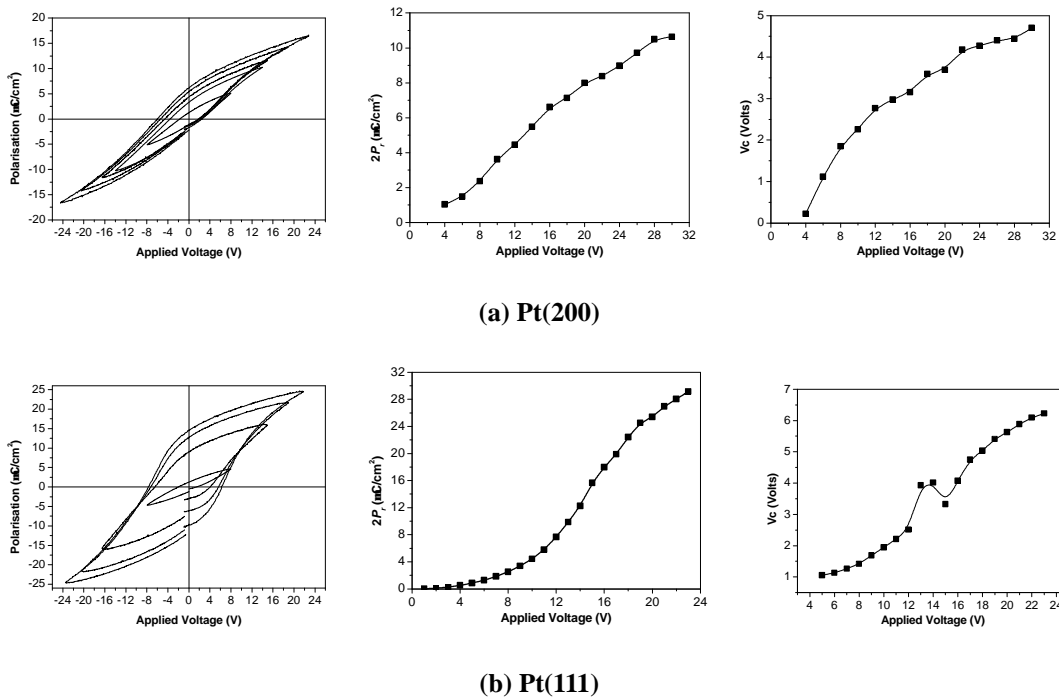


Fig. 6.16 Ferroelectric loops measured at various voltages and variations of $2P_r$ and V_c values of the BSmT thin film as a function of the applied maximum voltages

Fig. 6.17 shows a comparison of both films at a similar applied maximum voltage and Table 6.3 shows the detailed values. These data clearly show that the film grown on Pt (111) has a higher $2P_r$ and V_c . It may be related to the higher proportions of (111)-oriented grains in the films grown on Pt (111)/Si substrates, since the polar axis (a/b axis) of (111)-oriented grains is closer to the normal direction of the film surface.

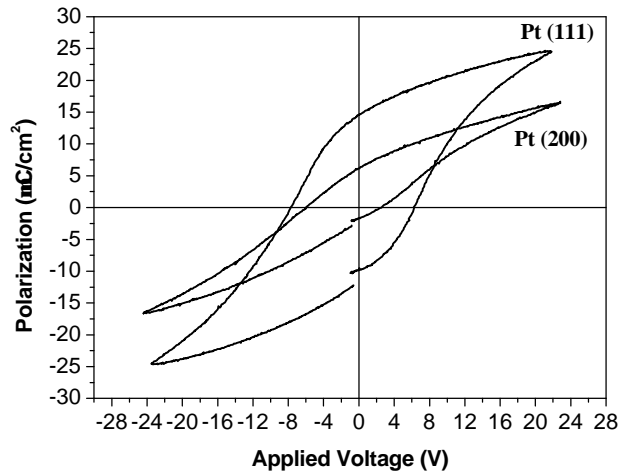


Fig. 6.17 Hysteresis loops of the films grown on Pt (111) and Pt (200) covered silicon substrates

Table 6.3 Comparison of properties of both film types

Sample	$2P_r$ ($\mu\text{C}/\text{cm}^2$, at 23 V)	V_c (V, at 23 V)
Pt 200	8.7	4.1
Pt 111	27.0	7.0

6.4 Effect of different doping level

6.4.1 Motivation

Since doping, especially lanthanide element doping, can greatly affect the properties of BiT films, in this section the effect of various doping levels of Sm on the film properties will be presented.

BLaT has been the most popular and extensively studied previously. The primary differences in BLaT with the increase of La content x are: (a) increase in lattice constant and volume,¹² (b) decrease in T_c ,¹³ (c) increase in P_r ,¹⁴ and (d) improvement in fatigue resistance.¹⁴ There have been few comprehensive studies on the effect of Sm doping on the properties of BiT thin films and understanding this is important for using such material for device applications.

6.4.2 Structural properties

6.4.2.1 XRD studies

Fig. 6.18 shows the XRD patterns of the BSmT films (with different doping levels) fabricated on Pt-coated Si substrates at 750 °C (thickness: ~470 nm). We can see that all the films were fully crystallised and have a bismuth-layered structure showing mixed orientations. From the intensities of (006)- and (117)-oriented grains, the degree of (117)-orientation was calculated (Equation 6.1) and is shown in Fig. 6.19. We can see that increasing Sm doping content increases the proportion of (117)-oriented grains.

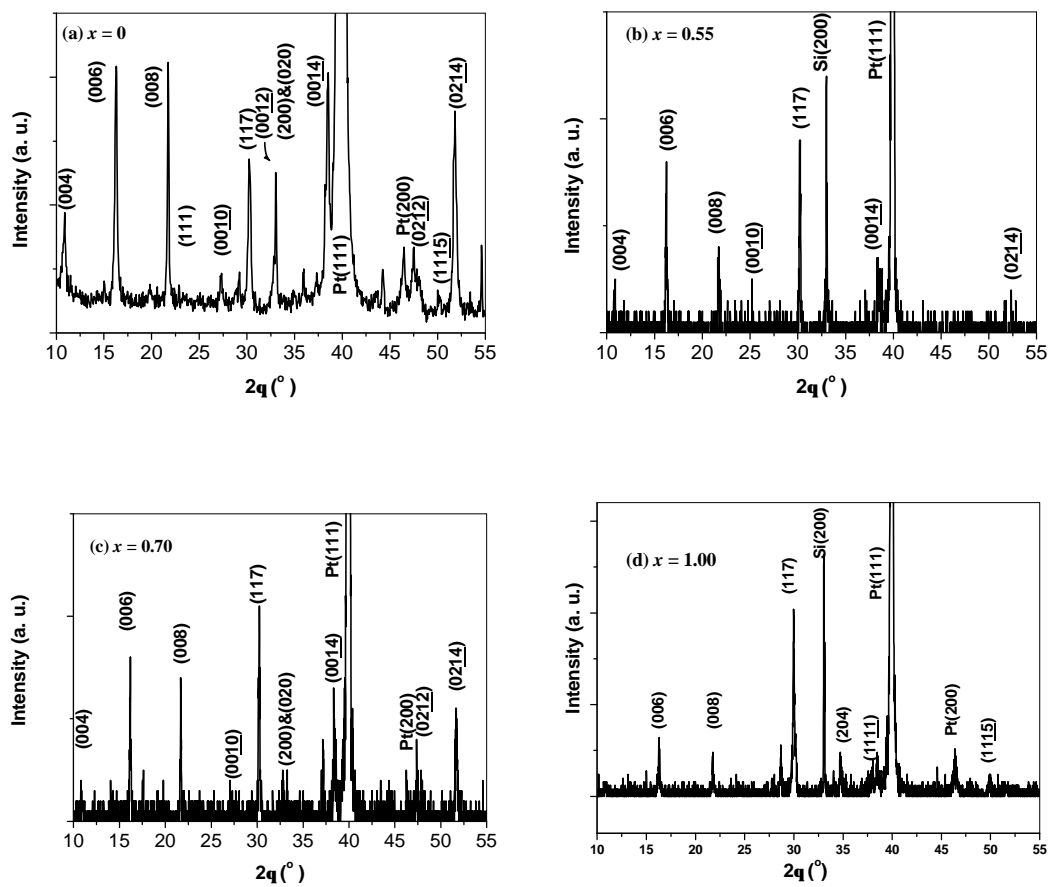


Fig. 6.18 XRD patterns of the BSmT films with different doping levels

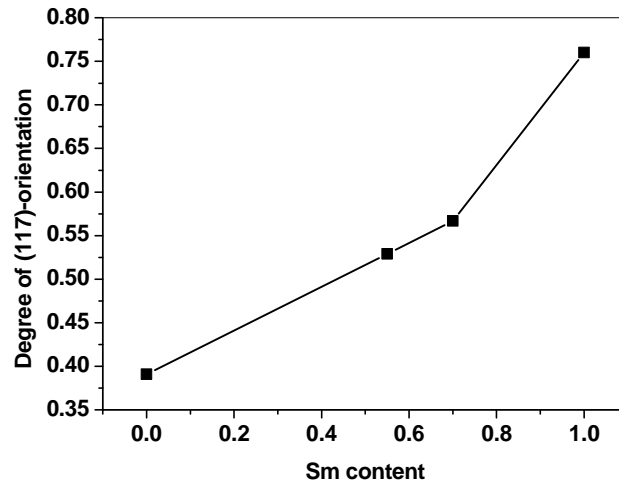


Fig. 6.19 Sm content, x , dependence of the degree of (117)-orientation

6.4.2.2 AFM studies

Fig. 6.20 shows the AFM images of the films with different Sm content (the image of the film with $x = 0$ was unavailable). The images reveal that with increasing Sm content from 0.55 to 1.00, the grain size of the film decreases, with an accompanying a decrease in surface roughness.

6.4.2.3 Raman spectroscopy

Fig. 6.21 shows the Raman spectra of $\text{Bi}_{4-x}\text{Sm}_x\text{Ti}_3\text{O}_{12}$ with $x = 0, 0.55, 0.70, 1.00$. The spectra show a series of modes around 230, 270, 320, 560, and 850 cm^{-1} . Raman features in the figure are similar to those reported by Melgarejo *et al.*¹⁵ for BNdT films and Tomar *et al.*¹⁶ for BLaT films.

Table 6.4 shows a comparison of typical mode frequencies at room temperature for different doping content. To clearly show the contrast between them, a detailed figure is shown as Fig. 6.22.

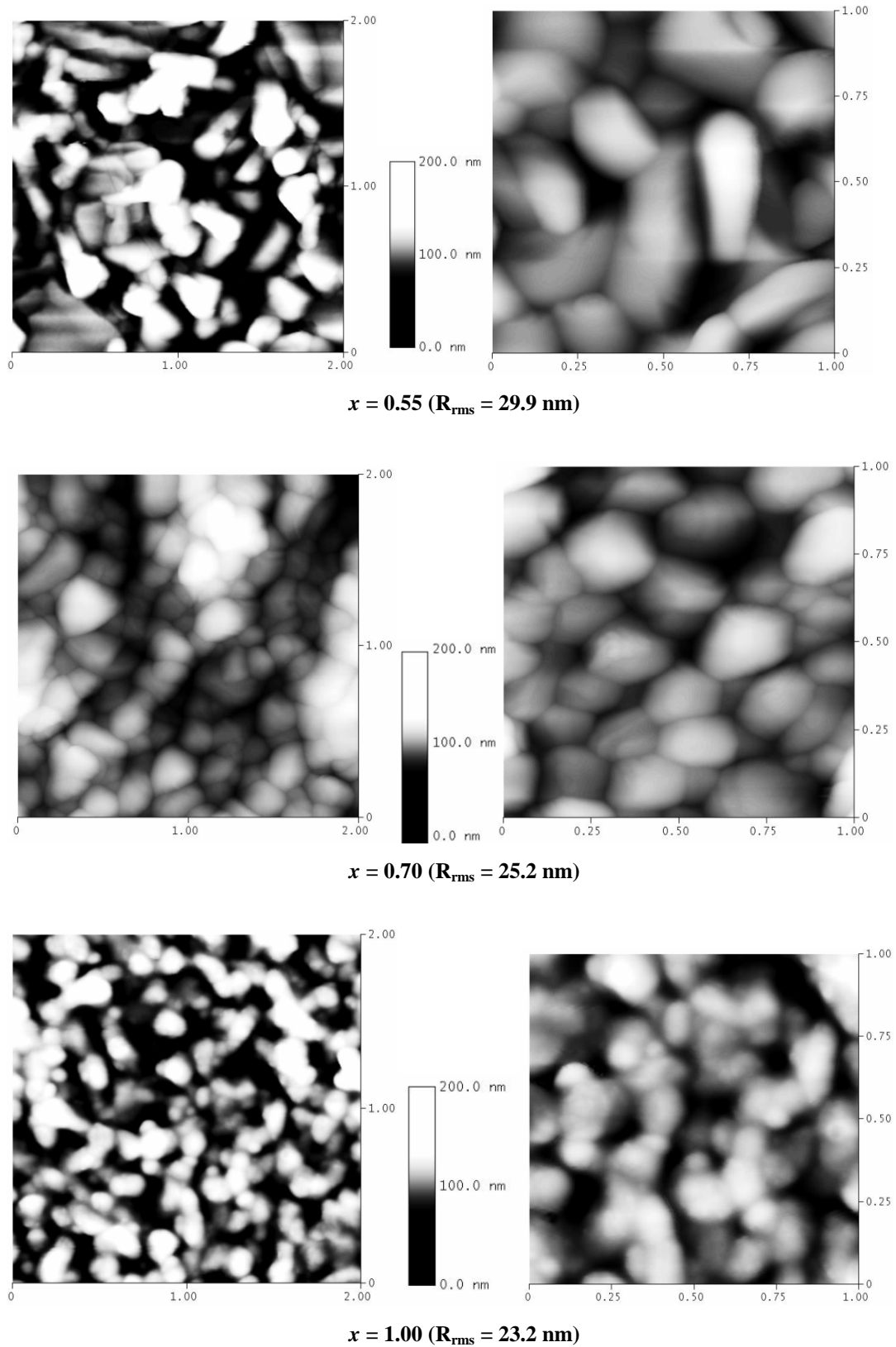


Fig. 6.20 AFM images of the films with different Sm content

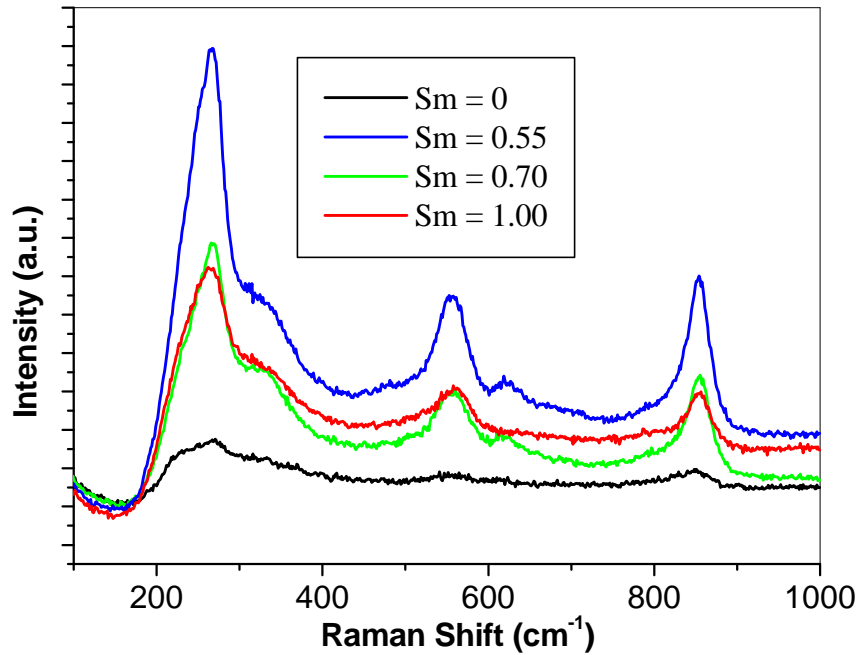


Fig. 6.21 Raman spectra of $\text{Bi}_{4-x}\text{Sm}_x\text{Ti}_3\text{O}_{12}$ with $x = 0, 0.55, 0.70, 1.00$

Table 6.4 Comparison of typical mode frequencies at room temperature

x	ν_6	ν_5	ν_4	ν_1	ν_2
0	231.8	270.5	324.8	555.8	850.7
0.55	-	267.0	325.4	556.1	854.2
0.70	-	265.8	327.6	561.1	855.4
1.00	-	262.3	332.3	562.3	856.6

A perfect TiO_6 octahedron has six Raman modes of ν_1 - ν_6 where ν_1 and ν_2 are bond stretching vibrations, ν_3 and ν_4 are a combination of stretching and bending vibrations and ν_5 and ν_6 are internal angle bending vibrations.¹⁷ Mode ν_6 is Raman inactive when the symmetry of the TiO_6 octahedron is O_h , but it becomes Raman active when distortion occurs in the TiO_6 octahedron. Based on the work of Kojima *et al.*¹⁷, we assigned the peaks at 231.8, 270.5, and 324.8 cm^{-1} in the undoped BiT film as the modes ν_6 , ν_5 , and ν_4 , respectively. Due to the limitation of the equipment, modes of

frequencies lower than 200 cm^{-1} could not be measured. The 560 cm^{-1} mode (ν_1) is attributed to a combination of stretching and bending of TiO_6 octahedra, whilst the 850 cm^{-1} mode (ν_2) is a pure stretching mode of TiO_6 .

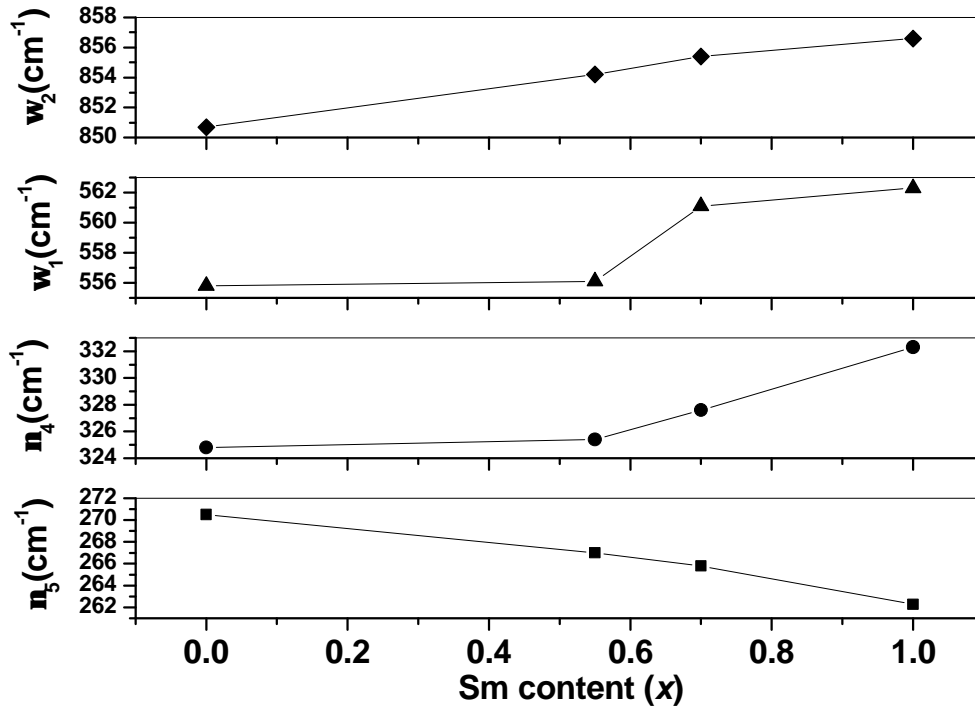


Fig. 6.22 Sm content, x , dependence of the Raman mode frequencies

We can see that the ν_6 mode (around 230 cm^{-1}) exists in the undoped BiT film, and becomes Raman inactive for Sm doped BiT films, which suggests that the symmetry of TiO_6 octahedron approaches O_h upon Sm substitution, attributable to the substitution of the electronically active Bi^{3+} ion with the electronically inactive Sm^{3+} ion. A similar phenomenon has been reported in BLaT films by Yau *et al.*¹⁸ They found that with increasing La content, the intensity of the ν_6 mode decreases and almost becomes Raman inactive between $x = 0.1$ and $x = 0.3$, since we only have four doping levels for our study, we can not clearly observe this transition. A study on undoped BiT and La-doped BiT films by Tomar *et al.*¹⁶ also showed the

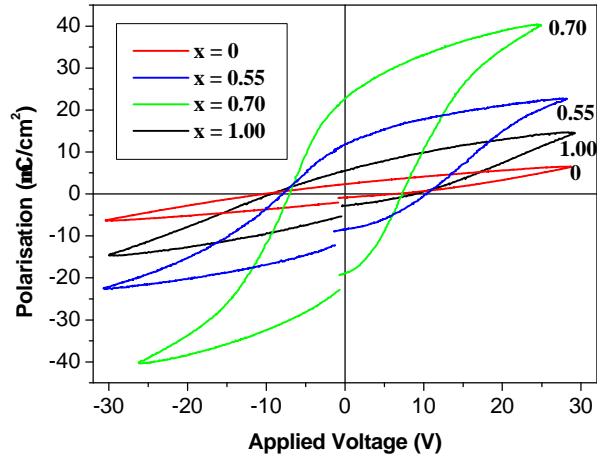
disappearance of the 230 cm^{-1} mode for La-doped films.

In Fig. 6.22, the pure bending mode (850 cm^{-1}) and the combination of the stretching and bending mode (560 cm^{-1}) both show changes in modeshift (upshift) with increasing Sm content, which reflect the change in O-Ti-O bending and stretching vibrations. The mode upshift suggests a decrease in distortion and increase in O_h symmetry of TiO_6 , as also partly suggested in the disappearance of ν_6 mode. Cohen¹⁹ discussed the origination of ferroelectricity in TiO_6 containing ferroelectrics and suggested that Ti-O hybridisation inside the TiO_6 is essential for ferroelectricity and can also cause a structural distortion of TiO_6 due to the Ti displacement towards one of the six oxygen atoms.¹⁹ Since Sm is electronically less active than Bi, and TiO_6 symmetry increases and distortion decreases with Sm addition, a decrease in Ti-O hybridisation is implied, which therefore may decrease the polarisation.

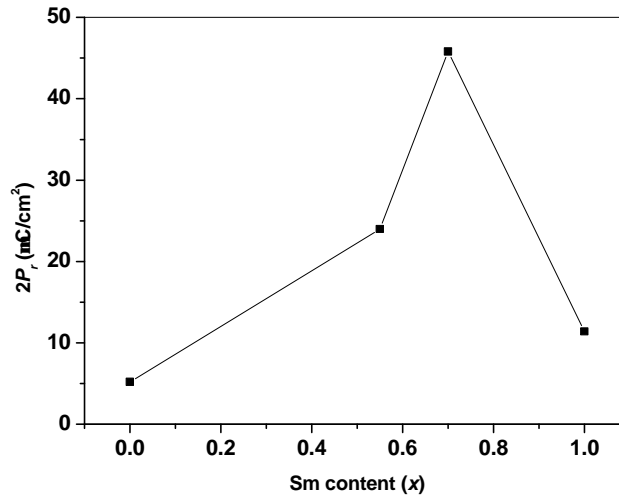
6.4.3 Electrical properties

6.4.3.1 Ferroelectric properties

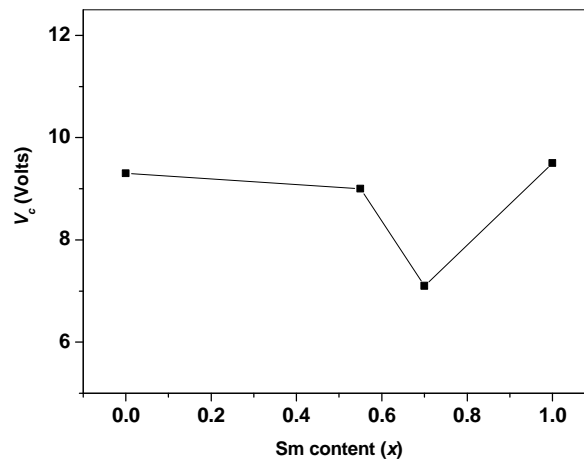
Fig. 6.23 shows ferroelectric hysteresis loops and the Sm content dependence of the $2P_r$ and V_c of the films. With the increase of Sm doping level, the $2P_r$ values increase from $5.4\text{ }\mu\text{C}/\text{cm}^2$ for undoped BiT film, to $24.0\text{ }\mu\text{C}/\text{cm}^2$ for $x = 0.55$, and then peaks at $x = 0.70$ ($45.6\text{ }\mu\text{C}/\text{cm}^2$). The $2P_r$ value decreases beyond $x = 0.70$ and shows a value of $11.4\text{ }\mu\text{C}/\text{cm}^2$ at $x = 1.00$. The V_c value shows similar tendency, which decreases first and then increase beyond $x = 0.70$.



(a)



(b)



(c)

Fig. 6.23 (a) Hysteresis loops; Sm content dependence of (b) $2P_r$ and (c) V_c of the films

6.4.3.2 Dielectric properties

The measurement of capacitance and dissipation factor ($\tan d$) values can give us more information about the polarisation in the films. The capacitance value increases with the increasing doping content and peaked at $x = 0.70$. It then decreases beyond $x = 0.70$, as shown in Fig. 6.24.

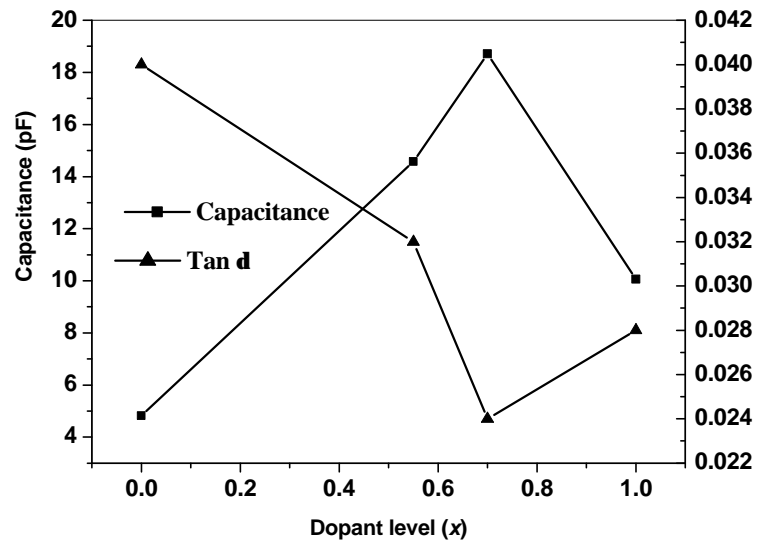


Fig. 6.24 Sm content dependence of the capacitance and dissipation factor of the films

6.4.3.3 Leakage current properties

Fig. 6.25 shows the leakage current density of the films with $x = 0$ and 0.55, which clearly denotes that the Sm doping decreased the leakage current density. That suggests that the Sm substitution is effective in reducing leakage current.

6.4.3.4 Electrical fatigue properties

Fig. 6.26 shows the fatigue properties of BSmT films with $x = 0.55, 0.70, 1.00$, measured with 1 MHz pulses (The film with $x = 0.0$ fatigues quickly after 1×10^7 cycles and the figure is not shown here). The films hardly fatigued, which suggests

that the Sm doping can improve the fatigue resistance of the BiT films.

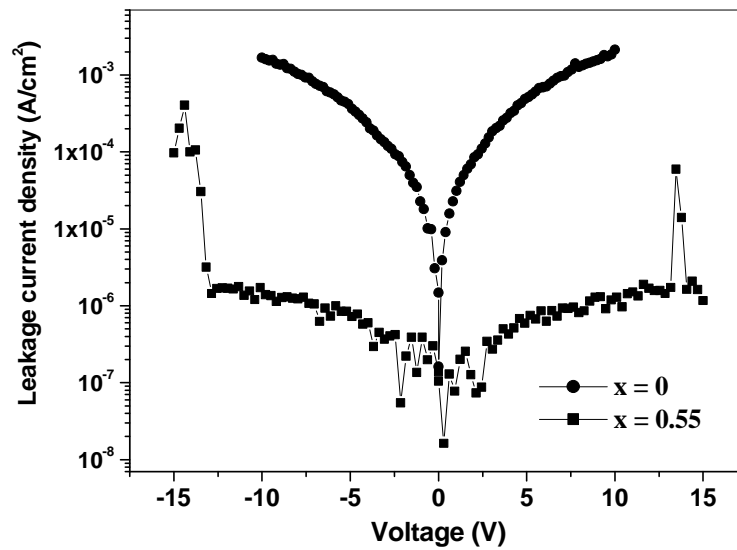


Fig. 6.25 Leakage current density of the films with $x = 0$ and 0.55

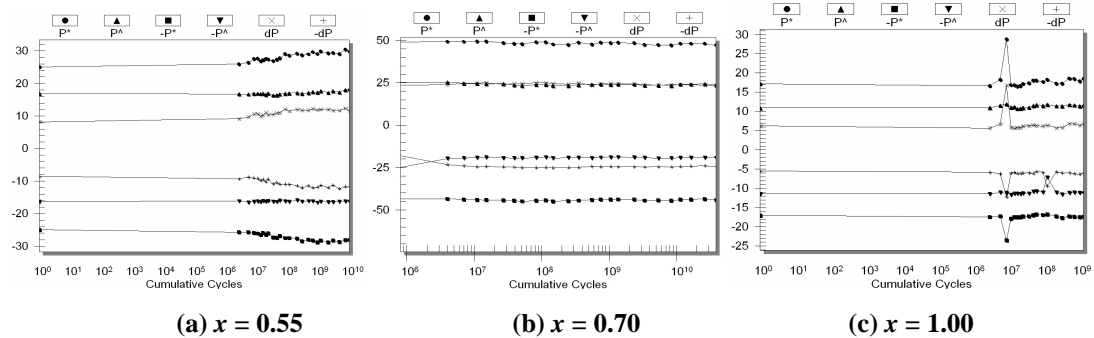


Fig. 6.26 Fatigue property of BSmT films with various Sm contents

6.4.4 Discussion and conclusions

The inclusion of Sm^{3+} in the perovskite block is expected to influence the structural and electrical properties of BiT films in several ways, as discussed below.

First, the introduction of Sm is likely to suppress the spontaneous polarisation value of the BiT films, and similar effect was reported in Sm-doped BiT ceramics.²⁰ The measurement of the intrinsic spontaneous polarisation can only be possible by the

fabrication of single crystal samples, since these will not be affected by the orientations of grains and strains, *etc.* However, the Sm doped BiT single crystal has not yet been prepared. Because of the similarity of La, Nd, and Sm, the results of La and Nd-doped BiT can give some similar suggestions on Sm-doped samples. Soga *et al.* prepared single crystal BiT and BLaT and measured the polarisation along $a(b)$ -axis of both samples, as shown in Fig. 6.27.²¹ This suggested that the doping of lanthanide elements may actually reduce the polarisation of BiT due to smaller ionic displacements along the a -axis. In another report, spontaneous polarisation of BLaT was estimated from epitaxially grown thin films by Sakai *et al.*²² In their study, the La-doped BiT films have a smaller remanent polarisation than undoped BiT films. We can expect that the measurements of polarisation on single crystal and epitaxial films were much closer to the theoretical values than the polycrystalline films with mixed-oriented grains. It can also be easily reflected by the reduction of the Curie temperature of the doped samples in single-crystal²¹ and ceramic²³ forms.

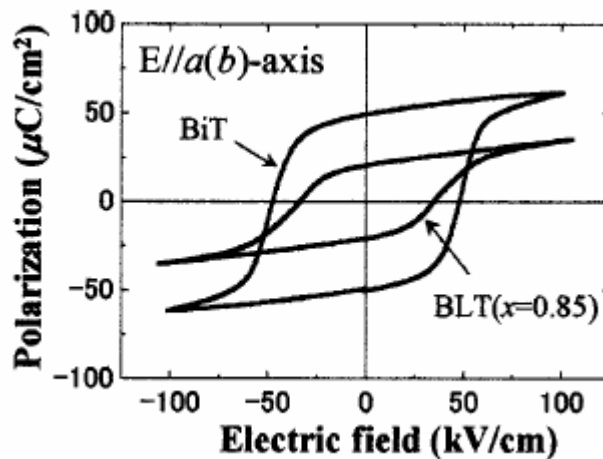


Fig. 6.27 Polarisation hysteresis loops for BiT and BLaT ($x = 0.85$) single crystals along the $a(b)$ axis measured at 25 °C²¹

Second, in polycrystalline films, the introduction of Sm suppresses the dominant

c-axis growth, as shown in XRD patterns of the films (Figs. 6.20 and 6.21). It is known that the polarisation is along *a/b*-axis instead of *c*-axis in BiT films and there were several reports that the *c*-axis oriented films have poor polarisation value as compared to the *a*- or *b*-axis oriented films.^{24,25,26,27} In this case, the enhancement of ferroelectric properties may be due to the preferred growth direction: the polarisation can be easily seen by the applied electric field through the film thickness.

Third, pinning of the domain wall motion is also one of the factors which affects ferroelectric properties. Defect complexes are widely known as pinning centres in oxide ferroelectrics^{28,29} and doping of lanthanide elements can suppress these, as suggested by the decrease of leakage current density, as shown in Fig. 6.25.

Combining the above analysis, we can see that from the Raman spectra, the intrinsic ferroelectricity within TiO₆ blocks may be reduced by the increased symmetry and decreased distortion in the TiO₆ octahedron, therefore, a decrease in Ti-O hybridisation and the resulting decrease in polarisation are expected. However, the increase in $2P_r$ with increasing Sm content may imply that the extrinsic effect, which is the crystallographic orientation of the films, dominates the ferroelectric properties. Although increasing Sm content decreases T_c ,²⁰ the preferential orientation closer to the polar axis (*a/b*-axis) favours the increase of $2P_r$. Beyond a certain doping level, the increase in the crystallographic orientation to *a/b*-axis cannot compensate for the decrease in intrinsic polarisation, resulting in the decrease of $2P_r$ after $x = 0.70$.

The decreased leakage current density suggests that the doping also reduces the defect complexes or oxygen vacancies. Therefore, the Bi in the A site become more stable than the undoped BiT, resulting in the reduction in dissipation factor and improved fatigue resistance.¹⁴ An alternative explanation is that the reduction in the oxygen

vacancy-related domain-pinning improves the fatigue resistance.^{30,28,31}

6.5 Effect of LaNiO₃ (LNO) buffer layer

6.5.1 Motivation

For BLSF thin films, bismuth volatility during high temperature annealing is a major drawback. A large number of studies aimed at overcoming this major problem have been carried out in one of the BLSF films, SBT, by growing SBT thin films on conducting oxide electrodes^{32,33,34,35}. Previously, the existence of metallic bismuth in the SBT thin films was reported by Scott *et al.*³⁶ According to Scott, metallic Bi might modify the interfacial characteristics of the film, which has a direct influence on the electrical properties of SBT based devices. In theory, thin films on metal electrodes exhibit higher leakage current density in comparison to oxide electrodes.³⁷ Due to the higher crystallisation temperature of bismuth containing ferroelectric thin films and in order to avoid the interdiffusion of Bi into Pt, it is necessary to anneal films at lower processing temperature or to grow films at an interfacial conducting oxide layer between Pt and films without sacrificing its ferroelectric properties. SBT films on LaNiO₃(LNO) electrodes were fabricated by Hu *et al.*³⁵ and a layer of second phase with a thickness of 30 nm was observed at the interface between the SBT thin film and the LNO oxide electrode.

In the previous parts of this chapter, relatively low temperature PLD-grown BSMT films on Pt-coated silicon substrates have been studied and the optimised annealing temperature was 700~750 °C, which was low enough but still relatively high for bismuth-containing ferroelectrics, due to unavoidable bismuth loss and bismuth diffusion into Pt electrodes. In this part, we then adopted LNO, the most attractive

candidate for electrodes in PZT-based ferroelectric memories,³⁸ as an interfacial layer to grow BSmT films and compared them to those grown without LNO electrodes.

6.5.2 Experimental details

BSmT and LNO films were grown by PLD using a multi-target process. LNO oxide electrodes of ~50 nm thickness were grown on commercial Pt/TiO_x/SiO₂/Si substrates at a substrate temperature of ~750 °C and an oxygen pressure of 13 Pa. The details of the parameters for depositing BSmT films were shown in Section 6.2.1 (For this film, target composition: Bi_{3.63}Sm_{0.70}Ti₃O₁₂; total number of pulses: 4000; pulse energy per spot: 225 mJ; deposition and annealing temperature: 750 °C). BSmT films deposited in the same deposition run with LNO electrodes (BSmT/LNO/Pt) and without LNO electrodes (BSmT/Pt) were measured for comparison. Film thickness of BSmT was determined by FE-SEM (~ 310 nm)

6.5.3 Results and discussion

6.5.3.1 AFM studies

AFM was used to analyse the influence of the LNO buffer layer on the surface topography of BSmT films, and typical AFM images of BSmT films grown on Pt and LNO are shown in Fig. 6.28. It was observed from the microstructure that the bottom electrodes directly influenced the grain size and the root mean square (RMS) surface roughness of the films. The films grown directly on Pt have larger grains (~200 nm) and intergranular regions filled with finer grains of ~100 nm. However, films grown with the LNO layer have a smaller grain size (~150 nm) and are surrounded by finer grains of ~25 nm. The RMS surface roughness of the BSmT/Pt and BSmT/LNO/Pt films was ~9.7 nm and ~14.8 nm, respectively.

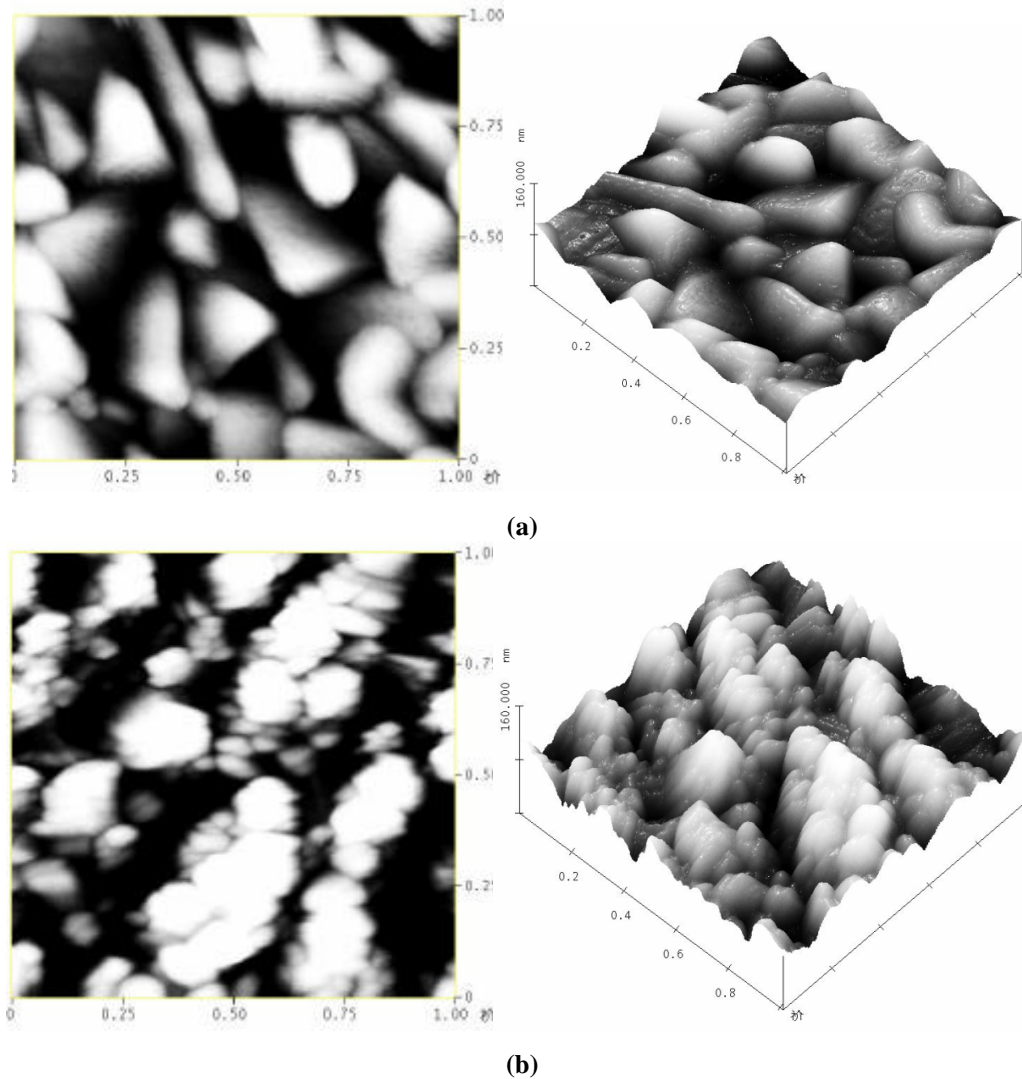


Fig. 6.28 AFM images of (a) BSmT/Pt films; (b) BSmT/LNO/Pt films

6.5.3.2 Ferroelectric properties

Ferroelectric hysteresis characteristics of BSmT films grown without and with LNO layer are shown in Fig. 6.29. Thin films of BSmT/Pt exhibit a $2P_r$ of $\sim 50 \mu\text{C}/\text{cm}^2$ and a V_c of $\sim 3.0 \text{ V}$ (E_c : $97 \text{ kV}/\text{cm}$ for $\sim 310 \text{ nm}$ -thick film). However, BSmT films on the LNO buffer layer showed degradation of the ferroelectric characteristics and exhibited a $2P_r$ of $\sim 14 \mu\text{C}/\text{cm}^2$ and V_c of $\sim 4.5 \text{ V}$ (E_c : $\sim 145 \text{ kV}/\text{cm}$). The degradation of polarisation with the LNO buffer layer has been explained as due to the formation of oxygen vacancy related defect dipoles at the interface, which might lead to poor ferroelectric properties.³⁵ A TEM study may be able to clarify which effect dominates.

Another possible reason could be the series resistance effect of the interfacial layer between the oxide electrode and BSmT films, which is due to the diffusion of Ni into the BSmT film and then formation of a thin resistive layer. Hu *et al.*³⁵ reported a layer of second phase with a thickness of 30 nm at the interface between an SBT thin film and a LNO oxide electrode, examined by TEM. They also observed a strong reduction in dielectric constant of SBT/LNO/Pt films, due to the formation of a low dielectric constant layer at the interface. This explanation might be also applicable to our results.

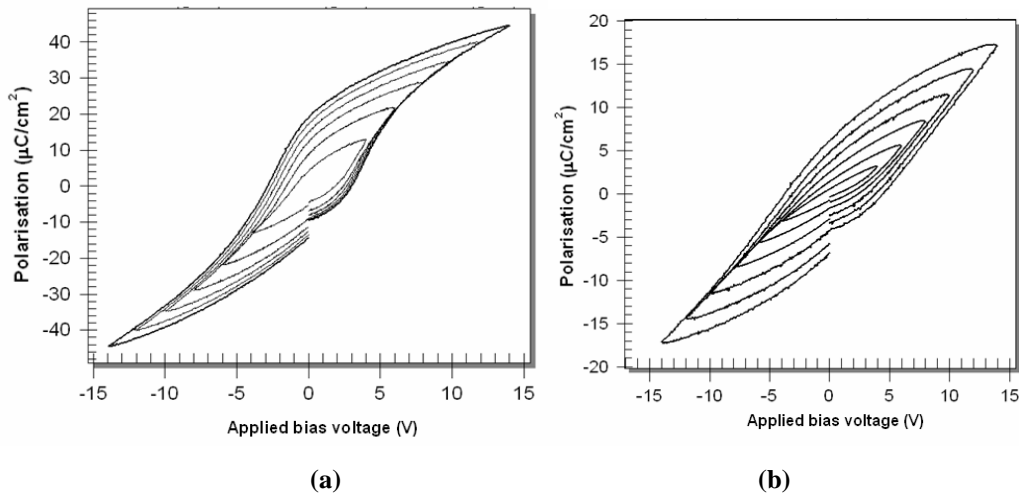


Fig. 6.29 Ferroelectric hysteresis loops of (a) BSmT/Pt; (b) BSmT/LNO/Pt films

Degradations of ferroelectric properties were also observed by Hu *et al.*³⁵ on SBT films. In their study, a small value of P_r could not be explained by their XRD data, thus, they also attributed this to the formation of the low dielectric constant layer at the interface.

The difference between their and our results is the V_c . In our study, the increase of V_c was observed in BSmT/LNO films instead of a reduction as reported by Hu *et al.*³⁵ in SBT/LNO films. Since the V_c is dependent on the energy required for the domain nucleation and domain wall movement, which is related to the pinning status of domain walls by the trapped charges formed at the interface and grain boundaries,

therefore, for the BSmT thin film deposited on the LNO electrode, the traps of the space charges in the second phase formed at the interface must be deeper than that for the BSmT thin films without the LNO layer, resulting in the larger value of V_c .

6.5.3.3 Leakage current properties

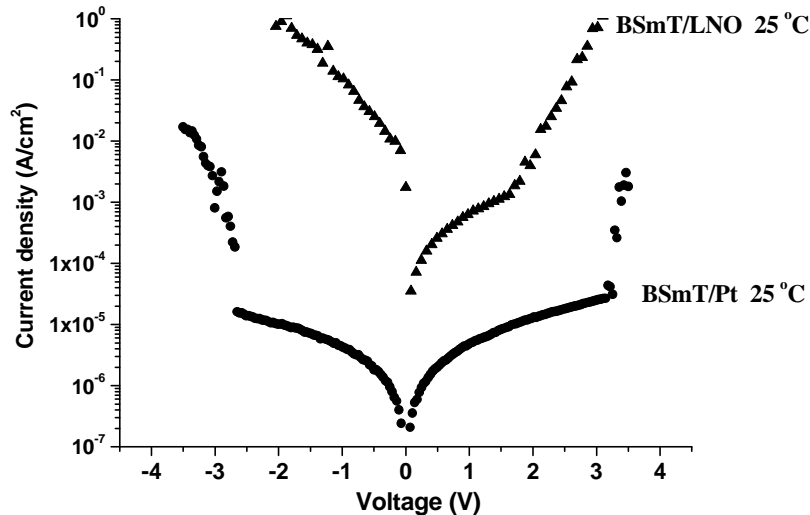


Fig. 6.30 Leakage current characteristics of BSmT/Pt and BSmT/LNO films

The J - V characteristics of the films were measured at room temperature and it was observed that the BSmT/Pt film has a much lower leakage current density ($\sim 10^{-5}$ A/cm² at 50 kV/cm) than that of BSmT/LNO films ($\sim 10^{-3}$ A/cm² at 50 kV/cm), as shown in Fig. 6.30.

The smaller leakage current (and the larger breakdown field) may be due to larger energy barrier of BSmT/Pt than that of BSmT/LNO. The values of barrier height between the film and the electrode estimated by Das *et al.*³⁹ at zero voltage for Pt/SBT/Pt and Pt/SBT/LNO capacitors were 1.27 and 1.12 eV, respectively. The decrease in barrier height with the introduction of the LNO interfacial layer were ascribed to the different work function of LNO or the nature of chemical bonding

between SBT and the LNO electrode.³⁹ In our BSmT/LNO interface, it might be possible that oxygen ions in LNO interact strongly with other oxygen ions and cations in BSmT, which changes the interfacial potential and results in a smaller barrier height. Another possible reason is that the higher leakage current may be caused by the higher surface roughness of the BSmT films on LNO electrode. Similar results were reported in SBT films³² and Ce-doped BiT films.⁴⁰

6.6 References

- 1 M. Grasserbauer and H. W. Werner, *Analysis of microelectronic materials and devices*. (John Wiley and Sons, Chichester, 1991).
- 2 Y. Shichi, S. Tanimoto, T. Goto, K. Kuroiwa, and Y. Tarui, *Japanese Journal of Applied Physics* **33**, 5172 (1994).
- 3 C. H. Liu and J. M. Wu, *Electrochemical and Solid State Letters* **9**, G23 (2006).
- 4 S. Y. Wu, *Ferroelectrics* **11**, 379 (1976).
- 5 M. Alexe, *Applied Physics Letters* **72**, 2283 (1998).
- 6 A. Q. Jiang, Z. X. Hu, and L. D. Zhang, *Journal of Applied Physics* **85**, 1739 (1999).
- 7 M. Toyoda, Y. Hamaji, K. Tomono, and D. A. Payne, *Japanese Journal of Applied Physics Part 1-Regular Papers Short Notes & Review Papers* **32**, 4158 (1993).
- 8 I. Radosavljevic, J. S. Evans, and A. W. Slight, *Journal of Solid State Chemistry* **136**, 63 (1998).
- 9 S. Kojima, A. Hushur, F. Jiang, S. Hamazaki, M. Takashige, M. S. Jang, and S. Shimada, *Journal of Non-Crystalline Solids* **293**, 250 (2001).
- 10 F. K. Lotgering, *Journal of Inorganic and Nuclear Chemistry* **9**, 113 (1959).
- 11 U. Chon, K. B. Kim, H. M. Jang, and G. C. Yi, *Applied Physics Letters* **79**, 3137 (2001).
- 12 T. Kojima, T. Sakai, T. Watanabe, H. Funakubo, K. Saito, and M. Osada, *Applied Physics Letters* **80**, 2746 (2002).
- 13 X. Wang and X. Yao, *Ferroelectrics Letters Section* **13**, 47 (1991).
- 14 B. H. Park, B. S. Kang, S. D. Bu, T. W. Noh, J. Lee, and W. Jo, *Nature* **401**, 682 (1999).
- 15 R. E. Melgarejo, M. S. Tomar, S. Bhaskar, P. S. Dobal, and R. S. Katiyar, *Applied Physics Letters* **81**, 2611 (2002).
- 16 M. S. Tomar, R. E. Melgarejo, A. Hidalgo, S. B. Mazumder, and R. S. Katiyar, *Applied Physics Letters* **83**, 341 (2003).

- 17 S. Kojima, R. Imaizumi, S. Hamazaki, and M. Takashige, *Japanese Journal of Applied Physics Part 1-Regular Papers Short Notes & Review Papers* **33**, 5559 (1994).
- 18 C. Y. Yau, R. Palan, K. Tran, and R. C. Buchanan, *Applied Physics Letters* **86**, art. no. 032907 (2005).
- 19 R. E. Cohen, *Nature (London)* **358**, 136 (1992).
- 20 O. AlvarezFregoso, *Journal of Applied Physics* **81**, 1387 (1997).
- 21 M. Soga, Y. Noguchi, M. Miyayama, H. Okino, and T. Yamamoto, *Applied Physics Letters* **84**, 100 (2004).
- 22 T. Sakai, T. Watanabe, H. Funakubo, K. Saito, and M. Osada, *Japanese Journal of Applied Physics Part 1-Regular Papers Short Notes & Review Papers* **42**, 166 (2003).
- 23 X. B. Chen, R. Hui, J. Zhu, W. P. Lu, and X. Y. Mao, *Journal of Applied Physics* **96**, 5697 (2004).
- 24 T. Watanabe, T. Kojima, H. Uchida, I. Okada, and H. Funakubo, *Japanese Journal of Applied Physics Part 2-Letters* **43**, L309 (2004).
- 25 H. Matsuda, S. Ito, and T. Iijima, *Applied Physics Letters* **83**, 5023 (2003).
- 26 A. Garg, A. Snedden, P. Lightfoot, X. Hu, J. F. Scott, and Z. H. Barber, *Ferroelectrics* **313**, 15 (2004).
- 27 A. Garg, A. Snedden, P. Lightfoot, J. F. Scott, X. Hu, and Z. H. Barber, *Journal of Applied Physics* **96**, 3408 (2004).
- 28 Y. Noguchi and M. Miyayama, *Applied Physics Letters* **78**, 1903 (2001).
- 29 Q. Tan, J. Li, and D. Viehland, *Applied Physics Letters* **75**, 418 (1999).
- 30 Y. Shimakawa, Y. Kubo, Y. Tauchi, H. Asano, T. Kamiyama, F. Izumi, and Z. Hiroi, *Applied Physics Letters* **79**, 2991 (2001).
- 31 H. N. Lee, D. Hesse, N. Zakharov, and U. Gosele, *Science* **296**, 2006 (2002).
- 32 R. R. Das, P. Bhattacharya, W. Perez, R. S. Katiyar, and S. B. Desu, *Applied Physics Letters* **80**, 637 (2002).
- 33 R. R. Das, P. Bhattacharya, W. Perez, and R. S. Katiyar, *Applied Physics Letters* **81**, 4052 (2002).
- 34 W. C. Shin, K. J. Choi, N. J. Seong, E. S. Choi, B. H. Kim, and S. G. Yoon, *Chemical Vapor Deposition* **8**, 221 (2002).
- 35 G. D. Hu, I. H. Wilson, J. B. Xu, C. P. Li, and S. P. Wong, *Applied Physics Letters* **76**, 1758 (2000).

- ³⁶ J. F. Scott, M. Alexe, N. D. Zakharov, A. Pignolet, C. Curran, and D. Hesse, *Integrated Ferroelectrics* **21**, 1 (1998).
- ³⁷ C. S. Hwang, B. T. Lee, C. S. Kang, J. W. Kim, K. H. Lee, and H. J. Cho, *Journal of Applied Physics* **83**, 3703 (1998).
- ³⁸ M. S. Chen, T. B. Wu, and J. M. Wu, *Applied Physics Letters* **68**, 1430 (1996).
- ³⁹ R. R. Das, P. Bhattacharya, R. S. Katiyar, and A. S. Bhalla, *Journal of Applied Physics* **92**, 6160 (2002).
- ⁴⁰ K. T. Kim, C. I. Kim, D. H. Kang, and I. W. Shim, *Journal of Vacuum Science & Technology A* **21**, 1376 (2003).

Chapter 7 CSD-derived Sm- and Nd-doped bismuth titanate polycrystalline ferroelectric thin films

7.1 Background

BLSF thin films have been fabricated using several techniques, which include MOCVD,^{1,2,3} sputtering,^{4,5} PLD,^{6,7,8} and CSD.^{9,10,11,12,13} Among the methods, CSD has been extensively employed in the past few years, including sol-gel process^{9,10,11} and metalorganic deposition (MOD)^{12,13}. It has several advantages of accurate composition control which is very important for multicomponent systems, ease of process integration with standard semiconductor manufacturing technology and relatively low costs.

Among the reports on CSD method to fabricate BLnT thin film, it can be found that metal alkoxide compounds are used as Bi, Ln (La, Sm, Nd), and Ti sources.^{14,15,16} BLnT films deposited by sol-gel and metalorganic solution growth techniques are generally polycrystalline, fine grained and often with segregated metallic Bi, necessitating 750 °C processing for improvement of film properties. When starting materials of multicomponent systems are all metal alkoxide precursors,^{17,18} the system will be so susceptible to ambient humidity that it should be handled under an inert atmosphere. Inorganic and organic salts have been used for CSD processing of multicomponent systems when it is difficult or unnecessary to use alkoxides, such as under humid ambient.¹⁹

In the present study, we successfully used nitrates to introduce bismuth and

samarium/neodymium instead of alkoxides as precursor materials to make a stable Bi-Sm(Nd)-Ti solution, which was insensitive to water and could be stable for more than eight months at room temperature. We investigated the condensation polymerisation and crystallisation behaviours of BSmT thin films during the baking and annealing stages by Fourier transform infrared spectroscopy (FT-IR), Raman spectroscopy, and XRD. We also characterised the structural and electrical properties of the Sm and Nd-doped BiT films.

7.2 CSD-derived BSmT films

7.2.1 Experimental results

7.2.1.1 Characterisation of precursors: *in-situ* FT-IR study

FT-IR can conveniently characterise structural changes that occur in the sol-gel process during the conversions from sol to gel and then to crystalline phase. *In-situ* FT-IR results of the precursor solution from room temperature to 300 °C are shown in Fig. 7.1. There are several peaks in the FT-IR spectrum of the Bi-Sm-Ti sol at 25 °C, which are ~735, ~815, ~880, ~1025, ~1335, ~1430, ~1520, ~1635, and ~3400 cm⁻¹. The peak around ~3400 cm⁻¹, corresponding to the vibration of O-H, decreases with increasing temperature and disappears around 100 °C, indicating evaporation of water. The peak of ~1335 cm⁻¹, corresponding to the stretching vibrations of the alkyl CH₃,²⁰ decreases with increasing temperature and disappears around 230 °C. The absorptions at ~1520 and ~1430 cm⁻¹ are assignable to asymmetric and symmetric ν_{COO} vibrations, respectively²¹. It should be noted that the asymmetric vibration of ν_{COO} shifted from ~1765 cm⁻¹ (in pure acetic acid, not shown here) to ~1520 cm⁻¹, which indicates that stable titanium alkoxo-acylates actually forms when mixing with acetic acid.²² The

peaks disappear with increasing temperature around 100 °C, indicating the evaporation of the acetic acid with the increase in temperature.

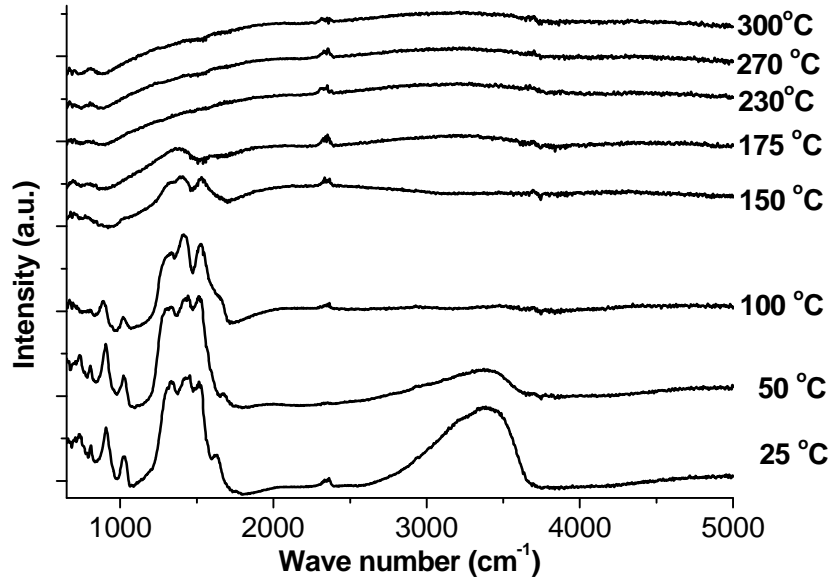
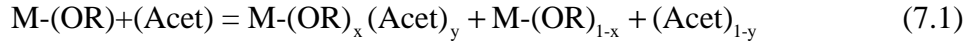


Fig. 7.1 FT-IR spectra of the Bi-Sm-Ti solutions at different temperatures

The acetic acid serves as chelating agent to improve the homogeneity of the precursor solution by generating a highly dense and homogeneous Ti-O-Ti polymeric network. Peaks at $\sim 1630\text{ cm}^{-1}$ are due to $\nu_{\text{C=O}}$ vibrations of conjugated carbonyl groups. The peaks around ~ 735 , ~ 810 and $\sim 880\text{ cm}^{-1}$, corresponding to NO_3^- , disappear around 150 °C, indicating the decomposition of bismuth nitrate and samarium nitrate. The amorphous Bi-Sm-Ti gel can be supposed to have a Ti-O-Ti framework with $\text{Bi}(\text{NO}_3)_3$ and $\text{Sm}(\text{NO}_3)_3$ situated in random positions.

The chemistry and homogeneity of the Bi-Sm-Ti solution have a strong influence on the crystallisation temperature of the BSmT thin films. The crystallisation temperature can be reduced by improving the homogeneity of the precursor solution by using a chelating agent such as acetic acid, which reacts chemically with the metal alkoxide,

giving rise to a new type of precursor $Ti(OR)_x(Acet)_y$, as shown in Equation (7.1). The hydrolysis of the precursors is shown in Equations (7.2) and (7.3).



The anions can coordinate in one or more of the modes, shown in Fig. 7.3.

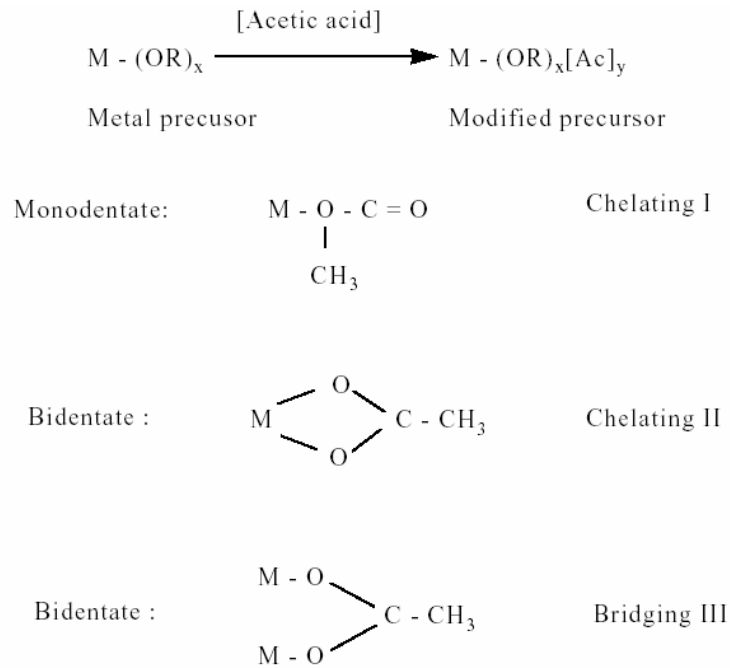


Fig. 7.3 Reaction of acetic acid with precursors

It was observed that most of the acetate groups exist as bridges in nature.^{23,24} There are two kinds of network in this hybrid solution: dense polymeric clusters and lower density polymer constituents. By adding additional acetic acid before hydrolysis steps (this is also why the nitrates should be completely dried before dissolving in acetic acid), a high fraction of the low density polymer constituent reacts with the acetic acid

and forms high density polymeric network, which is very resistive to hydrolysis and condensation. This tendency leads to the polycondensation process, and generates monolithic gels where high mass polymers are preferentially present rather than small colloidal particles. The hydrolysis of alkoxide is shown in (7.4), and condensation of two M-OH groups or reaction of an M-OR with M-OH group is described in (7.5) and (7.6).



Increasing the baking temperature to 300 °C results in the disappearance of most FT-IR vibration peaks, indicating most organic compounds have been evaporated and decomposed. This is analogous to the pre-baking stage of the BSmT film fabrication.

7.2.1.2 Structural properties

1. Raman spectroscopy

In order to study the annealing stage of the films, room temperature micro-Raman spectra for BSmT thin films annealed at different temperatures were measured, as shown in Fig. 7.4. The as-baked film shows a peak around 1040 cm⁻¹ which decreases with increasing temperature and disappears around 550 °C. This probably indicates that a CO₃²⁻ structure forms during this temperature range, after decomposition of Ac⁻. A peak around 570 cm⁻¹ also appears between the temperature range of 350 ~ 500 °C, which indicates an intermediate phase is formed during annealing. The BSmT thin film

annealed at 500 °C maintains an amorphous status. When the annealing temperature reaches 550 °C, broad peaks around ~ 530 and ~ 830 cm^{-1} are found and then disappear with increasing temperature. These correspond to a metastable fluorite phase ($\text{Bi}_2\text{Ti}_2\text{O}_7$), also observed by other researchers.^{25,26,27} Annealing the thin films at higher temperatures results in the perovskite structure, with three peaks at wavenumbers around 261, 553, and 850 cm^{-1} , which are similar to the PLD-grown films reported in Chapter 6. The intensity and sharpness of these three peaks increase with increasing annealing temperature above 600 °C, indicating improvement in crystalline quality of the perovskite structure, which is consistent with the XRD results.

Apart from these three main modes, the 325 cm^{-1} mode (seen as a bump on the right of the 260 cm^{-1} mode), which corresponds to the combination of stretching and bending of the TiO_6 octahedron²⁸, becomes sharper and more distinct with increasing annealing temperature. This change in the TiO_6 modes is most probably due to exaggerations of orthorhombic distortion and octahedral tilting at higher annealing temperature.^{28,29}

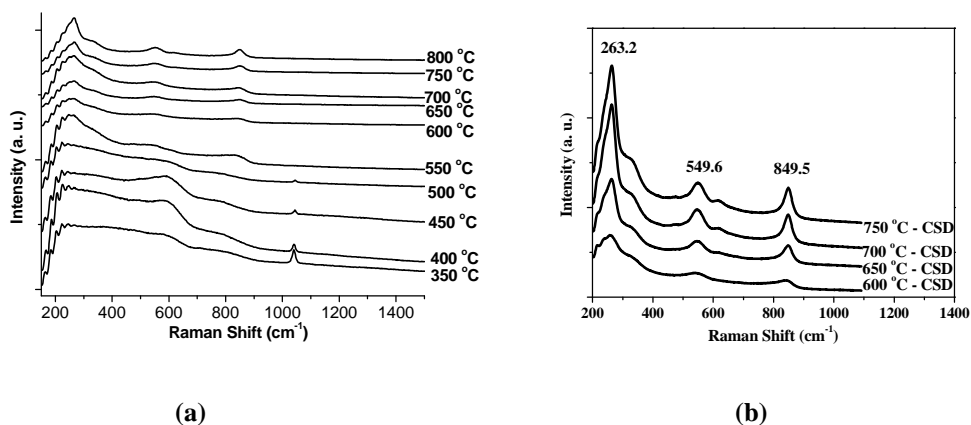


Fig. 7.2 Raman spectra of the films annealed at different temperatures. (a): 350 °C~800 °C; (b): 600 °C~800 °C.

2. XRD studies

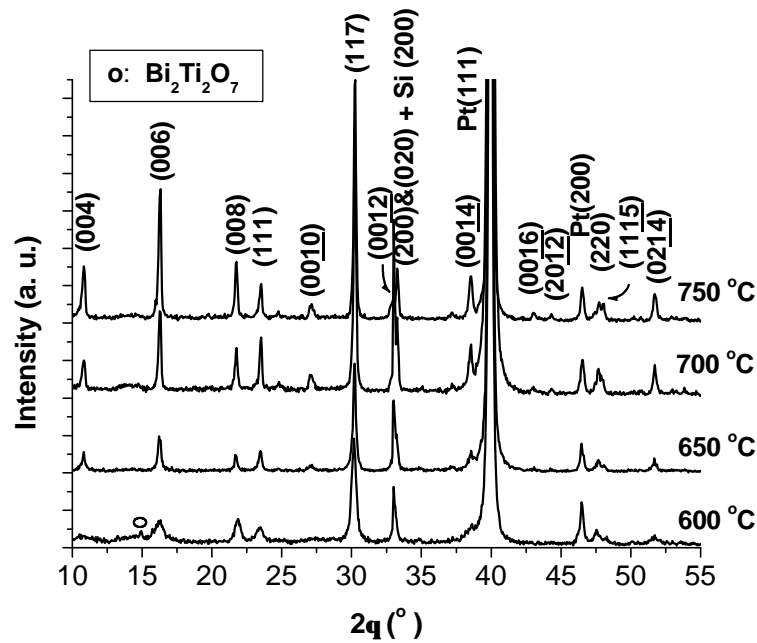


Fig. 7.3 XRD profiles of the films annealed at different temperatures

Fig. 7.3 shows the XRD 2θ patterns of the BSmT films (~ 370 nm thick) annealed for 10 minutes in an oxygen atmosphere at temperatures ranging from 600 °C to 750 °C. It can be seen that, as the annealing temperature increases, the crystallinity of the films improves (the peaks become sharper and more intense). The film annealed at 600 °C shows a fluorite phase at $2\theta \approx 15^\circ$, which was indexed as the $\text{Bi}_2\text{Ti}_2\text{O}_7$ cubic phase (JCPDS Card, 320118), indicating that the fluorite structure exists as an intermediate phase between the amorphous and perovskite phases of BSmT, as previously indicated in Raman spectra. With an increase in the annealing temperature, this fluorite peak disappeared and the peaks of the perovskite phase were enhanced. The perovskite phase was fully formed in films annealed at 650 °C and above and all films have a bismuth-layered structure showing mixed orientations. This result indicates that the Sm^{3+} ions in the BSmT films are incorporated into the

pseudo-perovskite structure, substituting for the Bi ions³⁰. The full width at half maximum (FWHM) of the perovskite phase peaks decreases with increasing annealing temperature (0.64°, 0.27°, 0.20°, 0.19° for peak (006), for films annealed at 600 °C, 650 °C, 700 °C, 750 °C, respectively), suggesting an increase in the grain size.

The degree of the (00*l*)-type preferential growth was determined by Lotgering's orientation factor (Equation (6.1)), as shown in Fig. 7.4. The result suggests that increasing annealing temperature favours the growth of *c*-axis-oriented grains, which was similarly reported from the results of PLD-grown films in Chapter 6.

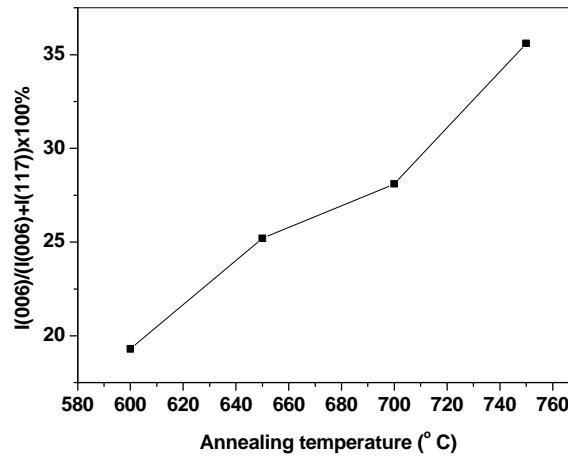


Fig. 7.4 Degrees of (00*l*)-type preferential growth

3. Surface morphology (AFM)

Fig. 7.5 shows AFM micrographs of the BSmT films. The RMS surface roughness ($1 \mu\text{m} \times 1 \mu\text{m}$) increased with increasing annealing temperature: 3.6 nm, 6.0 nm, 9.0 nm, and 11.0 nm, for the films annealed at 600 °C, 650 °C, 700 °C, and 750 °C, respectively. This was accompanied by an increase in grain size of the films, as seen from the AFM images and corroborated by the increase in XRD peak sharpness. The roughness values of the films annealed at 700 °C and 750 °C are comparable to that reported for 300~400 nm-thick (104)-oriented MOCVD-derived BSmT films ($R_{\text{rms}} =$

12.2 nm) annealed at 700 °C.³¹ CSD-derived 200 nm-thick BNdT films prepared at 700 °C have been reported to have a roughness of ~13.0 nm.³² The average lateral feature size of films annealed at 700 °C is ~70 nm.

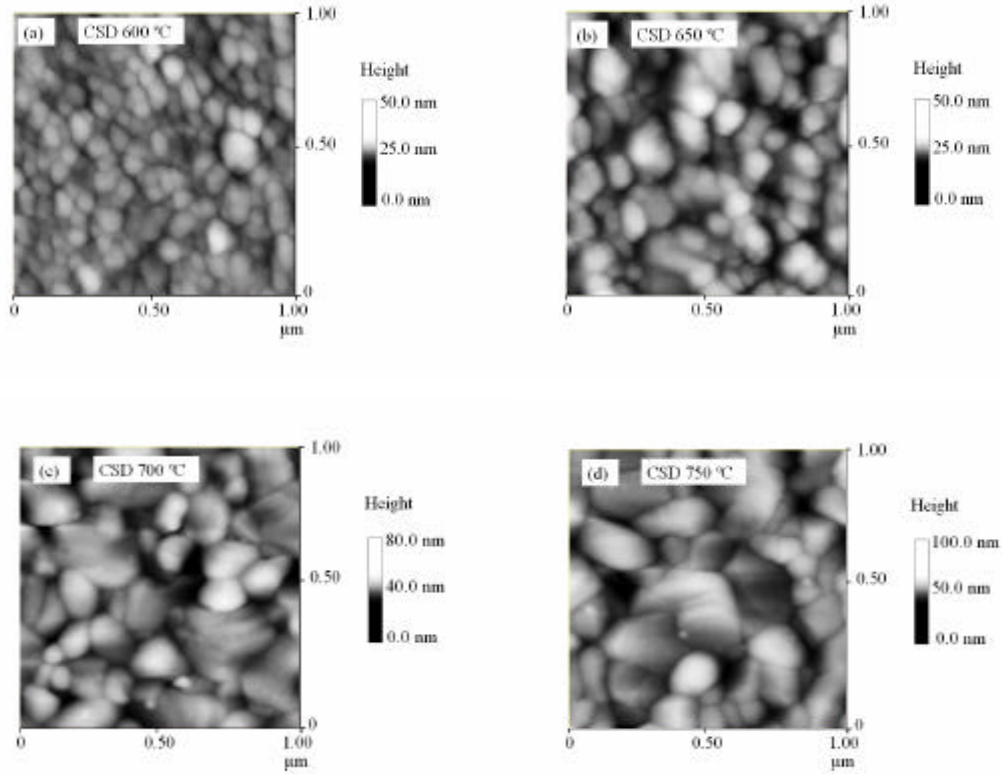


Fig. 7.5 AFM images of the films annealed at different temperatures

4. SEM results

Figs. 7.6(a) and 7.6(b) show FE-SEM images of cross-sections of BSmT films annealed at 700 °C, obtained in SEI and BSEI mode, respectively. Both images demonstrated that they exhibit a clear and sharp boundary between films and Pt bottom electrodes. A different image of larger magnification is also displayed (Fig. 7.6(c)), clearly showing a grainy structure. Fig. 7.7 shows the cross-sectional FE-SEM images of a film annealed at 750 °C, confirming an increase in grain size with a further increase in annealing temperature, but suggesting a slight reduction in density

in the 750 °C-annealed film.

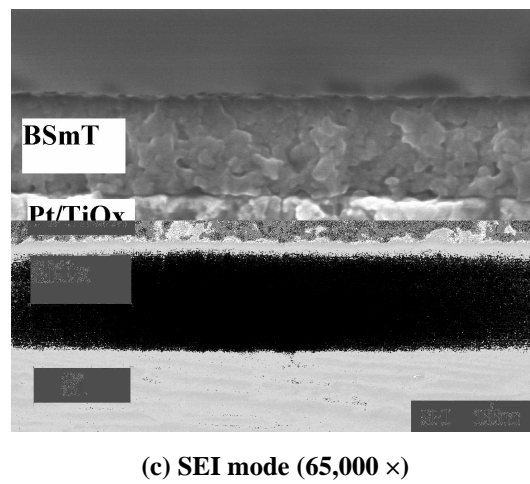
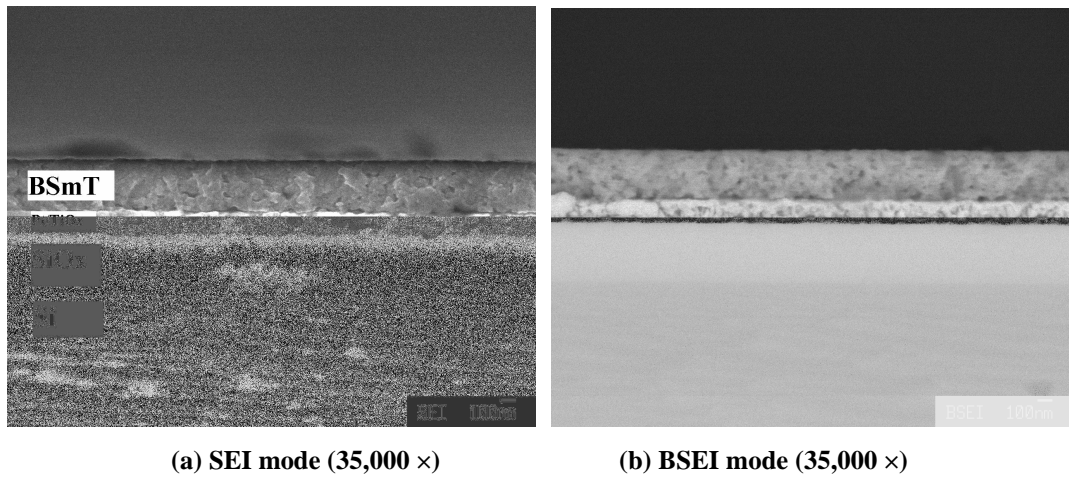


Fig. 7.6 Cross-sectional FE-SEM images of films annealed at 700 °C

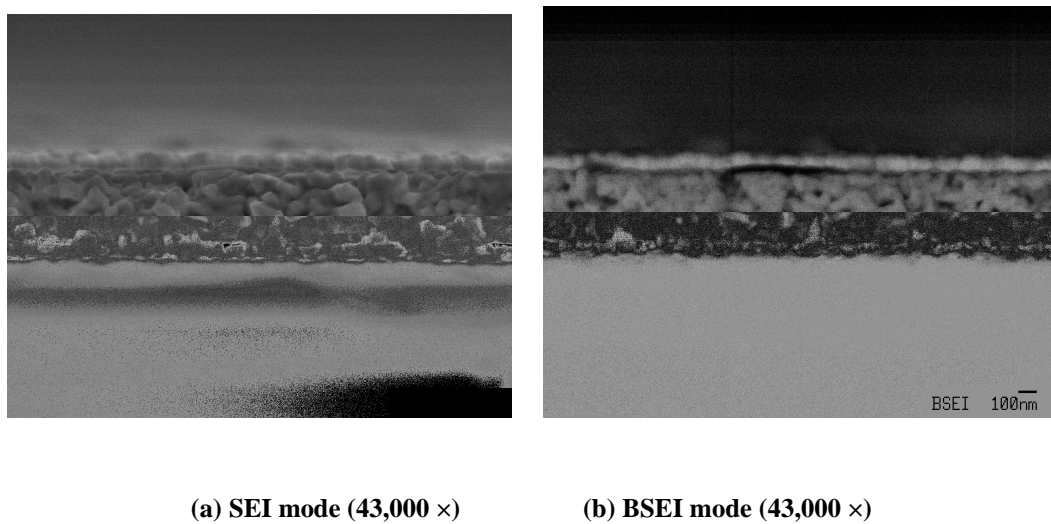


Fig. 7.7 Cross-sectional FE-SEM images of film annealed at 750 °C

For comparison, surface FE-SEM images of the films annealed at 600 °C and 700 °C are shown in Fig. 7.8. Grain growth with increasing annealing temperature is clearly illustrated by these images.

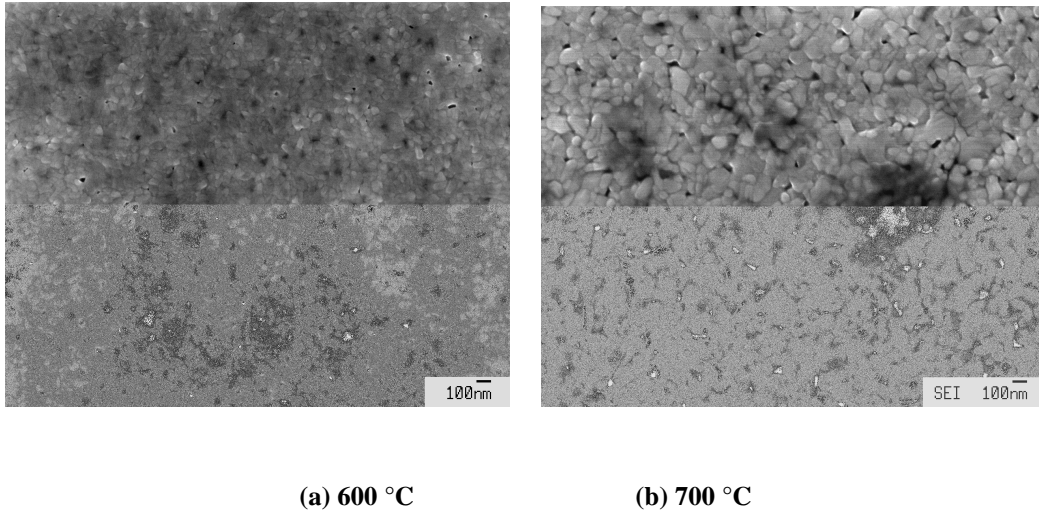


Fig. 7.8 Surface FE-SEM images of the film annealed at different temperatures

Cross-sectional FE-SEM images illustrate that the thickness of the films remain almost the same over this temperature range, suggesting very small shrinkage in film volume during film growth at this temperature range. The average cation ratio determined by EDX was Bi:Sm:Ti = $(4.00-x):x:(2.96\pm 0.05)$, where $x = 0.55\pm 0.04$.

7.2.1.3 Electrical properties

1. Dielectric properties

The dielectric constant (ϵ_r) and dissipation factor ($\tan d$) at room temperature are shown as a function of frequency in Fig. 7.9. The capacitance value measured using different top electrodes varied within less than 3%, indicating a high degree of uniformity in the films. For all films, ϵ_r was relatively unchanged from 10 kHz to 1 MHz (maximum variation: 9%). $\tan d$ values were below 0.030 from 10 kHz to 100 kHz (for all but the 600 °C-annealed film), and then increased gradually at higher

frequencies.

At 100 kHz, ϵ_r increased from ~102 to ~202 with increasing annealing temperature. There have been several reports in the literature suggesting that such an increase can be attributed to the increase in grain size and/or density of the films^{33,34}. In our case, the XRD traces and AFM results confirm the increasing grain size with increasing annealing temperature but, as discussed in the previous section, a drop in film density at the highest annealing temperature was apparent in the FE-SEM images. The continuous increase in ϵ_r suggests that the effect caused by the decrease in the density of the film annealed at 750 °C did not fully cancel the rise in ϵ_r due to increase in the grain size. The values of $\tan d$ at 100 kHz of the same set of films decreased from 0.0265 to 0.0195 with increasing annealing temperature until 700 °C, and then increased to 0.0260 at the annealing temperature of 750 °C, suggesting that $\tan d$ is predominantly affected by the film density. The increase in the $\tan d$ with increasing frequency becomes more obvious in the films annealed at higher temperature.

The values of ϵ_r at 100 kHz for the films annealed at 700 °C were ~168. These values of ϵ_r are smaller than that reported for a BSmT film on platinised silicon prepared by MOSD (387 at 1 MHz)³⁵, and higher than that of a MOSD-derived BNdT film (110 at 100 kHz)³⁶, but $\tan d$ in our films is much smaller than these latter two films (0.054 and 0.137, respectively). A comparative study by Maiwa *et al.* on CSD-derived polycrystalline BiT, BLaT and BNdT films on platinised silicon showed that the films had dielectric constants of ~150, ~180, ~225, respectively at 100 kHz, suggesting an enhancement of the polarisation by La and Nd substitution.¹⁷ Another comparative study by Zhang *et al.* on highly epitaxial *c*-axis-oriented BiT and BNdT films on LaNiO₃-coated LaAlO₃ substrates grown by PLD showed that films had dielectric

constants of ~ 130 and ~ 180 , respectively.³⁷

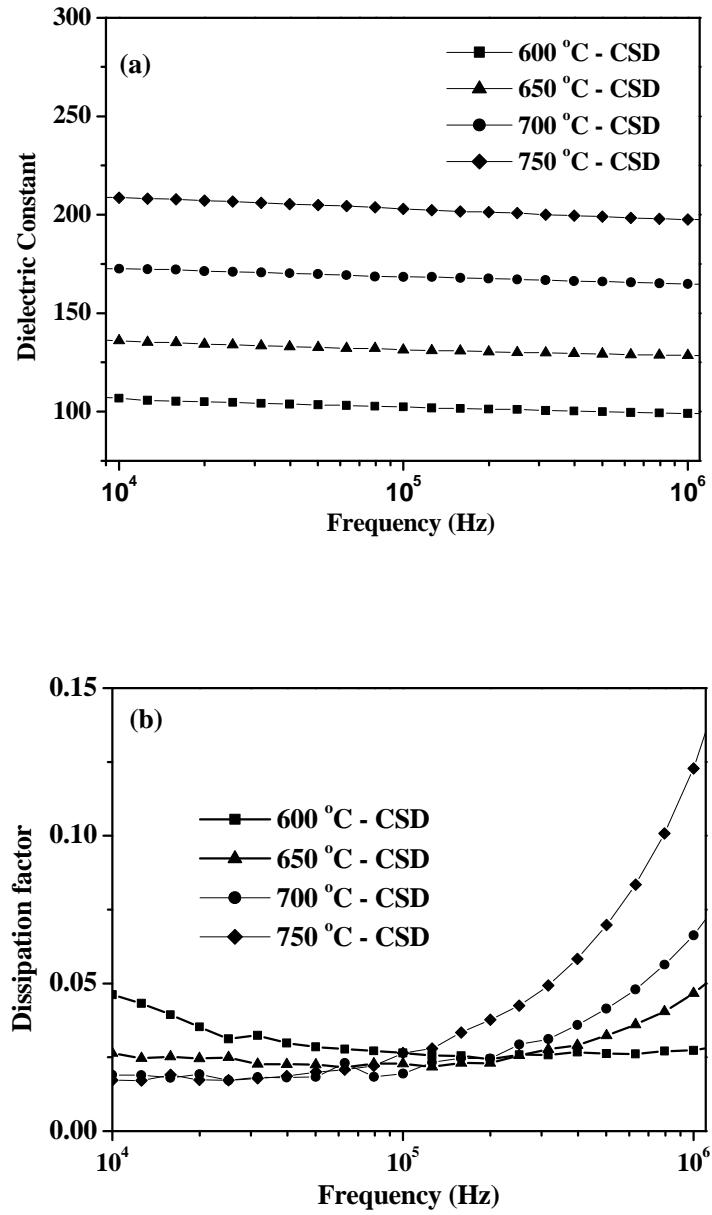


Fig. 7.9 (a) Dielectric constant and (b) Dissipation factor as a function of frequency

2. Ferroelectric hysteresis behaviour

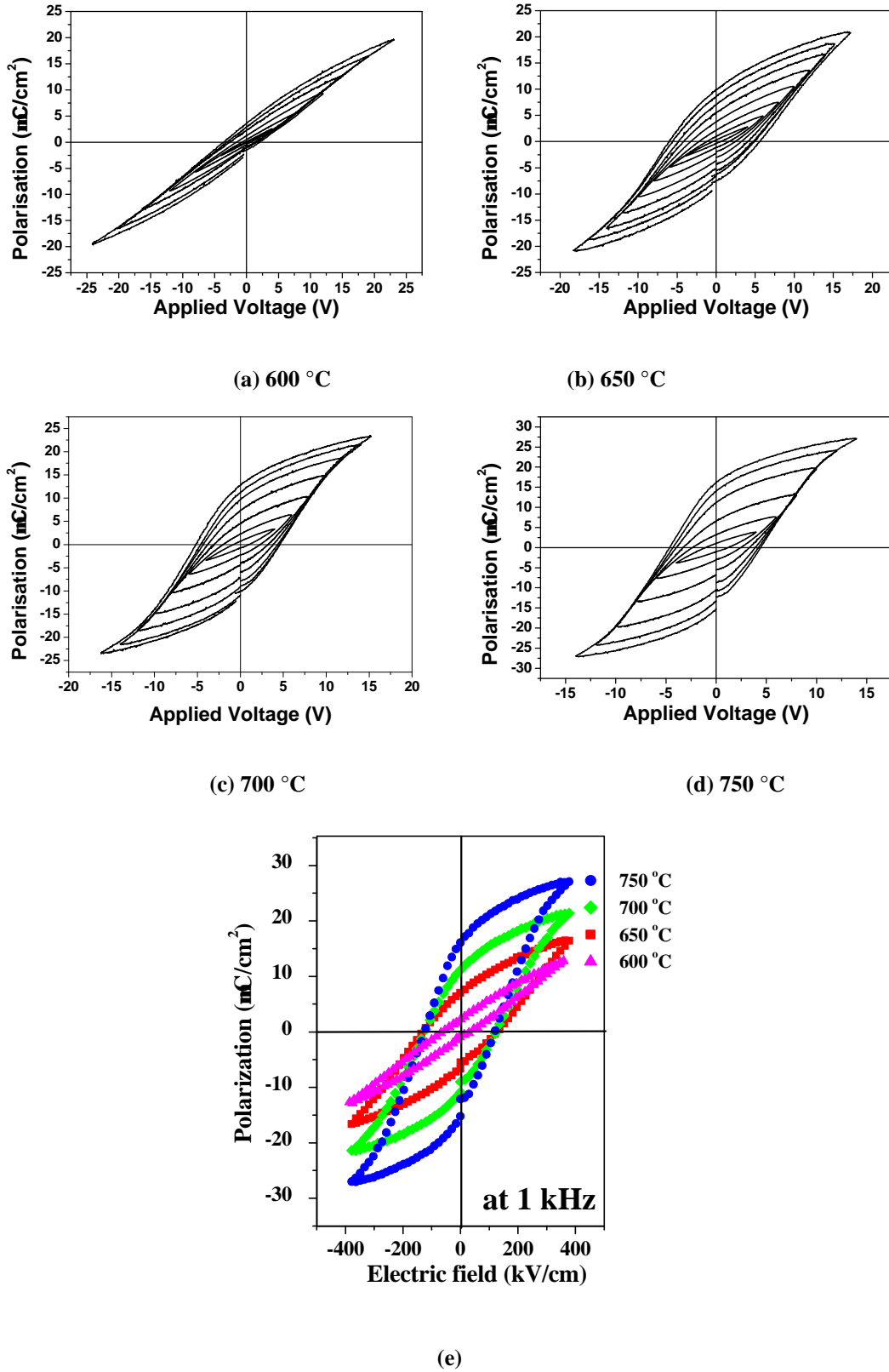


Fig. 7.10 *P-E* hysteresis loops of films annealed at (a) 600 °C, (b) 650 °C, (c) 700 °C, and (d) 750 °C; (e): a comparison of hysteresis loops measured at ~370 kV/cm

Fig. 7.10 shows the P - E hysteresis behaviour of the films. It can be seen that $2P_r$ increases with increasing annealing temperature. The $2P_r$ value of the film annealed at 750 °C was $33.4 \mu\text{C}/\text{cm}^2$, which is comparable to that of a BLaT thin film prepared by PLD ($2P_r = \sim 27 \mu\text{C}/\text{cm}^2$),³⁸ and that of a CSD-derived $\text{Bi}_{4-x}\text{Nd}_x\text{Ti}_3\text{O}_{12}$ ($x = 0.5$) thin film ($2P_r = \sim 35 \mu\text{C}/\text{cm}^2$)³⁹ (both on platinised silicon).

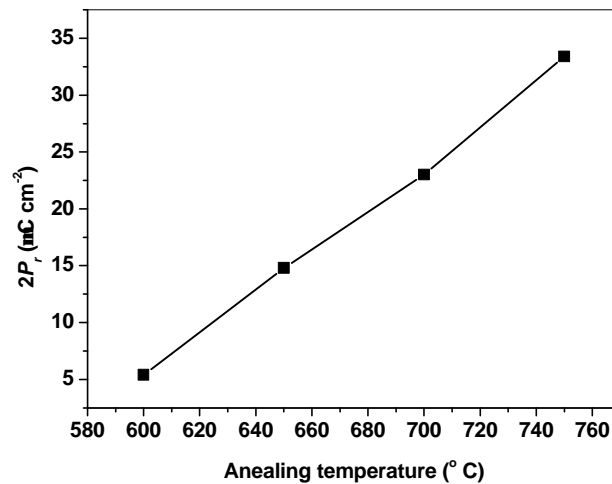


Fig. 7.11 $2P_r$ as a function of the annealing temperature

Fig. 7.11 shows the values of $2P_r$ as a function of the annealing temperature, suggesting an enhancement in ferroelectricity with increasing temperature.

3. Leakage current density characteristics

Fig. 7.12 shows the leakage current densities of BSmT films as a function of applied electric field. As the annealing temperature increased, the value of leakage current density increased: 7.4×10^{-7} , 1.4×10^{-6} , 4.0×10^{-6} , $1.5 \times 10^{-5} \text{ A}/\text{cm}^2$ at an applied DC field of $\sim 100 \text{ kV}/\text{cm}$ for 600 °C, 650 °C, 700 °C, and 750 °C annealed films respectively. This higher leakage current could be a result of the increased surface roughness (see Fig. 7.5): previous studies of SBT⁴⁰ and Ce-modified BiT⁴¹ thin films deposited on platinised Si substrates show similar effects. Leakage in the

CSD-derived film annealed at 700 °C is comparable to that of CSD-derived BNdT thin films as reported by Wu *et al.* (5.0×10^{-6} A/cm² at 100 kV/cm) ¹⁹ and MOCVD-derived BSmT reported by Kojima *et al.* ($\sim 10^{-5}$ A/cm²) ³¹.

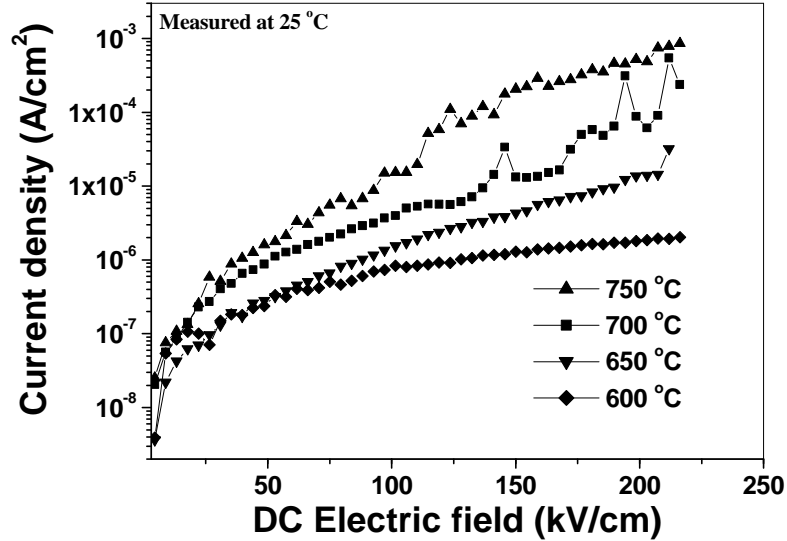


Fig. 7.12 *J-E* characteristics of the BSmT films

4. Electrical fatigue behaviour

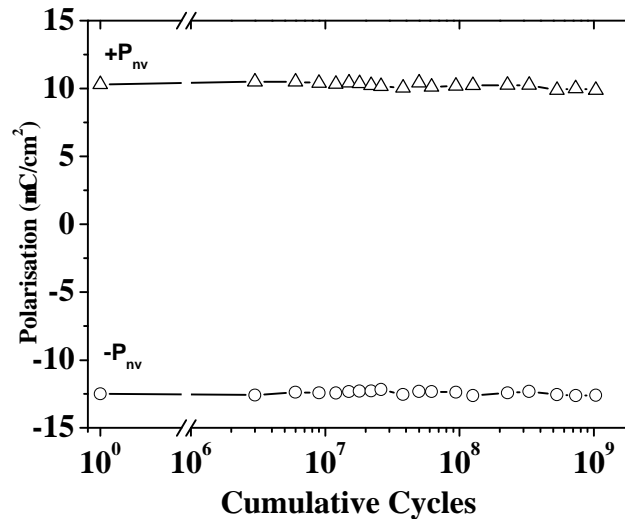


Fig. 7.13 Fatigue characteristics of the BSmT films

The films annealed at 600 and 650 °C fatigues quickly after 1.0×10^7 switching cycles. Fig. 7.13 shows the fatigue behaviour for the film annealed at 700 °C, with little change in the non-volatile polarisation (P_{nv}) up to 1.0×10^9 read/write switching cycles at a switching electric field of $\sim \pm 380$ kV/cm (*i.e.* ± 14 V). The films annealed at 750 °C show a similar behaviour to this.

7.2.2 Discussion and conclusions

In this study, an alkoxide-salt method was adopted to prepare the precursors for BSmT film fabrication. *In-situ* FT-IR studies on the decomposition of the precursor, which is an analogy of the pre-baking stage during film fabrication, reveals that acetic acid serves as chelating agent to improve the homogeneity of the precursor solution by generating a dense and homogeneous Ti-O-Ti polymeric network and, at a baking temperature of 300 °C, most organic compounds are evaporated and decomposed.

Raman spectroscopy reveals that an excitation of the active modes of perovskite phase becomes stronger with increasing temperature annealing above 600 °C, indicating the development of the crystallinity for the perovskite phase in BSmT films.

XRD and Raman results confirm the existence of the fluorite as an intermediate phase between the amorphous and perovskite phases of BSmT. Increasing annealing temperature favours the growth of *c*-axis-oriented grains and increases grain sizes.

AFM and SEM images, as well as XRD patterns, all indicate an increase of grain size with increase of annealing temperature. FE-SEM images show that the films have a clear and sharp boundary with Pt bottom electrodes and a grainy structure.

An increase in dielectric constant value with increasing annealing temperature was

observed, which may be attributed to the increase in grain size and/or density of the films. The values of $\tan \delta$ at 100 kHz of the same set of films decreased with increasing annealing temperature until 700 °C, and then increased at the annealing temperature of 750 °C, suggesting that $\tan \delta$ is predominantly affected by the film density, since a slight reduction in density was seen at this temperature.

Although the *c*-axis-oriented grains were favoured with increasing annealing temperature, the P_r increased with increasing annealing temperature, which was attributed to the enhancement of grain development. The higher leakage current measured after a higher annealing temperature could be the result of the increased surface roughness. The film annealed at 700 °C shows excellent electrical fatigue resistance. The electrical properties of the films fabricated in this study (dielectric and ferroelectric properties, leakage current characteristics and electrical fatigue properties), are comparable or superior to these previously reported for similar films developed by other techniques or using other doping elements.

7.3 Low temperature properties of BSmT films

7.3.1 Motivation

Previous sections have described polycrystalline BSmT films deposited by PLD and CSD on platinised silicon. They have large P_r and are almost fatigue-free, which suggests a promising ferroelectric material for Nv-RAM use.

Since the devices using Nv-RAM might be used at an extremely low temperatures, e.g. automobiles, in space or military applications, the performance of the lanthanide-substituted BiT films over a wide range of temperature must be tested to meet these special applications. In the simplest case, when reading and writing a

ferroelectric memory cell, a sufficient amount of charge will be necessary to enable precise data storage, which accordingly needs a large remanent polarisation in ferroelectric capacitors even at a very low temperature. Besides, the data obtained at low temperature can help us to fully understand some fundamental issues in this kind of new ferroelectric thin film, such as domain behaviour, leakage mechanisms, *etc.* Although there have been intensive investigations on the properties of BLnT films⁶⁻⁸, the detailed electrical properties of the films at low temperature have not yet been reported. In this section, we will report the electrical properties of BSmT thin films in the temperature range of 35 to 300 K.

7.3.2 Results and discussion

The BSmT thin films in this study were the CSD-derived 700 °C-annealed BSmT films in previous section (~370 nm thick).

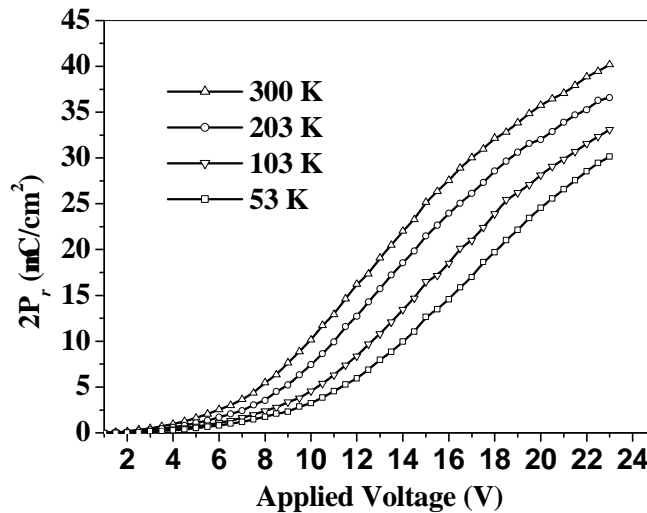


Fig. 7.14 $2P_r$ as a function of the applied voltage measured over the temperature range from 53 K to 300 K

Fig. 7.14 shows $2P_r$ as a function of the applied voltage measured over the temperature range from 53 to 300 K. For all temperatures, the $2P_r$ value increases

with increasing voltage and saturates at higher voltages. With decreasing measurement temperature, the saturation voltage increases.

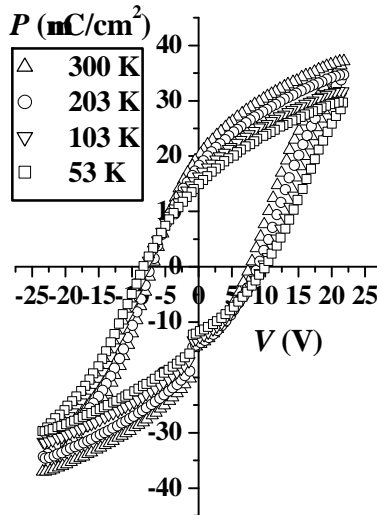


Fig. 7.15 P - V loops measured over the temperature range from 53 K to 300 K

Fig. 7.15 shows well saturated hysteresis loops of the film measured at different temperatures, showing clearly that the film has a decreasing $2P_r$ and increasing V_c with decreasing temperature.

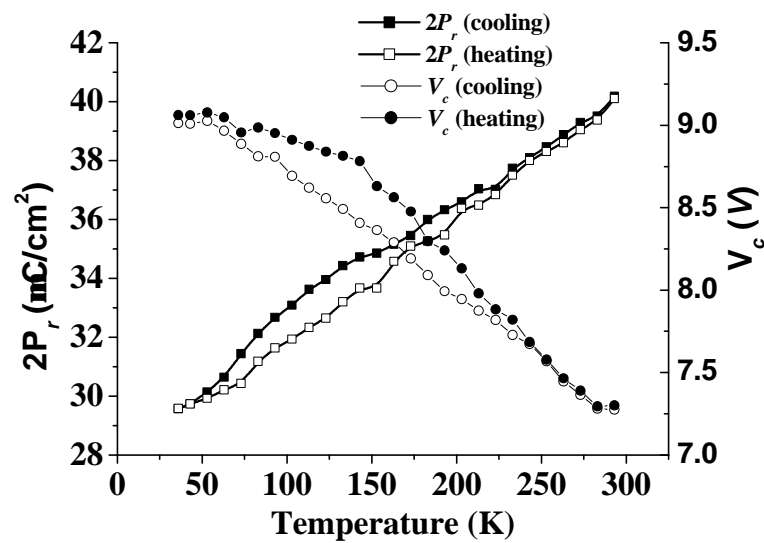


Fig. 7.16 Temperature dependence of $2P_r$ and V_c measured at a cooling and a heating cycle

Fig. 7.16 shows the detailed temperature dependence of $2P_r$ and V_c . The $2P_r$ decreases steadily from $\sim 40 \mu\text{C}/\text{cm}^2$ to $\sim 29 \mu\text{C}/\text{cm}^2$ with decreasing temperature, and upon subsequent temperature increase, recovers to the original value. V_c increases from ~ 7.3 to ~ 9.0 V with decreasing temperature and then recovers upon temperature increase. These results suggest that the degradation of the ferroelectricity was not caused by any irreversible damage to the sample during the temperature cycle. Furthermore, the $2P_r$ and V_c both show some hysteresis properties during the cooling and heating stages. We should note that even at temperatures as low as 35 K, the film shows rather high $2P_r$ ($\sim 29 \mu\text{C}/\text{cm}^2$), which suggests application over a very wide temperature range. Comparatively, the $2P_r$ value of SBT thin films reported by Yang *et al.*⁴² has a remarkable ($\sim 98\%$) reduction from 300 K to 100 K, and shows negligible ferroelectricity at 100 K.

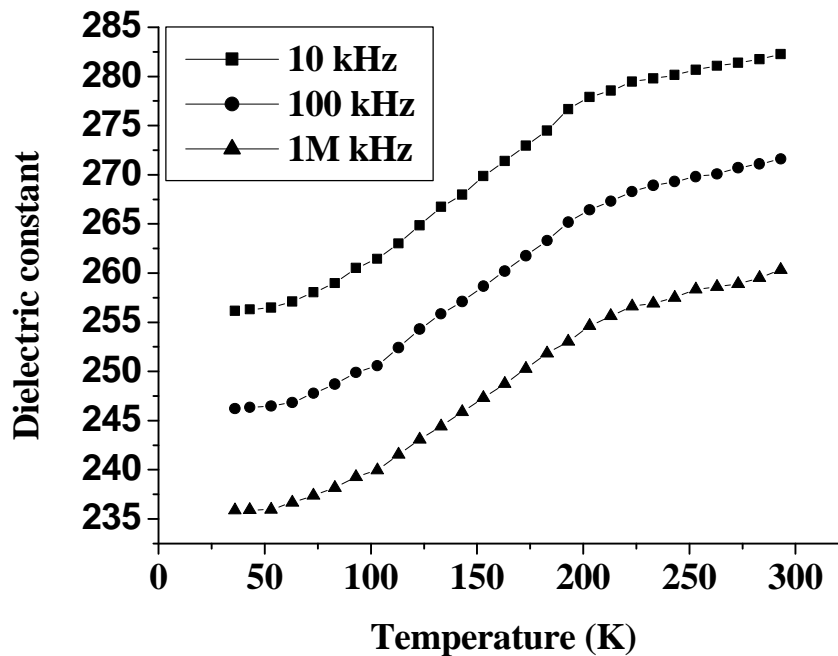


Fig. 7.17 Temperature dependence of ϵ_r of the film measured at a heating cycle at various frequencies

The temperature dependence of the dielectric constant (ϵ_r) measured at different frequencies during a heating cycle is shown in Fig. 7.17. From 35 to ~50K, the value of ϵ_r remains constant; from ~50K to ~200 K, it increases steadily; and from ~200 K to 300 K, the rate of increase stabilises.

There may be two possible reasons accounting for the shape of the curve: phase transition^{43,44,45,46} and/or domain wall pinning⁴⁷. Phase transition theory suggests a delicate phase transition near ~200 K. Sawaguchi and Cross⁴³ have reported dielectric measurements on single-crystal BiT along the c axis below room temperature, which showed some thermal hysteresis in spontaneous polarisation and a similar shape around 150 K in the ϵ_r - T curve. Their other studies^{44,45} also corroborated the temperature dependence of the energy separation in the orthorhombic and monoclinic states. Following their studies, Idink *et al.*⁴⁶ have carried out a detailed examination of the temperature dependence of BiT ceramics by Raman spectroscopy, observing a subtle phase transition in the 150~200 K region. They suggested that a possible subtle monoclinic-orthorhombic phase change, combined with a continuous ordering of dipoles associated with Bi^{3+} lone pair electrons and TiO_6 octahedra, might be responsible for this.⁴⁶ Since the moderate doping of similar lanthanide elements, such as Nd, does not significantly alter the phase structure at room temperature (orthorhombic),⁶ the same mechanism might also be applicable in our Sm-doped BiT thin films. This might also partly account for the hysteretic properties of the ferroelectricity with temperature cycles, as shown in Fig. 7.16, noting that the $2P_r$ - T curve becomes linear around ~230 K.

Although a phase transition might dominate, another possible mechanism, domain wall dynamics, might also exist. The roughly linear dependence of V_c over the whole

range of 50 ~ 300 K is reminiscent of the KH_2PO_4 (KDP) family and $\text{PbSc}_{1/2}\text{Ta}_{1/2}\text{O}_3$ (PST)⁴⁸. In the former case the phenomena were ascribed to domain wall freezing by considering that domain walls experience a finite viscosity in their motion through the lattice. In the PST case, the domain wall freezing theory was adopted but the temperature dependence of the de-pinning energy was used instead of the steady-state velocity or mobility, since a threshold temperature appeared in the e_r -T curve. In our case, the analogy of the domain wall motion can also be seemingly validated by the threshold temperature (~200 K), which results in a slow increase in e_r and lack of the hysteresis of P_r and E_c above 200 K. However, most interestingly, our results are more like KDP than PST, showing a temperature independent region in both e and E_c below ~50 K, which might be due to the existence of another temperature independent phase or complete freezing of domain walls.

Therefore in our case we could explain the behaviours by considering the two possible mechanisms: domain wall dynamics and phase transition.

1. In the domain wall dynamics mechanism, below 50 K, domain wall movement was frozen; at 50 K, domain walls begin to un-freeze resulting in de-pinning; 50 ~ 200 K, the domain walls unfreeze further due to the change in de-pinning energy; at ~200 K, domain wall un-freezing is complete.

2. In phase transition mechanism, below 50 K, a possible triclinic phase exists; at 50 K, phase transition from triclinic to monoclinic happens; at ~200 K, a delicate phase transition from monoclinic to orthorhombic begins.

Correspondingly, the decrease in the saturation polarisation at low temperatures can be attributed to the inability to reverse all the domains at the same electric field or decrease in spontaneous polarisation due to lattice distortion during the phase

transitions mentioned above.⁴⁸ Further temperature dependent high-resolution X-ray or neutron diffraction measurements would be necessary to elucidate the mechanism by observation (or not) of the phase transition.

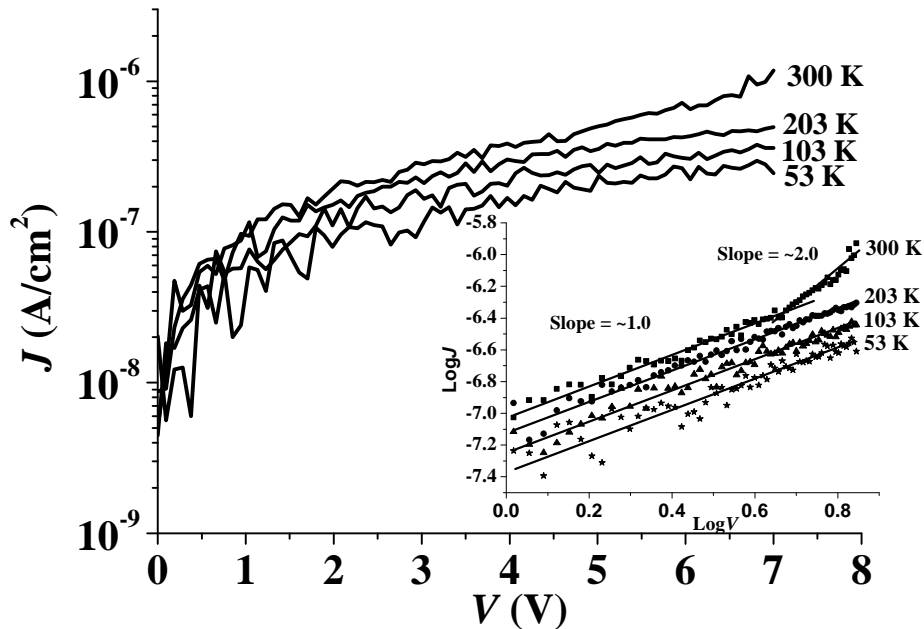


Fig. 7.18 J - V characteristics in the temperature range from 53 K to 300 K

Fig. 7.18 shows J - V characteristics of the same film in the temperature range from 53 K to 300 K. We can see an increase in the leakage current with increasing temperature, suggesting that a thermally assisted conduction process might dominate. At 300 K, there are three stages on the J - V curve: from 0 to 1.0 V, there is an extremely rapid exponential rise in $J(V)$ that has the form expected for injection tunnelling (through the electrode-film interface) into a high-dielectric material, which has been observed in both BST and PZT⁴⁹; from 1.0 to 4.0 V there is a rather flat linear (saturated) region, which can be fitted very well by $J \sim V^{1.0}$; from 4.0 to 7.0 V, the slope of $\text{Log} J$ vs. $\text{Log} V$ plots change to 2.0 (*i.e.* $J \sim V^{2.0}$, see the inset of Fig. 7.18) which agrees well with the

space charge limited current (SCLC) leakage mechanism. With decreasing temperature, the leakage mechanism becomes simpler: within the measured voltage range, the stage of $J \sim V^{2.0}$ (which corresponds to SCLC leakage) disappears. This might be related to the lower mobility of the charge carriers with decreasing temperature.

7.3.3 Conclusions

In summary, low temperature electrical properties of BSmT ferroelectric thin films have been investigated, which suggest that BSmT thin films are very promising for extremely low temperature nonvolatile memory applications.

7.4 CSD-derived BNdT films

7.4.1 Results and discussion

7.4.1.1 Structural properties

1. XRD results

Fig. 7.19 shows the XRD patterns of the BNdT films annealed at temperatures ranging from 600 °C to 750 °C (film thickness: ~ 450 nm). As annealing temperature increases to 600 °C, the BNdT thin film begins to crystallise. We can see that all the films have a bismuth-layered structure showing mixed orientations, and no pyrochlore phase. The correlation of the diffraction peaks of the BNdT with those of BiT implies that Nd substitution does not affect the layered-perovskite structure of BiT. The result indicates that the Nd^{3+} ions in the BNdT films do not form a pyrochlore phase, but dissolve into the pseudo-perovskite structure. Therefore, we can expect that the Nd

ions (1.11 \AA) can substitute for Bi ions (1.17 \AA)^{50,30}. The peak intensities increased, and the FWHM of the peaks decreased with increasing annealing temperature; it can be assumed that the grain size of the film was increasing as annealing temperature increased.

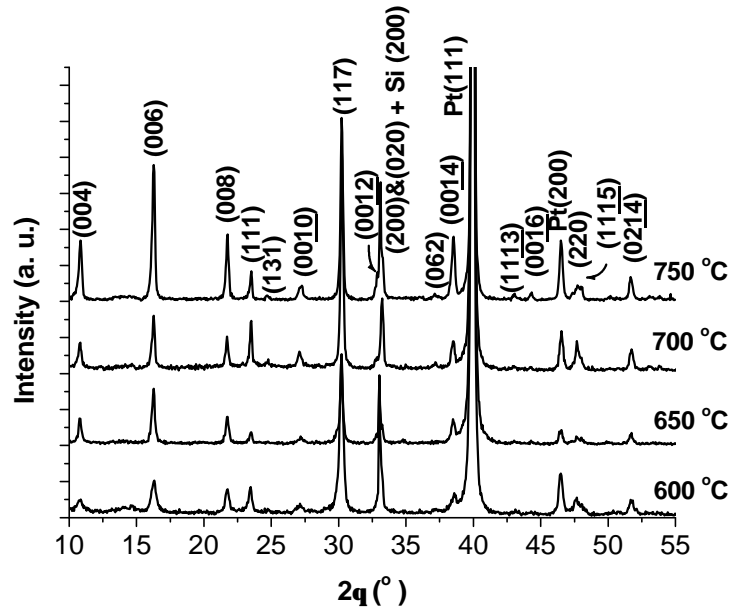


Fig. 7.19 XRD patterns of BNdT thin films annealed at various temperatures

2. Raman spectroscopy

Fig. 7.20 shows Raman spectra of BNdT films annealed at various temperatures. The Raman spectra of BNdT films exhibit intense phonon modes at ~ 268 , ~ 550 , and $\sim 850 \text{ cm}^{-1}$ and several small peaks just above 200 cm^{-1} (the spectra below 200 cm^{-1} were not measured due to equipment limitations). The peak around 268 cm^{-1} corresponds to the TiO_6 octahedron torsional bending mode, which is representative of the pseudo-perovskite structure in the BNdT. Peaks around 550 cm^{-1} and 850 cm^{-1} are related to the TiO_6 stretching mode.⁴⁶ These three peaks become stronger and sharper with increase of the annealing temperature, which indicates that the

crystallisation of the perovskite structure is enhanced.

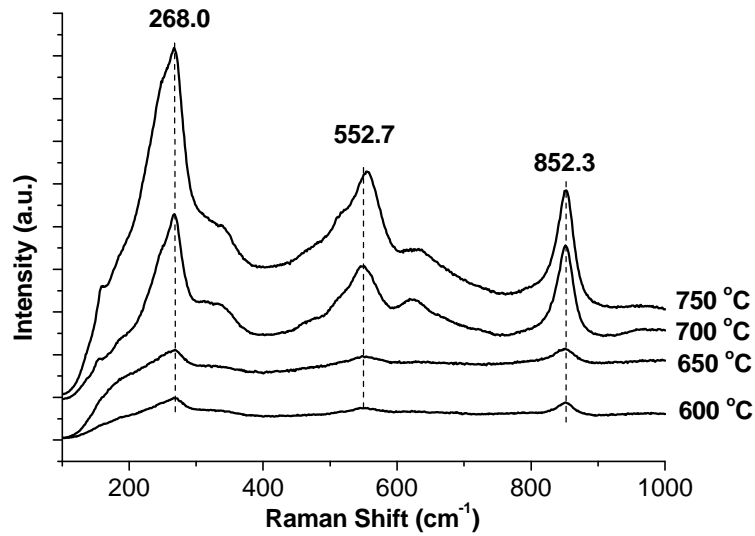


Fig. 7.20 Raman spectra of BNdT films annealed at different temperatures

2. AFM images

Fig. 7.21 shows AFM micrographs of the BNdT thin films as a function of annealing temperature. From these analyses, we found that the RMS surface roughness of the BNdT thin films increased with increasing annealing temperature, which is similar to the BSmT films. The effect may be related to the increase of the grain size with increasing annealing temperature. The values of RMS surface roughness of BNdT films ($1\mu\text{m} \times 1\mu\text{m}$) were 4.2 nm, 6.5 nm, 9.4 nm, and 12.2 nm, for the annealing temperature of 600 °C, 650 °C, 700 °C, and 750 °C, respectively.

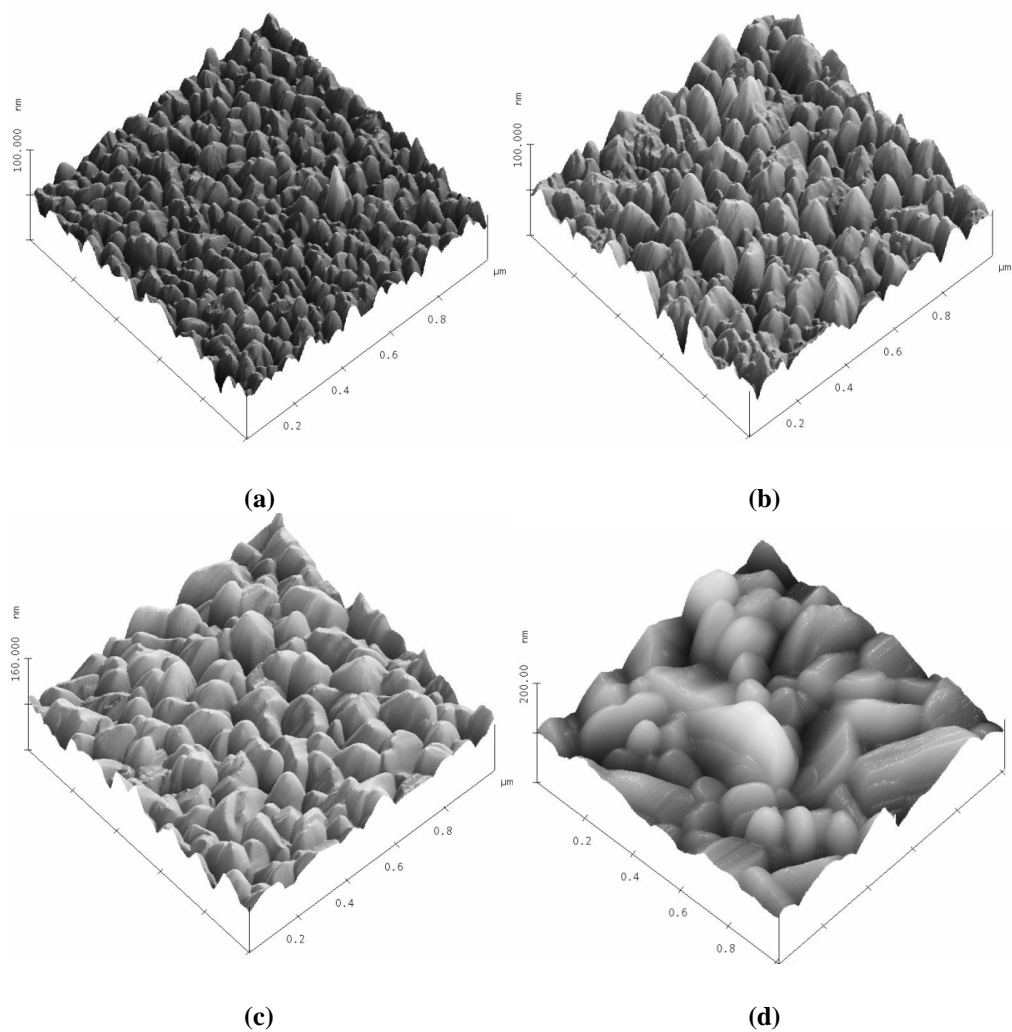


Fig. 7.21 AFM surface images of the BNdT films annealed at: (a) 600 °C, (b) 650 °C, (c) 700 °C, and (d) 750 °C

3. SEM images

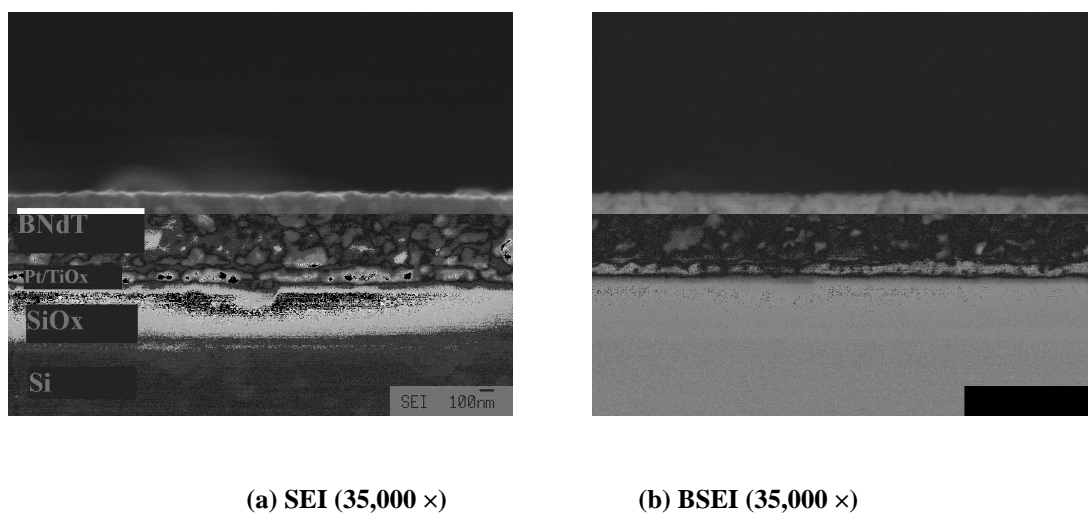
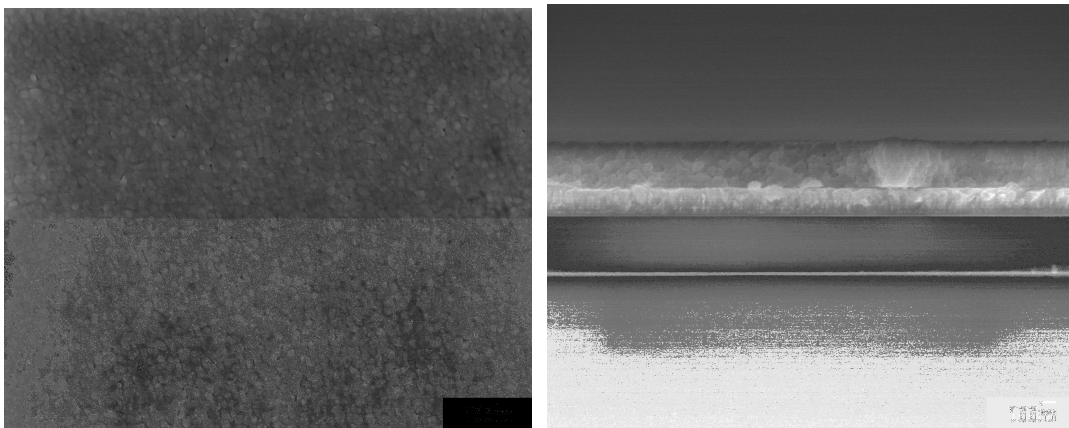


Fig. 7.22 Cross-sectional FE-SEM images of the film annealed at 650 °C. (a) SEI mode; (b) BSEI mode

Fig. 7.22 shows cross-sectional FE-SEM images of the film annealed at 650 °C. From the image of SEI mode, the film has a dense granular structure. The image of BSEI mode suggests that the film has a clear boundary with the bottom electrode layer.

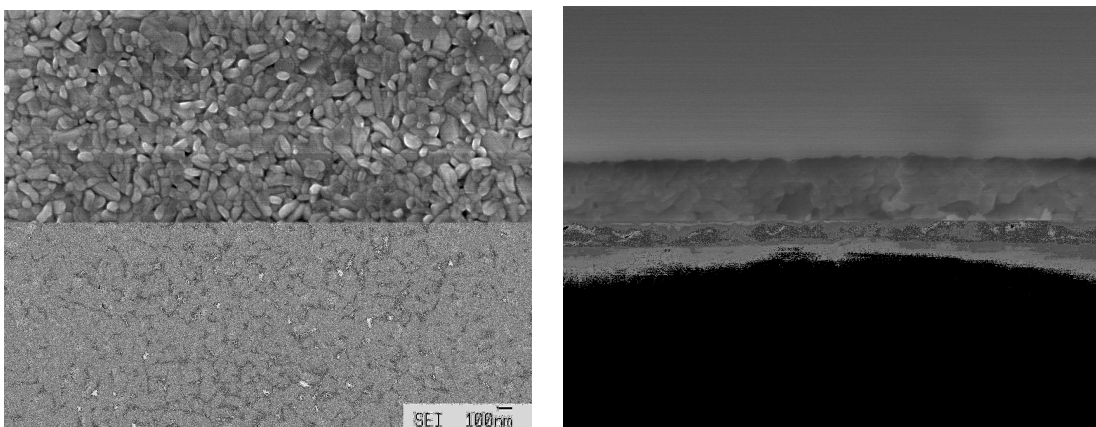
Fig. 7.23 shows FE-SEM images of films annealed at different temperatures, which confirm increasing grain size with increasing annealing temperature. The thickness remains little changed within this temperature range.



(a)

(b)

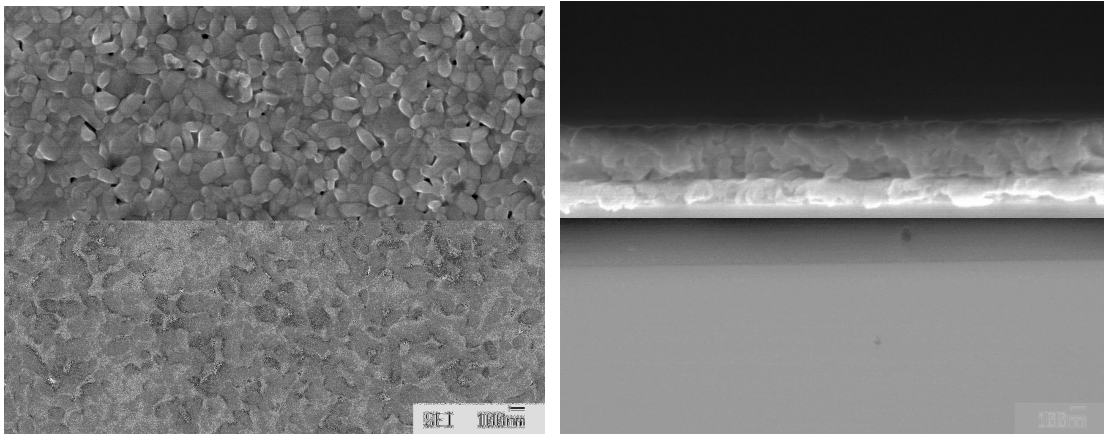
(a) Top view; (b) Cross-sectional FE-SEM images of film annealed at 600 °C



(c)

(d)

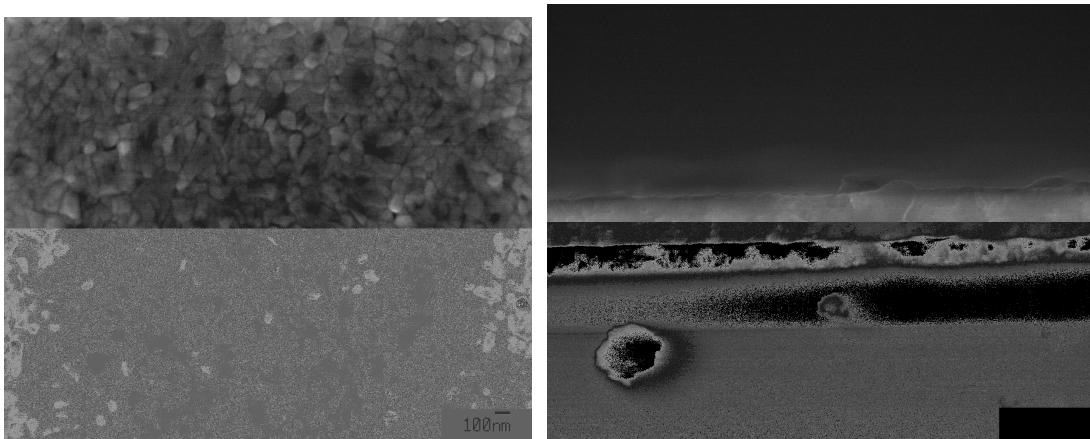
(c) Top view; (d) Cross-sectional FE-SEM images of film annealed at 650 °C



(e)

(f)

(e) Top view; (f) Cross-sectional FE-SEM images of film annealed at 700 °C.



(g) Top view; (h) Cross-sectional FE-SEM images of film annealed at 750 °C

Fig. 7.23 FE-SEM images of films annealed at different temperatures

7.4.1.2 Electrical properties

1. Ferroelectric hysteresis loops

Figs. 7.24 and 7.25 show the polarisation-electric field (P - V) hysteresis curves of the BNdT thin films annealed at temperatures ranging from 600 °C to 750 °C. The $2P_r$ increases with increasing annealing temperature. The improved ferroelectric properties for the BNdT thin films annealed above 650 °C may be attributed to increased crystallisation and larger grain size in comparison with the films annealed

below 650 °C. Fig. 7.24 (c) and 7.24(d) show well-defined P - V loops. The $2P_r$ and V_c values of BNdT films annealed at 700 °C and 750 °C were 35.6 and 41.4 $\mu\text{C}/\text{cm}^2$, 4.5 and 4.3 V (100.0 and 95.6 kV/cm at a film thickness of 450 nm) at an applied electric field of 400 kV/cm. This is higher than that of a BLaT thin film ($2P_r = 27 \mu\text{C}/\text{cm}^2$)⁵¹, and that of a CSD-derived BNdT thin film reported by others ($2P_r = 17.0 \mu\text{C}/\text{cm}^2$)⁵². The reason for this result may be explained by a large tilting of TiO_6 octahedra in a layered structure due to substitution of Nd^{3+} for Bi^{3+} . Since the ferroelectric properties are related to stoichiometry, grain size, and crystallinity of the film, the precise mechanism for the difference requires further investigation.

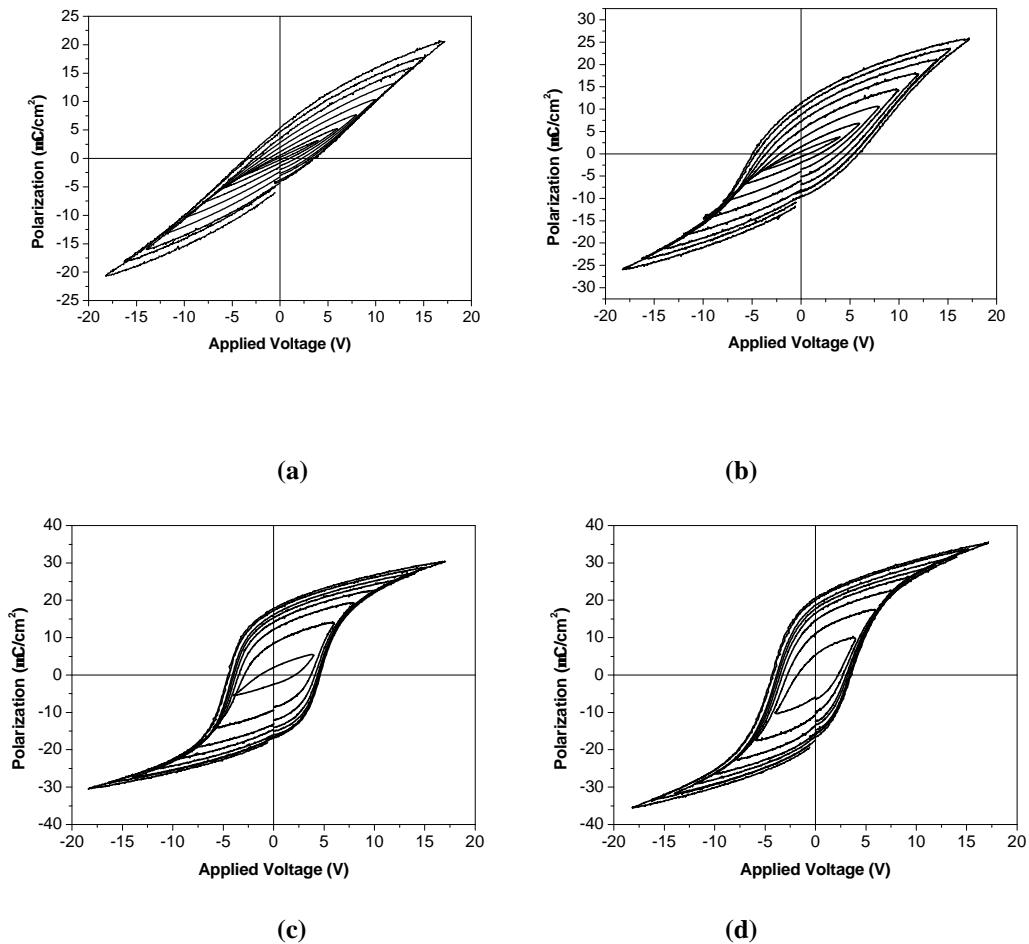


Fig. 7.24 P - V hysteresis curves of the BNdT thin films annealed at: (a) 600 °C, (b) 650 °C, (c) 700 °C, and (d) 750 °C measured at various applied voltages (4 V ~ 18 V)

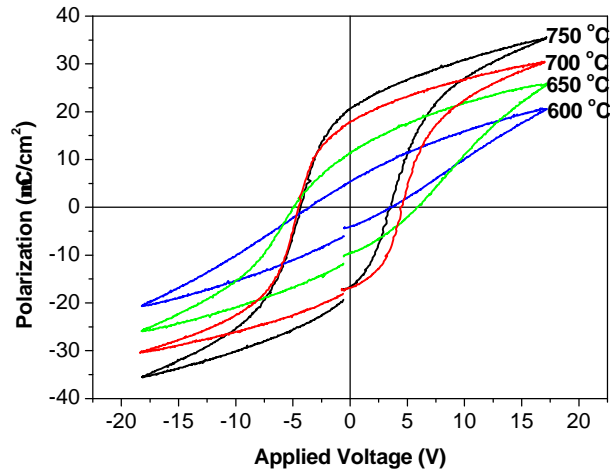


Fig. 7.25 *P-V* loops of BNdT films measured at 18 V

2. Leakage current properties

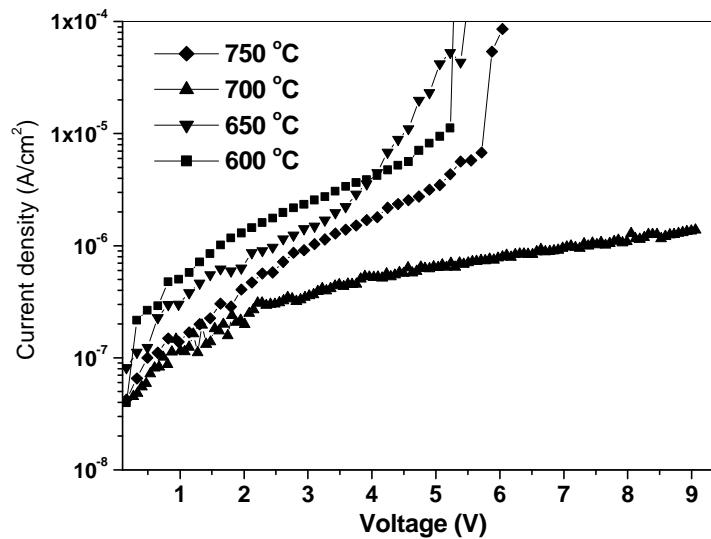


Fig. 7.26 *J-V* of BNdT films annealed at various temperatures

Fig. 7.26 shows the *J-V* curves of BNdT films annealed at various temperatures. As seen from the figure, the leakage current density is critically dependent on the annealing temperature. The leakage current density of the BNdT thin films annealed at 600 °C, 650 °C, 700 °C, and 750 °C were 2.0×10^{-5} , 5.0×10^{-6} , 5.0×10^{-7} , 2.5×10^{-6} A/cm², respectively, at an applied DC voltage of 4.5 V (~ 100 kV/cm). As the

annealing temperature increases from 600 °C to 650 °C, the leakage current densities for the BNdT thin films decreased first, then increased at temperatures above 700 °C. It is assumed that higher leakage current may be caused by the higher surface roughness of the BNdT thin film, which causes an increase in the leakage current. Similar results were reported by previous researchers on Ce-substituted BiT thin films⁴¹. But Kojima *et al.* did not find any effect of surface roughness on the leakage in their lanthanide doped epitaxial BiT films³¹. Previous studies on various ferroelectric perovskite oxides indicate that conduction mechanisms can be affected by the grain size.^{53,54} The film annealed at 750 °C has worse leakage current property due to the higher roughness of the film surface as analysed above.

3. Electrical fatigue behaviour

The BNdT films annealed at lower temperatures (600 °C and 650 °C) fatigue quickly after 1.0×10^7 switching cycles. Fig. 7.27 shows the fatigue behaviour of the BNdT film annealed at 700 °C.

The film shows little change in the switching polarisation (P^*) and in the nonswitching polarisation (P^\wedge) up to 1.0×10^{10} read/write switching cycles at a switching electric field of 330 kV/cm (*i.e.*, ± 15 V). The values of the non-volatile charge [*i.e.* $(+P^*)-(+P^\wedge)$, $(-P^*)-(-P^\wedge)$] are approximately $35.0 \mu\text{C}/\text{cm}^2$, and basically remain constant throughout the switching cycles. The fatigue-free characteristics can be related to the chemical stability of the perovskite layers against oxygen vacancies, since oxygen vacancies were found at both the $(\text{Bi}_2\text{O}_2)^{2+}$ and the $(\text{Bi}_2\text{Ti}_3\text{O}_{10})^{2-}$ perovskite layers, which will compensate for space charges.³⁸ The film annealed at 750 °C showed a similar behaviour to this.

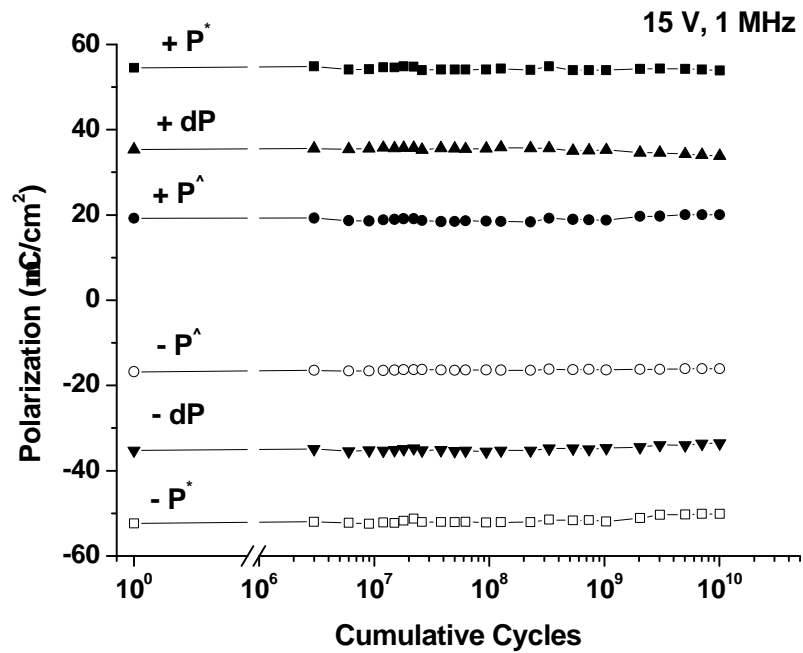


Fig. 7.27 Fatigue characteristics of BNdT film annealed at 700 °C with 1 MHz bipolar pulses at 15 V

7.4.2 Conclusions

Precursors of Bi-Nd-Ti which were stable for at least eight months were successfully developed and the BNdT films were fabricated using the spin-coating technique.

The ferroelectric properties were enhanced with increasing annealing temperature. $2P_r$ and E_c of the films annealed at 700 °C and 750 °C are 35.6 $\mu\text{C}/\text{cm}^2$ and 100 kV/cm, 41.4 $\mu\text{C}/\text{cm}^2$ and ~96 kV/cm, respectively. The film annealed at 700°C and 750 °C both show an excellent electrical fatigue resistance.

Therefore, CSD-derived BNdT films show excellent structural and electrical properties and are suitable for Nv-RAM use.

7.5 Effect of annealing atmospheres on CSD-derived BNdT films

7.5.1 Motivation

The leakage current of BNdT films must be minimised to preserve stored information as an electron charge in FeRAM cells.⁵⁵ It is generally recognised that in ferroelectric films the conduction mechanism is Schottky emission in which leakage currents are controlled by the Schottky barrier.⁴⁹ It was reported that the higher leakage current of ferroelectric thin films could be reduced by activated oxygen annealing⁵⁶ or controlling gas ratio of $O_2/(O_2+Ar)$ during deposition of films^{57,58} These results could be explained by the variation of oxygen vacancies in the films reported. Oxygen vacancies in ferroelectric films, which are usually generated during fabrication of the films, might be reduced by introducing oxygen atoms or repressing the out diffusion of oxygen.

In this section, the results on the effect of annealing atmospheres on CSD-derive BNdT films will be presented.

7.5.2 Experimental procedure

The procedures of fabricating precursors for the BNdT films were the same as the BSmT films, except using Nd nitrate instead of Sm nitrate. After film deposition, films were then annealed at 700 °C for 30 minutes, instead of 10 minutes, in different atmospheres with different oxygen partial pressures (P_{O_2}) *i.e.* flowing oxygen (BNdT- O_2), air (BNdT-air), and nitrogen (BNdT- N_2) atmosphere.

7.5.3 Results and discussion

7.5.3.1 Structural properties

1. XRD studies

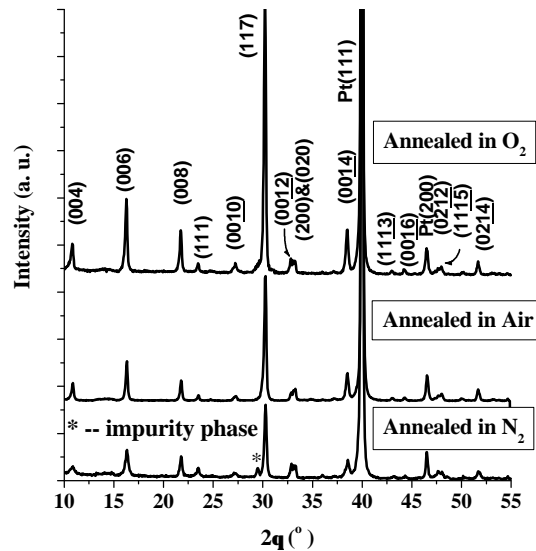


Fig. 7.28 XRD profiles of BNdT films annealed in different atmospheres

Fig. 7.28 shows the XRD θ - 2θ patterns of the BNdT films annealed in different atmospheres. It can be seen that, on increasing the partial pressure of oxygen (P_{O_2}) in the annealing ambient, the crystallinity of the films improves (peaks become sharper and more intense). The perovskite phase was fully formed in the films annealed in oxygen and air, which both have a bismuth-layered structure showing mixed orientations. Apart from the main bismuth-layered perovskite phase, the BNdT- N_2 film also shows an unidentified impurity phase. This result indicates that the Nd^{3+} ions in the BNdT films are incorporated into the pseudo-perovskite structure for the films annealed in air and O_2 .³⁰ The FWHM of the perovskite phase peaks decreases with increasing oxygen partial pressure (0.70° , 0.25° , and 0.20° for peak (006), for the films

annealed in N₂, air and O₂, respectively), corresponding to an increase in the grain size. As the oxygen partial pressure was increased, the proportion of (117)-oriented grains, calculated from the equation $(117) \% = I_{(117)} / (I_{(006)} + I_{(117)})$, increased from ~71.2% to ~75.0% to ~80.1%, showing clearly that oxygen ambience affects the crystallographic orientations of the films, probably by assisting the growth of (117)-oriented grains.

2. AFM studies

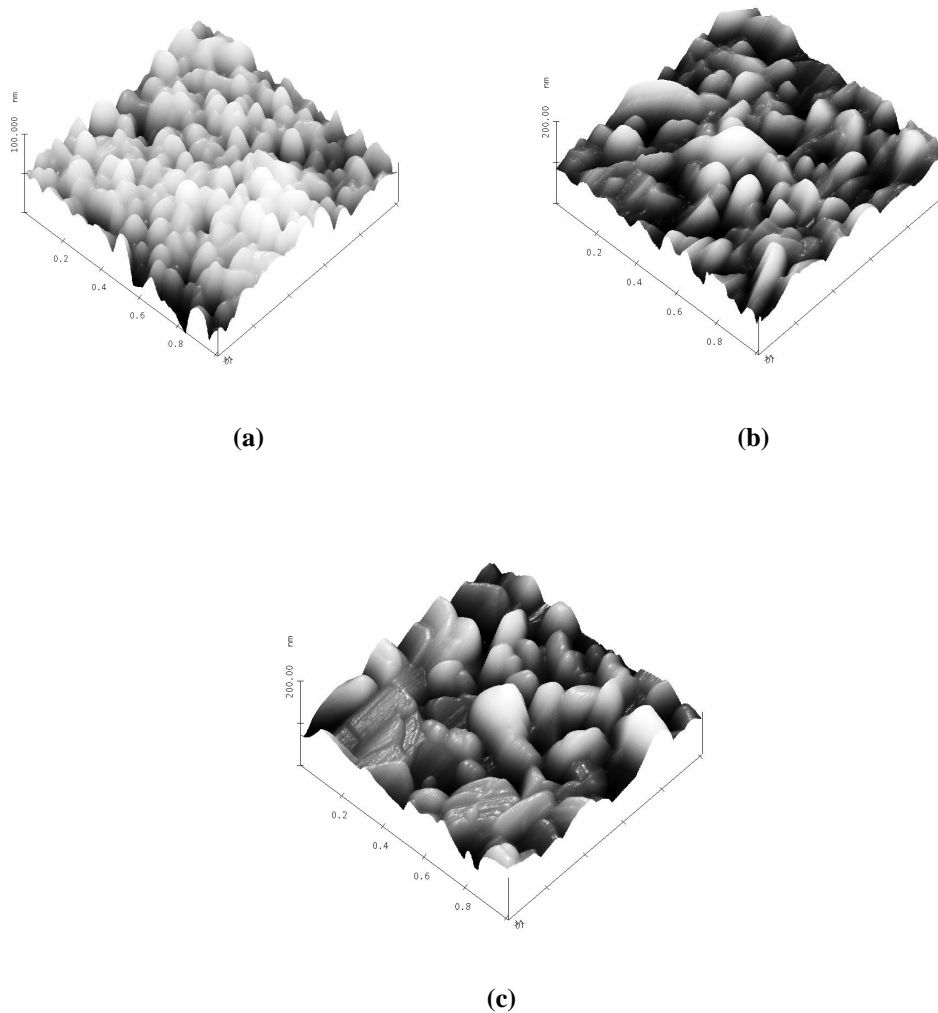


Fig. 7.29 AFM images of BNdT films annealed in: (a) N₂, (b) air, and (c) O₂

Fig. 7.29 shows AFM micrographs of BNdT films annealed under different conditions.

The RMS surface roughness ($1 \mu\text{m} \times 1 \mu\text{m}$) of the films is $\sim 11.2 \text{ nm}$, $\sim 14.6 \text{ nm}$, and $\sim 15.6 \text{ nm}$, for the film annealed in N_2 , air and O_2 , respectively. This is accompanied by an increase in the average grain size of the films from $\sim 7 \text{ nm}$ to $\sim 20 \text{ nm}$, as seen from the AFM images, which suggests that the partial pressure of oxygen assisted grain growth of the BNdT films. The roughness value of BNdT- O_2 is comparable to that reported for 200 nm-thick CSD-derived BNdT films prepared at $700 \text{ }^\circ\text{C}$ ($\sim 13.0 \text{ nm}$).³²

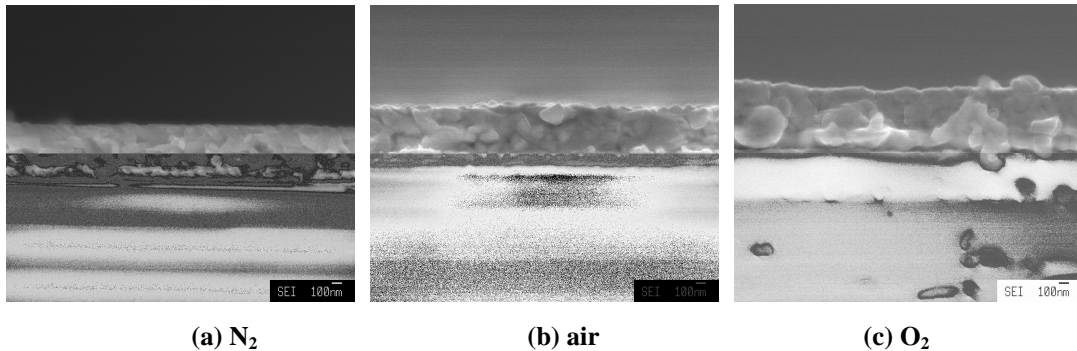


Fig. 7.30 Cross-sectional FE-SEM images of BNdT films annealed in (a) N_2 , (b) air, and (c) O_2

FE-SEM images, shown in Fig. 7.30, confirmed the increase of grain size with increasing P_{O_2} in the annealing ambient. The thickness of the films was almost the same ($350 \sim 400 \text{ nm}$).

3. Raman spectroscopy

Fig. 7.31 shows Raman spectra of the same set of films. The peak at $\sim 265 \text{ cm}^{-1}$ corresponds to the TiO_6 octahedron torsional bending mode, which is representative of the pseudo-perovskite structure in the BNdT.⁵⁹ Peaks around 550 cm^{-1} and 850 cm^{-1} are related to the TiO_6 stretching mode.⁵⁹ Three films all show similar peaks, which are consistent with the XRD results.

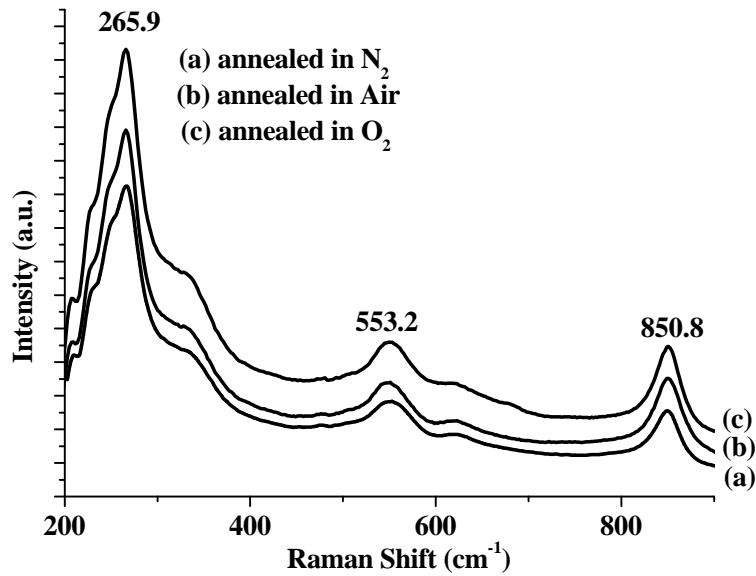


Fig. 7.31 Raman spectra of BNdT films annealed in: a) N₂, b) air, c) O₂

7.5.3.2 Electrical properties

1. Ferroelectric hysteresis behaviour

Fig. 7.32 shows P - E hysteresis loops of the BNdT films at an applied electric field of ~ 520 kV/cm and the electric field dependence of $2P_r$. The $2P_r$, E_c value of the film annealed in O₂, air and N₂, was ~ 57.2 $\mu\text{C}/\text{cm}^2$, ~ 145 kV/cm; ~ 26.6 $\mu\text{C}/\text{cm}^2$, ~ 160 kV/cm; and ~ 19.7 $\mu\text{C}/\text{cm}^2$, ~ 185 kV/cm respectively. As expected from structural properties, the BNdT-O₂ shows the highest $2P_r$ and lowest E_c and $2P_r$ decreased with decreasing P_{O2}.

There are several possible reasons for the increasing $2P_r$ and decreasing E_c with increasing P_{O2} in the annealing ambient.

1. Improved crystallisation. From the XRD, AFM, and FE-SEM results, we can clearly observe the enhanced phase formation and grain growth: the higher the P_{O2},

the higher proportion of the perovskite phase and the larger the grain size.

2. More (117)-oriented grains. As previously discussed, bismuth layer-structured perovskite ferroelectric thin films are highly anisotropic. From the results of the PLD-grown BNdT films on different single crystal substrates, the *c*-axis-oriented films have very weak polarisation as compared to the more *a/b*-axis-oriented films (in our study, (118) and (104)-oriented films). Therefore, any tilt of the *a/b*-axis of grains towards the direction normal to the film surface plane should increase the polarisation of the film. As the XRD results suggested, more (117)-oriented grains were found in O₂-annealed BNdT film, thus, higher $2P_r$ value were achieved as anticipated.

3. Reducing oxygen vacancy. When defect concentration (mainly oxygen vacancies) decreases, the domain pinning by the defects will decrease, and consequently, domain switching will increase, which results in a polarisation increase.

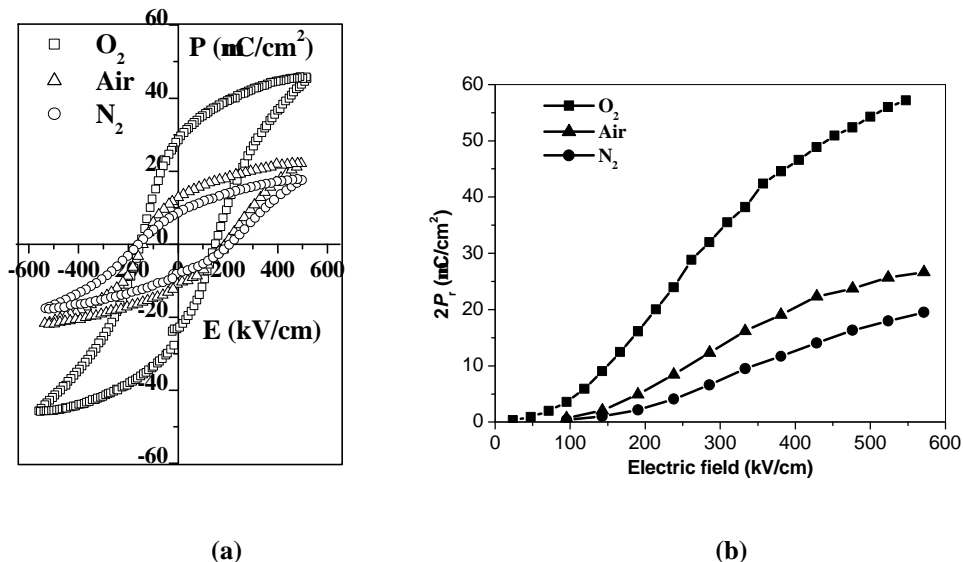


Fig. 7.32 (a) Hysteresis loops; (b) electric field dependence of $2P_r$ for the films annealed in different atmospheres

2. Leakage current characteristics

Fig. 7.33 shows the leakage current densities of BNdT films as a function of applied electric field. The three films show very distinct leakage properties: the BNdT-O₂ film has the highest dielectric breakdown field (~ 320 kV/cm) and lowest leakage current (8×10^{-7} A/cm at 200 kV/cm). In contrast, the BNdT-N₂ film has the worst properties: lowest breakdown field (~ 60 kV/cm) and highest leakage current (2×10^{-3} A/cm at 60 kV/cm). The BNdT-air film is in the middle. The value of leakage current density before obvious dielectric breakdown was: $\sim 10^{-6}$, $\sim 10^{-4}$, and $\sim 10^{-3}$ A/cm² for O₂-, air-, and N₂-annealed films respectively. Leakage in the O₂-annealed film is comparable to that of CSD-derived BNdT thin films as reported by Wu *et al.* (5.0×10^{-6} A/cm² at 100 kV/cm)¹⁹ and MOCVD-derived BSmT reported by Kojima *et al.* ($\sim 10^{-5}$ A/cm²).⁶⁰ Oxygen vacancies are generated by processes such as



and these may act as electron trap sites, causing a high leakage current.

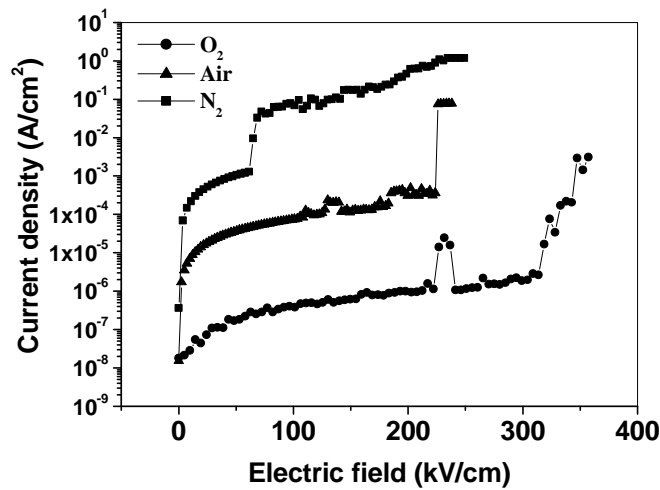


Fig. 7.33 *J-E* curves of the films annealed in different atmospheres

3. Electrical fatigue behaviour

Fig. 7.34 shows the fatigue behaviour for the films annealed in different ambiances. We can see that the O₂-annealed film has little change (~4 %) in the nonvolatile polarisation (P_{nv}) up to 5.0×10^9 read/write switching cycles at a switching electric field of $\sim \pm 330$ kV/cm (*i.e.* ± 14 V), while the air-annealed film has ~10% reduction after the same number of switching cycles. However, the N₂-annealed film has a very poor fatigue resistance, with more than 30 % reduction in P_{nv} even after just 1.0×10^8 read/write switching cycles.

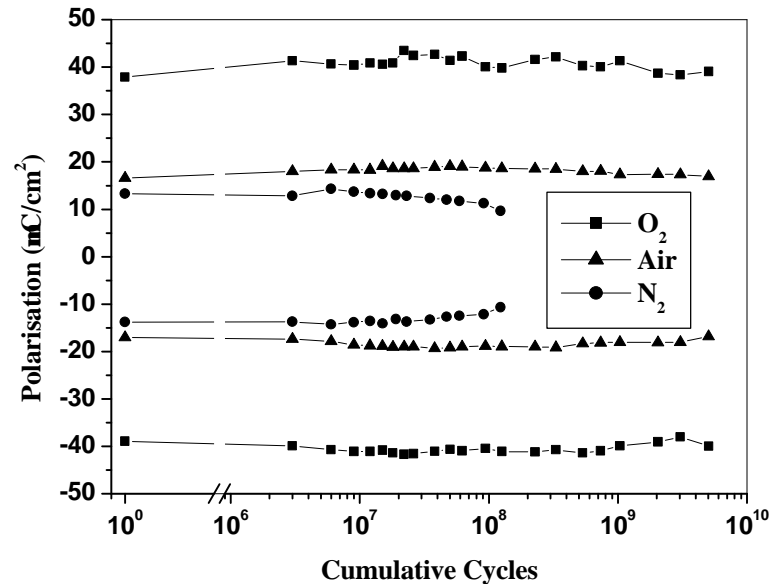


Fig. 7.34 Electrical fatigue characteristics of the films annealed in different atmospheres

There are several possible explanations for our results about fatigue properties.

1. Volatility of bismuth and stability of the metal-oxygen octahedra. Park *et al.*²³ reported fatigue-free properties in BLaT films. They ascribed this to some Bi ions near TiO₆ octahedron layers substituting with La ions and therefore, the La doping suppressing the volatility of bismuth and increasing the stability of metal-oxygen

octahedra. In our case, lower P_{O_2} during annealing may increase the volatility of bismuth ions and thus reduce the stability of the metal-oxygen octahedra. Therefore, the worst fatigue properties were obtained in N_2 -annealed films.

2. Probability of oxygen vacancy diffusion. High oxygen vacancies increase the probability of domain wall pinning.

7.5.4 Conclusions

The results of Nd-doped BiT films annealed at different oxygen partial pressure (O_2 , air, N_2) showed that:

1. Oxygen ambience affected structural properties of the films by enhancing the growth of perovskite phase (phase formation), increasing grain size (grain growth), and assisting the growth of (117)-oriented grains (crystallographic orientations).

2. As a result, the best electrical properties (high $2P_r$, low E_c , low leakage current density, and best fatigue resistance) were achieved in O_2 -annealed films.

3. Oxygen vacancies play an important role in the electrical properties of BNdT ferroelectric films.

7.6 Discussion and conclusions

Table 7.1 compares some properties of Sm- and Nd-doped BiT films annealed at 700 °C and 750 °C. From the table we can clearly see that for both film types, the 750 °C-annealed film has better electrical properties than the 700 °C-annealed one. For films annealed at the same temperature, Nd-doped films have higher $2P_r$ and lower E_c .

Table 7.1 Properties of BSmT and BNdT films annealed at 700 °C and 750 °C

700 °C						
	Grain size (nm)	Roughness (RMS; nm)	$2P_r$ ($\mu\text{C}/\text{cm}^2$)	V_c (V) E_c (kV/cm)	ϵ_r	J (A/cm^2) at 100 kV/cm
BSmT	100~150	~9.0	23.0	~6.3 ~170	~170	4.0×10^{-6}
BNdT	100~150	~9.4	35.6	~4.5 ~100		5×10^{-7}
750 °C						
BSmT	150~200	~11.0	33.4	~4.5 ~122	~202	1.5×10^{-5}
BNdT	150~200	~12.2	41.4	~4.3 ~96		2.5×10^{-6}

For comparison, a list of the other films on Pt/Si substrates developed by other techniques or doped with other lanthanide elements is displayed in Table 7.2.

Table 7.2 mainly shows La-, Nd-, Sm-doped BiT films, and some other doping elements (Eu, Pr) are also included. It can be seen that the $2P_r$ of our films are larger than the average value of La-doped films reported, and comparable to the Nd- and Sm-doped films reported by others. The E_c values of our films are also comparable to the reported values. However, the E_c values are still slightly higher than ideal values, which may be improved by doping other B-site elements, such as W, V, and Nb.⁷¹

Low temperature electrical properties of BSmT ferroelectric thin films have been investigated, suggesting that BSmT thin films are very promising for extremely low temperature nonvolatile memory applications.

Table 7.2 Properties of BLnT films on Pt-coated Si (unless specified)

	Methods	Ferroelectric properties of films		
		Films (<i>x</i> , doping level)	$2P_r$ ($\mu\text{C}/\text{cm}^2$)	E_c (kV/cm)
This study	CSD (sol-gel)	BSmT (0.50)	33.4	122
	CSD (sol-gel)	BNdT (0.50)	41.4	116
References	CSD ⁶¹	BLaT (0.75)	20.0	95
	CSD ⁶²	BLaT (0.75)	27.0	~70
	CSD ¹⁷	BLaT (0.75)	16.0	90
	PLD ³⁸	BLaT (0.75)	24.0	50
	PLD ⁶³	BLaT (0.75)	54.0	54
	MOCVD ¹ SRO/STO	BLaT (0.56)	34.0	145
	CSD ³⁵ (MOSD)	BSmT (0.85)	49.0	100
	PLD ⁶⁴	BSmT (0.70)	42.0	130
	CSD ⁶⁵	BNdT (0.46)	50.0	V_c : 10 V
	MOCVD ¹ SRO/STO	BNdT (0.56)	50.0	135
	CSD ¹⁹	BNdT (0.85)	20.0	~50
	CSD ⁶⁶	BNdT (0.85)	56.0	156
	CSD ⁶⁷	BNdT (0.50)	38.0	
	CSD ⁶⁸	BNdT (0.50)	64.0	126
	CSD ¹⁷	BNdT (0.75)	52.0	60
	CSD ⁶⁹ (Sol-gel)	BEuT (0.60)	38.0	150
	CSD ⁷⁰ (MOSD)	BPrT (0.85)	40.0	

7.7 References

- 1 T. Kojima, T. Sakai, T. Watanabe, H. Funakubo, K. Saito, and M. Osada, *Applied Physics Letters* **80**, 2746 (2002).
- 2 W. C. Shin, N. J. Seong, K. J. Choi, S. N. Ryoo, D. J. Kim, H. J. Kim, and S. G. Yoon, *Electrochemical and Solid State Letters* **7**, F15 (2004).
- 3 H. Bachhofer, H. von Philipsborn, W. Hartner, C. Dehm, B. Jobst, A. Kiendl, H. Schroeder, and R. Waser, *Journal of Materials Research* **16**, 2966 (2001).
- 4 M. Tanaka, T. Higuchi, K. Kudoh, and T. Tsukamoto, *Japanese Journal of Applied Physics Part 1-Regular Papers Short Notes & Review Papers* **41**, 1536 (2002).
- 5 W. Jo, *Applied Physics A-Materials Science & Processing* **72**, 81 (2001).
- 6 A. Garg, Z. H. Barber, M. Dawber, J. F. Scott, A. Snedden, and P. Lightfoot, *Applied Physics Letters* **83**, 2414 (2003).
- 7 R. R. Das, P. Bhattacharya, W. Perez, and R. S. Katiyar, *Japanese Journal of Applied Physics Part 1-Regular Papers Short Notes & Review Papers* **42**, 162 (2003).
- 8 J. R. Duclere, L. Hamedi, M. Guilloux-Viry, and A. Perrin, *Ferroelectrics* **254**, 53 (2001).
- 9 L. Shen, D. Q. Xiao, P. Yu, J. G. Zhu, D. J. Gao, G. L. Yu, and W. Zhang, *Materials Transactions* **44**, 1324 (2003).
- 10 P. Fuierer and B. Li, *Journal of the American Ceramic Society* **85**, 299 (2002).
- 11 T. H. Park, K. H. Yang, D. K. Kang, T. Y. Lim, K. H. Auh, and B. H. Kim, *Journal of Materials Science* **38**, 1295 (2003).
- 12 K. T. Kim and C. I. Kim, *Microelectronic Engineering* **71**, 266 (2004).
- 13 J. H. Ma, X. J. Meng, J. L. Sun, and J. H. Chu, *Journal of Inorganic Materials* **20**, 430 (2005).
- 14 H. Matsuda, S. Ito, T. Iijima, T. Mashimo, H. Okino, and T. Yamamoto, *Japanese Journal of Applied Physics Part 1-Regular Papers Short Notes & Review Papers* **43**, 6689 (2004).
- 15 Y. Yin, D. Su, J. Lou, J. Ma, W. Li, X. M. Lu, J. S. Zhu, and Y. Wang, *Integrated Ferroelectrics* **65**, 69 (2004).

- 16 T. W. Chiu, N. Wakiya, K. Shinozaki, and N. Mizutani, *Journal of the Ceramic Society of Japan* **112**, 266 (2004).
- 17 H. Maiwa, N. Iizawa, D. Togawa, T. Hayashi, W. Sakamoto, M. Yamada, and S. Hirano, *Applied Physics Letters* **82**, 1760 (2003).
- 18 T. Hayashi, N. Iizawa, D. Togawa, M. Yamada, W. Sakamoto, and S. Hirano, *Japanese Journal of Applied Physics Part 1-Regular Papers Short Notes & Review Papers* **42**, 1660 (2003).
- 19 D. Wu, A. D. Li, and N. B. Ming, *Journal of Applied Physics* **95**, 4275 (2004).
- 20 A. D. Li, D. Wu, H. Q. Ling, T. Yu, M. Wang, X. B. Yin, Z. G. Liu, and N. B. Ming, *Journal of Applied Physics* **88**, 1035 (2000).
- 21 K. Nakamoto, *Infrared Spectra of Inorganic and Coordination Compounds*. (Wiley/Interscience, London, 1970).
- 22 S. Doeuff, M. Henry, C. Sanchez, and J. Livage, *Journal of Non-Crystalline Solids* **89**, 206 (1987).
- 23 D. P. Birnie and N. J. Bendzbo, *Materials Chemistry and Physics* **59**, 26 (1999).
- 24 S. M. Tracey, S. N. B. Hodgson, A. K. Ray, and Z. Ghassemlooy, *Journal of Materials Processing Technology* **77**, 86 (1998).
- 25 M. Takashige, S. Hamazaki, Y. Takahashi, F. Shimizau, T. Yamaguchi, M. S. Jang, and S. Kojima, *Japanese Journal of Applied Physics Part 1-Regular Papers Short Notes & Review Papers* **39**, 5716 (2000).
- 26 N. Sugita, M. Osada, and E. Tokumitsu, *Japanese Journal of Applied Physics Part 1-Regular Papers Short Notes & Review Papers* **41**, 6810 (2002).
- 27 S. Kojima, A. Hushur, F. Jiang, S. Hamazaki, M. Takashige, M. S. Jang, and S. Shimada, *Journal of Non-Crystalline Solids* **293**, 250 (2001).
- 28 M. Osada, M. Tada, M. Kakihana, T. Watanabe, and M. Funakubo, *Japanese Journal of Applied Physics Part 1-Regular Papers Short Notes & Review Papers* **40**, 5572 (2001).
- 29 S. Kojima, R. Imaizumi, S. Hamazaki, and M. Takashige, *Japanese Journal of Applied Physics Part 1-Regular Papers Short Notes & Review Papers* **33**, 5559 (1994).
- 30 G. Dietz, M. Schumacher, M. Waster, S. K. Striffer, C. Basceri, and A. I. Kingon, *Journal of Applied Physics* **82**, 2359 (1997).
- 31 T. Kojima, T. Watanabe, H. Funakubo, K. Saito, M. Osada, and M. Kakihana,

- Journal of Applied Physics **93**, 1707 (2003).
- 32 W. Sakamoto, Y. Mizutani, N. Iizawa, T. Yogo, T. Hayashi, and S. Hirano, Japanese Journal of Applied Physics Part 2-Letters **42**, L1384 (2003).
- 33 R. R. Das, P. Bhattacharya, and R. S. Katiyar, Applied Physics Letters **81**, 1672 (2002).
- 34 B. Su and T. W. Button, Journal of Applied Physics **95**, 1382 (2004).
- 35 U. Chon, K. B. Kim, H. M. Jang, and G. C. Yi, Applied Physics Letters **79**, 3137 (2001).
- 36 C. H. Yang, Z. Wang, H. Y. Xu, Z. H. Sun, F. Y. Jiang, and Jpzjr Han, Journal of Crystal Growth **262**, 304 (2004).
- 37 S. T. Zhang, X. J. Zhang, H. W. Cheng, Y. F. Chen, Z. G. Liu, N. B. Ming, X. B. Hu, and J. Y. Wang, Applied Physics Letters **83**, 4378 (2003).
- 38 B. H. Park, B. S. Kang, S. D. Bu, T. W. Noh, J. Lee, and W. Jo, Nature **401**, 682 (1999).
- 39 U. Chon, J. S. Shim, and H. M. Jang, Solid State Communications **129**, 465 (2004).
- 40 R. R. Das, P. Bhattacharya, W. Perez, R. S. Katiyar, and S. B. Desu, Applied Physics Letters **80**, 637 (2002).
- 41 K. T. Kim, C. I. Kim, D. H. Kang, and I. W. Shim, Journal of Vacuum Science & Technology A **21**, 1376 (2003).
- 42 P. X. Yang, D. L. Carroll, J. Ballato, and R. W. Schwartz, Applied Physics Letters **81**, 4583 (2002).
- 43 E. Sawaguchi and L. E. Cross, Materials Research Bulletin **5**, 147 (1970).
- 44 L. E. Cross and R. C. Pohanka, Materials Research Bulletin **6**, 939 (1971).
- 45 R. C. Pohanka and L. E. Cross, Journal of Applied Physics **39**, 3992 (1968).
- 46 H. Idink, V. Srikanth, W. B. White, and E. C. Subbarao, Journal of Applied Physics **76**, 1819 (1994).
- 47 F. Xu, S. Trolier-McKinstry, W. Ren, B. M. Xu, Z. -L. Xie, and K. J. Hemker, Journal of Applied Physics **89**, 1336 (2001).
- 48 M. Dawber, S. Rios, J. F. Scott, Q. Zhang, and R. W. Whatmore, *Fundamental Physics of Ferroelectrics 2001*. (2001).
- 49 J. F. Scott, *Ferroelectric Memories*. (Springer, Berlin, 2000).
- 50 R. D. Shannon, Acta Materialia **A32**, 751 (1976).
- 51 P. H. Park, B. S. Kang, S. D. Bu, T. W. Noh, J. Lee, and W. Jo, Nature (London)

- 401**, 682 (1999).
- 52 D. Wu, Y. D. Xia, A. D. Li, Z. G. Liu, and N. B. Ming, *Journal of Applied Physics* **94**, 7376 (2003).
- 53 H. Chen, K. R. Udaykumar, and L. E. Cross, *MRS Proceeding* **433**, 325 (1996).
- 54 M. M. Gallego and A. R. West, *Journal of Applied Physics* **90**, 394 (2001).
- 55 D. Wu, A. D. Li, and N. B. Ming, *Journal of Applied Physics* **97**, 106110 (2005).
- 56 S. M. Cho and D. Y. Jeon, *Thin Solid Films* **338**, 149 (1999).
- 57 S. Takehiro, S. C. Chen, and M. Yoshimaru, *Japanese Journal of Applied Physics* **56**, 347 (1995).
- 58 J. H. Joo, J. M. Seon, Y. C. Jeon, K. Y. Oh, J. S. Roh, and J. J. Kim, *Applied Physics Letters* **70**, 22 (1997).
- 59 H. Idink, V. Srikanth, W. B. White, and E. C. Subbarao, *Journal of Applied Physics* **76**, 1819 (1994).
- 60 T. Kojima, T. Watanabe, H. Funakubo, K. Saito, M. Osada, and M. Kakihana, *Journal of Applied Physics* **93**, 1707 (2003).
- 61 X. Wang and H. Ishiwara, *Applied Physics Letters* **82**, 2479 (2003).
- 62 U. Chon, G. C. Yi, and H. M. Jang, *Applied Physics Letters* **78**, 658 (2001).
- 63 Y. Fujisaki, K. Iseki, and H. Ishiwara, *Journal of Applied Physics* **42**, L267 (2003).
- 64 X. B. Hu, A. Garg, J. Wang, and Z. H. Barber, *Integrated Ferroelectrics* **61**, 123 (2004).
- 65 R. E. Melgarejo, M. S. Tomar, S. Bhaskar, P. S. Dobal, and R. S. Katiyar, *Applied Physics Letters* **81**, 2611 (2002).
- 66 G. Jang, K. Kim, and D. Yoon, *Journal of Korean Physics Society* **45**, 693 (2004).
- 67 Y. C. Chen, Y. M. Sun, C. P. Lin, and J. Y. Gan, *Journal of Crystal Growth* **268**, 210 (2004).
- 68 H. Uchida, H. Yoshikawa, I. Okada, H. Matsuda, T. Iijima, T. Watanabe, T. Kojima, and H. Funakubo, *Applied Physics Letters* **81**, 2229 (2002).
- 69 W. J. Kim, S. S. Kim, K. W. Jang, J. C. Bae, T. K. Song, and Y. I. Lee, *Journal of Crystal Growth* **262**, 327 (2004).
- 70 U. Chon, J. S. Shim, and H. M. Jang, *Journal of Applied Physics* **93**, 4769

(2003).

- ⁷¹ E. K. Choi, S. S. Kim, J. K. Kim, J. C. Bae, W. J. Kim, Y. I. Lee, and T. K. Song, *Japanese Journal of Applied Physics Part 1-Regular Papers Short Notes & Review Papers* **43**, 237 (2004).

Chapter 8 Piezoelectric properties of Sm-doped bismuth titanate ferroelectric thin films

8.1 Motivation

Along with high switching polarisation and excellent fatigue resistance, the high values of piezoelectric coefficients of lead-free bismuth-layered perovskite thin films offer promise for MEMS.^{1,2} Recently, Maiwa *et al.*² have demonstrated that BNdT thin films are very promising candidates for lead-free thin-film piezoelectrics. However, detailed information about the electromechanical properties of lead-free bismuth-layered perovskite thin films is not yet available. Results of piezoelectric properties, such as piezoelectric constant (d_{33}) and effective electrostriction coefficients (Q_{eff}), are normally essential input parameters for thermodynamical calculations and are very useful in the design and fabrication of MEMS. The determination of these parameters in thin films can also provide fundamental information when compared with corresponding bulk materials, which can elucidate the substrate clamping effect, domain contribution and size effect. Direct strain measurements are difficult in thin films due to an extremely low deformation level³.

For ferroelectric materials with a centrosymmetric paraelectric phase, the piezoelectric effect can be considered as the electrostriction effect biased by the spontaneous polarisation P :⁴

$$d_{33} = 2Q_{11}\epsilon_{33}P_s \quad , \quad (8.1)$$

where d_{33} is the piezoelectric coefficient of the film, Q_{11} is the electrostriction coefficient, ϵ_{33} is the dielectric constant, P_s is the spontaneous polarisation. Considering the phenomenological equation regarding the intrinsic piezoelectric effect

$$d_{zz} = 2Q_{eff(E)}\epsilon_{33}P_s \quad , \quad (8.2)$$

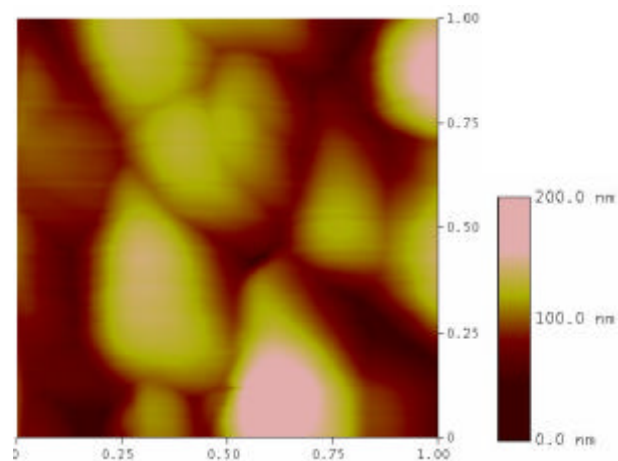
where d_{zz} is the piezoelectric coefficient along the film normal, $Q_{eff(E)}$ is the effective electrostriction coefficient which may depend on the domain configuration (*i.e.* on the applied electric field). Therefore, the absolute value of Q_{eff} can be estimated if d_{zz} , ϵ_{33} and P_s are known. Effective electrostriction coefficients (Q_{eff}) are essential input parameters for thermodynamical calculations and are very useful in the design and fabrication of MEMS.

Here we report the use of PFM to characterise the piezoelectric properties of BSmT films and their nanoscale piezoresponse behaviour, which include observation of domain switching, and determination of piezoelectric constant (d_{33}) and effective electrostriction coefficients (Q_{eff}). The samples used in this chapter are PLD-grown and CSD-derived BSmT films, as described in the previous chapters.

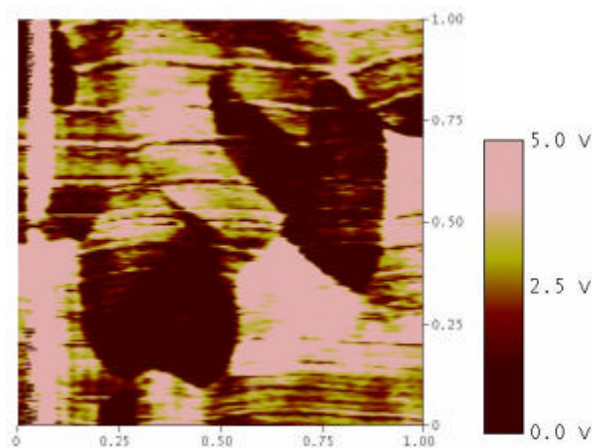
8.2 Results and discussion

8.2.1 Domain imaging

Fig. 8.1 shows simultaneously obtained topographic and piezoresponse images of a PLD-grown ~470-nm-thick polycrystalline BSmT film after poling with 10 V DC bias. The details of the film preparation were described in Section 6.2.1.2, and the film was grown at 750 °C and 225 mJ.



(a)



(b)

Fig. 8.1 Simultaneously obtained: (a) topographic and (b) piezoresponse images of a PLD-grown BSmT film. Bright and dark regions on the piezoresponse image correspond to positive and negative domains, respectively (The scan area is 1.00 $\mu\text{m} \times 1.00 \mu\text{m}$)

The topographic image reveals the crystallite structure of the film with clearly

resolved morphological features. The corresponding piezoresponse image shows regions of bright, dark and grey contrast. The bright areas and dark areas represent regions with opposite d_{33} piezoelectric constants and antiparallel polarisation vectors normal to the film surface. By monitoring the phase of the piezoresponse signal it was determined that bright regions in Fig. 8.1(b), which vibrate in phase with the AC imaging voltage, represent positive domains (polarisation is toward the bottom electrode), whereas dark regions correspond to negative domains with the polarisation vector orienting upward. From comparison of crystallite structure with the piezoresponse image, a strong effect of the film crystallinity on the domain arrangement can be seen: quite often domains are limited by the grain boundaries.

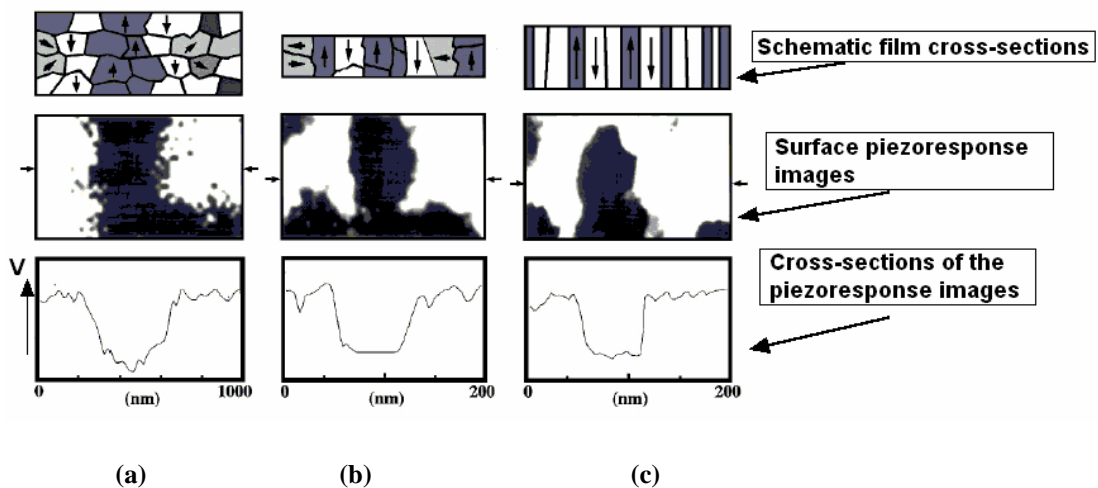


Fig. 8.2 Schematic diagrams showing possible film microstructures, piezoresponse images and corresponding cross-sectional plots illustrating different SFM imaging resolutions: (a) relatively thick film; (b) relatively thin film; (c) columnar film. Cross sections were taken along the lines marked by arrows in the piezoresponse images⁵

A piezoresponse image of a well-oriented thin film, such as a single-crystal or epitaxial one, can be easily understood, provided the film is fully characterised prior to the PFM measurements. In a film oriented along the polar axis, dark and bright regions correspond to opposite domains with the polarisation vector normal to the film plane. However, for polycrystalline films, piezoresponse images present a much

more complex variation of contrast that reflects the complex arrangement of domains in the polycrystalline ferroelectric films.

A problem of microstructure-domain correlation in ferroelectric thin films is one of the important issues that can be addressed using PFM.

There are several possible reasons for grey piezoresponse contrast:⁵

1. There may be several randomly polarised grains stacked in the direction normal to the film plane (Fig. 8.2(a)). The piezoresponse signal detected in the PFM piezoresponse mode is integrated over the entire range of the film thickness, and its amplitude and the phase provide information about the integral strain induced along the film thickness and about the direction of the polarisation, respectively. The applied electric field compresses grains with a given direction of polarisation and expands grains with opposite polarisation. If all grains in the direction normal to the film surface are polarised randomly, the integral piezoelectric response will be equal to zero because of compensation. As a result, grey contrast will be observed in the piezoresponse image. This situation is likely to occur in films with grains that are relatively small compared with the film thickness.⁶

2. There could be domains with the polarisation vector deviating from the direction normal to the film plane. The piezoelectric signal from these domains will be weaker than from domains oriented with their polar axis normal to the surface plane of the film, and in the PFM piezoresponse images they should be represented by regions with contrast intermediate between dark and bright.

In our study, XRD analysis showed that there are fractional amounts of (00 l)-, and (117)-oriented grains in the film (see Figs. 6.2 and 6.4). Therefore, taking into account

the BSmT film thickness of 470 nm, which is relatively thick, it is reasonable to assume that grey regions in the piezoresponse images in Fig. 8.1 represent domains with the polarisation vector deviating from the direction normal to the film plane (Fig. 8.2(a)).

3. There may be an amorphous or a non-ferroelectric structure that does not exhibit piezoelectric properties. Confirmation of this hypothesis may require localised diffraction analysis to verify that the particular grey area is indeed amorphous.

8.2.2 Domain manipulation (writing and switching)

For a CSD-derived 700 °C-fabricated ~370 nm-thick BSmT film (preparation details were described in Section 3.1.2), a 10 $\mu\text{m} \times 10 \mu\text{m}$ area was scanned by PFM and the topographic and piezoresponse images are shown in Figs. 8.3(a) and 8.3(b), respectively. The piezoresponse image shows a uniform distribution, suggesting random orientation of the polarisations.

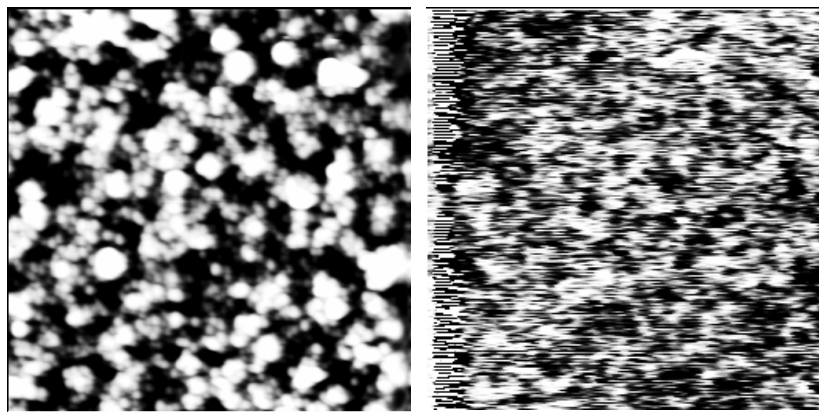
To study the switching properties of the BSmT thin film, a 6 $\mu\text{m} \times 6 \mu\text{m}$ square was written with -6 V applied between the tip and bottom electrode to form a dark background region. Subsequently, a further -10 V and -15 V were applied on the same area. The central dark square area became darker and darker with the increasing poling voltages, as shown in Figs. 8.3(c)-(e).

Then, a 2 $\mu\text{m} \times 2 \mu\text{m}$ square was written with +15 V within the background area (Fig. 8.3(f)). It was found that the BSmT thin films can be nearly uniformly polarised without being affected by the film roughness (the RMS roughness is about 12 nm).

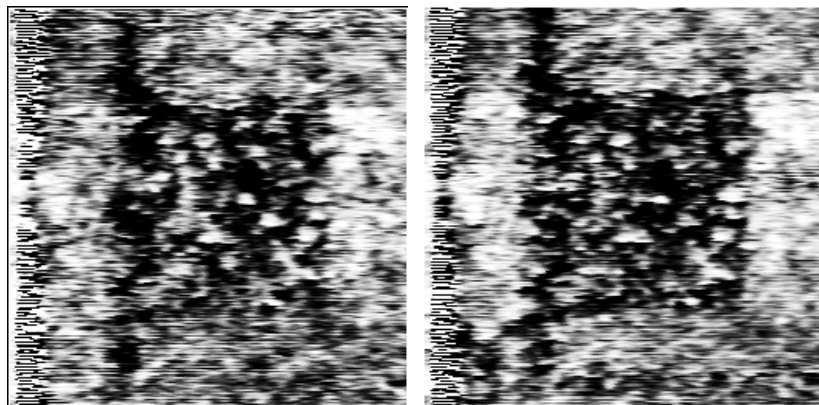
Subsequently, the square with the size of 6 $\mu\text{m} \times 6 \mu\text{m}$, which was used as a dark

background with the white square in its central area, was completely poled by a +15 V scanning. After this operation, the area was switched to the opposite polarisation direction, which was denoted by the white colour, as shown in Fig. 8.3(g).

To further confirm the switching, a $2\ \mu\text{m} \times 2\ \mu\text{m}$ size within the central area of the white square was switched by applying -15 V voltage, which turned the area dark, as shown in Fig. 8.3(h).



(a) Topography ($10\ \mu\text{m} \times 10\ \mu\text{m}$) (b) Piezoresponse (original)



(c) -6 V poling

(d) -10 V poling

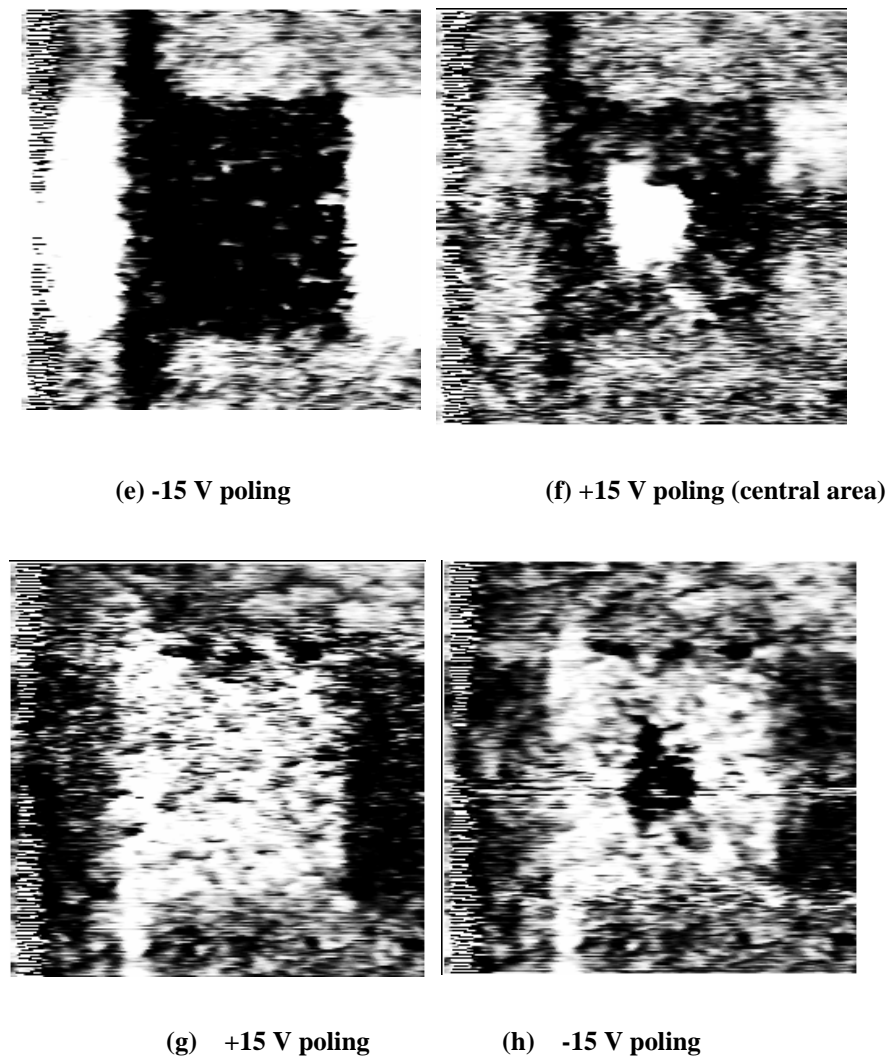


Fig. 8.3 Simultaneously obtained (a) topographic and (b) domain images of a BSmT thin film. (c)-(h): The white area was written by positive voltages, while the black region was written by negative voltages

From this simple demonstration, we can see that domain manipulation would be very useful to fabricate nanoscale devices, after careful domain writing and switching.

8.2.3 Local ferroelectric measurement - d_{33} hysteresis measurement

Fig. 8.4(a)-(d) shows piezoelectric hysteresis loops obtained at different locations (grains marked with A, B, C, and D) at the surface of the CSD-derived BSmT film (see Section 8.2.2) on a Pt-coated silicon substrate. Fig. 8.4(e) shows the surface

image marked with the grains from which the loops were measured. We can see that the shapes of the loops vary with different locations. This large spatial variation may stem from the following:

1) Different crystallographic orientations.^{7,8,9} As stated in previous chapters, CSD-derived BSmT films on platinised silicon substrates are polycrystalline and randomly oriented. Since the BSmT films are highly anisotropic with polar axis in the *a-b* plane, large differences in polarisation between grains would be expected.

2) Fluctuations of chemical composition in different grains. During the decomposition of the precursor during fabrication, small deviations in chemical composition may be possible, and there may be bismuth-excess and bismuth deficient grains, which can greatly affect polarisation.

3) An inhomogeneous distribution of the tip-generated field⁹ (combined with a grain size effect). Fig. 8.5 illustrates the different domain switching process during the macroscopic (plane plate capacitor) and microscopic (PFM) cases. In the macroscopic scenario (Fig. 8.5(a)), a number of domains nucleate at the electrodes, and the domain size distribution during the growth process determines the hysteresis loop shape. In PFM, the electric field is concentrated directly below the tip, resulting in preferential domain nucleation at the tip-surface junction (Fig. 8.5(b)).

The reversal of the electrical polarisation in ferroelectrics is a complicated process. When switching occurs in the inhomogeneous electric field of the AFM tip, the general stages of the polarisation reversal are the same as in the case of a 'classic' switching in a homogeneous field created by plain electrodes. However, the character of these stages may significantly vary relative to that in homogeneous fields. The switching starts with nucleation of a new domain near the tip of the AFM. The

direction of the polarisation vector of this domain coincides with that of the normal component of the external electric field. The newly formed domain then expands by motion of the domain walls.

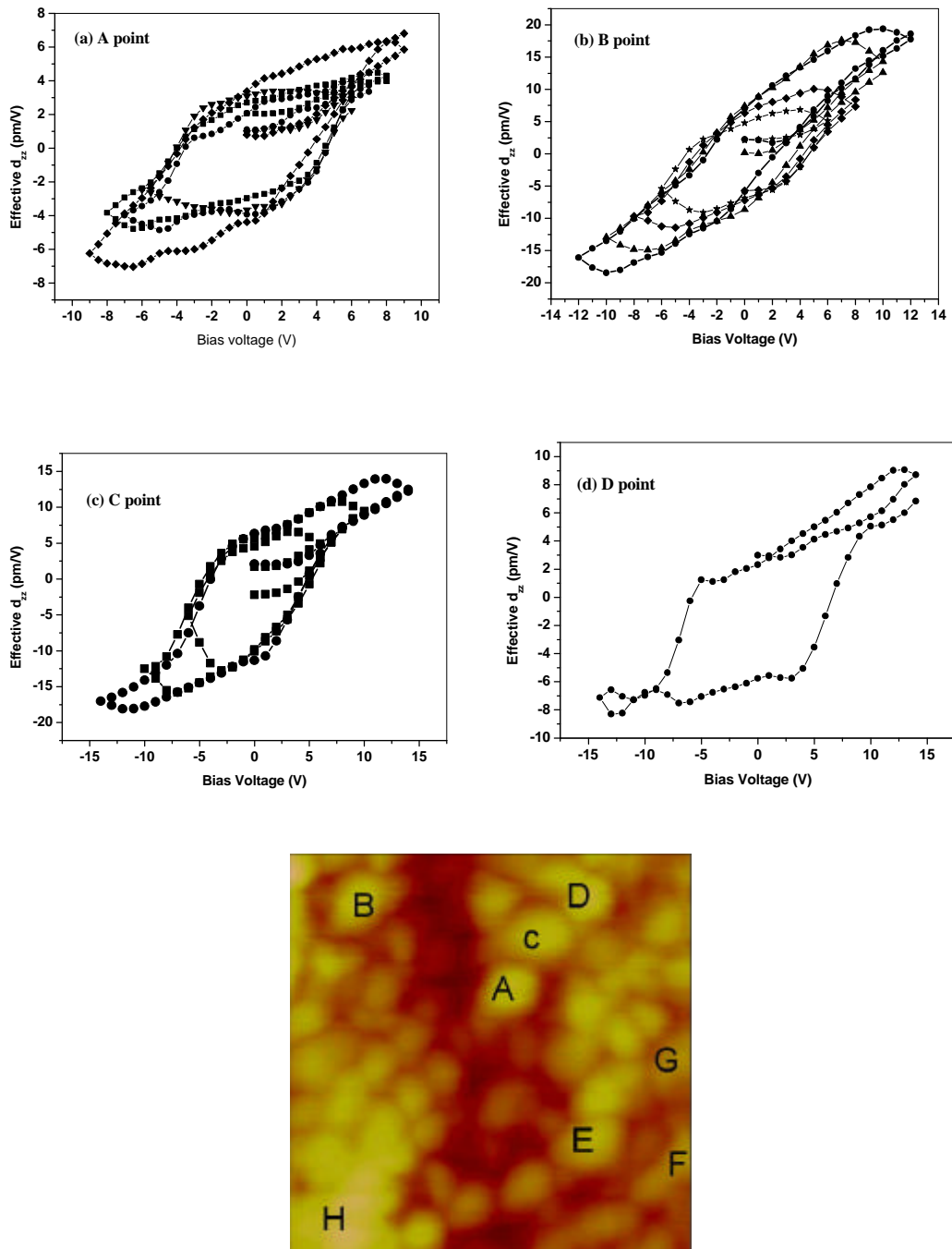


Fig. 8.4 (a)-(d): Piezoelectric hysteresis loops measured with different applied voltages, obtained at different locations at the surface of a CSD-derived BSmT film (only data from A, B, C, and D points are shown here). (e): surface image ($2\ \mu\text{m}$ by $2\ \mu\text{m}$) marked with the grains from which the loops were measured

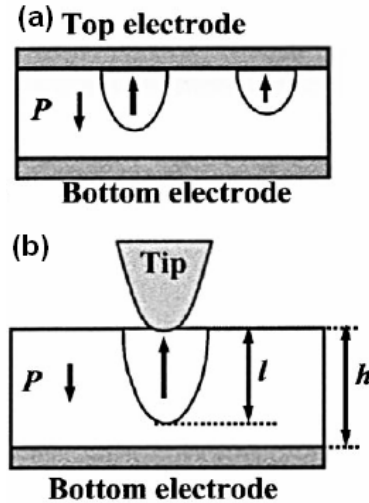


Fig. 8.5 Schematics of the polarisation switching process in a) macroscopic hysteresis loop measurement; b) in the PFM experiment⁹

4) Grain size effect. Shvartsman *et al.*¹⁰ observed a clear correlation between the values of the effective piezoelectric coefficients and the size of the respective grains in relaxor ferroelectric thin films $\text{Pb}(\text{Mg}_{1/3}\text{Nb}_{2/3})\text{O}_3\text{-PbTiO}_3$. In their study, small grains exhibit slim hysteresis loops with low remanent d_{eff} (effective d_{33}), whereas relatively high piezoelectric activity and pronounced coercivity were characteristic of larger grains. The origin of both effects was attributed to the existence of strong internal bias field and mechanical clamping. In our measurement, no systematic correlation between grain size and polarisations were observed due to the strong anisotropy of the film (see Fig. 8.4), however, some variations may stem from the grain size, which may account for the differences in mechanical clamping.

8.2.4 Local piezoelectric measurement – Q_{eff}

As just mentioned, to determine Q_{eff} , the measurement of d_{zz} , \mathbf{e}_{33} and P_s are needed. Therefore, the experimental procedure had three parts.

1. Measurement of d_{zz} (see Section 3.2.1). The hysteresis loops were obtained by sweeping the bias voltage and recording the piezoresponse signal.

2. Measurement of ϵ_{33} . The measurements were carried out using an HP 4192A impedance analyser. A capacitor structure of $200\ \mu\text{m} \times 200\ \mu\text{m}$ was used, as shown in Fig. 8.12. An AC bias of 50 mV at 1 kHz coupled with a DC bias of $0 \rightarrow 14\ \text{V} \rightarrow -14\ \text{V} \rightarrow 0$ at a step of 1 V cycle was applied to the capacitor, while the capacitance at each point was measured, then converted to the dielectric constant at each DC bias. e -V loops were then drawn.

3. Measurement of P_s . The measurement adopted the structure shown in Fig. 8.6 and a RT 6000 ferroelectric measurement system was used. P - V hysteresis loops were recorded at different bias voltages at 1 kHz.

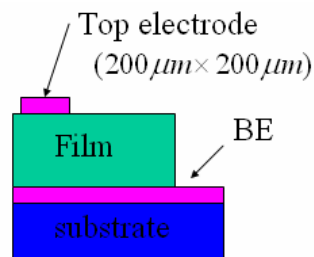
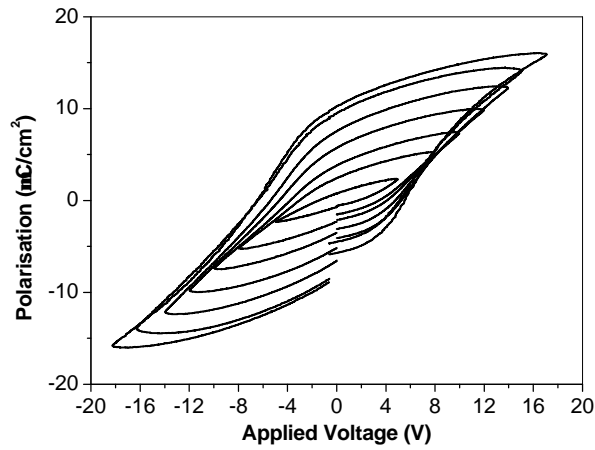
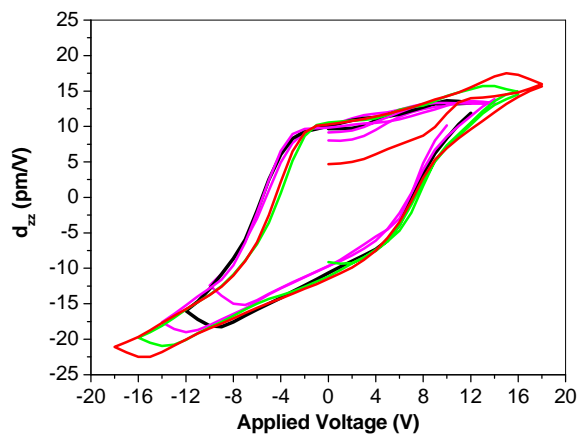


Fig. 8.6 Schematic of capacitor structure for macroscopic electric property measurements

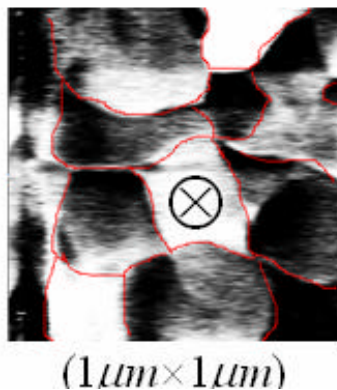
Typical P - V hysteresis loops measured at different applied bias voltages on a PLD-grown BSmT film (doping level: $x = 0.70$; see Section 6.4) are shown in Fig. 8.7(a). The corresponding d_{zz} - V hysteresis loops measured at different maximum applied bias voltages are shown in Fig. 8.7(b). A high similarity of the two loops was achieved, validating the results of PFM measurement, although the measurement was carried out on one grain of the film surface, as shown in Fig. 8.7(c).



(a)



(b)



(c)

Fig. 8.7 (a) Typical P - V hysteresis loops measured at different applied bias voltages; (b) Corresponding d_{zz} - V hysteresis loops measured at different applied bias voltages; (c) The film surface of PFM measurement (the circle shows the measurement point)

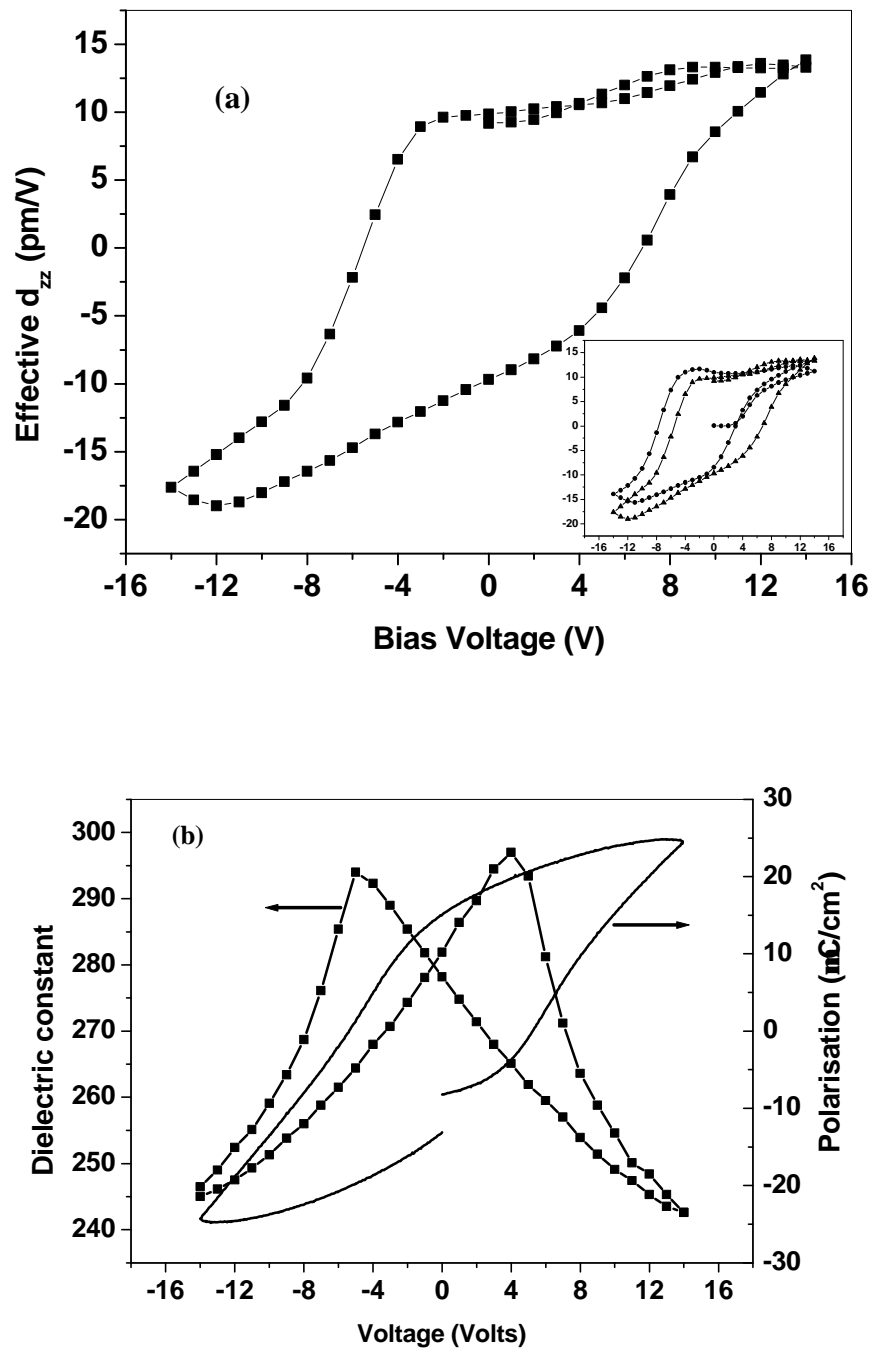


Fig. 8.8 (a) Piezoelectric, (b) dielectric and polarisation hysteresis loops of BSMT films. Inset of (a): Piezoelectric hysteresis loops measured at the same point

Fig. 8.8(a) shows a typical local piezoelectric loop measured by PFM obtained from the same PLD-grown film. Corresponding macroscopic dielectric constant, applied voltage (e - V) and polarisation, applied voltage (P - V) loops measured using the

deposited electrodes ($200\ \mu\text{m} \times 200\ \mu\text{m}$) are shown in Fig. 8.8(b). The coercive voltage $((+V_c)-(-V_c))/2$ determined by d_{33} - V , P - V and e - V loops are 6.2 V, 5.3 V, and 4.5 V respectively (with the coercive voltage for e is defined as a field at the maxima of e - V curves). d_{33} - V and e - V hysteresis measurements are quasistatic (the corresponding frequency is in the order of mHz), whilst polarisation taken at a frequency of 1 kHz is dynamic. Therefore we would expect the coercive voltage derived by e - V to be smaller than that of P - V , as observed, since it is a typical feature of ferroelectric thin films to display smaller static coercive fields than dynamic ones. However, the coercive voltage of the d_{33} loop shows the largest value despite the quasistatic measurement, which may be the result of electric field concentration directly below the tip, resulting in only a small volume of domain switching at the tip-surface junction. In the P - V measurement, a possible macroscopic scenario is that a number of domains nucleate at the top electrode at the same time⁹. An alternative explanation is that, in d_{33} measurement, only a partial electric field is applied due to a poor electrical contact between the tip and the bare film surface¹¹. It can also be seen that there is a horizontal asymmetry of the d_{33} -loop, due either to asymmetry of the boundary conditions at the top and bottom interfaces¹² or to a larger internal space charge field resulting from trapped electronic charges near the ferroelectric-electrode interfaces^{13,14}.

Imprint behaviour, defined as a preference of one polarisation state over the opposite one¹⁵, is also observed. The most important manifestations of imprint are a shift of hysteresis loop along the voltage axis and the instability of one of the polarisation states. However, only application of PFM can provide a nanoscale insight into the scaling and intrinsic variability issues^{16,17}. For macroscopic measurement of polarisation, this may result in a shift of the hysteresis loop along the electric field

axis, as the vertical position of the loop is arbitrarily set. This is because the polarisation measurement is performed by charge integration and thus requires an integration constant which is chosen arbitrarily. Therefore, for the measurement systems, the polarisation hysteresis loops are usually centred along the polarisation axis.¹⁸ These result in a shift along the electric field axis which is described in terms of an internal bias field.¹⁹ In contrast, the displacement measured in any piezoelectric-based method is well defined and therefore has an absolute value.

The inset of Fig. 8.8(a) shows two typical piezoresponse loops measured at the same point, separated by a series of switching pulses. These display a consistent d_{33} - V property for positive polarisation direction, different negative switching behaviour, and vertical and horizontal shifts. These phenomena may stem from the existence of an internal space charge field, which causes a preferential downward pre-polarisation state and the corresponding imprint. Other mechanisms have been proposed, such as domain locking near the ferroelectric-electrode interface,²⁰ mechanical strain conditions at the interface,^{21, 22} and residual stress in the grains.²³ A horizontal shift in d_{33} - V loops has changed the asymmetry of the loop by causing different positive and negative coercive field, as discussed above.

The electric field dependence of the Q_{eff} derived using Equation (8.2) and data from Fig. 8.8 for the entire hysteresis loop is shown in Fig. 8.9.

It can be seen that Q_{eff} is rather stable ($(1.27-1.72) \times 10^{-2} \text{ m}^4/\text{C}^2$) when the applied field, and consequently the domain structure of the films, change dramatically, except where this method is not applicable, because P_s is close to zero, when V is close to V_c .²⁴

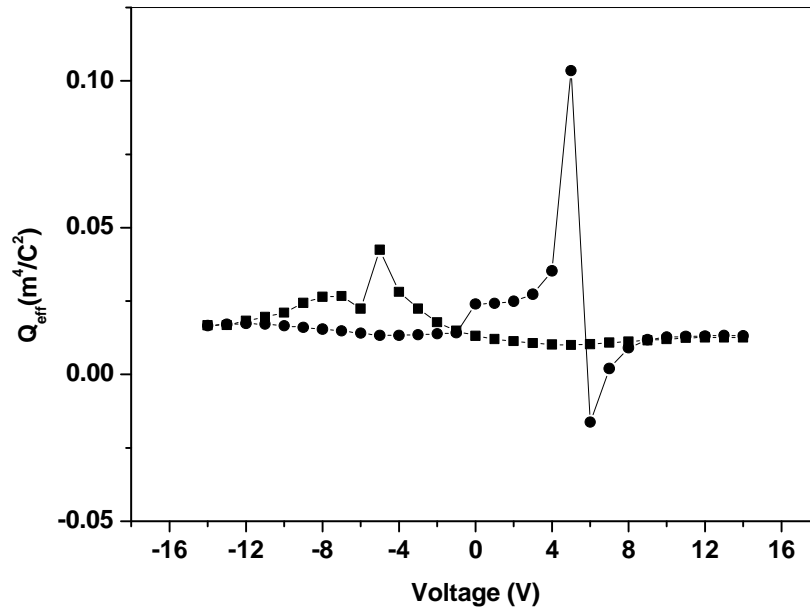


Fig. 8.9 Q_{eff} of BSmT films as a function of applied bias voltage

In-field hysteresis loops were measured, with the probing AC voltage superimposed on the triangular waveform DC bias in order to measure the piezoelectric constant as a function of the applied field simultaneously. Therefore, the high voltage linear part of the loop is due to a real increase of the piezoelectric constant and can be used to estimate the local Q_{eff} . Equation (8.3) shows the relationships by considering the total polarisation P of the poled volume²⁵.

$$d_{zz} = 2Q_{eff} \mathbf{e}_{33} (P + \mathbf{e}_{33} E) \quad (8.3)$$

The slope of the linear component can be obtained by differentiating Equation (8.3) with respect to E for those regions where the ferroelectric polarisation P is constant, *i.e.* at the saturation stage (which is very important):

$$\frac{\Delta d_{zz}}{\Delta E} = 2Q_{eff}(\mathbf{e}_{33})^2 \quad (8.4)$$

From the above analysis and other reports²⁴, $Q_{eff(E)}$ is independent of E at a high electric field ($V > V_s$, where V_s is the bias voltage beyond which the polarisation is saturated). We also assume e_{33} is a constant at a high bias electric field, beyond the saturation of polarisation (e_{33} under high DC bias were unable to be measured for Fig. 8.8(b)).

When $E = 0$, the relations between the P_r and remanent d_{zz} , $(d_{zz})_r$, is given by

$$(d_{zz})_r = 2Q_{eff(V=0)}\mathbf{e}_{33(V=0)}P_r \quad (8.5)$$

So $Q_{eff(V>V_s)}$ and $Q_{eff(V=0)}$ can be estimated respectively from Equations (8.4) and (8.5) if the e_{33} at zero bias and beyond saturation are known from other measurements and $(d_{zz})_r$ is determined.

Fig. 8.10 shows effective d_{zz} - V loops measured at higher electric fields in order to obtain the linear part of the loop with a minimum effect of the unsaturated part of the loop. The remanent d_{zz} (measured at zero bias field) is almost constant beyond 14 V, corresponding to saturated polarisation. The inset shows a sample of a linear fit of hysteresis loop when $V_{max} = 40$ V, which is the equipment limitation. Linear fits of the loops at various V_{max} (24 V ~ 40 V, not all shown here) have been carried out and the values are quite consistent with a range of 0.577~0.628 pm/V². Combining this value with Equation (8.5), and a film thickness of ~400 nm, $e_{33} = 280 e_0$ at zero bias and

$242e_0$ beyond $V_{\max} = 14 \text{ V}$, $(d_{zz})_r$ is $10.5\sim 12.7 \text{ pm/V}$ and $P_r = 15.1 \text{ } \mu\text{C/cm}^2$.

Substituting these values into Equations (8.4) and (8.5), the $Q_{\text{eff}} (V > V_s)$ and

$Q_{\text{eff}} (V=0)$ are $(2.67 \pm 0.12) \times 10^{-2} \text{ m}^4/\text{C}^2$ and $(1.55 \pm 0.15) \times 10^{-2} \text{ m}^4/\text{C}^2$, respectively.

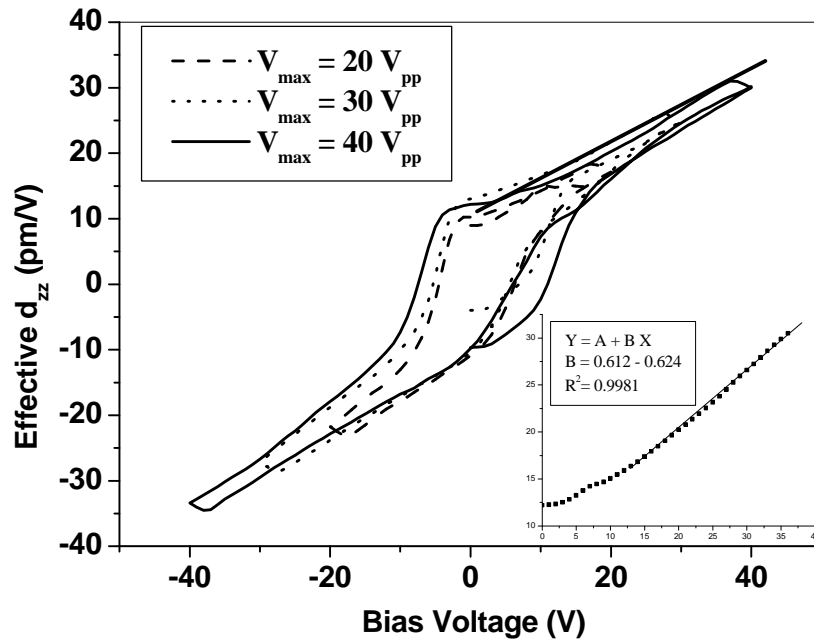


Fig. 8.10 Effective d_{zz} - V loops at higher electric fields. Inset: a linear fit of hysteresis loop when $V_{\max} = 40 \text{ V}$

Table 8.1 Values of Q_{eff} derived using the different voltage ranges

Method	Q_{eff} ($\times 10^{-2} \text{ m}^4/\text{C}^2$)	$Q_{\text{eff}} (V > V_s)$ ($\times 10^{-2} \text{ m}^4/\text{C}^2$)	$Q_{\text{eff}} (V=0)$ ($\times 10^{-2} \text{ m}^4/\text{C}^2$)
$d_{zz} = 2Q_{\text{eff}}(E) \mathbf{e}_{33} P_s$	1.27~2.43		1.31
$\frac{\Delta d_{zz}}{\Delta E} = 2Q_{\text{eff}} (\mathbf{e}_{33})^2$	1.40~2.79	2.67±0.12	1.55±0.15
$(d_{zz})_r = 2Q_{\text{eff}}(V=0) \mathbf{e}_{33}(V=0)^2 P_r$			

The values of Q_{eff} derived using the different voltage ranges are shown in Table 8.1.

From Table 8.1, we can see that $Q_{eff(V=0)}$ are basically the same because the same methods were adopted at zero bias field. The variation is due to a slightly higher zero bias d_{zz} value being adopted when calculating high bias voltage value.

Values of Q_{eff} and d_{zz} (biased and non-biased) obtained in this work are reported in Table 8.2 and are compared with other ferroelectric materials reported by other authors.

Table 8.2 Piezoelectric parameters of some ferroelectric materials

Materials	Q_{eff}	d_{zz} (pm/V)	d_{zz} (pm/V)
	($\times 10^{-2} \text{ m}^4/\text{C}^2$)	Zero bias	Bias
BSmT (this work) (370 ~ 450 nm)	1.27-2.79	10.5~12.7	~30.0 (at 40 V)
PbZr _x Ti _{1-x} O ₃ (PZT) film (250 ~ 350 nm)	1.2~2.5 ²⁴		
SBT film (~ 300 nm)	2.0~4.0 ²⁴	8 ²⁴ (~ 300 nm)	17 at 300 kV/cm ²⁶ (~ 300 nm)
BiT film (~ 250 nm)	0.142~0.152 ⁴	4 ²⁷ (~ 200 nm)	
BiT ceramics		20 ²⁷	
Nd-doped BiT film		38 ² (~ 1.0 μm)	
Pr-doped BiT film		60 ²⁸ (~ 1.5 μm)	

From Table 8.2, we can see that Q_{eff} value of the BSmT films reported in this work is comparable to typical film piezoelectrics PZT and SBT, and much higher than undoped BiT films. For piezoelectric coefficients, the BSmT film has a much higher d_{zz} than SBT films, BiT ceramics and its thin films. It is lower than other much thicker lanthanide-doped bismuth titanate films (1- μm thick Nd-doped and 1.5- μm Pr-doped BiT films). Strong thickness-dependence of piezoelectric properties has been observed in $\text{Pb}(\text{Mg}_{1/3}\text{Nb}_{2/3})\text{O}_3\text{-}0.1\text{PbTiO}_3$ thin films²⁹ and 400% larger d_{33} values have been obtained in a 400-nm-thick film than a 200-nm-thick one. Therefore for a detailed comparison a comparably thick BSmT film would be necessary. In conclusion, Sm-doped BiT films are promising piezoelectric materials for MEMS use.

8.2.5 Piezoelectric properties of PLD- and CSD-derived BSmT films

Piezoelectric properties of both film types (PLD and CSD) were measured by the PFM. Fig. 8.11 shows topographic and piezoresponse images of PLD-grown (Figs. 8.11(a) and 8.11(b) and CSD-derived (Figs. 8.11(c) and 8.11(d)) films (Figs. 8.11(a) and 8.11(c) are topographic images and Figs. 8.11(b) and 8.11(d) are piezoresponse images). By monitoring the phase of the piezoresponse signal, it was determined that the bright regions in Figs. 8.11(b) and 8.11(d), which vibrate in phase with the AC imaging voltage, represent positive domains (polarisation is towards the top electrodes), whereas dark regions correspond to negative domains with the polarisation vector oriented downward.

From the figures we can see that the PLD-grown film has a more distinct domain structure, which may stem from a higher piezoelectric coefficient than that of the CSD-derived film, and/or different grain structures of the films. The columnar grains

of the PLD films are more likely to lead to single-grain domains through the film thickness, which can be efficiently switched in comparison with more multi-grain domains for CSD films. We can also see, in top-view images, a strong correlation between topographic grain structure and domain structure in both film types.

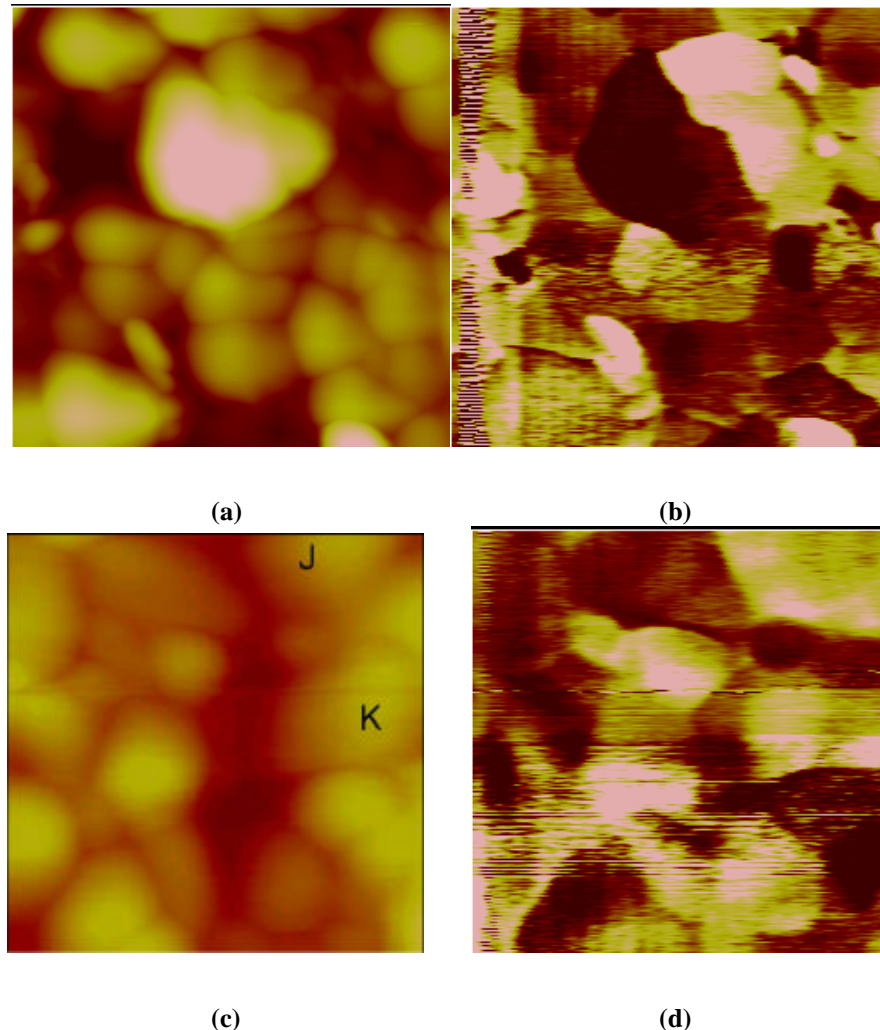


Fig. 8.11 ($1\ \mu\text{m} \times 1\ \mu\text{m}$) PFM images of (a) (b) PLD-grown; (c) (d) CSD-derived BSmT films

To further characterise the films, the piezoresponse signal was measured as a function of the poling voltage. The probing tip was positioned at the centre of a negatively polarised grain where the DC voltage poling pulses were applied. The clear ferroelectric hysteresis behaviour of the piezoresponse signal is a proof of domain polarisation reversal occurring under the applied voltages. The large spatial variation of the local PFM measurement, *i.e.* different loop shapes for different grains were

observed in both film types, as shown previously for CSD-derived films.

Typical square-shaped saturated d_{zz} -loops of PLD-grown and CSD-derived films measured at different bias voltages are shown in Figs. 8.12(a) and 8.12(b), suggesting distinct local scale ferroelectricity. The remanent d_{zz} , i.e. d_{zz} measured at zero bias field, is ~ 10.5 pm/V and ~ 6.1 pm/V for PLD and CSD films, respectively.

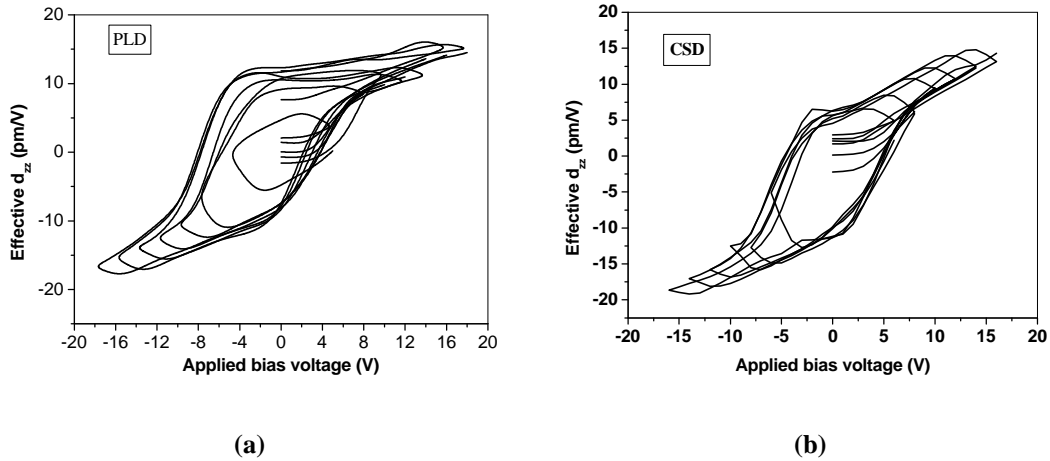


Fig. 8.12 Typical d_{zz} -loops of (a) PLD-grown films, (b) CSD-derived films measured at different applied bias voltages

Since normal hysteresis measurement captures the superpositive response of all of the linear and non-linear components whilst the remanent hysteresis measurement subtracts the nonswitching part of the normal hysteresis loop, the remanent hysteresis loops are more like the shapes of effective d_{zz} - V loops (*i.e.* more square). The P_r values derived from remanent hysteresis loops are ~ 15 $\mu\text{C}/\text{cm}^2$ and ~ 10 $\mu\text{C}/\text{cm}^2$, respectively, for PLD- and CSD-derived BSmT films. These values correlate well with the remanent d_{zz} values of both films, which are ~ 10.5 pm/V and ~ 6.1 pm/V for PLD- and CSD-derived films, respectively.

To reveal more detailed comparison between PLD and CSD BSmT films, the ferroelectric hysteresis and remanent hysteresis loops of the two film types are shown in Fig. 8.13 (The details of the measurement were described in Section 3.2.2.2.)

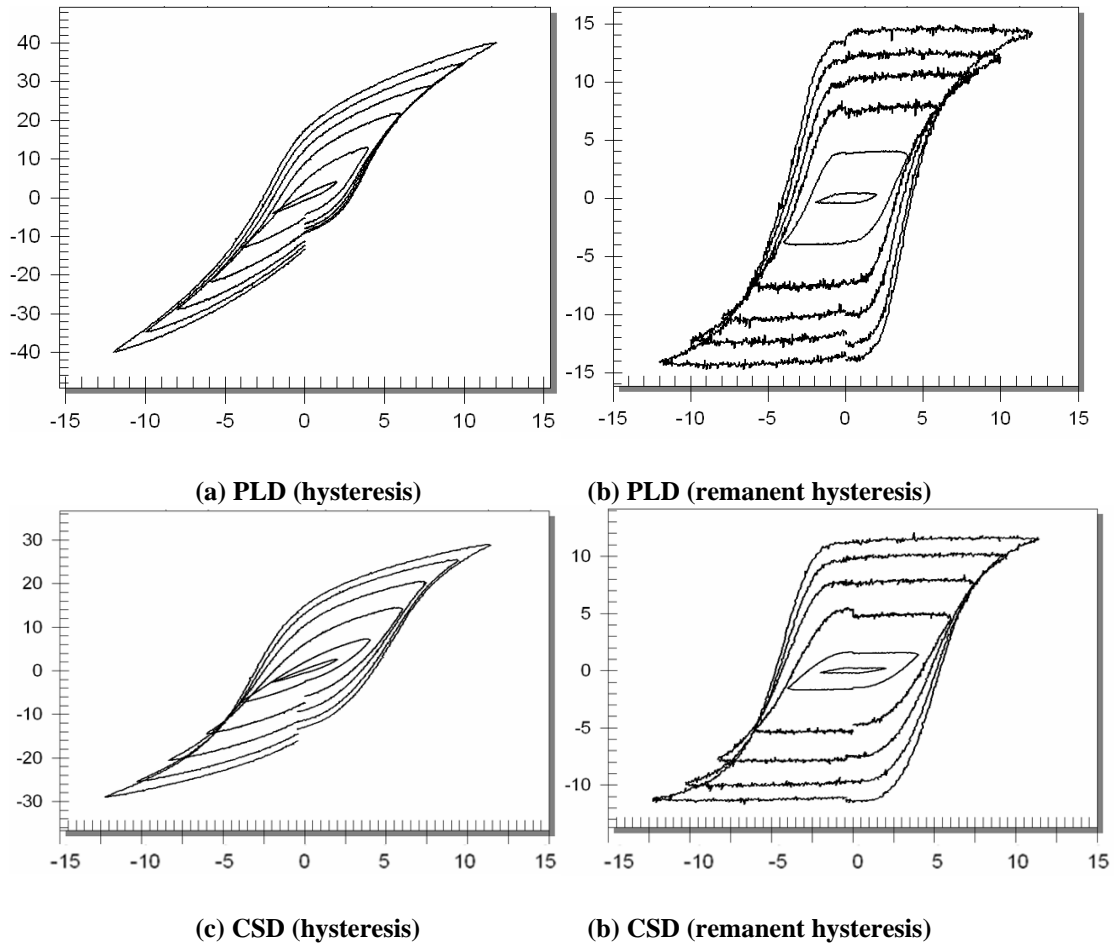


Fig. 8.13 Normal hysteresis and remanent hysteresis loops of PLD-grown BSmT films ((a) and (b), respectively) and CSD-derived BSmT films ((c) and (d), respectively)

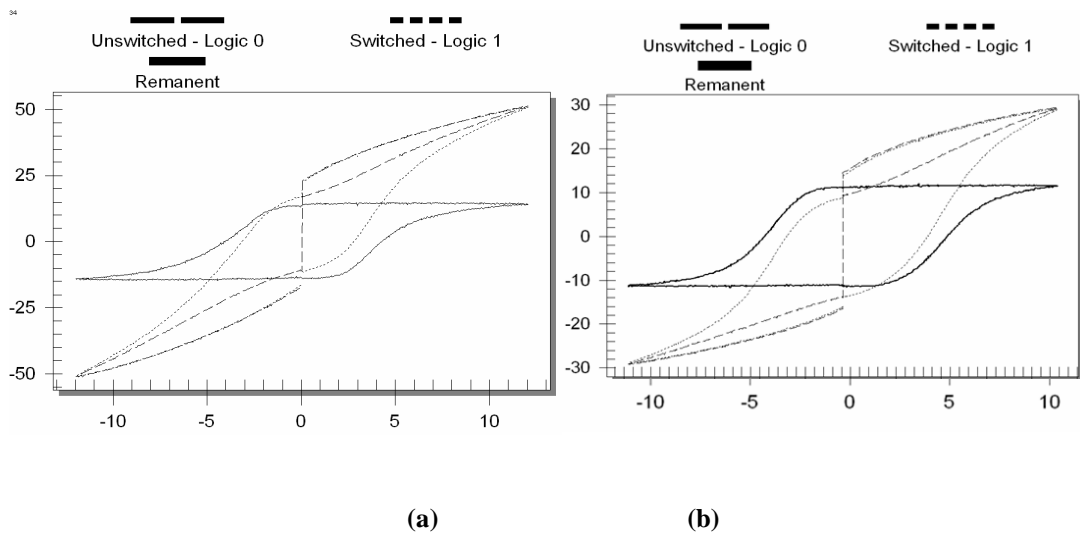


Fig. 8.14 Hysteresis loops of the (a) PLD-; (b) CSD-derived films

Fig. 8.14 shows detailed information about all parts of hysteresis loops (switched non-switched, and remanent parts), we can see that the proportions of the remanent

part in the whole polarisation for both films are ~30% and ~34%, for PLD and CSD-derived films. This reflects that both films have similar switched and non-switched proportions, despite very different fabrication procedures.

8.3 Conclusions

Piezoresponse force microscopy (PFM) was adopted to characterise Sm-doped bismuth titanate (BSmT) films. Domain structures were clearly observed in a PLD-grown BSmT film, which were closely related to the grain structures. Domain manipulation was carried out in a CSD-derived BSmT film, showing the film can be nearly uniformly polarised, which can be used in nanoscale device fabrication. Clear hysteresis loops were measured by PFM, which was an important proof of ferroelectricity.

Large spatial variations of piezoelectric hysteresis loops for the film surface of a CSD-derived BSmT film were observed and the possible reasons for that were proposed, such as different crystallographic orientations, fluctuations of chemical compositions in different grains, an inhomogeneous distribution of tip-generated field and grain size effect.

Effective electrostriction coefficient of a PLD-grown BSmT film was measured by combining results for the macroscopic polarisation, dielectric constant measurement and microscopic piezoelectric constant and showed that BSmT films had better piezoelectric properties (higher Q_{eff} , higher d_{zz}) than SBT films, un-doped BiT ceramics and films. It suggests that BSmT films are promising piezoelectric materials for MEMS use.

8.4 References

- 1 W. H. Ma and D. Hesse, *Applied Physics Letters* **85**, 3214 (2004).
- 2 H. Maiwa, N. Iizawa, D. Togawa, T. Hayashi, W. Sakamoto, M. Yamada, and S. Hirano, *Applied Physics Letters* **82**, 1760 (2003).
- 3 A.L. Kholkin, V.V. Shvartsman, and A.Y. Emelyanov, *Applied Physics Letters* **82**, 2127 (2003).
- 4 D. Damjanovic, *Reports on Progress in Physics* **61**, 1267 (1998).
- 5 A. Gruverman, O. Auciello, and H. Tokumoto, *Annual Reviews of Material Science* **28**, 101 (1998).
- 6 A. Gruverman, O. Auciello, and H. Tokumoto, *Journal of Vacuum Science & Technology B* **14**, 602 (1996).
- 7 A. Gruverman, *Applied Physics Letters* **76**, 106 (2000).
- 8 A. Roelofs, U. Boettger, R. Waser, F. Schlaphof, S. Trogisch, and L. M. Eng, *Applied Physics Letters* **77**, 3444 (2000).
- 9 S. V. Kalinin, A. Gruverman, and D. A. Bonnell, *Applied Physics Letters* **85**, 795 (2004).
- 10 V.V. Shvartsman, A.Y. Emelyanov, A.L. Kholkin, and A. Safari, *Applied Physics Letters* **81**, 117 (2002).
- 11 G. Zavala, J. H. Fendler, and S. Trolier-McKinstry, *Journal of Applied Physics* **81**, 7480 (1997).
- 12 A. Gruverman, O. Auciello, and H. Tokumoto, *Applied Physics Letters* **69**, 3191 (1996).
- 13 W. L. Warren, D. Dimos, and R. M. Waser, *MRS Bulletin* **21**, 40 (1996).
- 14 S. Dunn, *Journal of Applied Physics* **94**, 5964 (2003).
- 15 J. F. Scott, *Ferroelectric Memories*. (Springer, Berlin, 2000).
- 16 M. Alexe, C. Harnagea, D. Hesse, and U. Gosele, *Applied Physics Letters* **79**, 242 (2001).
- 17 A. Gruverman, B. J. Rodriguez, A. I. Kingon, R. J. Nemanich, J. S. Cross, and M. Tsukada, *Applied Physics Letters* **82**, 3071 (2003).
- 18 Radiant Technologies Inc., RT6000 Standardised ferroelectric test system operation manual.

- ¹⁹ J. Lee and R. Ramesh, *Applied Physics Letters* **68**, 484 (1996).
- ²⁰ W. H. Ma and D. Hesse, *Applied Physics Letters* **84**, 2871 (2004).
- ²¹ A. Gruverman, B. J. Rodriguez, A. I. Kingon, R. J. Nemanich, A. Tagantsev, J. S. Cross, and M. Tsukada, *Applied Physics Letters* **83**, 728 (2003).
- ²² I. Szafraniak, C. Harnagea, R. Scholz, P. Bhattacharya, D. Hesse, and M. Alexe, *Applied Physics Letters* **83**, 2111 (2003).
- ²³ A.L. Kholkin, E. L. Colla, A. K. Tagantsev, D. V. Taylor, and N. Setter, *Applied Physics Letters* **68**, 2577 (1996).
- ²⁴ A. L. Kholkin, E. K. Akdogan, A. Safari, P.-F. Chauvy, and N. Setter, *Journal of Applied Physics* **89**, 8066 (2001).
- ²⁵ M. Alexe, C. Harnagea, W. Erfurth, D. Hesse, and U. Gosele, *Applied Physics A* **70**, 247 (2000).
- ²⁶ A. L. Kholkin, K. G. Brooks, and N. Setter, *Applied Physics Letters* **71**, 2044 (1997).
- ²⁷ E. C. Subbarao, *Physical Review* **122**, 804 (1961).
- ²⁸ H. Matsuda, S. Ito, and T. Iijima, *Applied Physics Letters* **85**, 1220 (2004).
- ²⁹ V. Nagarajan, C. S. Ganpule, B. Nagaraj, S. Aggarwal, S. P. Alpay, A. L. Roytburd, E. D. Williams, and R. Ramesh, *Applied Physics Letters* **75**, 4183 (1999).

Chapter 9 Conclusions and future work

9.1 Conclusions

9.1.1 PLD-grown W-substituted SBT thin films

We fabricated SBT and W-doped SBT ferroelectric thin films by PLD on platinised silicon substrates. The effects of fabrication temperature (from 700 °C to 800 °C) and W-doping level (10 mol% and 20 mol%) on film properties were studied. The crystallinity of SBTW films improved with increasing fabrication temperatures, resulting in enhanced ferroelectric properties and dielectric properties above the fabrication temperature of 750 °C: 10 mol% W-doped films fabricated at 800 °C showed a $2P_r$ of $8 \mu\text{C}/\text{cm}^2$. W-doping of 20 mol% also reduced the coercive voltage ($2V_c$) from 4.0 V to 2.5 V. W-doping lowered the required annealing temperature of SBT films, which can explain the improvement of crystallinity, dielectric and ferroelectric properties. The lower required fabrication temperature will increase the chances of applications of SBT films in silicon integrated technology.

9.1.2 PLD-grown epitaxial BNdT films

Dense ceramic samples of $\text{Bi}_{4-x}\text{Nd}_x\text{Ti}_3\text{O}_{12}$ and $\text{Bi}_{4-x}\text{Sm}_x\text{Ti}_3\text{O}_{12}$ ($x = 0, 0.55, 0.70, 0.85, 1.00$) were fabricated by solid state processing for PLD targets. XRD results confirmed that Sm or Nd doping successfully incorporate into the perovskite lattice.

Highly epitaxially (001)-, (118)-, and (104)-oriented BNdT films were grown by PLD on (001)-, (011)-, and (111)-oriented STO single crystal substrates, respectively.

Two-dimensional epitaxial relationships between the BNdT films and their corresponding STO substrates were derived as: BNdT(001)//STO(001), BNdT(118)//STO(011), BNdT(104)//STO(111), and BNdT[$\bar{1}10$]/STO[100]. A three-dimensional orientation relationship between films and substrates was derived as: BNdT(001)//STO(001), BNdT[$\bar{1}10$]/STO[100]. The RMS surface roughness of (001)-, (118)-, and (104)-oriented BNdT films was 0.7 nm, 10.8 nm and 14.2 nm, over areas of $2 \times 2 \mu\text{m}^2$.

Films showed strong dependence of ferroelectric properties on the crystalline orientation. The highest remanent polarisation was exhibited by (104)-oriented films, whilst *c*-axis-oriented films showed very weak ferroelectric activity. These data confirm that the polar axis of the BNdT films remains in the *a-b* plane instead of along the *c* axis, as recently suggested by other researchers. In addition, the (104)-oriented film showed better leakage characteristics than the (118)-oriented one. No significant fatigue was observed in the films of (118)- and (104)-orientations.

9.1.3 PLD-grown polycrystalline BSMT films

The fabrication procedures for PLD-grown BSMT films on platinised silicon substrates were optimised by varying fabrication temperature and laser fluence. The fluorite phase ($\text{Bi}_2\text{Ti}_2\text{O}_7$) was observed as an intermediate phase and fully transformed to the perovskite phase ($\text{Bi}_4\text{Ti}_3\text{O}_{12}$) in the 750 °C-fabricated film. A comparison of films grown using targets with and without bismuth excess suggested that using bismuth excess targets can facilitate the crystallisation of the perovskite phase.

The film deposited at the optimised conditions (225 mJ and 750 °C) has uniformly-distributed, closely-packed grains, a dense columnar structure, and is

continuous and chemically homogenous. Moreover, EDX results suggest that it has successful substitutions of Sm for Bi, and the film composition is close to the intended value.

Effects of Pt bottom layer orientation and Sm doping level on BSmT film properties were studied. Silicon substrates with (111)- and (200)-preferred oriented Pt bottom layer were used to deposit BSmT film by PLD. A higher proportion of (117)-oriented grains was achieved for the films grown on Pt(111)/Si substrates (54.0%) than Pt(200)/Si substrates (19.5%). Both films show similar surface topography and a comparable surface roughness. An examination of atomic configurations confirmed good match of atomic planes of Pt (200) and BSmT (00 l) if the following orientation relationship is satisfied: BSmT (00 l) // Pt (200) and BSmT [001] // Pt [110]. The atomic arrangement between Pt (111) and BSmT (117) planes needs further investigation.

The film grown on Pt(111) has a higher $2P_r$ than the film grown on Pt(200), which may be related to the higher proportions of (117)-oriented grains. This suggests that the polar axis of the Sm doped films is close to within the a - b plane, since in that case the polar axis of the (117)-oriented grains is closer to the normal direction of the film surface.

Films of different Sm doping levels were fabricated on Pt-coated silicon substrates. XRD results show that the increasing Sm doping content increases the proportion of (117)-oriented grains.

The inclusion of Sm³⁺ in the perovskite block is expected to influence the structural and electrical properties of BiT films in several ways by suppressing the P_s value (intrinsic effect) or increasing the non- c -axis-oriented grain growth (extrinsic effect).

In our study, remanent polarisations increase with the increasing Sm content up to $x = 0.70$, then decrease with a further increase of x , which imply that the extrinsic effect (the crystallographic orientation of the films) dominates the ferroelectric properties during $x = 0 \sim 0.70$, then with a further increase of doping level, the effect of the decrease in P_s value dominates.

After Sm doping, the Bi in the A sites becomes more stable than the undoped BiT, or, the oxygen vacancy-related domain-pinning reduces, resulting in the reduction in dissipation factor and improved fatigue resistance.

For comparison, films grown on Pt/Si both with and without a LNO buffer layer between film and Pt layer substrates were fabricated by PLD. The bottom electrodes directly influenced the grain size and the surface roughness of the films. Films grown on Pt/Si have larger grains within a finer grained matrix. However, films grown on LNO/Pt/Si have a uniform and smaller grain size, but are rougher (the RMS surface roughness of the BSmT/Pt and BSmT/LNO/Pt films was ~ 9.7 nm and ~ 14.8 nm, respectively). There was an observation of a degradation of polarisation on LNO/Pt/Si. Unexpectedly, a BSmT/Pt film has a much lower leakage current density than a BSmT/LNO film, which may be related to the higher surface roughness for the film with the LNO buffer layer.

9.1.4 CSD-derived polycrystalline BSmT and BNdT films

In this study, an alkoxide-salt method was adopted to prepare the precursors for BSmT and BNdT film fabrication. Precursors of Bi-Sm(Nd)-Ti which were stable for at least eight months in air ambient were successfully developed and BSmT(BNdT) ferroelectric films were fabricated using the spin-coating technique.

In-situ FT-IR studies on the decomposition of the Bi-Sm-Ti precursor, which is an analogy of the pre-baking stage during film fabrication, reveals that acetic acid serves as chelating agent to improve the homogeneity of the precursor solution by generating a dense and homogeneous Ti-O-Ti polymeric network and, at a baking temperature of 300 °C, most organic compounds are decomposed and evaporated.

Raman spectroscopy reveals that an excitation of the active modes of perovskite phase becomes stronger with increasing temperature annealing above 600 °C, indicating the development of the crystallinity for the perovskite phase in BSmT films.

XRD and Raman results confirm the existence of fluorite as an intermediate phase between the amorphous and perovskite phases of BSmT. Increasing annealing temperature favours the growth of *c*-axis-oriented grains and increases grain sizes.

AFM and SEM images, as well as XRD patterns, all indicate an increase of grain size with increase of annealing temperature. FE-SEM images show that the films have a clear and sharp boundary with Pt bottom electrodes and a grainy structure.

An increase in dielectric constant value with increasing annealing temperature was observed, which may be attributed to the increase in grain size and/or density of the films. The values of dissipation factor at 100 kHz of the same set of films decreased with increasing annealing temperature until 700 °C, and then increased at the annealing temperature of 750 °C, suggesting that $\tan \delta$ is predominantly affected by the film density, since a slight reduction in density was seen at this temperature.

Although the *c*-axis-oriented grains were favoured with increasing annealing temperature, the P_r increased with increasing annealing temperature, which was attributed to the enhancement of grain development. The higher leakage current

measured after a higher annealing temperature could be the result of the increased surface roughness. The BSmT and BNdT films annealed at 700 °C and 750 °C show excellent electrical fatigue resistance. The electrical properties of the films fabricated in this study (dielectric and ferroelectric properties, leakage current characteristics and electrical fatigue properties), are comparable or superior to those previously reported for similar films developed by other techniques or with other doping elements.

A summary of previous studies of La-, Nd-, Sm-doped BiT films, and some other doping elements (Eu, Pr) was given. It can be seen that the $2P_r$ of our films are larger than the average value of La-doped films reported, and comparable to the Nd- and Sm-doped films reported by others. The E_c values of our films are also comparable to the reported values.

Low temperature electrical properties of BSmT ferroelectric thin films have been investigated, suggesting that BSmT thin films are very promising for extremely low temperature nonvolatile memory applications.

The results of BNdT films annealed at different oxygen partial pressure (O_2 , air, N_2) showed that:

- 1). Oxygen ambience affected structural properties of the films by enhancing the growth of perovskite phase (phase formation), increasing grain size (grain growth), and assisting the growth of (117)-oriented grains (crystallographic orientations).
- 2). As a result, the best electrical properties (high $2P_r$, low E_c , low leakage current density, and best fatigue resistance) were achieved in O_2 -annealed films.
- 3). Oxygen vacancies play an important role in the electrical properties of BNdT ferroelectric films.

9.1.5 Piezoelectric properties of BSMT films

Piezoresponse force microscopy (PFM) was adopted to characterise BSMT films. Domain structures were clearly observed in a PLD-grown BSMT film, which were closely related to the grain structures. Domain manipulation was carried out in a CSD-derived BSMT film, showing the film can be nearly uniformly polarised, and thus has applications in nanoscale device fabrication. Clear hysteresis loops were measured by PFM, which was an important proof of ferroelectricity.

Large spatial variations of piezoelectric hysteresis loops across the surface of a CSD-derived BSMT film were observed and the possible reasons for that were proposed, such as different crystallographic orientations, fluctuations of chemical compositions in different grains, an inhomogeneous distribution of tip-generated field and grain size effect.

Effective electrostriction coefficient of a PLD-grown BSMT film was measured by combining macroscopic polarisation, dielectric constant measurement and microscopic piezoelectric constant, and showed that BSMT films had better piezoelectric properties (higher Q_{eff} , higher d_{zz}) than SBT films, un-doped BiT ceramics and films. It suggests that BSMT films are promising piezoelectric materials for MEMS use.

9.2 Future work

1. Optimisation of film composition.

Further optimisation can be done using a combination of A- and B-site doping, such as both Sm (or Nd) and W (or V) doping. The goal is to both increase the remanent

polarisations and decrease the coercive field. EDX analysis is needed to measure film compositions.

2. Structural characterisation, especially high resolution TEM.

For epitaxial films, high resolution TEM would be very useful to reveal the growth mechanism and the orientation relationships between films and substrates.

A detailed high resolution TEM study of polycrystalline films on Pt/Si substrates would clarify the mechanism for preferred film orientation development.

In the current study, a serial resistance effect of the interfacial layer between the oxide electrode and BSmT films was proposed to account for the degradation of polarisation in the BSmT films grown with LNO buffer layer on Pt/Si substrates. A direct observation (or not) of this layer using a high resolution TEM study would clarify this situation.

3. Impedance measurements in the high temperature range (200 ~ 550 °C).

High temperature complex dielectric and impedance analysis can reveal the mechanisms of charge migrations and dielectric relaxation; therefore, it can help us to understand electrical degradation (fatigue, imprint) and long-term instability (retention). It can also clarify the conductivity mechanisms about the contributions of different charge carriers in grains, grain boundaries and interfaces.

Some preliminary measurements on BSmT films have been carried out in the present study (results not shown in the thesis), however, due to time limitation, they have not been finalised. A complete analysis therefore is needed in the future.

4. DC leakage current measurements are needed over a wider temperature range, such

as at high temperature (up to 300~400 °C), to reveal the conductivity mechanism in the films.

5. Retention properties of the films at different temperature from room temperature up to 150 °C would provide a complete assessment of the films and their suitability for FeRAM applications.

6. Films showing satisfactory electrical properties can be used for FeRAM device fabrication in the near future to assess their viability for commercial applications.